Valentine Kanyanta *Editor*

Microstructure-Property Correlations for Hard, Superhard, and Ultrahard Materials

Springer

Microstructure-Property Correlations for Hard, Superhard, and Ultrahard Materials

Valentine Kanyanta
Editor

Microstructure-Property Correlations for Hard, Superhard, and Ultrahard Materials

Springer

Editor
Valentine Kanyanta
Principal Research Scientist
Element Six Limited
Oxfordshire, UK

ISBN 978-3-319-29289-2 ISBN 978-3-319-29291-5 (eBook)
DOI 10.1007/978-3-319-29291-5

Library of Congress Control Number: 2016937000

Printed on acid-free paper

This Springer imprint is published by Springer Nature
The registered company is Springer International Publishing AG Switzerland

Contents

Contributors

Declan Carolan ELEVATE Marie Curie Research Fellow, Department of Mechanical Engineering, Imperial College London, London, UK

Alojz Ivankovic Professor of Engineering Mechanics, School of Mechanical and Materials Engineering, University College Dublin, Dublin, Ireland

Valentine Kanyanta Principal Research Scientist, Element Six Limited, Oxfordshire, UK

Maweja Kasonde Research Fellow, Element Six Limited, Oxfordshire, UK

Walace Matizamhuka Senior Lecturer, Department of Metallurgical Engineering, Vaal University of Technology, Vanderbijlpark, South Africa

Stan Veprek Professor Emeritus, Department of Chemistry, Technical University Munich, Munich, Germany

Maritza G.J. Veprek-Heijman Department of Chemistry, Technical University Munich, Munich, Germany

Christopher John Howard Wort New Technology Manager, Element Six Limited, Oxfordshire, UK

Chapter 1
Hard, Superhard and Ultrahard Materials: An Overview

Dr. Valentine Kanyanta, CEng MIMechE

Abstract This chapter gives general overview of hard, superhard and ultrahard materials, which include oxides, borides, nitrides and carbides of metals, cermets, carbon nitrides, cubic boron nitride (c-BN) and diamond. These materials are widely adopted in many industrial applications where high hardness, high incompressibility and sometimes chemical inertness and thermal stability are primary requirements. Applications range from abrasives (e.g. polishing, grinding, cutting tool materials and wear-resistant coatings) to medical implants such as the hip-joint prosthesis. The chapter also discusses the influence of crystal structure, microstructures and processing parameters on material's macroscopic properties and behaviour. These different material characteristics are closely interrelated, and understanding their influence on material behaviour is fundamental to the development of suitable superhard and ultrahard materials required for current and emerging applications. It is obvious that in order to design a material with tailored properties, an understanding of how the microstructure affects the properties of the material, as well as how such a microstructure is realised via different synthesis and processing routes, is essential. Even equally important is having appropriate tools for structure characterisation and mechanical property measurements, which enables the derivation of accurate microstructure–property relationships.

1 Introduction

Hard, superhard and ultrahard materials such oxides, borides, nitrides and carbides of metals, cermets, carbon nitrides, cubic boron nitride (c-BN) and diamond are widely adopted in many applications where high hardness, high incompressibility and chemical inertness are a primary requirement. These include as abrasives for polishing, grinding, cutting tool materials and wear-resistant coatings and medical implants like the wearing parts of hip-joint prosthesis as shown in Figs. 1.1, 1.2, 1.3 and 1.4.

Dr. V. Kanyanta, CEng MIMechE (✉)
Principal Research Scientist, Element Six Limited, Oxfordshire, UK
e-mail: valentine.kanyanta@e6.com

V. Kanyanta (ed.), *Microstructure-Property Correlations for Hard, Superhard, and Ultrahard Materials*, DOI 10.1007/978-3-319-29291-5_1

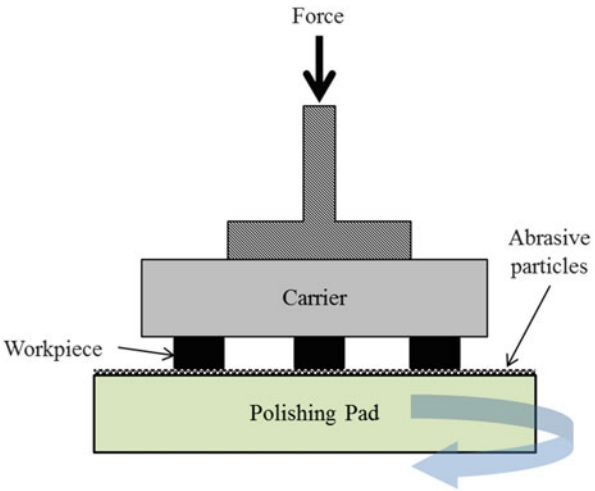

Fig. 1.1 Hard, superhard and ultrahard materials used in the form of abrasive particles in lapping or polishing operations. The most commonly used are alumina, silicon carbide and diamond. Lapping and polishing are usually final finishing operations that produce flat surfaces with extreme dimensional accuracy, remove surface imperfections and refine surface finish to achieve required roughness (Doi et al. 1999). The abrasive particles are suspended in a viscous or liquid media such as oil or grease

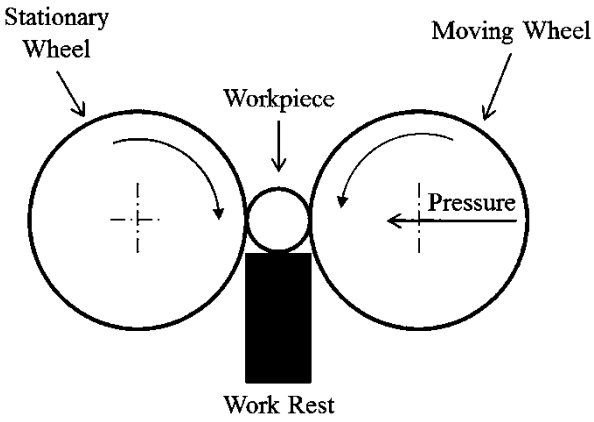

Fig. 1.2 Superhard and ultrahard materials such as cubic boron nitride and diamond and commonly used in vitrified grinding wheel for grinding operations (Jackson 2007; Lin et al. 2007). The diamond or c-BN grits are bonded in a glass matrix and onto a grinding wheel to form the cutting surface

Their outstanding mechanical, thermal, chemical and at times electrically insulating properties make them preferred materials for these applications. For example, the ability to retain high hardness and stiffness at elevated temperatures is especially important for high-speed dry machining of nickel-based and titanium-based superalloys (Wang and Rahman 2014; Liu et al. 2013; da Silva et al. 2013; Dudzinski et al. 2004; Kitagawa et al. 1997; Zhu et al. 2013; Patil et al. 2014; Pusavec et al. 2014; Wardany et al. 1996; Focke et al. 1978). The cutting tool material should also offer sufficient resistance to chemical diffusion wear, especially at elevated

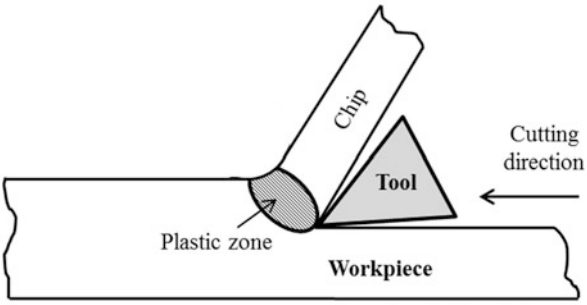

Fig. 1.3 An example of the use of hard, superhard and ultrahard materials as cutting tools in machining and cutting operations. The tool can be as a single crystal or in a polycrystalline form where, for example diamond or c-BN particles are sintered together (usually at higher temperatures and pressures) to form a fully bonded and in some cases intergrown (i.e. particles intergrown into each other) polycrystalline material

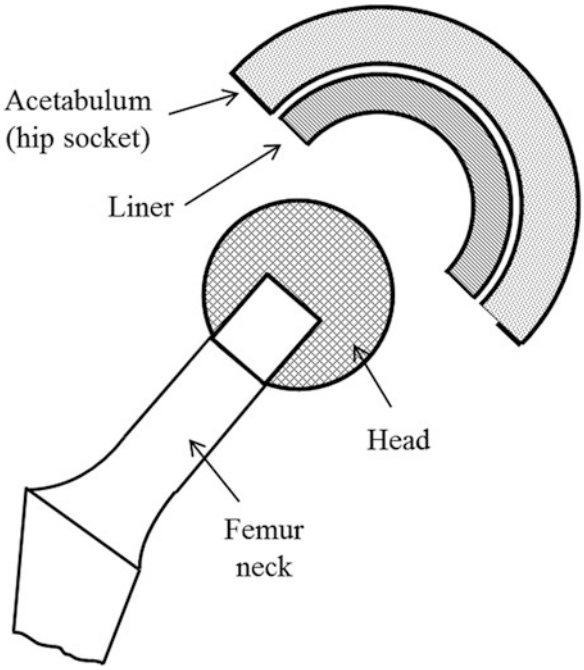

Fig. 1.4 The figure illustrates the use of diamond and diamond-like materials in biomedical applications, for example, forming part of the hip-joint prosthesis such as the acetabulum/liner and femur head (Pope et al. 2004; Nibennaoune et al. 2011). Diamond coatings and materials are seen as an efficient and reliable solution (or alternative) to the use of materials such as titanium alloys, ceramics and polymers which degrade after about a few years of use (Nibennaoune et al. 2011)

temperatures (Calatoru et al. 2008). In addition, as applications become more challenging with the development of new difficult to machine materials, the ever-increasing need to reduce machining costs, increase efficiency and achieve superior surface finish requirements for e.g. aerospace and automotive components, so does the need for tools with super- and ultrahardness increase. A detailed discussion of the industrial applications for superhard and ultrahard materials is presented in Chap. 2, except for hard materials which are discussed in the current chapter.

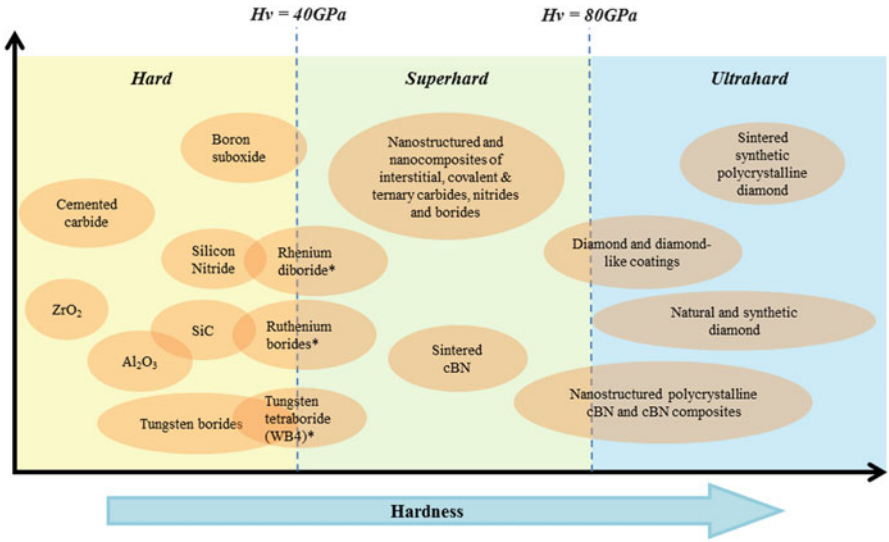

Fig. 1.5 Hardness classification of materials into the three categories, i.e. hard, superhard and ultrahard. Note that the "true" hardness of rhenium diboride (ReB2), ruthenium diboride and tungsten tetraboride (WB4) is still a subject of debate. In certain literature, values >40 GPa have been reported (Chung et al. 2007; Mohammadia et al. 2011), while this is disputed in other works as discussed in great detail in Chaps. 4 and 6. However, unlike the manufacturing of traditional superhard materials which require the use of high-pressure synthetic methods of several gigapascals, rhenium diboride and tungsten tetraboride can be synthesised in bulk quantities via arc melting under ambient pressure (Chung et al. 2007; Mohammadia et al. 2011). The reader can also consult the work by Lowther (2014) entitled "From Diamond to Superhard Borides and Oxides"

Superhard materials are defined as those with a load invariant Vickers hardness greater than 40 GPa and ultrahard materials as having a hardness exceeding 80 GPa. Note that at times the term "superhard" is used to describe all materials with a hardness of 40 GPa and above, including ultrahard materials. Hard materials would generally include materials with reasonably high hardness in comparison to most engineering materials such as refractory metals and high-speed steels and up to a hardness of 40 GPa. Figure 1.5 shows how the materials can be classified into these three groups, i.e. hard, superhard and ultrahard, based on their Vickers hardness values. Some of the hardness values of the so-called new superhard materials (e.g. marked with * in Fig. 1.5) are still debatable. For example, some literature have reported the hardness of rhenium diboride (ReB2) as about 48 GPa (Chung et al. 2007) and that of tungsten tetraboride (WB4) to be about 43 GPa (Mohammadia et al. 2011), which are close to the hardness of cubic boron nitride. However, these results are disputed in other studies where hardness values of these materials are shown to be less than 30 GPa (see Chaps. 4 and 6).

Diamond is the only known material which is intrinsically ultrahard. Its Vickers hardness is usually between 80 and 100 GPa (Sokolov et al. 2012; Diamond Materials 2015). In certain literatures, values of up to 150 GPa are reported

(Sokolov et al. 2012).[1] Examples of intrinsically superhard materials are cubic boron nitride (c-BN), carbon nitrides and ternary compounds such as boron carbon nitrides (BCN). The hardness of c-BN is about 50 GPa (Spriggs 2002). Cubic boron nitride is also known for its good hot hardness and better resistance to thermal–chemical degradation. Unlike diamond, c-BN has better thermal stability and chemical resistance which makes it a suitable material for machining ferrous metals (SandvikCoromant 2015; Element Six 2015; Greim and Schwetz 2006). Diamond is not normally employed in machining of ferrous materials due to its high reactivity to iron. In addition, diamond has poor thermal stability at temperatures above 700 °C (Westraadt et al. 2015).

Current research work has also shown that super- and ultrahardness can be achieved extrinsically by engineering the material's microstructure such as in nanostructured materials and nanocomposites. One example is titanium nitride and silicon nitride nanocomposites where hardness values of 50 GPa have been reported as later discussed in Chap. 6 (superhard and ultrahard nanostructured materials and coatings). There are also other materials reported in literature, e.g. C60 fullerite materials that are thought to have similar hardness to diamond or even harder than diamond (Blank et al. 1994, 1998a, b). However, in this particular case, there is no enough physical evidence so far to suggest that this is truly the case.

Although hard, superhard and ultrahard materials are widely used, the relationships between their microstructures, processing parameters and the resulting macroscopic properties are still poorly understood in comparison to other engineering materials such as steels. This has significant consequences on the ability to develop materials with desired properties. Therefore, the objective of this book is to discuss microstructure–property correlations, exploring key microstructure features and how they affect the properties of a material. This understanding is fundamental to the development of suitable superhard and ultrahard materials required for current and emerging applications. This is because the macroscopic properties of a material are a function of its crystal structure, microstructure and how the material is processed (manufacturing and other secondary processes such as heat treatments). The behaviour of the material during application is determined by these properties. The schematic representation of this interdependency or relationship between behaviour, properties, microstructure and processing parameters is shown in Fig. 1.6.

[1] The wide variations in the reported hardness values of diamond are partly due to defects and impurities in the crystal and the influence of residual strain. Sokolov et al. (2012) showed that the hardness of diamond single crystals can be increased up to 160 GPa via high- pressure and high-temperature treatment (HPHT treatment). They also showed that the toughness can likewise be improved via the same process. The treatments were done at temperatures of 2000–2700 °C and pressures between 5 - and 7 GPa, which resulted in an increase in the hardness of type I1a natural diamond single crystals from 80 to 100 GPa and that of type IIa monocrystals from 100 to 150 GPa (Sokolov et al. 2012). It is thought that this increase is due to changes in the defect and impurity structure induced by the transformation of defects mainly related to nitrogen impurities, as well as due to changes in internal stresses. The hardness of diamond crystals also varies in different crystallographic planes (Kraus and Slawson 1939).

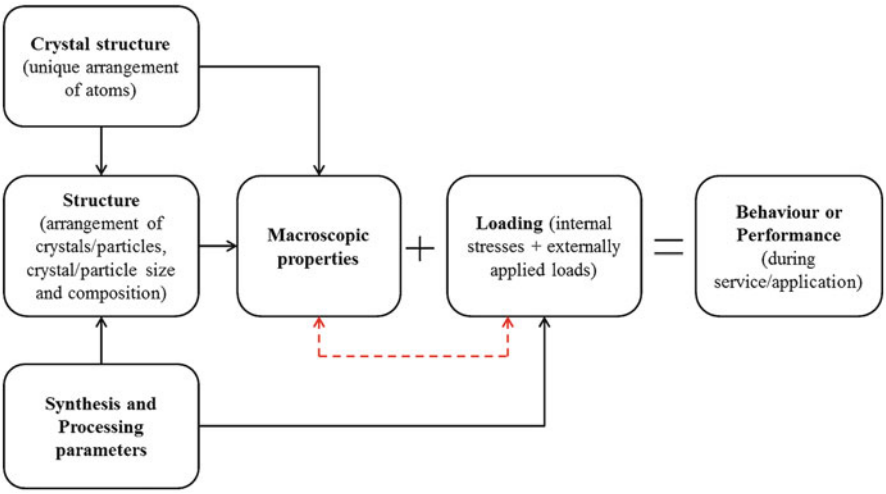

Fig. 1.6 Figure showing material behaviour as a result (or function) of the interrelationships between crystal/atomic structure, structure (nano-/micro-scale), synthesis and processing, properties and applied loads

- **Crystal structure:** The crystal structure is the unique arrangement of atoms, ions or molecules in a crystalline material. Properties such as hardness, shear modulus and shear strength (cleavage) are determined by the crystal structure. The two aspects of the crystal structure are the nature of interatomic bonds (whether covalent, metallic or ionic) and the crystal lattice system, i.e. cubic, tetragonal, orthorhombic, hexagonal, trigonal, triclinic and monoclinic structure. For example, diamond is intrinsically superhard or ultrahard because the interatomic bonding between the carbon atoms is characterised by short covalent bonds arranged in a cubic structure. This provides high resistance to plastic deformation which results in high hardness (Spriggs 2002). The same applies to why cubic boron nitride is intrinsically superhard (Greim and Schwetz 2006)
- **Structure (microstructure or nanostructure):** In a crystalline material, the microstructure or nanostructure is defined by the arrangement of crystals. Factors influencing the structure include the synthesis and processing parameters, crystal size/shape, size distribution and the composition of constituent material phases. The structure has a strong influence on mechanical properties like strength, toughness, ductility, hardness, corrosion resistance, wear resistance and how these properties change with temperature and strain rate. These properties in turn govern material behaviour during application as already discussed above. The relationship between microstructures and properties is discussed in greater detail in Chaps. 3, 4, 5 and 6. Chapter 6 particularly looks at superhard and ultrahard nanostructured materials and coatings, highlighting the conditions that should be met for achieving super- and ultrahardness in nanostructured materials and nanocomposites.

- **Synthesis and processing parameters:** Synthesis and processing parameters have been shown to have a strong influence on resulting structure and material properties (Meyers and Chawla 2008; Zhou et al. 2013), as well as the extent of residual stresses in a material (Sokolov et al. 2012; Kanyanta et al. 2014a; Chen et al. 2010). Synthesis and processing produce the structure which in turn affects properties. Therefore, the choice of an appropriate processing route is critical to realising desire properties.
- **Behaviour:** The behaviour of a material during application is a compound function of several parameters. Ideally one would think of two main factors as influencing material behaviour, i.e. material properties and loading (which include pre-existing internal stresses or residual stresses and externally applied loads). The geometry of a cutting tool, for example, can be classified under loading as it modifies how the load is applied on the cutting surface. Pre-existing residual stresses are mainly a result of synthesis and/or processing conditions. For example, Kanyanta et al. (2014a) showed how the residual stress state in a polycrystalline diamond cutting tool can be optimised with appropriate choice of high-pressure and high-temperature down-ramp conditions following the sintering process. McNamara et al. (2015) were also able to show that residual stresses at a microstructure level in an already sintered ultrahard material (i.e. polycrystalline diamond) can be optimised further with thermal treatments.

There is also another relationship between macroscopic properties and loading conditions as the properties of most materials change with temperature, strain rate and other environmental factors (e.g. humidity and chemical reactivity) (Kanyanta and Ivankovic 2010; Petrovic et al. 2012). Given this sometimes very strong interaction between properties and loading conditions and the effect on resulting material behaviour, it is imperative that the loading conditions chosen in laboratory tests are closely representative of the application of interest.

The relationships between these different aspects of material's mechanical behaviour (Fig. 1.6) are quite complex and not as straightforward as they may first appear. In addition, one would need appropriate characterisation techniques in order to accurately study the structure and measure microscopic and macroscopic properties. Whereas such methods and techniques are well developed for other materials, it is not yet the case for superhard and ultrahard materials. These challenges are discussed later in Chaps. 4 and 5 and the best approaches for accurate determination of material characteristics (i.e. structure and properties) presented. Identifying and using appropriate microstructure characterisation and mechanical property measurement techniques is essential to developing accurate microstructure–property relationships. It is obvious that having or using inappropriate techniques/tools would lead to inaccurate results. To add to the complexity, as the structure becomes nanosize particulate, image analysis using standard techniques such as scanning electron microscopy (SEM) becomes more challenging. Similar difficulties are also highlighted in mechanical property measurements, such as hardness and fracture toughness which are respectively discussed in Chaps. 4 and 5. It is shown in Chap. 4 that in order to reliably measure the hardness of

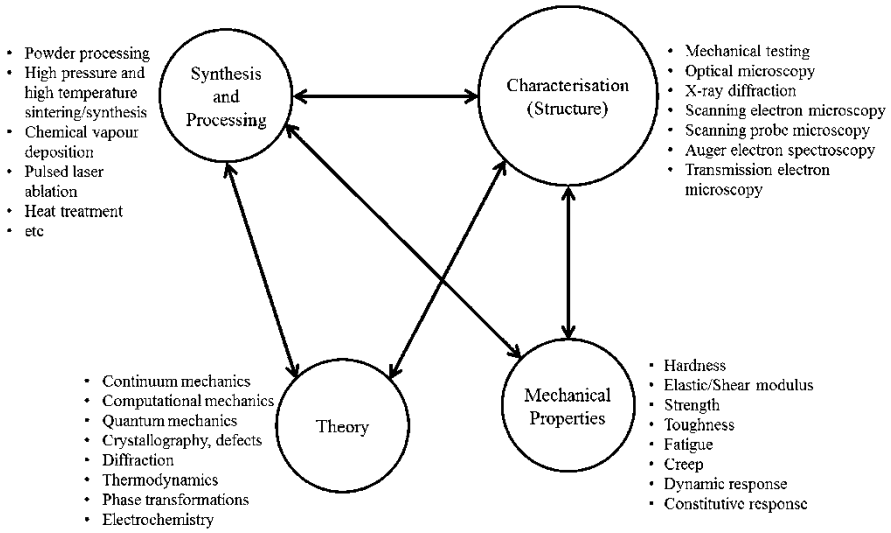

Fig. 1.7 The "iterative materials tetrahedron" applied to mechanical behaviour of materials (Meyers and Chawla 2008)

nanostructure materials and nanocomposites, one may require different techniques to those employed for other materials with microstructures having coarser particles. This in itself is already a complex relationship between structure and the characterisation technique employed, as well as between processing, structure and characterisation.

In addition to Fig. 1.6, a schematic framework known as "iterative materials tetrahedron" (Meyers and Chawla 2008) can be used to illustrate different aspects of mechanical behaviour of materials and their relationships, i.e. synthesis/processing, characterisation, theory and properties (Fig. 1.7). These four factors are interrelated such that a change to one affects the other three characteristics. For example, changing the synthesis or processing route will affect the choice of characterisation technique, mechanical property measurement method and the constitutive material model to apply. The iterative tetrahedron also shows that the derivation of fundamental material behaviour theory has to consider both the structure (from atomistic scale to micro-/mesoscale) and the process used to realise such as structure (i.e. synthesis and/or processing route).

2 Hard Materials

Hard materials are mainly used in applications requiring good resistance to abrasion wear and better ability to withstand high temperatures and corrosive environments. Traditional applications are as abrasive materials for polishing, grinding and cutting

tools used in machining operations. However, owing to their high thermal stability and corrosion resistance, hard materials are also widely used as thermal and chemical barrier coatings on components (Rosso et al. 2001; Herrmann and Klemm 2014). The current discussion looks at three groups of hard materials that have significant industrial applications, i.e. oxides, carbides and nitrides of metals and cermets.

2.1 Carbides and Nitrides of Metals

Carbides are compounds composed of carbon and a less electronegative element, e.g. calcium carbide (CaC_2), silicon carbide (SiC), tungsten carbide (WC), cementite (Fe_3C), etc. Carbides of group IV–VI transition d-metals such as titanium, zirconium, hafnium, vanadium, niobium, tantalum, chromium, molybdenum and tungsten are of especial interest to abrasive applications because of their refractory nature and high hardness (Santhanam 1996; Oyama 1996; Grossman et al. 1999; Novion and Landesman 1985; Rogl and Bittermann 1999). These are also referred to as interstitial compounds[2] with carbon atoms occupying the interstices, or holes, in the lattice of close-packed metal atoms (Oyama 1996). Figure 1.8 shows an example of the crystal structure of a transition metal carbide, with the carbon atoms ("red") sitting in the interstices of close-parked metal atoms (e.g. titanium or tungsten). These carbides also have metallic properties and exhibit a range of stoichiometries, e.g. titanium carbide, that make them useful as hard coatings on

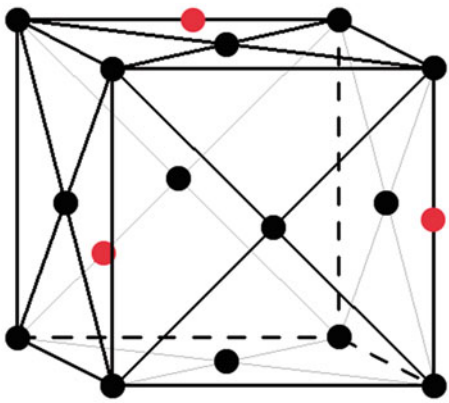

Fig. 1.8 An example of crystal structure of an interstitial carbide, i.e. transition metal carbide with the carbon atoms (*red*) sitting in the interstices of close-parked metal atoms (e.g. titanium or tungsten). Interstitial nitrides have a similar crystal structure except that the carbon atoms are replaced by nitrogen atoms

[2] An interstitial compound is formed when an atom of sufficiently small radius such as hydrogen, boron, carbon and nitrogen sits in an interstitial "hole" in a metal lattice. The most common ones with important industry applications are transition metal carbides and nitrides, e.g. titanium carbide and tungsten carbide.

metal or metal containing cutting tools (Ettmayer and Lengauer 1994). In terms of general abrasive applications, tungsten carbide (WC) is the most widely used especially in the form of cemented carbide where the WC particles are bonded together via a liquid-phase sintering process using a metal binder. Silicon carbide and boron carbide, B4C, are the other two interesting materials although different from transition metal carbides. These two materials have higher hardness compared to their transition metal carbide counterparts owing to the short covalent bonds between Si or B atoms and carbon atoms.

Nitrides are quite similar to carbides and can also be classified into three general areas depending on the nature of interatomic bonds, i.e. ionic, interstitial and covalent (Oyama 1996). Interstitial nitrides (i.e. nitrides of group IV–VI transition d-metals) have similar atomic structure to interstitial carbides, except that carbon atoms are now replaced by nitrogen atoms. Therefore, the properties of these materials in terms of hardness and stiffness are very similar to those of their carbide counterparts. In addition to high hardness, interstitial nitrides are also known for their good chemical resistance and are usually employed as hard chemical-resistant coatings (see Chap. 6). Covalent nitrides like boron nitride, similar to covalent carbides (e.g. silicon carbide or boron carbide), are extremely hard and have very high melting points.

2.2 Cermets

Cermets are hard and wear-resisting materials mainly based on the carbides or nitrides of metals and bonded with a lower melting point metal such as cobalt, nickel, etc. The most common ones are carbides of transition metals (e.g. tungsten, tantalum, titanium, molybdenum, niobium and vanadium) bonded with cobalt via a liquid-phase sintering process (Wang et al. 2016; Childs 2000; Cardinal et al. 2009). The hard particles are "glued" together by the metal alloy to form a metallic composite. These cermets or hard metals combine the high hardness and strength of metallic carbides (e.g. tungsten carbide, titanium carbide, tantalum carbides) or carbon nitrides (e.g. TiCN) with the toughness and plasticity of a metallic alloy binder such as cobalt, nickel and iron (Cardinal et al. 2009). In this case, the hardness and toughness of the bulk material can be tailored as required, for example, high toughness can be achieved with higher amounts of the metallic binder phase. Cemented tungsten carbide (WC) is the most widely used material of all the cemented carbides, nitrides and carbon nitrides. Its industrial applications include mining, oil and gas, bearings and as general wear parts.

The earliest cemented carbides are thought to have been developed at the beginning of the twentieth century with the first patent filed in 1923 by Treuhand-Gesellschaft für elektrische Glühlampen mbH in Berlin, Germany (Schröter 1923; Green et al. 1996: 744; Childs 2000). However, it was not until after the Second World War (WW2) that the market for cemented carbides really took off. The reader can consult literature by Schubert and Lassner (2010), Konyashin and Klyachko (2015) and Childs (2000) which give a very good extensive overview

of the history of cemented tungsten carbide and its adoption as a material of choice in many industrial applications. Today cemented WC, in particular WC–Co (sintered cemented WC using cobalt as the binding agent), is among the widely used in the abrasives industry. These include as cutting tools in machining, mining, oil and gas and wire drawing dies, as general wear parts including bearings and as materials for, e.g. anvils used in high-pressure and high-temperature presses for diamond and c-BN synthesis (Schubert and Lassner 2010; Childs 2000). Cemented carbides can be used to machine a range of materials including metals, wood, plastics, composites and soft ceramics (Schubert and Lassner 2010). Other novel potential applications of cemented carbides include as part of high-tech rocket and aircraft guidance systems (Yulin 2007). Research studies have already employed steel-reinforced carbide components (or steel bone carbide (SBC)) to form a vital part of missile inertial guidance systems. This is owing to the material's outstanding physical and mechanical properties such as high stiffness or incompressibility.

Figure 1.9 shows the estimated proportions of cemented carbides used in machining and wear parts applications in 2008 in terms of tonnage (Schubert and Lassner 2010). Although metal cutting only represents 22 %, it represents the highest turnover (65 %) in terms of new material variants due to the high degree of innovation. Most of the innovation in this area is on achieving the right combination of hardness and toughness required in continuous and interrupted machining.

Cemented carbides are manufactured via powder metallurgy (PM) process. This involves the mixing of respective powders (e.g. WC and Co/Fe/Ni) using ball milling or attrition milling in order to form a powder mix. Different shaping technologies can then be employed to form a part with desired geometry. These technologies include die pressing or direct forming, extrusion and powder injection moulding (PIM). Current technologies also include additive manufacturing

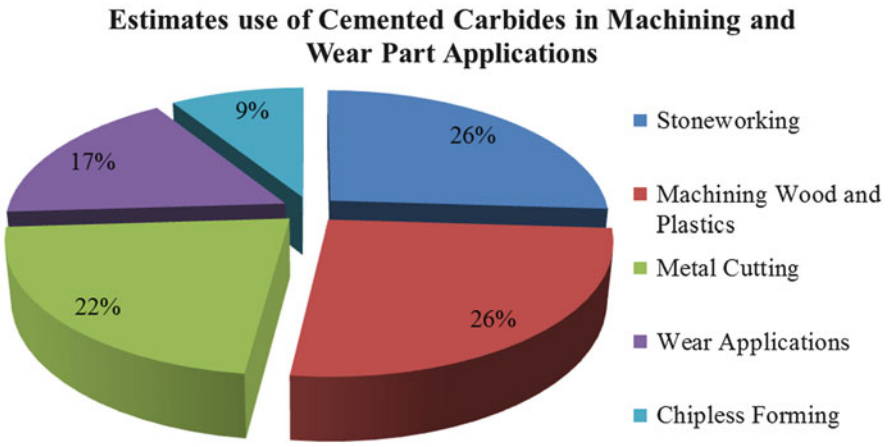

Fig. 1.9 Estimated proportions of cemented carbide materials (mainly cemented tungsten carbide) used in machining and wear parts applications in 2008 in terms of tonnage (Schubert and Lassner 2010)

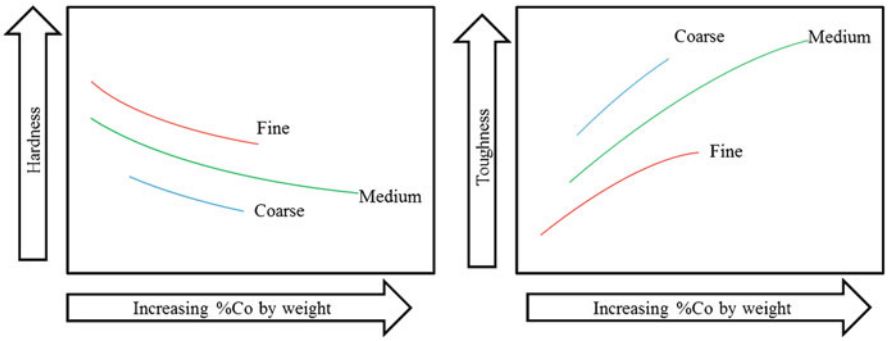

Fig. 1.10 Variations in the hardness (*left*) and toughness (*right*) of different WC–Co grades, i.e. fine, medium and coarse, with increasing cobalt (Co) content. The WC particle sizes for fine, medium and coarse are 1–2 um, 3–4 um and >5 um, respectively

methods such as 3D printing and laser sintering. The formed part, produced either through pressing, extrusion or injection moulding, is then subjected to high-temperature sintering process in order to obtain a fully dense liquid-phase sintered body (da Silva et al. 2001; Kim et al. 2003). Current methods also employ spark plasma sintering (Eriksson et al. 2013). The process and the reactions that take place during the sintering process are quite complex. The reader can consult the extensive published literature for details (Lay and Missiaen 2014; Kim et al. 2003; Christensen and Wahnstrom 2006; Eriksson et al. 2013; Kumar et al. 2011; da Silva et al. 2001; Wang et al. 2008; Chang et al. 2015; Sun et al. 2015).

The main advantage with cermets is the wide range of hardness and toughness values that can be achieved by simply changing the proportions of the hard particles (e.g. WC) and the metallic binder phase as illustrated in Fig. 1.10. The hardness of the bulk material can also be tailored by changing the particle size of the hard phase, which is in agreement with the well-established Hall–Petch relationship[3] (Hall 1951; Petch 1953). The interspacing between hard WC particles and the cobalt binder free mean path are important parameters in deriving the right properties of cemented carbides. Therefore, there is a limit to how much metallic binder can be used in these composites. When the proportion of the binder phase is very small, it can result in incomplete wetting of the particles. If the proportion is too high, you lose the hardness and strength of the material. It is also important to note that these parameters are not independent of the WC particle size. It is this multiple interdependency between different factors that makes the engineering of cemented carbide materials quite complex.

[3] Hall–Petch relationship assumes grain boundaries as a barrier to dislocation movement. Therefore, as the grain size decreases (or grain boundaries increase), it becomes difficult for dislocations to transverse these boundaries, and hence the yield strength of the material increases. It is important to note that there is a limit to this mode of strengthening. This is why infinitely strong materials do not exist. See Chap. 7 for a more detailed discussion.

The trends in Fig. 1.10 are derived from the actual published data (Okamoto et al. 2005; Sandvik Hard Materials 2005). The reader is advised to consult published literature for the actual values of how hardness and toughness (and other properties such as strength) change with changes in WC–Co compositions and particle size. However, the main purpose here is to show expected material behaviour trends rather than the absolute values. The average WC particle sizes for fine, medium and coarse in Fig. 1.10 are 1–2 um, 3–4 um and >5 um, respectively.

2.3 *Oxides of Metals*

The most commonly used oxides for abrasive applications are aluminium oxide (or alumina) and zirconium oxide. Examples of the applications include polishing, grinding, wear pads, protective coatings on tools and other wearing parts and sandblasting. Aluminium oxide in its crystalline form[4] has a Vickers hardness of between 20 GPa and 30 GPa (Bl'anda et al. 2013a, b; Alcalá et al. 2002), which is better than most cemented carbides. On the other hand, zirconium oxide has a much lower hardness usually below 8 GPa (Din and Kaleem 1998). Apart from the high hardness, these materials also offer high corrosion resistance and ability to withstand high temperatures without chemical degradation. The biggest drawback with aluminium oxide is its relatively low fracture toughness compared to cemented carbides, which is usually no greater than 5 MPa/m$^{0.5}$. This limits its use in applications such as cutting tools for machining. Higher toughness values of up to 10 MPa/m$^{0.5}$ are realisable with zirconium oxide. However, this is still much lower than what can be achieved with tougher cemented carbide grades.[5] In addition, zirconium oxide does not offer any significant benefit over cemented carbides in terms of hardness (see Fig. 1.5).

Like in cemented carbides, the hardness and toughness of these oxides can be improved by addition of other elements or compounds. For example, Din and Kaleem (1998) were able to enhance the hardness of partially stabilised zirconium oxide by addition of cerium oxide. Perkins (2006) was able to demonstrate that doping aluminium oxide with rare earth elements enhances the toughness of the material. This was thought to be caused by the segregation of these elements to the grain boundaries which affect the grain boundary strength and changes the mode of fracture from that of trans-granular fracture to intergranular fracture. Other examples include the use of techniques such as biomimicry and three dimensionally interpenetrating structure composites to engineer ceramic composites with signif-

[4] The hardness of amorphous alumina is about 3–4 times lower than crystalline alumina (Alcalá et al. 2002).

[5] Commercially available cemented tungsten carbide (WC–Co) grades used as cutting tools have toughness values of up to 25 MPa/m$^{0.5}$.

icantly enhanced mechanical properties that make them more "usable" industrial materials (Chang et al. 2010; Bl'anda et al. 2013a, b; Livanov et al. 2015; Roya et al. 2012).

3 Superhard and Ultrahard Materials

The only two traditional materials that fall into this category of superhard and ultrahard materials are cubic boron nitride and diamond, respectively. Other materials may include carbon nitrides, ternary compounds of nitrides, cubic BC2N (Solozheko et al. 2001), carbides and borides and some nanostructured materials and nanocomposites discussed later in Chap. 6. Diamond has Vickers hardness greater than 80 GPa, which makes it ultrahard. Cubic boron nitride (c-BN), which is the second hardness material, has a Vickers hardness value of about 50 GPa. Some of the new nanostructured materials and nanocomposites have been reported to have hardness values comparable to that of cubic boron nitride and in some cases close to that of diamond. One example is the quasi-ternary nc-TiN/Si3N4/TiSi2 nanocomposites which are thought to reach hardness values in excess of 50 GPa as discussed in Chaps. 4 and 6. Some publications claim values of about 100 GPa although this is highly disputable. This is discussed in great detail in Chap. 6.

3.1 Diamond

Diamond is intrinsically ultrahard (i.e. Vickers hardness >80 GPa) because of its short covalent bonds (1.54 Å) between its carbon atoms and cubic crystal structure. It is a metastable allotrope of carbon[6] with atoms arranged in a modified version of face-centred cubic (fcc) crystal structure referred to as the "diamond cubic" or "diamond lattice". Figure 1.11 shows two examples of carbon allotropes, i.e. diamond and graphite.

Unlike natural diamonds whose properties can widely vary due to variations in defect density and level of impurities, synthetic diamond can be manufactured with more controlled and consistent properties. Therefore synthetic diamonds are preferred for most industrial applications. The other reason is of course the relative lower cost and ability to make it in sufficiently high volumes using high-pressure presses or chemical vapour deposition. These two manufacturing methods are discussed further in Chap. 2. Controlling the type and level of impurities or defects in diamond crystal can significantly improve its mechanical properties such as

[6] Because of its valence, carbon has the ability to form many allotropes. The common ones are diamond and graphite. In recent years, many other allotropes of carbon have been discovered, e.g. buckminsterfullerene, graphene, amorphous carbon and carbon nanotubes (Loos 2015).

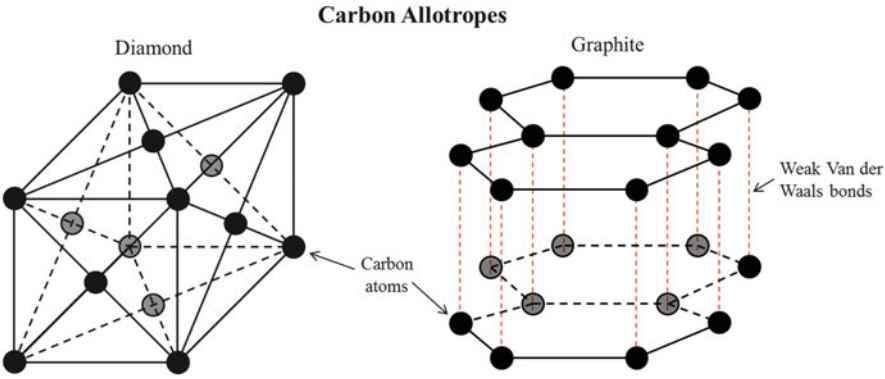

Fig. 1.11 Examples of carbon allotropes, i.e. diamond (*left*) and graphite (*right*). Graphite has a much lower hardness compared to diamond because of its layered crystal structure with very weak van der Waals bonds holding the layers together. Several other carbon allotropes exist (Loos 2015)

strength, hardness and toughness. For example, doping of diamond with elements such as nitrogen can be used to tailor its strength (Espinosa et al. 2006; Catledge et al. 1999).

Owing to its extremely high hardness, diamond is widely used in industrial applications requiring very high resistance to abrasion wear. It can be used as single crystals (for machining or as abrasive particles in lapping, polishing and grinding operations) or as a polycrystalline material where individual grains are connected together via grain boundaries. One area where diamond is predominantly being used is in oil and gas drilling, mainly as polycrystalline diamond cutting tools. These tools consist of a polycrystalline diamond layer in situ sintered onto a tungsten carbide substrate via a HPHT sintering route. The use of diamond in oil and gas has transformed the economics of the drilling activities by increasing efficiency, offering high penetration/drilling rates and reducing drilling times and providing longer tool life which means less number of drill bit changes (Scott 2006). The later reduces downtime and enables better planning of drilling activities. Figure 1.12 shows the growth in the use of diamond as cutting tools in oil and gas drilling applications. By 2004, diamond accounted for nearly 60 % of the footage drilled. Today, it is the material of choice in this application. Although polycrystalline diamond is successfully used in oil and gas drilling, it still at times suffers from catastrophic failures due to its inherent low fracture toughness. It also has poor thermal stability at high temperatures (Westraadt et al. 2015). Therefore, research and innovation on polycrystalline diamond materials is still ongoing in order to improve toughness and thermal stability (Kanyanta et al. 2014a, b; McNamara et al. 2015; Westraadt et al. 2015; Keshavan et al. 2008).

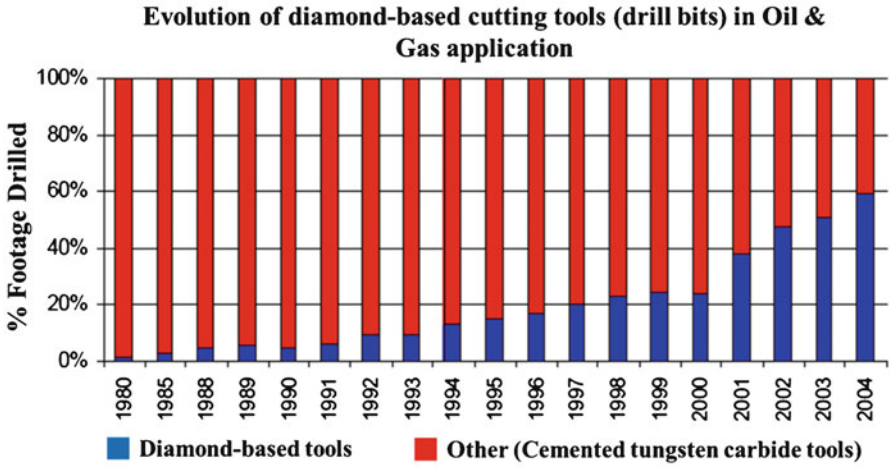

Fig. 1.12 Growth in the use of diamond-based tools (mainly HPHT sintered polycrystalline diamond) in oil and gas drilling application (*Source*: Scott 2006, *The History and Impact of Synthetic Diamond Cutters and Diamond Enhanced Inserts on the Oil and Gas Industry* (Scott 2006))

3.2 Cubic Boron Nitride

Cubic boron nitride or c-BN is the second hardness material after diamond. Its synthesis process involves the dissolution of hexagonal boron nitride (h-BN[7]) in a solvent–catalyst such as an alkaline metal or its nitride, followed by spontaneous nucleation of c-BN under high-pressure and high-temperature (HPHT) conditions (Eko et al. 2013). The high hardness and bulk modulus of c-BN are due to the short covalent bonds (i.e. 1.57 Å) between boron and nitrogen atoms and the close-packed cubic crystal structure (Fig. 1.13). However, unlike diamond, c-BN is insoluble in iron, nickel, cobalt and other metal alloys making it suitable for machining of ferrous materials and cobalt-based or nickel-based superalloys. In addition, c-BN also has better thermal stability compared to diamond (Goel et al. 2012). It can be used at temperatures of up to 2000 °C[8], whereas diamond starts to oxidise at temperatures above 600 °C or 700 °C in open atmosphere (Westraadt et al. 2015). Chapter 2 presents a more extensive discussion on the industrial applications of both c-BN and diamond.

[7] Hexagonal boron nitride (h-BN) is a more stable crystalline form compared to c-BN (just like graphite is more stable than diamond) and has a layered structure similar to graphite (Fig. 1.9). Within each layer, strong covalent bonds exist between boron and nitrogen atoms. However, the layers are only held together by weak van der Waals forces which make h-BN relatively soft (or less resistant to plastic deformation) compared to c-BN.

[8] c-BN is also susceptible to transformation to h-BN at high temperatures. However, in relative terms, it is much more thermally stable than diamond.

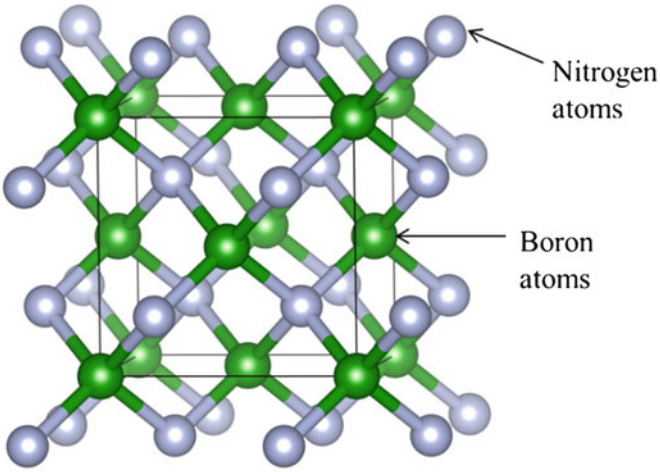

Fig. 1.13 Crystal structure of cubic boron nitride. Its high hardness is due to the short covalent bonds (i.e. 1.57 Å) between boron and nitrogen atoms and the close-packed cubic crystal structure

3.3 Nanostructured Materials and Nanocomposites of Carbides, Nitrides and Borides

Nanostructured materials and nanocomposites of interstitial, covalent and ternary compounds of carbides, nitrides and borides are a promising area of research for development of new superhard materials (Chen et al. 2011). Already superhard nanocomposites of these compounds have been prepared with hardness values greater than that of cubic boron nitride, e.g. quasi-ternary nc-TiN/Si3N4/TiSi2 nanocomposites and other related materials discussed in Chap. 6. This continues to be an interesting area of future research especially if diamond and c-BN are to be replaced by cheaper superhard materials which do not need the use of high pressures of several gigapascals required in the manufacturing of synthetic diamond and c-BN. For example, rhenium diboride and tungsten tetraboride can be synthesised in bulk quantities via arc melting under ambient pressure (Chung et al. 2007; Mohammadia et al. 2011). Apart from Chap. 6, the reader can also consult the work by Lowther (2014) entitled "From Diamond to Superhard Borides and Oxides" which looks at other materials that can potentially be superhard. However, one should bear in mind the important discussions presented in Chap. 6 that not all materials and systems (including those discussed by Lowther (2014) and in other literature) can be superhard. Furthermore, although hardness enhancement can be achieved in nanostructured materials, it is limited by grain boundary shear when the crystallite size decreases to 10–15 nm called the "strongest size". However, when low-energy grain boundaries such as stacking faults and twins are introduced, the grain boundary shear can be reduced resulting in significant hardness enhancement. The reader is advised to read Chap. 6 which discusses these mechanisms in great detail.

4 Book Overview: Why Microstructure–Property Correlation Is Important

It is obvious that in order for one to design a material with tailored properties, an understanding of how the microstructure affects the properties of the material is essential. There is also a need to understand how such a microstructure can be arrived at by establishing the influence of processing parameters as earlier illustrated in Figs. 1.6 and 1.7. Arriving at this microstructure–property correction is not trivial. Of fundamental importance is ensuring that correct analytical tools and experimental techniques for analysing the microstructure and accurate determination of properties are used. This is the central theme to this book and extensively discussed in the chapters presented later on (i.e. Chaps. 2–7). With an exception of Chap. 2 which discusses the applications of superhard and ultrahard materials, Chaps. 3–6 focus on the principles of microstructure–property correlations in superhard and ultrahard materials. Although Chaps. 3–6 focus on superhard and ultrahard materials, as these are the most challenging materials when it comes to characterisation and properties measurements, reference is also made to hard materials such as oxides, carbides, nitrides and borides. This book is also designed to enhance the understanding of mechanical material behaviour and why the choice of appropriate characterisation and properties measurements tools is important to deriving accurate microstructure–property correlations.

Chapter 3 explores the correlations between the microstructures and resulting properties from a theoretical framework, looking at key microstructure features and their effect on mechanical properties such as hardness, fracture toughness, strength, wear and thermal properties. The chapter discusses a number of analytical and empirical structure–property–behaviour model(s) and the difficulty in extending these theories to hard and superhard materials, as well as nanostructured materials. The focus of Chap. 4 is on the measurements of hardness of hard and superhard materials and coatings. It highlights the difficulties associated with the use of indentation methods when applied to super- and ultrahard materials and suggests ways in which incorrect measurements can be avoided. This includes the use of a classical two-step method, where, after the indentation with a given load, the size of remnant indentation is measured by a microscope, in order to verify results obtained from “nanoindentation”. The chapter also gives special attention to the measurement of the mechanical properties of super- and ultrahard thin films on softer substrates. Chapter 5 looks at fracture toughness measurements of hard and superhard materials and highlights significant limitations associated with several fracture testing methods. The book concludes with a very extensive discussion on superhard and ultrahard nanostructured materials, composites and coatings (Chap. 6) and a brief overview of the future of hard and superhard material design, processing and manufacturing, mainly in terms of the use of additive manufacturing technologies such as 3D printing and injection moulding.

References

Alcalá G, Skeldon P, Thompson GE, Mann AB, Habazaki H, Shimizu K (2002) Mechanical properties of amorphous anodic alumina and tantala films using nanoindentation. Nanotechnology 13(4):451–455

Bl'anda M, Balko J, Duszová A, Hvizdoš P, Dusza J, Reveron H (2013a) Hardness and indentation fracture toughness of alumina-silicon carbide nanocomposites. Acta Metallurgica Slovaca Conf 3:270–275

Bl'anda M, Hvizdoš P, Kvetková L, Dusza J (2013b) Nanoindentation study of coarse grain alumina. Powder metallurgy progress. J Sci Technol Part Mater 13(3–4):116–120

Blank V, Popov M, Buga S, Davydov V, Denisov VN, Ivlev AN, Mavrin BN, Agafonov V, Ceolin R, Szwarc H, Rassat A (1994) Is C60 fullerite harder than diamond? Phys Lett A 188:281–286

Blank V, Popov M, Pivovarov G, Lvova N, Gogolinsky K, Reshetov V (1998a) Ultrahard and superhard phases of fullerite C60: comparison with diamond on hardness and wear. Diamond Relat Mater 7(2–5):427–431

Blank VD, Buga SG, Serebryanaya NR, Dubitsky GA, Mavrin B, Popov MY, Bagramov RH, Prokhorov VM, Sulynov SA, Kulnitskiy BA, Tatyanin YV (1998b) Structures and physical properties of superhard and ultrahard 3D polymerized fullerites created from solid C60 by high pressure high temperature treatment. Carbon 36:665–670

Calatoru VD, Balazinski M, Mayer JRR, Paris H, L'Espérance G (2008) Diffusion wear mechanism during high-speed machining of 7475-T7351 aluminum alloy with carbide end mills. Wear 265(11–12):1793–1800, ISSN 0043–1648

Cardinal S, Malchère A, Garnier V, Fantozzi G (2009) Microstructure and mechanical properties of TiC–TiN based cermets for tools application. Int J Refract Met Hard Mater 27:521–527

Catledge SA, Vohra YK (1999) Effect of nitrogen addition on the microstructure and mechanical properties of diamond films grown using high-methane concentrations. J Appl Phys 86:698. doi:10.1063/1.370787

Chang H, Binner J, Higginson R (2010) Dry sliding wear behaviour of Al(Mg)/Al2O3 interpenetrating composites produced by a pressureless infiltration technique. Wear 268:166–171

Chang S-H, Chang M-H, Huang K-T (2015) Study on the sintered characteristics and properties of nanostructured WC–15 wt% (Fe–Ni–Co) and WC–15 wt% Co hard metal alloys. J Alloys Compd 649:89–95

Chen F et al (2010) Thermal residual stress of polycrystalline diamond compacts. Trans Nonferrous Metals Soc China 20(2):227–232

Chen YM, Zhang GY, Yang SR, Zhang JY (2011) Growth and characterization of self-assembled boron carbon nitride needle-like nanostructures. Adv Mater Res 216:723–727

Childs T (2000) A6.2 cemented carbides and cermets, tool material properties in "Metal machining: theory and applications", pp 388–389, ISBN 0 340 69159 X, ISBN 0 470 39245 2 (Wiley), Anord, London. Copublished by John Wiley & Sons Inc., New York-Toronto

Christensen M, Wahnström G (2006) Strength and reinforcement of interfaces in cemented carbides. Int J Refract Met Hard Mater 24(1–2):80–88

Chung H-Y, Weinberger MB, Levine JB, Kavner A, Yang J-M, Tolbert SH, Kaner RB (2007) Synthesis of ultra-incompressible superhard rhenium diboride at ambient pressure. Science 316 (436):436–439

Da Silva AGP, Schubert WD, Lux B (2001) The role of the binder phase in the WC-Co sintering. Mater Res 4(2):59–62

Da Silva RB, Machado ÁR, Ezugwu EO, Bonney J, Sales WF (2013) Tool life and wear mechanisms in high speed machining of Ti–6Al–4V alloy with PCD tools under various coolant pressures. J Mater Process Technol 213(8):1459–1464, ISSN 0924–0136

De Novion CH, Landesman JP (1985) Order and disorder in transition metal carbides and nitrides: experimental and theoretical aspects. Pure Appl Chem 57(10):1391. doi:10.1351/pac198557101391

Diamond Materials (2015) http://www.diamond-materials.com/EN/cvd_diamond/mechanical_properties.htm

Din S, Kaleem A (1998) Vickers hardness study of zirconia partially stabilized with lanthanide group oxides. Mater Chem Phys 53(1):48–54, ISSN 0254–0584

Doi TK, Kasai T, Tonshoff HK (1999) Lapping and polishing. In: Marinescu LD, Tonshoff HK, Inasaki I (eds) Handbook of ceramic grinding & polishing. William Andrew Publishing, Norwich, pp 354–442. ISBN 9780815514244

Dudzinski D, Devillez A, Moufki A, Larrouquère D, Zerrouki V, Vigneau J (2004) A review of developments towards dry and high speed machining of Inconel 718 alloy. Int J Mach Tool Manuf 44(4):439–456, ISSN 0890–6955

Eko A, Fukunaga O, Ohtake N (2013) The microstructure of cBN-metal composites synthesized from hBN with metallic solvents. Int J Refract Met Hard Mater 41:73–77, ISSN 0263–4368

Element Six (2015) CBN (cubic boron nitride) http://www.e6.com/wps/wcm/connect/E6_Content_EN/Home/Materials+and+products/CBN/

El-Wardany TI, Mohammed E, Elbestawi MA (1996) Cutting temperature of ceramic tools in high speed machining of difficult-to-cut materials. Int J Mach Tool Manuf 36(5):611–634, ISSN 0890–6955

Eriksson M, Radwan M, Shen Z (2013) Spark plasma sintering of WC, cemented carbide and functional graded materials. Int J Refract Met Hard Mater 36:31–37, ISSN 0263–4368

Espinosa HD, Peng B, Moldovan N, Xiao X, Auciello O, Carlisle J (2006) Mechanical properties of undoped and doped ultrananocrystalline diamond: elasticity, strength, and toughness. In: Shenderova OA, Gruen DM (eds) Ultrananocrystalline diamond. William Andrew Publishing, Norwich, pp 303–331. ISBN 9780815515241

Ettmayer P, Lengauer W (1994) Carbides: transition metal solid state chemistry. In: Bruce King R (ed) Encyclopedia of inorganic chemistry. John Wiley & Sons, New York. ISBN 0-471-93620-0

Focke AE, Westermann FE, Kemphaus J, Shih WT, Hoch M (1978) Wear of superhard materials when cutting super-alloys. Wear 46(1):65–79, ISSN 0043–1648

Goel S, Luo X, Reuben RL, Rashid WB (2012) Replacing diamond cutting tools with CBN for efficient nanometric cutting of silicon. Mater Lett 68(1):507–509, ISSN 0167-577X

Green RE et al (eds) (1996) Machinery's handbook, 25th edn. Industrial Press, New York. ISBN 978-0-8311-2575-2

Greim J, Schwetz KA (2006) Boron carbide, boron nitride, and metal borides. Ullmann's Encycl Ind Chem. doi:10.1002/14356007.a04_295.pub2

Grossman JC, Mizel A, Côté M, Cohen ML, Louie SG (1999) Transition metals and their carbides and nitrides: trends in electronic and structural properties. Phys Rev B 60(6):6343–6347

Hall EO (1951) The deformation and ageing of mild steel: III discussion of results. Proc Phys Soc Sect B 64:747–753

Herrmann M, Klemm H (2014) 2.15 – corrosion of ceramic materials. In: Sarin VK (ed) Comprehensive hard materials. Elsevier, Oxford, pp 413–446. ISBN 9780080965284

Jackson MJ (2007) Sintering and vitrification heat treatment of cBN grinding wheels. J Mater Process Technol 191(1–3):232–234, ISSN 0924–0136

Kanyanta V, Ivankovic A (2010) Mechanical characterisation of polyurethane elastomer for biomedical applications. J Mech Behav Biomed Mater 3(1):51–62, ISSN 1751–6161

Kanyanta V, Ozbayraktar S, Maweja K (2014a) Effect of manufacturing parameters on polycrystalline diamond compact cutting tool stress-state. Int J Refract Met Hard Mater 45:147–152

Kanyanta V, Dormer A, Murphy N, Ivankovic A (2014b) Erratum to 'Impact fatigue fracture of polycrystalline diamond compact (PDC) cutters and the effect of microstructure'. [Int J Refract Met Hard Mater 46:145–151], Int J Refract Met Hard Mater 47:150, ISSN 0263–4368

Keshavan MK et al (2008) Polycrystalline diamond constructions having improved thermal stability. Granted patent US8028771 B2

Kim S, Han S-H, Park J-K, Kim H-E (2003) Variation of WC grain shape with carbon content in the WC-Co alloys during liquid-phase sintering. Scr Mater 48(5):635–639

Kitagawa T, Kubo A, Maekawa K (1997) Temperature and wear of cutting tools in high-speed machining of Inconel 718 and Ti6Al6V2Sn. Wear 202(2):142–148, ISSN 0043–1648

Konyashin I, Klyachko LI (2015) History of cemented carbides in the Soviet Union. Int J Refract Met Hard Mater 49:9–26

Kraus EH, Slawson CB (1939) Variations of hardness in the diamond. Mineral Soc Am 24:661–676

Kumar A, Singh K, Pandey OP (2011) Sintering behavior of nanostructured WC–Co composite. Ceram Int 37(4):1415–1422

Lay S, Missiaen J-M (2014) 1.03 – microstructure and morphology of hardmetals. In: Sarin VK (ed) Comprehensive hard materials. Elsevier, Oxford, pp 91–120. ISBN 9780080965284

Lin K-H, Peng S-F, Lin S-T (2007) Sintering parameters and wear performances of vitrified bond diamond grinding wheels. Int J Refract Met Hard Mater 25(1):25–31

Liu Z, An Q, Xu J, Chen M, Han S (2013) Wear performance of (nc-AlTiN)/(a-Si3N4) coating and (nc-AlCrN)/(a-Si3N4) coating in high-speed machining of titanium alloys under dry and minimum quantity lubrication (MQL) conditions. Wear 305(1–2):249–259, ISSN 0043–1648

Livanov K, Jelitto H, Bar-On B, Schulte K, Schneider GA, Wagner DH (2015) Tough alumina/polymer layered composites with high ceramic content. J Am Ceram Soc 98:1285–1291. doi:10.1111/jace.13413

Loos M (2015) Chapter 3 – allotropes of carbon and carbon nanotubes. In: Loos M (ed) Carbon nanotube reinforced composites. William Andrew Publishing, Oxford, pp 73–101. ISBN 9781455731954

Lowther JE (2014) From diamond to superhard borides and oxides. In: Sarin VK (ed) Comprehensive hard materials. Elsevier, Oxford, pp 15–33. ISBN 9780080965284

McNamara D, Alveen P, Damm S, Carolan D, Rice JH, Murphy N, Ivanković A (2015) A Raman spectroscopy investigation into the influence of thermal treatments on the residual stress of polycrystalline diamond. Int J Refract Met Hard Mater 52:114–122, ISSN 0263–4368

Meyers MA, Chawla KK (2008) Materials: structure, properties, and performance in mechanical behavior of materials, 2nd edn. Cambridge University Press, Cambridge, United Kingdom. ISBN 9780521866750

Mohammadia R, Lech AT, Xie M, Weaver BE, Yeung MT, Tolbert SH, Kaner RB (2011) Tungsten tetraboride, an inexpensive superhard material. Proc Natl Acad Sci USA 108 (27):10958–10962. doi:10.1073/pnas.1102636108

Nibennaoune Z, George D, Ahzi S, Remond Y, Gracio J, Ruch D (2011) Diamond coating of hip joint replacement: improvement of durability, integrated systems, design and technology 2010, Springer, Berlin, pp 13–22. Online ISBN978-3-642-17384-4, Print ISBN978-3-642-17383-7

Okamoto S, Nakazono Y, Otsuka K, Shimoitani Y, Takada J (2005) Mechanical properties of WC/Co cemented carbide with larger WC grain size. Mater Charact 55(4–5):281–287, ISSN 1044–5803

Oyama ST (1996) The chemistry of transition metal carbides and nitrides. Springer, Netherlands, ISBN: 978-94-010-7199-4 (Print) 978-94-009-1565-7 (Online)

Patil NG, Asem A, Pawade RS, Thakur DG, Brahmankar PK (2014) Comparative study of high speed machining of inconel 718 in dry condition and by using compressed cold carbon dioxide gas as coolant. Procedia CIRP 24:86–91, ISSN 2212–8271

Perkins JM (1978–2006) Microstructure and properties of (rare earth) doped oxide ceramics. PhD thesis, University of Warwick

Petch NJ (1953) The cleavage strength of polycrystals. J Iron Steel Inst 174:25–28

Petrovic M, Ivankovic A, Murphy N (2012) The mechanical properties of polycrystalline diamond as a function of strain rate and temperature. J Eur Ceram Soc 32(12):3021–3027, ISSN 0955–2219

Pope BJ, Taylor JK, Dixon RH, Gardinier CF, Pope LM, Blackburn DC, Vail MA (2004) Prosthetic hip joint having a polycrystalline diamond articulation surface and a plurality of substrate layers U.S. Patent 6793681

Pusavec F, Deshpande A, Yang S, M'Saoubi R, Kopac J, Dillon OW Jr, Jawahir IS (2014) Sustainable machining of high temperature nickel alloy – Inconel 718: part 1 – predictive performance models. J Clean Prod 81:255–269, ISSN 0959–6526

Rogl P, Bittermann H (1999) Ternary metal boron carbides. Int J Refract Met Hard Mater 17 (1–3):27–32, ISSN 0263–4368

Rosso M, Scrivani A, Ugues D, Bertini S (2001) Corrosion resistance and properties of pump pistons coated with hard materials. Int J Refract Met Hard Mater 19(1):45–52, ISSN 0263–4368

Roya S, Gibmeiera J, Kostova V, Weidenmanna KA, Nagelb A, Wannera A (2012) Internal load transfer and damage evolution in a 3D interpenetrating metal/ceramic composite. Mater Sci Eng A 551:272–279

Sandvik Coromant (2015) Polycrystalline cubic boron nitride. http://www.sandvik.coromant.com/en-us/knowledge/materials/cutting_tool_materials/polycrystalline_cubic_boron_nitride/pages/default.aspx

Sandvik Hard Materials (2005) Cemented carbide, Sandvik new developments and applications http://www2.sandvik.com/sandvik/0130/HI/SE03411.nsf/88c2e87d81e31fe5c1256ae80035acba/651f6e334db04c46c125707600562c88/$FILE/Cemented%20Carbide.pdf

Santhanam AT (1996) Application of transition metal carbides and nitrides in industrial tools. In: Oyama ST (ed) The chemistry of transition metal carbides and nitrides. Springer, Netherlands, pp 28–52, ISBN: 978-94-010-7199-4 (Print) 978-94-009-1565-7 (Online)

Schröter K (1923) German Patent No. 420,689 (GesintertehartеMetalllegierung und Verfahren-zuihrerHerstellung) – submitted on 30 Mar 1923

Schubert WD, Lassner E (2010) Cemented carbides: a success story. Institute of Chemical Technologies and Analytics – Vienna University of Technology and Wolfgang Böhlke (CERATIZIT Luxembourg SA)

Scott DE (2006) The history and impact of synthetic diamond cutters and diamond enhanced inserts on the oil and gas industry. Ind Diamond Rev:66(1), pp. 48–55

Sokolov AN, Shul'zhenko AA, Gargin VG, Loshak MG, Aleksandrova LI, Nikolenko AS, Strel'chuk VV, Katrusha AN, Kutsai OM (2012) Structure and hardness of octahedral natural diamond single crystals depending on the HPHT treatment conditions. J Superhard Mater 34(3):166–172

Solozhenko VL, Andrault D, Fiquet G, Mezouar M, Rubie DC (2001) Synthesis of superhard cubic BC2N. Appl Phys Lett 78(10):1385. doi:10.1063/1.1337623

Spriggs GE (2002) SpringerMaterials. In: Beiss P, Ruthardt R, Warlimont H (eds) Properties of diamond and cubic boron nitride Landolt-Börnstein – Group VIII advanced materials and technologies 2A2 (Powder Metallurgy Data. Refractory, Hard and Intermetallic Materials) http://materials.springer.com/lb/docs/sm_lbs_978-3-540-45660-5_7

Sun Y, Su W, Yang H, Ruan J (2015) Effects of WC particle size on sintering behavior and mechanical properties of coarse grained WC–8Co cemented carbides fabricated by unmilled composite powders. Ceramics International, ISSN 0272–8842. doi:10.1016/j.ceramint.2015.07.086

Wang Z, Rahman M (2014) 11.10 – high-speed machining. In: Hashmi S, Batalha GF, Van Tyne CJ, Yilbas B (eds) Comprehensive materials processing. Elsevier, Oxford, pp 221–253. ISBN 9780080965338

Wang X, Fang Z, Sohn H (2008) Grain growth during the early stage of sintering of nanosized WC–Co powder. Int J Refract Met Hard Mater 26:232–241

Wang Y, Kou Z, Liu Y, Liu F, Duan W, Deng J, Ma Y, Ma D, Tan L, Li C, Zhang Y, He D (2016) Ti (C, N)-based cermets sintered under high pressure. Int J Refract Met Hard Mater 54:203–209, ISSN 0263–4368

Westraadt JE et al (2015) Characterisation of thermally degraded polycrystalline diamond. Int J Refract Met Hard Mater 48:286–292

Yulin X (2007) Steel boned carbides are reliable guides for China's space flight programme. Metal Powder Rep 62(4):16–18, ISSN 0026–0657

Zhou F, Wang Q, Yue B, Wu X, Zhuge L, Cheng X (2013) Mechanical properties and bonding structure of boron carbon nitride films synthesized by dual ion beam sputtering. Mater Chem Phys 138(1):215–224. doi:10.1016/j.matchemphys.2012.11.049

Zhu D, Zhang X, Ding H (2013) Tool wear characteristics in machining of nickel-based superalloys. Int J Mach Tool Manuf 64:60–77, ISSN 0890–6955

Chapter 2
Applications for Superhard and Ultra-Hard Materials

Dr. Christopher John Howard Wort

Abstract The highest performing abrasive materials are classified as either superhard or ultra-hard, based on their measured hardness. Synthetic diamond, in its various formats, is the only ultra-hard material currently used for industrial applications. The largest current application area for synthetic diamond is still in the abrasives markets which are expanding as new, 'difficult-to-machine' materials (such as CFC and MMC materials) become more widely used. The advent of CVD diamond technology has opened up a vast and diverse range of new applications beyond machining and wear parts. It is the unique combination of extreme properties available in diamond, beyond its exceptional hardness, that allows these applications to be realised, and CVD diamond is currently used in submarines (for sensors) to satellites (for windows and heat spreaders) and everywhere in between.

Cubic boron nitride (cBN), in its various formats, is a truly superhard material which currently compliments diamond in abrasive markets due to its ability to very effectively precision machine ferrous-based materials (unlike diamond). Currently, cBN and PCBN are only commercially produced by HPHT techniques for abrasive applications; however, it is likely that in the near future, CVD techniques to produce pure cBN layers and large monocrystals will be available. If this is the case, then cBN would find new applications beyond its use as an abrasive, such as in electronics and optical markets.

This chapter not only describes the major current applications for diamond and cBN but also gives details about potential novel and exciting industrial applications of the future, based around the unique combination of extreme properties available in diamond and cBN, beyond simply their exceptional hardness.

Dr. C.J.H. Wort (✉)
New Technology Manager, Element Six Limited, Oxfordshire, UK
e-mail: Chris.Wort@e6.com

V. Kanyanta (ed.), *Microstructure-Property Correlations for Hard, Superhard, and Ultrahard Materials*, DOI 10.1007/978-3-319-29291-5_2

1 Introduction

The terms 'superhard' and 'ultra-hard' materials refer to a small class of materials that exhibit a load independent hardness value in excess of 40GPa and 80GPa, respectively (Wentorf et al. 1980). Diamond, with a Vickers hardness in excess of 100GPa (70–150GPa (Haines et al. 2001)), is the only known ultra-hard material commercially produced for industrial applications. The close-packed hexagonal form of carbon known as Lonsdaleite, which appeared to exist in extraterrestrial sources (but never seen during diamond synthesis or extreme pressure experiments) and can exhibit a hardness greater than diamond (Carlomagno and Brebbia 2011), has recently been found to actually be faulted and twinned cubic diamond (Németh et al. 2014) and, as such, Lonsdaleite does not exist as a discrete material.

The cubic form of boron nitride (cBN) has a hardness of >40GPa (Leichtfried et al. 2002) and is commercially produced for industrial applications and is considered below. At extremely high pressures (around 50GPa), it is possible to produce cubic boron carbonitride (cBCN) samples (Solozhenko et al. 2001), but due to the need to use a diamond anvil cell to produce it, cBCN is not available for industrial applications, so not considered here.

All the other 'hard' materials (as shown in Table 2.1) have a hardness below the 40GPa 'bar' too low to earn the accolade of superhard; however, the rare wurtzite form of boron nitride (wBN) has been produced via static high-pressure or dynamic shock methods (Soma et al. 1974). The limits of its stability are not well defined. Both cBN and wBN are formed by compressing h-BN, but the formation of wBN occurs at much lower temperatures close to 1700 °C (Vel et al. 1991) and is worthy of a very brief mention in this chapter.

Borides of osmium (OsB_2) and rhenium (ReB_2) are not considered here and deemed to be only of academic interest at this time.

Table 2.1 Materials under consideration

Vickers hardness of selected hard materials	
Material	Vickers hardness (GPa)
Diamond	115
Lonsdaleite	152
c-BC_2N	76
cBN	48
OsB_2	37
B_4C	30
WB_4	~30
ReB_2	~20
wBN	~34

The majority of the data reproduced here is courtesy of Element Six which is a major supplier of not only super- and ultra-hard materials produced by high-pressure high-temperature (HPHT) techniques but also diamond produced by chemical vapour deposition (CVD) techniques

2 Properties of Ultra-Hard Materials

The stable form of crystalline carbon at STP is graphite, whereas at higher temperatures and pressure (above the well-known Berman-Simon line), the cubic form of carbon is stable and is diamond. The structure of diamond is shown in Fig. 2.1.

Diamond is metastable at STP, so if created by, for example, HPHT techniques, above the Berman-Simon line, it retains its unique, ultra-hard cubic structure when taken down to STP. Prior to the 1950s, only natural diamond was available for niche abrasive applications where nothing else would do. However, with the advent of HPHT processes to synthesise diamond, the demand for diamond abrasive materials has increased considerably year on year. Figure 2.2 shows the development of synthetic, ultra-hard and superhard materials over time, with key innovation dates (courtesy of Element Six) that have led to new, ultra-hard materials becoming available.

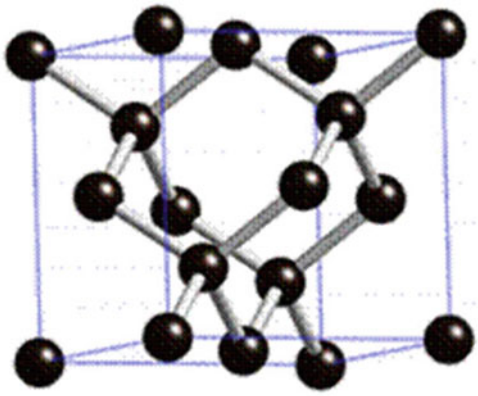

Fig. 2.1 The cubic structure of diamond

Fig. 2.2 The development of synthetic diamond and CBN materials (courtesy of Element Six (E6))

Diamond is quite a remarkable material due to it being mono-elemental and bonded in a very tight and stiff covalent lattice. This gives rise to many of diamond's unique and extreme properties.

3 HPHT Synthetic Diamond Materials

Applications for HPHT diamond can be subdivided into two categories. The first category contains applications that basically rely primarily on the extreme hardness of diamond single-crystal materials (grits and plates), whilst the second category relies on not only the hardness but also the toughness properties of HPHT sintered, polycrystalline composites of diamond (PCD). Figure 2.3 shows the application areas for each of these categories which are described in more detail below.

4 Brief Introduction to Abrasive Machining

By using grinding, lapping and polishing processes, diamond is used to precision machine 'difficult-to-machine' materials (usually hard and brittle materials, such as ceramics and glasses but also non-ferrous metals (and alloys), such as titanium which, although ductile, is very tough at elevated temperatures making it difficult to machine). Grinding, lapping and polishing processes using diamond are all relying

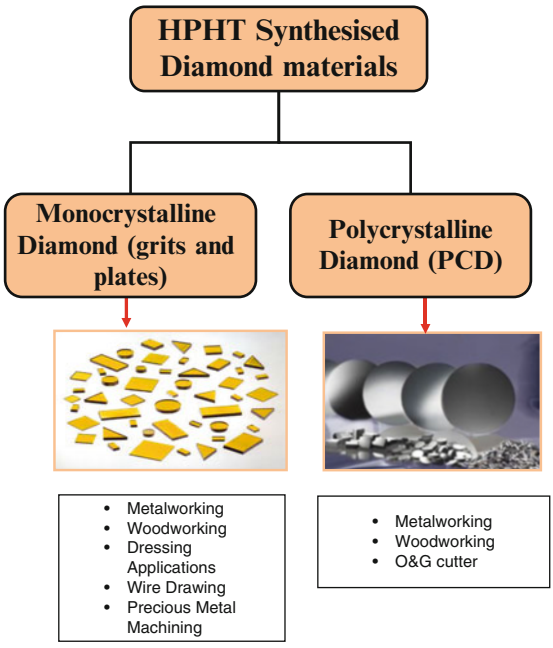

Fig. 2.3 Abrasive applications for HPHT synthetic diamond (courtesy of E6)

not only on the extreme hardness and stiffness of diamond (allowing penetration into the workpiece without distortions) but also the chemical inertness of diamond when it abrades against (or cuts into) another material.

In general, materials abrade differently depending upon their hardness and microstructure and the way in which they are machined.

The main difference between grinding and lapping/polishing processes is that whilst grinding processes have the abrasive retained in a solid matrix, both lapping and polishing use a loose abrasive in a slurry. Polishing is basically lapping on a far finer scale and lapidary (reducing the size of the abrasive in a sequence of steps) is used to sequentially remove subsurface damage induced by the previous lapping/polishing step. In general, ductile materials (which are machined by plastic flow) are easier to machine than brittle materials (which are machined by chipping and fracturing) in the sense that a smooth surface can be achieved over a wide range of parameters, resulting in a constant chip thickness (desirable).

Ductile machining processes lead to a low dynamic load on the tool and relatively low cutting forces (within a comparable class of materials). Materials machined in a ductile mode result in a smooth surface; however, due to stress induced into the surface through incorrect machining parameters, the surface integrity could be low (e.g. residual stresses and surface hardness can be critically high, in tensile as well as in compressive state). However, the best machining results in terms of workpiece shape accuracy and surface quality (roughness and hardness) can only be achieved by a ductile mode machining, which is why machinists always try to establish this condition. By definition, this condition always requires plastic deformation beyond the yield point of the material. Even for brittle materials, polishing and lapping processes are inherently ductile removal processes, whereas grinding of brittle materials can be either a ductile or brittle removal processes depending on workpiece material and machining parameters (Bifano et al. 1991).

Bifano et al. (1991) found that ductile-regime grinding can be achieved by ensuring that the grinding apparatus has a stiff structural loop, real-time control of the grinding infeed, relative isolation from environmental disturbances and state-of-the-art wheel trueing techniques. In addition, he concluded that all brittle materials will undergo plastic flow rather than fracture if the depth of machining is small enough and that there is a correlation between the grinding infeed rate that corresponds to the brittle-to-ductile transition for a particular brittle material and the properties *(Kc, H* and *E)* of the material.

The main parameter influencing the machining of the brittle materials is the undeformed chip thickness which dictates the transition between the ductile to brittle machining. As such, it is the depth of cut (or protrusion size of grit) which is the key parameter, with smaller depths of cut more likely to remove material in a ductile rather than brittle mode. By controlling a stiff, accurate grinding apparatus so that it has an exceptionally small scale of material removal, brittle materials can be ground in a ductile manner. As a result, brittle workpieces can be machined in a deterministic process, whilst producing surface finishes characteristic of those achieved in nondeterministic, inherently ductile processes such as lapping and polishing (Bifano et al. 1991; Venkatachalam et al. 2013, 2015; Andersson et al. 1999).

So, from the above, we would like the diamond abrasive to induce plastic flow in the workpiece to give a precision finish. That can be achieved by selecting the correct size and nature of the diamond abrasive. This is where the diamond abrasive supplier is able to offer a product well matched to a machining requirement (material and process) by engineering the diamond particles in terms of size and particle strength (the ease with which the brittle diamond particles fracture to maintain a good cutting edge rather than rounding). For example, finer diamond particles are generally tougher than larger particles (as the flaw size is smaller after milling down from a larger size) and will generally give a finer finish, albeit more slowly than a courser grit. Diamond abrasives synthesised under different conditions, or milled material vs as-grown material, also exhibit different fracture characteristics.

5 Applications for Diamond Synthetic Diamond Grit

Diamond grit is produced by HPHT processes using a solvent catalyst (Hall 1960), and depending upon the synthesis conditions (by varying: temperature (T), pressure (P), driving force for crystallisation (DFc) and time), it is possible to tailor the size, shape and distribution of the grits produced by changing the growth rates of the <100> and <111> crystal directions. This is shown schematically along with typical HPHT synthesis conditions in Fig. 2.4 below.

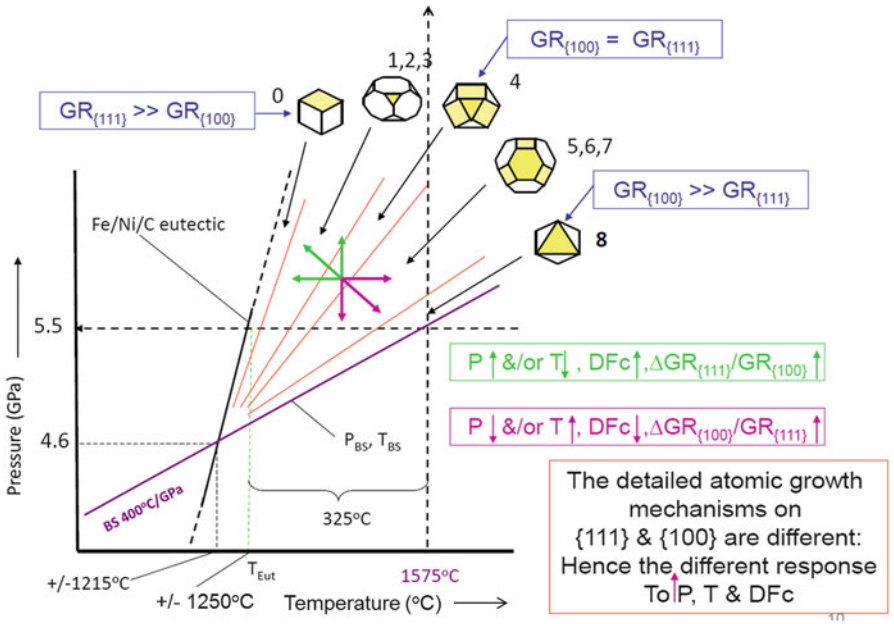

Fig. 2.4 The effect of HPHT synthesis conditions on diamond crystal morphology (DFc is driving force for crystallisation) (courtesy of G Davis (E6))

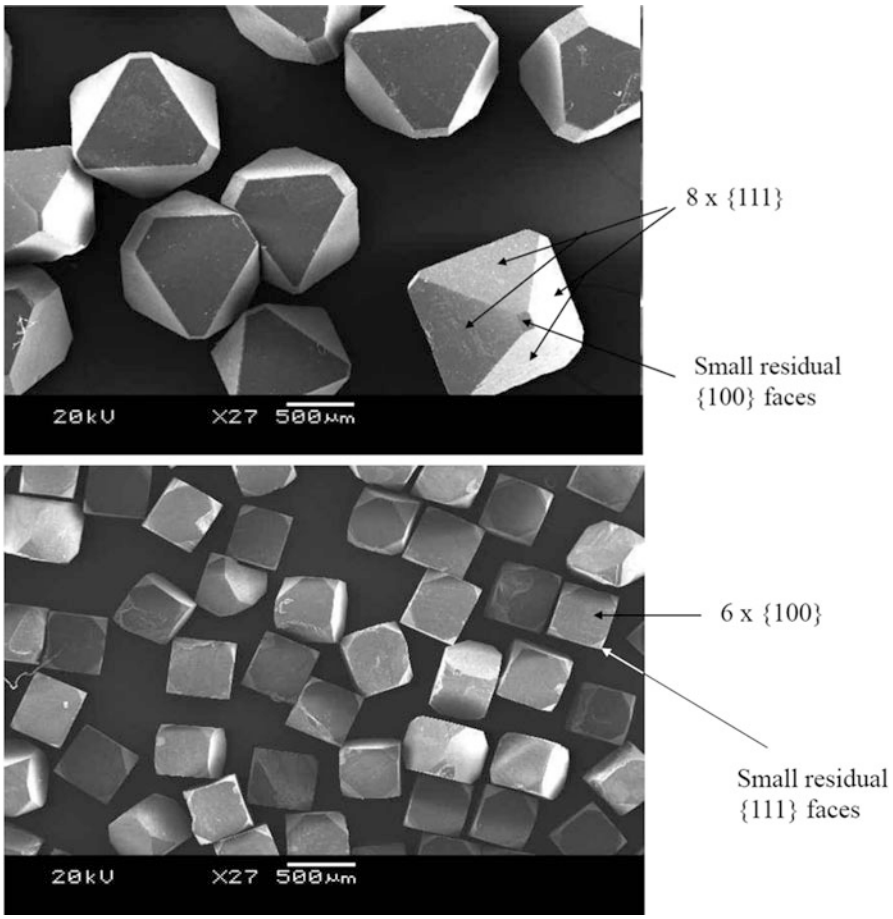

Fig. 2.5 Showing that synthesis conditions affect the morphology of the grits produced. Predominantly ranging from octahedra shown (*at the top*) through to cubic morphology (*at the bottom*) (courtesy of E6)

By operating at pressures above 5.5 Gpa, the synthesis temperature range (above the Berman-Simon line) is around 300 °C, with higher temperatures giving octahedral crystals, whilst lower synthesis temperatures provide cubic morphology crystals. This is shown in the SEM micrographs of Fig. 2.5 below. In general, cubo-octahedral crystals (equal mix of {100} and {111} facets) are preferred for abrasive applications.

Impurity atoms can absorb and be incorporated into the crystal growth steps during diamond synthesis. The dominant impurity in HPHT crystals is nitrogen, where single N atoms are incorporated substitutionally into the diamond lattice within the range typically 90–200 ppm. The single substitutional N gives synthetic diamond crystals (classified as Type Ib) their distinctive yellow colour. The vast

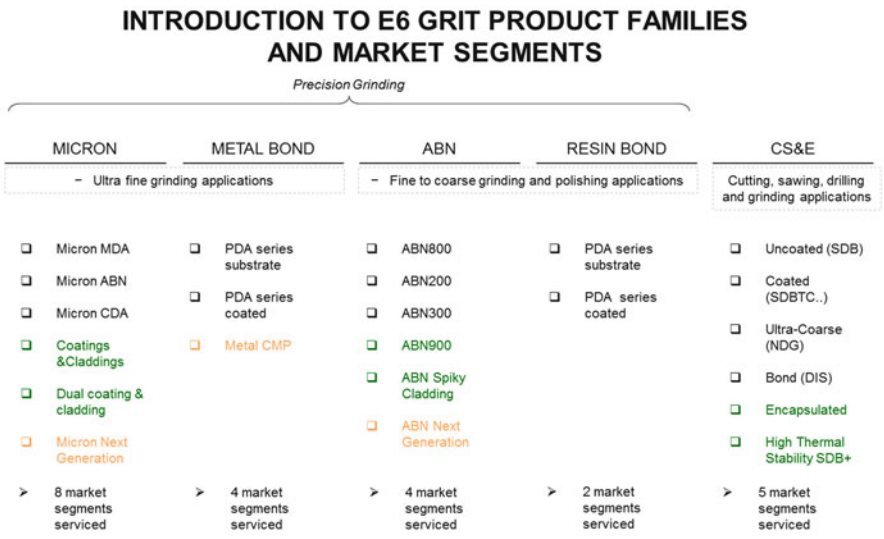

Fig. 2.6 The range offered by one such supplier (E6) of diamond and cBN abrasives (www.e6.com)

majority of HPHT-synthesised diamond is type 1b and is used in abrasive applications; however, by reducing the nitrogen content and adding a boron source to the synthesis capsule, electrically conducting diamond can be synthesised (Dubrovinskaia et al. 2006). Engis market is electrically conducting boron-doped diamond grit as 'Hyprez'. Boron-doped diamond can be used to enhance the conductivity of PCD (aiding electric discharge wire cutting) and potentially has uses in electrochemical applications (www.engis.com.pdf.FastLapCatalog.pdf).

Diamond suppliers offer a wide range of engineered abrasives (www.engis.com.pdf.FastLapCatalog.pdf; www.e6.com), often with a variety of metallic or ceramic coatings (to aid incorporation and retention into and in grinding wheel matrices, respectively). The range offered by one such supplier (Element Six), with the number of markets served by each, is shown in Fig. 2.6.

If the aim is simply material removal (i.e. rough machinability in a narrow sense), then one can find that during the cutting of some brittle materials, lower cutting forces (which can result in lower workpiece distortion) have been observed (Venkatachalam et al. 2013, 2015). This is due to the high brittleness and low fracture toughness of the workpiece material resulting in a brittle material removal mode by intensified chipping. In this mode, the specific microstructure of the material plays an important role, and if chipping or crack formation is occurring, the resultant surface roughness will be comparably high with poor form shape accuracy. The abrasive cutting edges are loaded dynamically due to a less stable and controllable material removal process. In the brittle machining mode, the chips are often very small as intensive cracking occurs. The brittle material removal mode starts before the material yield point is reached, which is why crack formation and rough surfaces result.

6 Applications for Synthetic HPHT and CVD Diamond Monocrystals

Typically, HPHT monocrystals are type 1b and are used in precision machining applications, although through the use of getters to remove N from the synthesis process, transparent HPHT diamond can be grown and has been used, for example, as X-ray monochromators (Stoupin et al. 2014) due to the low stress and crystalline quality of such material. CVD monocrystals would be classed as Type IIa diamond (no detectable nitrogen in the IR spectrum). Both forms of synthetic monocrystals are pure diamond and can be used for precision machining applications, such as wire drawing and single-point turning. In addition, the CVD monocrystalline material can be produced in a purity and crystal perfection that opens up applications in nonabrasive markets including electronics, optics, sensors and quantum optics. In quantum optical materials, all the defects are minimised during the growth process and then a specific defect (the NV centre) is generated using native or implanted nitrogen (this is described in more detail later). Irradiated, annealed and finely crushed (to nm sizes) certain HPHT monocrystalline materials can also be used in quantum applications as fluorescent tags in vivo (Le Sage et al. 2013). At the time of writing, the largest commercially available synthetic diamond monocrystals would be around 10 mm × 10 mm; however, the size of CVD monocrystals is getting larger year on year, mainly driven by optical and electronic application requirements. Figure 2.7 shows a selection of diamond monocrystalline plates suitable for cutting tool applications and Fig. 2.8 shows typical application areas.

Single-crystal synthetic diamond materials are also used in the healthcare sector, primarily through products used in laser treatments, surgical applications and radiotherapy dosimetry detectors.

Synthetic diamond has a unique combination of optical and thermal properties, as well as being biocompatible, which enables it to be used in a wide range of demanding therapeutic and curative laser applications. Major applications currently cover noninvasive surgery where synthetic diamond optical components (probes) are part of a fibre optical system delivering high-power laser beams used as a ‘lancet of light’. These laser-based technologies may replace traditional surgery with the benefits of limiting the burden for the patient and allowing the operation to be performed in a minimum time span and therefore at a lower overall cost (www.e6.com).

The consistency and reliability of supply currently available in synthetic diamond materials has helped increase the use of synthetic diamond in surgical applications, such as synthetic diamond knives for ophthalmology (see Fig. 2.9), synthetic diamond milling tools for intraocular lenses and ultramicrotome knives.

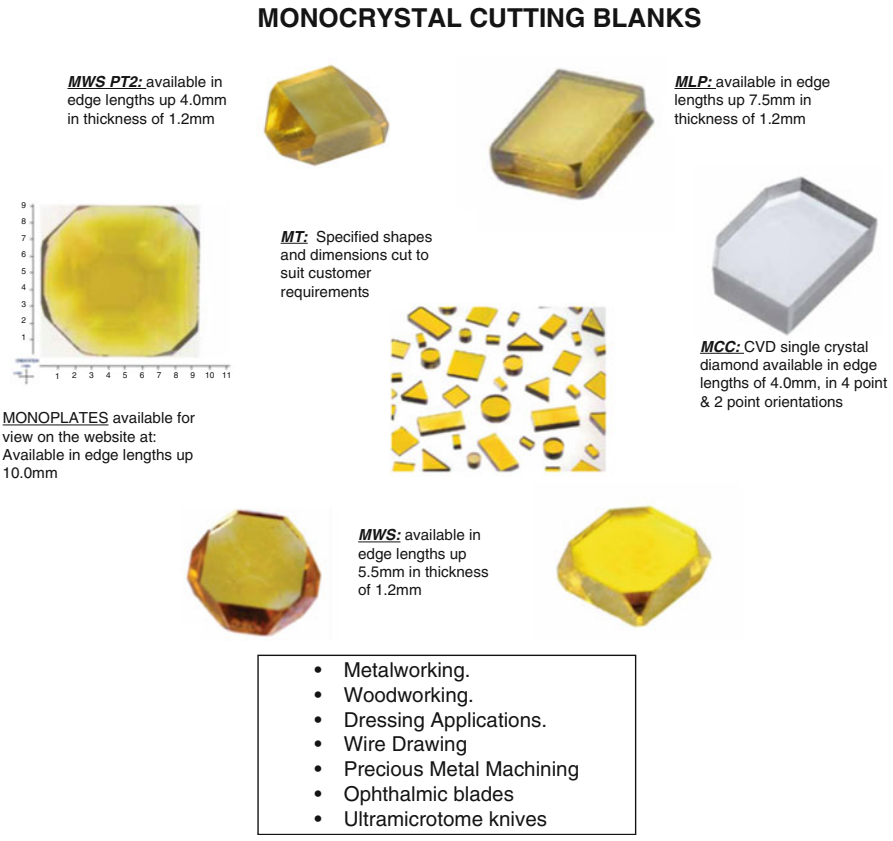

Fig. 2.7 Diamond monocrystalline plates commercially available for cutting applications (courtesy of E6)

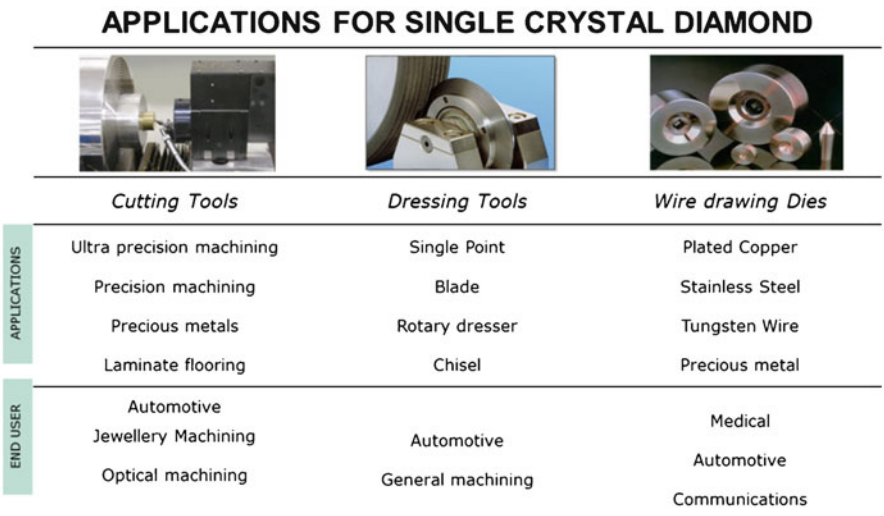

Fig. 2.8 Typical abrasive application areas for diamond monocrystalline plates (courtesy of E6)

Fig. 2.9 Synthetic diamond knives for ophthalmology (courtesy of E6)

7 Applications for HPHT Polycrystalline Diamond (PCD)

7.1 Introduction to PCD and HPHT Sintering

Polycrystalline diamond (PCD) is formed by sintering diamond particles under HPHT conditions. Sintering is a thermal treatment for bonding particles into a coherent, predominantly solid structure via mass transport events that often occurs on an atomic scale. There are various methods used to do this on an industrial scale, and the PCD properties can be tailored to specific applications by selecting the size distribution (modal mix) of the diamond particles and the HPHT sintering conditions. Powders can be densified by plastic flow at pressures above the yield strength, which decreases at elevated temperatures. Pressure applied during the sintering cycle aids densification by plastic flow, and at high temperatures and low stresses, diffusional effects are important. Under high-pressure and high-temperature conditions, both plastic flow and diffusion aid sintering.

To form free-standing PCD, the diamond particles are mixed with a solvent catalyst (usually Fe, Ni or Co mixtures) which, when it melts under the HPHT conditions, dissolves some of the finer diamond particles and graphitic phases (produced during the cold compaction phase) to form a saturated solution. New diamond is deposited on the original particles to liquid-phase sinter (LPS) the PCD into a dense, well-intergrown ceramic. To form backed PCD (a relatively thin PCD layer supported by a metallic substrate, usually WC/Co), LPS is again used, but the sintering metal comes from the diffusion of liquid Co from the substrate itself. The interfacial bonding between the WC/Co substrate and the PCD layer is usually very good, allowing the backed PCD to be planarised and subsequently diced into cutting tools. Figure 2.10 schematically shows the HPHT process to manufacture PCD by liquid-phase sintering, whilst Fig. 2.11 shows the various HPHT process steps. Figure 2.12 shows well-sintered PCD material.

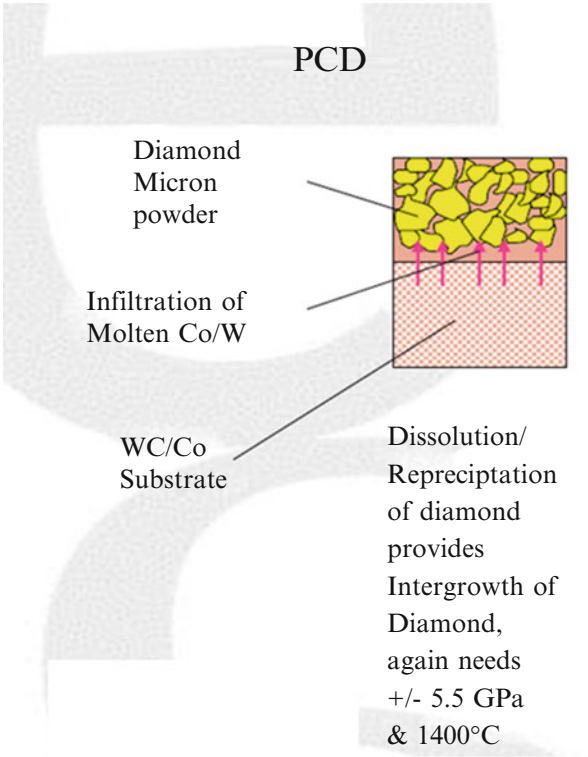

Fig. 2.10 Schematically showing the HPHT process to manufacture PCD by liquid-phase sintering (courtesy of E6)

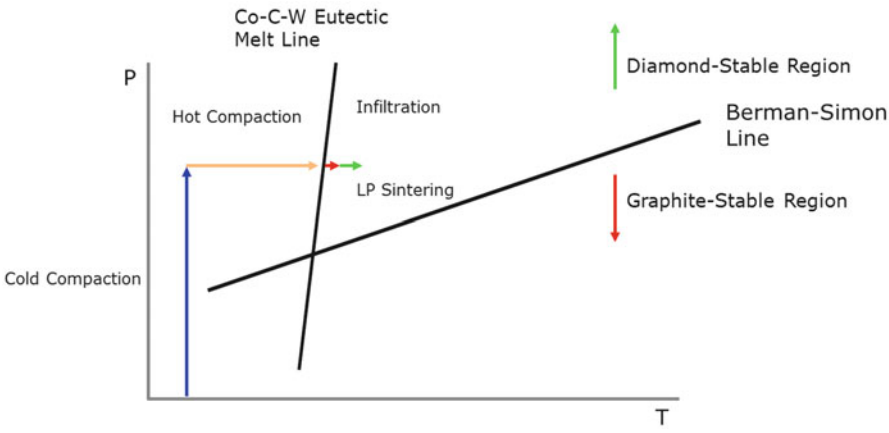

Fig. 2.11 Showing the HPHT process steps to manufacture PCD by liquid-phase sintering

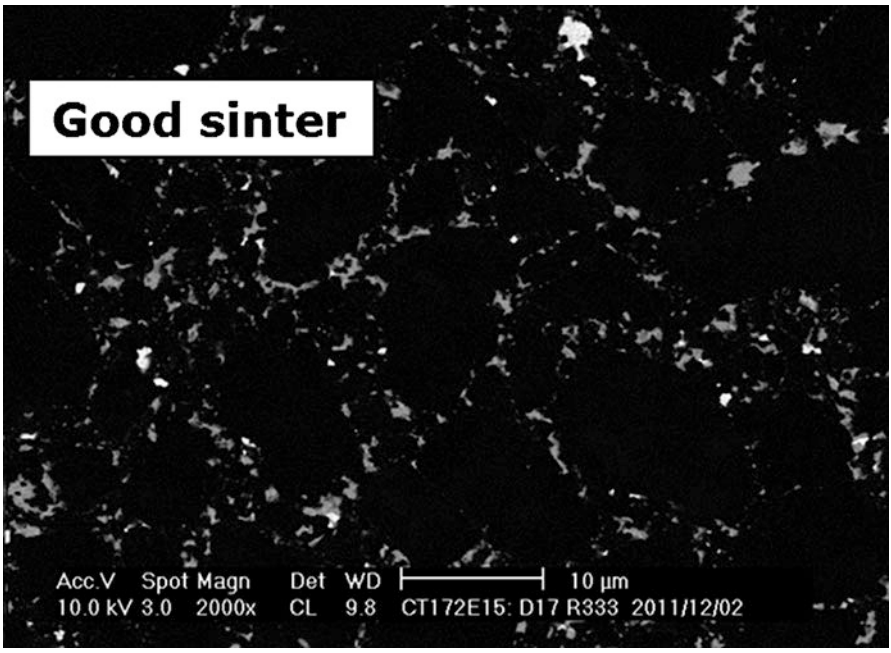

Fig. 2.12 Showing well-sintered PCD material (courtesy of E6)

7.2 Abrasive Applications for PCD

The total market opportunity (TAM) for high-pressure high-temperature (HPHT) produced 'superabrasive' materials in 2014 was estimated to be around £1.5B per annum of which the oil and gas (O&G) cutter market alone is estimated to be worth £0.33B pa. with around 32,000 O&G cutters being produced per week to service the circa. 2500 rigs worldwide.

Figure 2.13 shows where PCD sits on a hardness against toughness diagram for precision machine tool materials. Although not quite as hard as pure diamond, PCD is still far harder than other materials and has an increased toughness over pure diamond. That being the case, PCD is often the material of choice when precision machine requires a tough and abrasion-resistant materials.

Finer-grained PCD tends to be harder and more abrasion resistant than courser-grained PCD but not as tough. As a result, finer-grained PCD material is specified for the machining of abrasive materials, whereas courser-grained PCD is better suited to interrupted cutting. If diffusion from the WC/Co substrate is used to sinter the PCD, finer-grained PCD materials are more limited in thickness than the courser-grained PCD materials, as it is harder for the Co to diffuse through the tighter matrix during sintering (Table 2.2).

PCD is usually supplied to tool makers as a polished disc of PCD backed by a WC/Co substrate. The included metal aids the cutting of the PCD into tool blanks (prior to precision grinding) using electrical discharge machining. The metallic

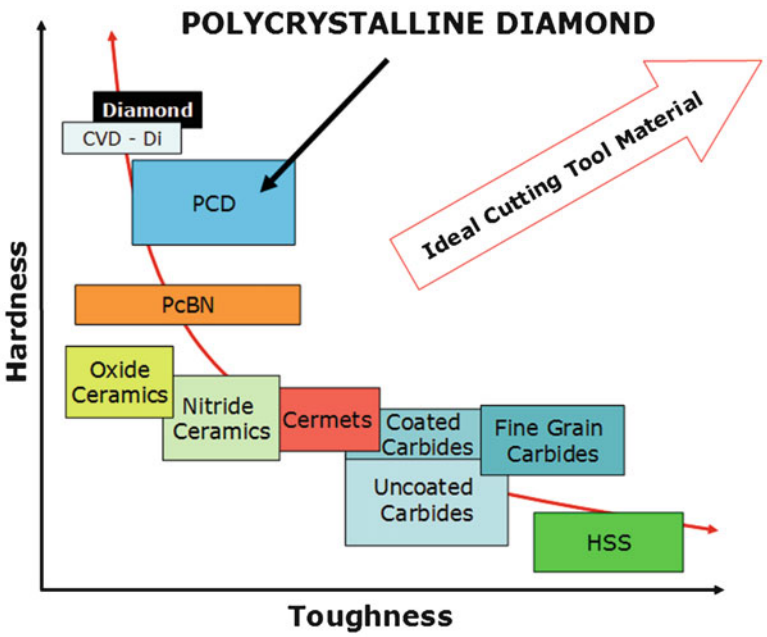

Fig. 2.13 Showing where diamond, PCD and PCBN fit on the ideal cutting tool graph (courtesy of E6)

Table 2.2 Recommended PCD material and cutting speeds for various materials

Work material	Process	Cutting speed (m/min)	First choice PCD
AlSi > 12 %Si MMC	Turning/boring	500	CTM302
	Milling	500–1000	CTM302 (CMX850)
AlSi < 12 % Si	Turning/boring	500–1000	CMX850
	Milling	−1500	CMX850
Carbides and ceramics	Sintered	20–50	CTM302
	Green	100–200	CTM302
Bi-metals	Milling	200–400	CTM302
Grey Iron	Turning/boring/ reaming	300	CTM302
CGI and SGI	Turning/boring	200	CTM302
	Milling	300 (800)	CTM302 (DBW85)
Fibre composites	Turning/boring	200–500	CTM302
	Milling/routing	200–1000	CMX850
Titanium	Turning/boring	100–200	CMX850
	Milling	200–400	CMX850

Note: finer-grained PCD (CMX850) and a courser-grained material (CTM302) (courtesy of Element Six)

phase within the PCD also increases the toughness of the PCD as the metal tends to put the PCD into compression (a result of differing thermal expansion coefficients). Provided the PCD operational temperature does not exceed around 500 °C, there is no downside in having the metal present during precision machining.

PCD is also finding applications as a wear part for extreme environments; however, due to difficulties in fabricating precision polished, 3D shapes and the limitation in area imposed by HPHT techniques, PCD wear parts are currently only addressing a relatively small market.

7.3 PCD for Oil and Gas Cutters

A particularly harsh application for PCD materials is encountered when drilling for oil and gas (O&G). Figure 2.14 shows a typical WC/Co drill bit head which will have around 50 PCD cutters brazed into the 'wings' and Fig. 2.15 shows a typical

Fig. 2.14 Typical drill bit with fixed cutters

Fig. 2.15 A typical PCD cutter (courtesy of E6)

PCD cutter. During the exploration for O&G, many different rock formations could be encountered, some will be more abrasive than other, and many will consist of hard phases mixed in with a softer phase, causing impacts on the cutter cutting edge whilst drilling. These impacts can cause micro-cracks, chipping and spalling which, when severe, prevent the progressing of the drilling. Figures 2.16 and 2.17 show cutters that have spalled during operation.

In all O&G drilling operations, the drill string operator would like to hit the target depth without incurring costly downtime required to replace the PCD cutters. To this end, PCD cutters for O&G applications are engineered by the manufacturers

Fig. 2.16 A spalled cutter

Fig. 2.17 Seriously damaged cutters via spalling

to give not only consistent and predictable wear rates but also an inherent toughness to prevent spalling.

Quite often the high temperature encountered during drilling necessitates the removal of Co from the cutter. This has several affects: on the plus side, the removal of Co increases the thermal stability of the cutter (reduces graphitisation at elevated temperatures) and prevents accelerated wear caused by stresses induced due to the thermal expansion mismatch between Co and the PCD matrix. However, removing the Co phase tends to reduce the toughness of the PCD. As a result, cutter suppliers generally offer differing depths of Co removal depending on the application requirement. At present there is no 'standard' cutter or one size fits all but rather a range of cutter designs suited to different drilling requirements.

8 Chemical Vapour Deposition (CVD) Diamond

8.1 Brief Introduction to CVD Diamond

Whereas HPHT techniques synthesise diamond in its region of bulk thermodynamic stability (above the Berman-Simon line), CVD techniques synthesise diamond in its region of bulk metastability by using surface kinetics/chemistry to maintain the diamond structure during growth. There are many ways to do this (Klages 2000); however, all the CVD techniques require the following:

- A gaseous source of carbon heated to above circa. >1600 °C
- A means to generate atomic hydrogen at the growing surface
- A substrate to deposit the diamond on maintained at >600 °C

Typically, the gaseous source of carbon would be methane (as it is cheap and can be bought in a highly pure form), and the heating source is usually a hot filament or a plasma discharge (usually at microwave frequencies), both of which also generate the atomic hydrogen in sufficient quantities necessary for the CVD diamond growth process. Hot-filament processes have the advantage of larger area deposition (300 mm wafers) at the expense of linear growth rate (which is <1um/h) and quality. The highest-quality CVD diamond materials (in terms of crystalline perfection and purity) are grown by microwave plasma-assisted CVD (MPACVD) techniques, where growth rates in excess of 5um/h can yield electronic quality single or polycrystalline material with a very low defect density. However, thin film cutting tools (where the quality is less important so long as it is a diamond layer) are often grown using a hot-filament process.

By varying the CVD deposition parameters, such as gas pressure, substrate temperature, substrate type, methane/hydrogen concentration, flow rate and gaseous additives (e.g. for B-doping), different types of CVD diamond can be optimised for any given application. Figure 2.18 schematically shows a generic MPACVD reactor system and Fig. 2.19 a hot-filament system manufactured by sp3 inc.

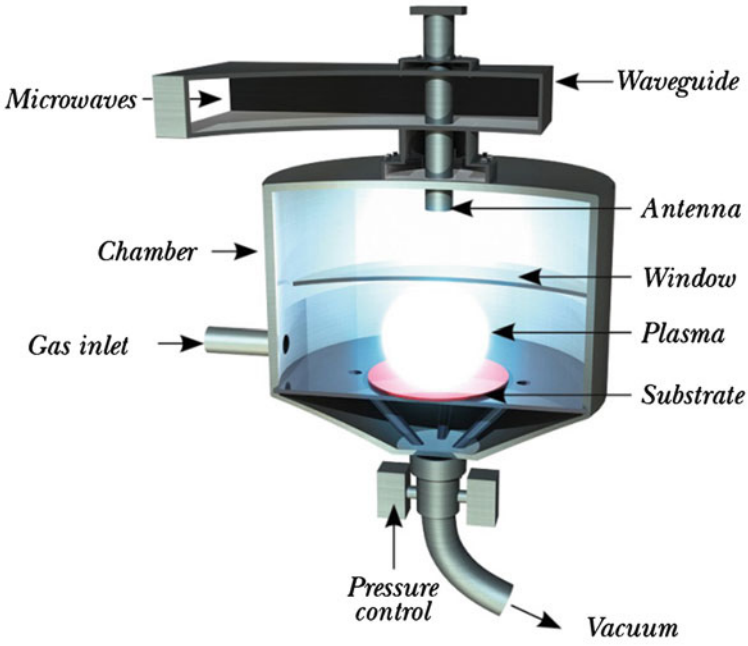

Fig. 2.18 Schematically showing a generic MPACVD reactor system

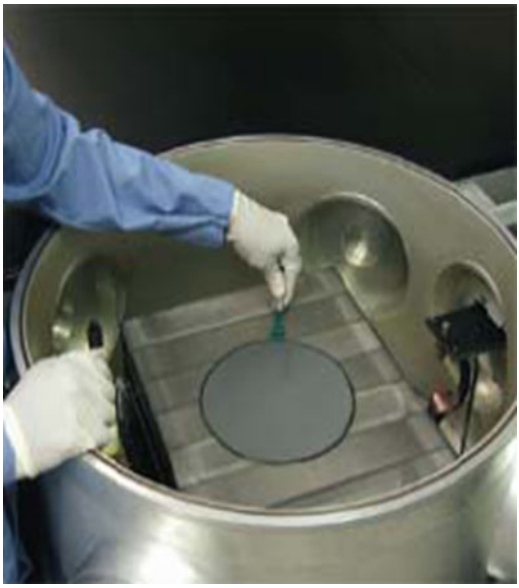

Fig. 2.19 A hot-filament deposition system manufactured by sp3 inc

8.2 Applications for Polycrystalline CVD Diamond

Whereas the extreme hardness opens up the abrasive applications for diamond, applications for diamond synthesised by chemical vapour deposition (CVD) techniques utilise combinations of other extreme properties of diamond. The list below shows the unique combination of extreme properties available in CVD diamond. The more of diamond's extreme properties required by an application, the more likely diamond is the preferred solution:

1. Very broad transmission spectrum
2. Highest thermal conductivity known
3. Highest resistance to thermal shock
4. Low thermal expansion coefficient
5. High chemical (and bio) inertness
6. Highest Young's modulus known
7. Highest Vickers hardness of any material
8. High tensile strength
9. Good electrical insulator when intrinsic
10. Good electrical conductor when doped
11. Low dielectric constant
12. Low dielectric loss
13. Wide electronic bandgap
14. High electronic mobility

There are many potential applications that could be served by CVD diamond, and new applications appear on a regular basis as engineers become more familiar with the properties and availability of CVD diamond materials. Many applications are well covered in other articles (Susmann et al. 2000), such as diamond for use as a heat spreader for electronic devices, IR windows and thin film cutting tools. For this article I have tried to concentrate on the major applications and newer applications for CVD diamond that are not covered in much detail elsewhere.

9 CVD Diamond as an Extreme Performance Optical Material

9.1 Diamond Windows for High Power Transmission

CVD diamond can be fabricated as either planar plates or shaped components in a thickness suitable for processing into optical elements. One of the first applications for polycrystalline CVD diamond windows was for use as high-power exit windows for CO2 lasers (Susmann et al. 2000). As shown in Fig. 2.20, high-quality CVD diamond is transparent from around 0.3um to 3um and then for all

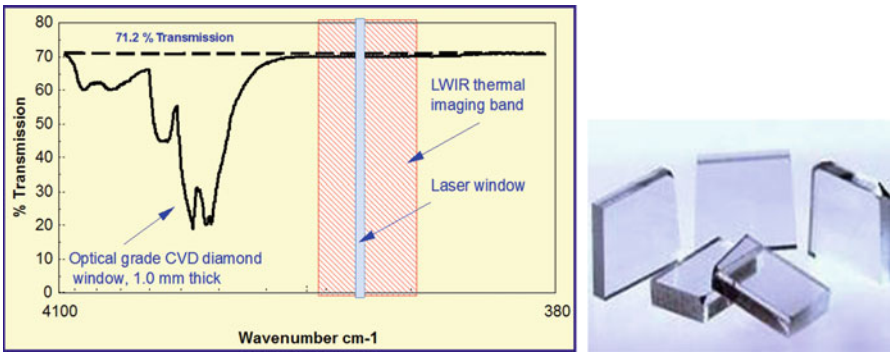

Fig. 2.20 The IR transmission of uncoated, high-quality CVD diamond windows and CVD diamond material

Table 2.3 The salient properties of interest for a CO_2 laser output window (Susmann et al. 2000)

Property (at 300 K)	CVD diamond	ZnSe
Thermal conductivity (W/mK)	1800–2100	16
Thermal expansion (ppm/K)	0.9	7.6
Thermo-refraction (dn/dT) (1/K)	1E-5	6 E-5
Fracture strength (MPa)	400–600	50
Typical thickness (mm)	0.7–1.0	6
Young's modulus (GPa)	1050	70
Bulk absorption (1/cm)	<0.07	0.0005

wavelengths >7.0um. In the mid-IR range of 3–7um, the multi-phonon absorption present in all diamond limits its use to above or below this wavelength region.

There are several other materials that could be used for output windows on CO_2 lasers, with ZnSe being a prime candidate as it has a very low absorption loss at the CO_2 laser wavelength of 10.6 μm (although this is generally nullified by the need for antireflection coating); however, as shown in Table 2.3 below, apart from a lower absorption coefficient than diamond, ZnSe is inferior in every other respect, and this is a good example of the unique combination of properties available with diamond.

It is of vital importance that the exit beam remains undistorted when passing through the output window. Distortions in the window are caused by localised heating when laser beam power is absorbed. The perfect power transmission window would thus have (a) a very low overall absorption (absorption coefficient of window and coatings x window thickness), (b) a low thermal expansion coefficient (less change in geometry with temperature), (c) a high thermal conductivity (ability to spread heat away from heated volume), (d) a high strength and Young's modulus (allowing a thinner window to be used) and (e) a low change in refractive index with temperature. Figure 2.21 shows the temperature profile for a diamond and ZnSe CO_2 laser window when passing a 5 kW beam.

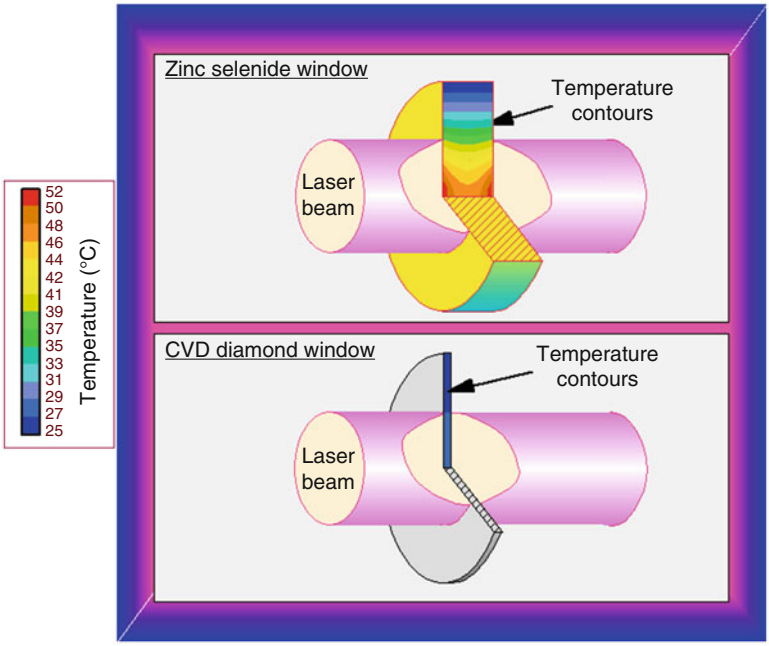

Fig. 2.21 Temperature profile for ZnSe and CVD diamond windows, 5 kW laser beam (Susmann et al. 2000)

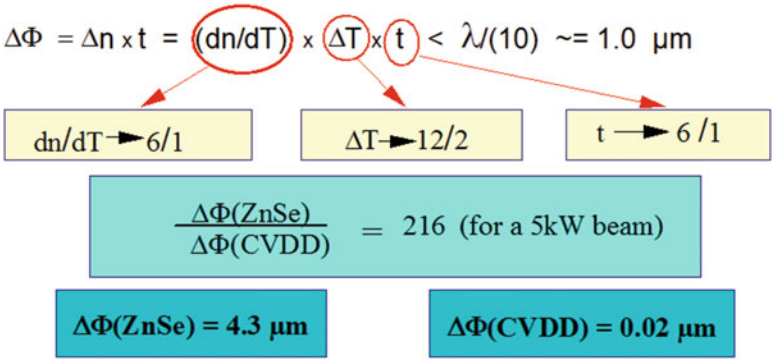

Fig. 2.22 Diamond is over 200× better than ZnSe for CO_2 laser exit windows (Susmann et al. 2000)

When all the salient features are considered for this power transmission window, diamond is over 200× better than ZnSe allowing more perfect beams (less phase change) and higher powers to be deployed as shown in Fig. 2.22.

This is also true for other power transmission windows used at other wavelengths, such as the windows used for high-power (1 MW at 144GHz) gyrotrons for fusion experiments (Susmann et al. 2000). The gyrotron windows differ from the IR

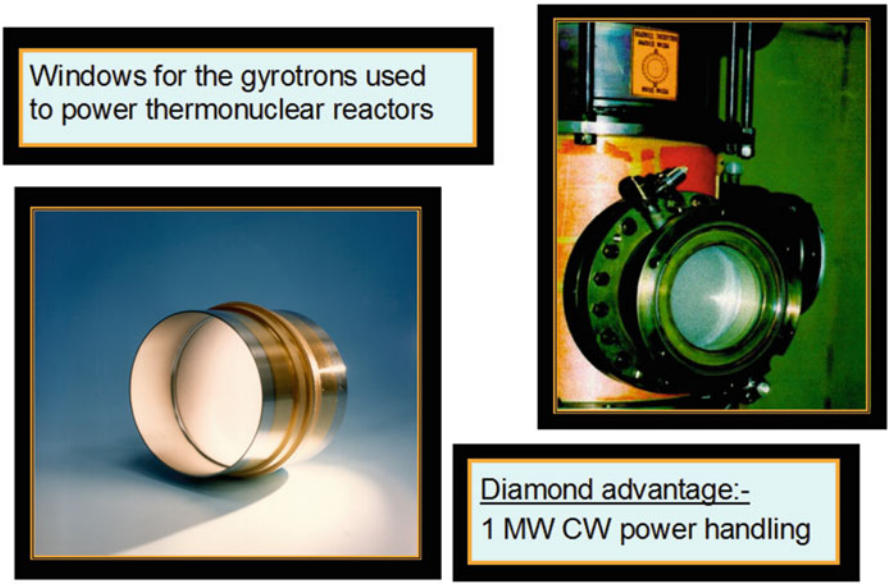

Fig. 2.23 High-power transmission CVD diamond gyrotron windows (Susmann et al. 2000)

windows as they are fabricated to be an integral number of half wavelengths in terms of electromagnetic thickness, thus not requiring any antireflection elements. This has the advantage that the window surfaces are pure diamond and are thus completely scratch resistant. By placing a water-cooling circuit at the window periphery, powers in excess of 1 MW have been successfully transmitted through CVD diamond gyrotron windows—a factor of 4× greater than that of a cryogenically cooled alternative window (Susmann et al. 2000). Figure 2.23 shows a CVD diamond gyrotron window used for several international thermonuclear experiments.

9.2 CVD Diamond Domes for Heat-Seeking Missile Applications

As shown above, diamond is highly transparent in the long-wave IR (LWIR—8 to 14 um) region of the spectrum. This, when combined with exception hardness and a high thermal shock resistance (due to a high thermal conductivity and low thermal expansion coefficient), allows diamond to be considered for LWIR heat-seeking missile applications (Mollart Tim et al. 2001). The CVD diamond synthesis process allows the diamond to be uniformly deposited onto an accurately formed hemispherical mandrel. Once released from the mandrel, the outer and inner surface dome surfaces can be processed (form generated and polished) to ensure the

Fig. 2.24 A polished CVD diamond dome

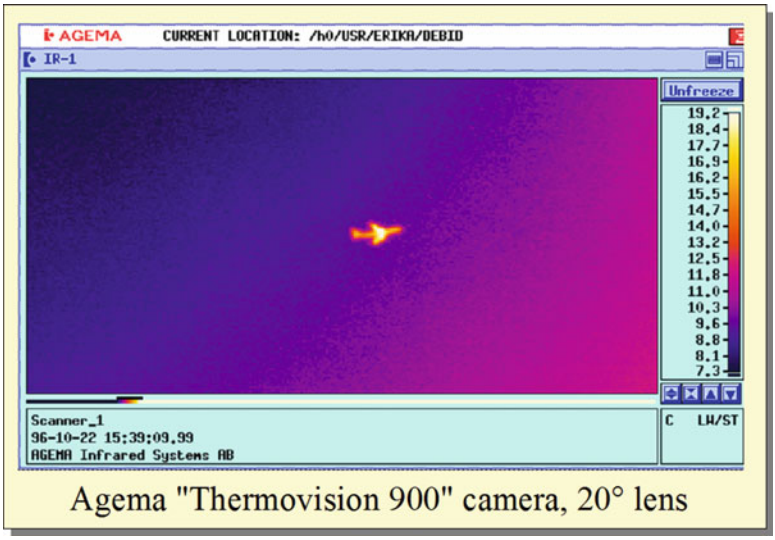

Fig. 2.25 LWIR image through the dome

necessary concentricity for LWIR imaging. Figure 2.24 shows a polished CVD diamond dome suitable for LWIR imaging, whilst Fig. 2.25 shows the LWIR image taken through the dome.

The ability to manufacture and process non-planar diamond samples (Susmann et al. 2000) opens up other extreme performance applications including medical prosthetic devices (hip joints) and loudspeaker ‘tweeters’.

Fig. 2.26 A diamond tweeter

9.3 Loudspeaker Tweeters

The combination of a low density and high Young's modulus and strength make diamond a very high-performance high-sound frequency material. Figure 2.26 shows an as-grown CVD diamond dome (around 40um thick) mounted on a voice coil by Bowers and Wilkinson Ltd (B&W). It is currently used to give almost perfect sound reproduction for the upper range of the audible spectrum. Alternative tweeter materials such as aluminium or beryllium can give undistorted pistonic action at frequencies up to around 30 kHz and 50 kHz, respectively. However, the imperfect pistonic motion (dome distortion) at higher frequencies can cause unwanted break-up frequencies that can be heard in the audible region (below 20 kHz). Diamond, being far stiffer, can maintain the perfect pistonic motion without distortion at frequencies up to around 70 kHz, giving an almost perfect sound reproduction. This is shown in Fig. 2.27. Bowers and Wilkins are currently using diamond tweeters in their top-of-the-range 800 series loudspeaker systems, as shown in Fig. 2.28.

9.4 Diamond Hip Joints

CVD diamond is an ideal hip joint material due to its low coefficient of friction, low wear rate and high biocompatibility. However, since CVD diamond is a brittle material, the prosthetics industry is unlikely to adopt a CVD diamond joint until the

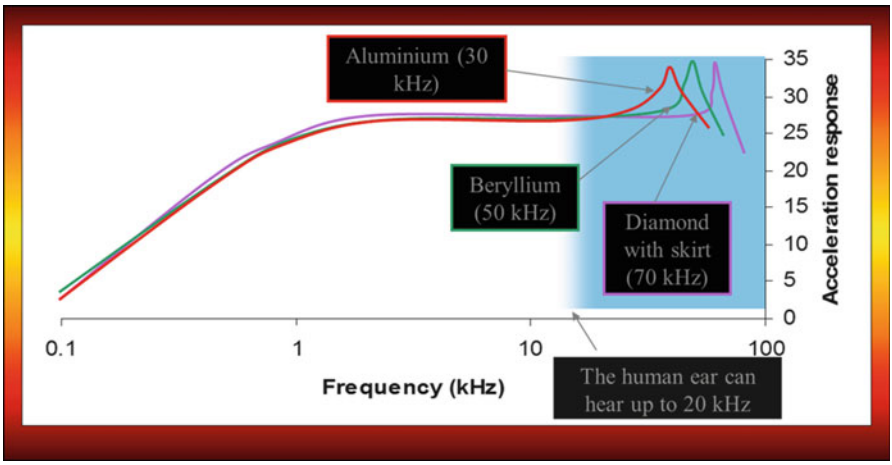

Fig. 2.27 The break-up frequency of different tweeter materials (courtesy of Bowers & Wilkins Ltd)

Fig. 2.28 The B&W 800 series with a CVD diamond tweeter (courtesy of Bowers & Wilkins Ltd)

toughness is far higher than currently demonstrated. In terms of wear, prototype CVD diamond hip joints have been tested for over 2 million test cycles (on a hip simulator), and the wear was demonstrated to be very low compared to other hip joint materials. Figure 2.29 shows a prototype CVD diamond hip joint.

PCD hip joints have also been fabricated (Pope et al. 2006) and evaluated, and whilst the toughness of PCD is not a limiting factor, the biocompatibility of the Co phase could potentially be an issue. This is a future application for either tougher CVD diamond or leached/back-infiltrated PCD.

Fig. 2.29 Prototype hip joint with both ball and cup surfaces made from CVD diamond hemispheres

Table 2.4 Material properties and figures of merit (normalised to Si) at room temperature for Si, 4H-SiC, GaN and diamond

	Si	SiC-4H	GaN	Diamond
Bandgap (eV)	1.1	3.2	3.44	5.47
Breakdown field (MV/cm)	0.3	3	5	20
Electron mobility (cm^2/Vs)	1450	900	440	4500
Hole mobility (cm^2/Vs)	480	120	200	3800
Thermal conductivity (W/cmK)	1.5	5	1.3	24
Johnson's figure of merit	1	410	280	8200
Keyes' figure of merit	1	5.1	1.8	32

4H is the polytype of SiC that is considered best suited for power electronic devices (highest mobility having a combined high mobility and high thermal conductivity). The diamond values are those recently reported for electronic grade CVD diamond (Isberg et al. 2002)

9.5 CVD Diamond for Electronics and Radiation Detectors

Diamond is extreme in this group of wide bandgap materials that includes silicon carbide (SiC) and gallium nitride (GaN). Diamond electronic devices, such as power diodes and high-frequency field effect transistors, were expected to deliver outstanding performance due to the material's excellent intrinsic properties, which include high carrier mobility and high breakdown field (Isberg et al. 2002). Table 2.4 summarises semiconductor material electronic properties and their thermal conductivities. Unfortunately, despite considerable effort over the last 20 years, researchers have not been able to achieve the required performance from doped diamond (in particular, n-type diamond that appears to be very elusive). Intrinsic-based devices and unipolar devices have been demonstrated (Wort and Balmer 2008) but generally do not perform as well as one might expect.

In contrast to the limitations of doped diamond, the intrinsic properties of diamond make it an ideal material for a variety of detectors: it is radiation hard

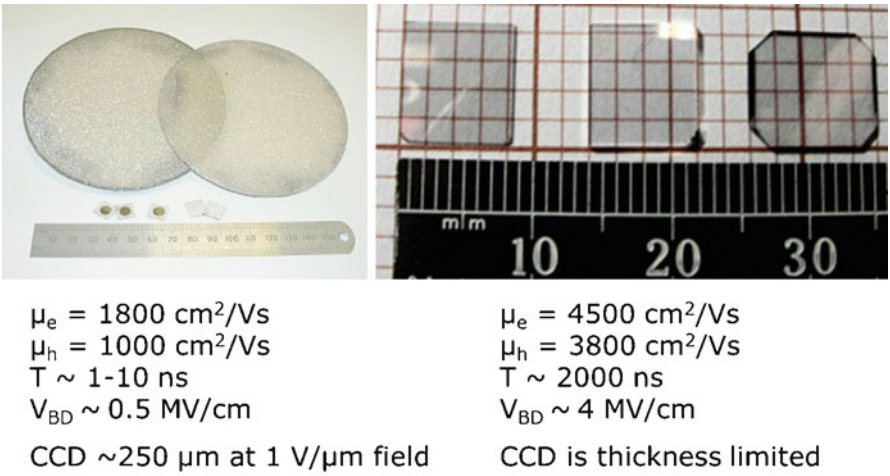

Fig. 2.30 Element Six has two 'electronic grades' of CVD diamond, polycrystalline (LHS) and monocrystalline (RHS)

due the high density of strong bonds; the wide bandgap makes the devices blind to solar radiation and can allow very small signals to be detected with low noise levels; the high thermal conductivity makes temperature control straightforward; and the structures are often very simple—typically consisting of either an i layer or a p-i bilayer with an appropriate pattern of metallisation to form ohmic contacts on one or both sides.

Element Six has two 'electronic grades' of CVD diamond as shown in Fig. 2.30. Polycrystalline material (available in wafers up to 118 mm in diameter) is suitable for many detector applications, whilst the high-purity, single-crystal material (currently available in wafers up to a maximum of 8×8 mm) is required for active electronic devices, such as FETs. Both materials are available to a thickness in excess of 1 mm.

A key parameter is the charge collection distance (how far the charge generated can move under an applied field before it is lost by recombination). A typical construction of a diamond solid-state ionisation chamber is shown in Fig. 2.31. Extremely high-quality SSC-diamond material is available (Isberg et al. 2002) and allows the development of a range of radiation hard detectors for X-rays, ultraviolet light (UV), alpha particles, neutrons and other nuclear and subnuclear particles.

Neutron detectors made from polycrystalline CVD diamond have been demonstrated, but they are not suitable as the basis of a commercial device as the response is too noisy and broad. SSC-diamond gives much lower level of defects and a cleaner, larger signal, together with a higher sensitivity.

The SSC-diamond neutron detector envisaged consists of an i-diamond layer with a thin, heavily boron-doped layer on top (^{10}B has a high neutron capture cross section). The ^{10}B-neutron interaction yields an alpha particle, which generates charge as it crosses the i-diamond layer; it is this charge that is measured to give the signal. A typical construction is shown schematically in Fig. 2.32.

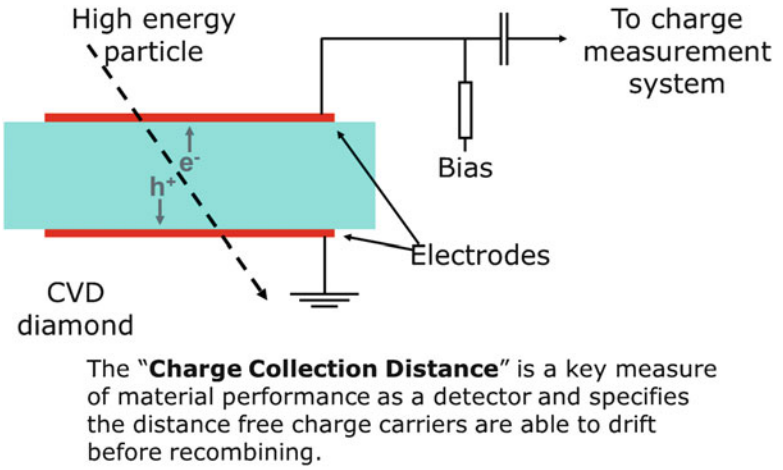

Fig. 2.31 A typical construction of a diamond ionisation chamber (courtesy of E6)

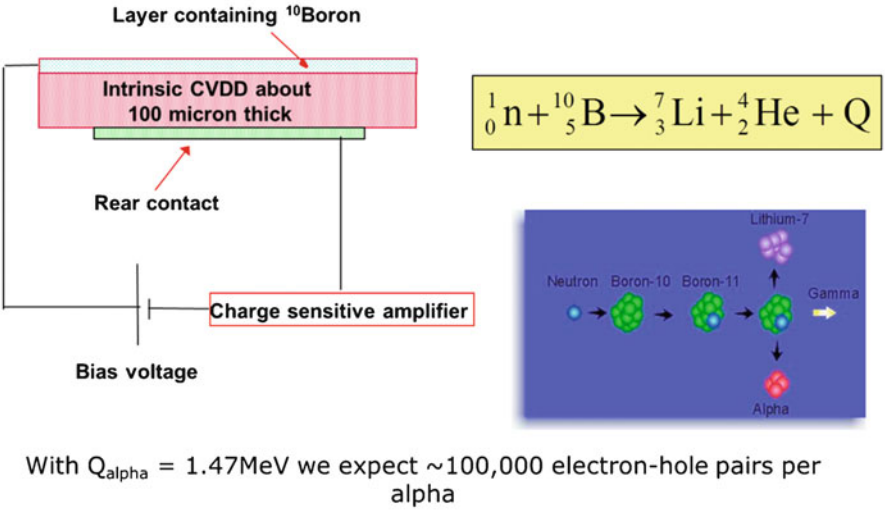

Fig. 2.32 A typical construction of a diamond neutron detector, where the ^{10}B layer yields a 1.47 MeV alpha particle which generated e-h pairs for detection in the diamond ionisation chamber

Diamond is close to ideal as choice of material for dosimetry detectors in radiotherapy. The Z-value is close to that of water (i.e. tissue equivalent), the sensitivity is high and it withstands high doses of radiation without degrading. The problem with polycrystalline CVD or natural single-crystal diamond is variability within and/or between samples; SSC-diamond offers optimum performance

in a simple and highly reliable package once the material and contact technology have been optimised for this application.

CVD diamond radiation detectors have been used in the following applications:

- Particle physics—beam condition monitors, trackers and beam abort systems
- Dosimetry—radiation therapy, equipment calibration and active exposure monitoring
- Nuclear applications—homeland security, nuclear reactors and fusion experiments
- Synchrotrons—white beam monitoring
- UV detectors—photolithography, flame detection and solar physics
- Alpha/beta—air flow and survey metres and waste incineration

9.6 Boron-Doped Diamond for Electrochemistry

It is relatively easy to boron-dope CVD diamond by simply adding diborane (usually diluted with hydrogen or Argon) into the CVD diamond synthesis chamber. Low levels of boron doping lead to semiconducting, p-type diamond, whilst higher levels can lead to quasi-metallic conduction, with a low defect density, when the boron concentration exceeds 3×10^{20} ppm (Koppang et al. 1999) giving a resistivity of typically $0.4 - 1.0 \times 10^{-3}$ Ωm. Figure 2.33 shows the effect of boron concentration on electrical conductivity.

Since the diamond surface is mechanically robust and chemically inert, boron-doped diamond exhibits (a) a very wide electrochemical window (the range of

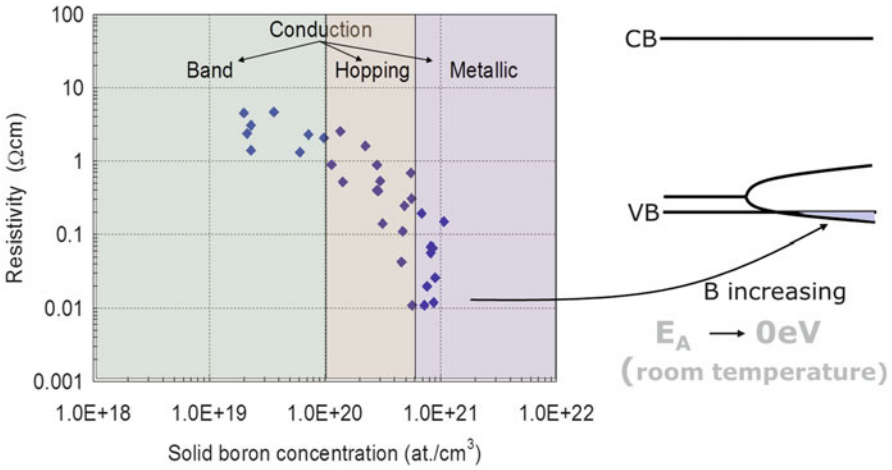

Fig. 2.33 The effect of boron concentration on CVD diamond electrical resistivity (courtesy of E6)

voltage that can be applied to the electrode before water is either reduced or oxidised), (b) a low background current and (c) long-term stability (Granger et al. 1999; Nebel and Ristein 2004).

The other properties of diamond make it a unique electrode material, namely:

- Biocompatible
- Varied surface terminations possible
- Chemically inert
- Non-fouling
- Mechanically robust
- Non-porous

Highly doped diamond can be used as an electrode in numerous electrochemical applications, ranging from water sanitation and ozonised water generation to electrochemical sensors of hostile environments (Koppang et al. 1999). The wide electrochemical window is shown in Fig. 2.34, compared with other electrode materials.

The wide electrochemical window allows a whole host of redox reactions within the voltage window in an aqueous solution, allowing small perturbations to the

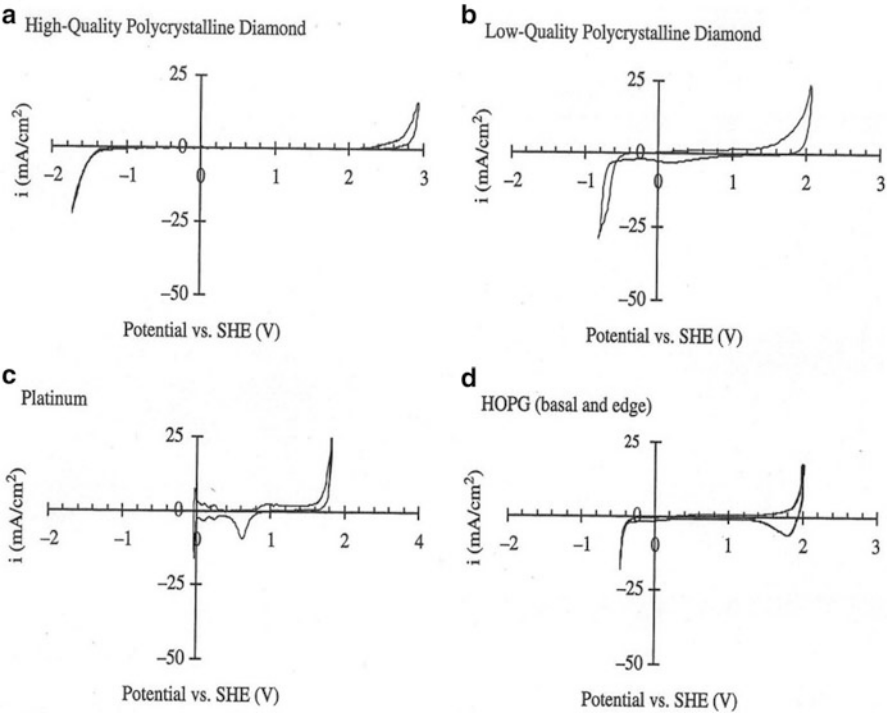

Fig. 2.34 Cyclic voltammogram showing the wide electropotential window for boron-doped diamond, with low background current and noise

cyclic voltammogram to indicate the presence and amount of a particular species when compared to a calibrated reference. In addition, oxidising radicals can be produced within the electrolyte or at the diamond—electrolyte surface. These two facts allow diamond electrodes to be used as electrochemical sensors and electrodes for water treatment.

9.7 Electrochemical Sensors Based on b-Doped Diamond

The very wide electrochemical window available with b-doped diamond allows it to be used for a wide range of robust and chemically inert sensing applications. Sensors can be configured in many different ways, specifically depending on the species of interest. Figure 2.35 shows a typical coplanar sensor structure for more general applications.

To make a simple coplanar sensor electrode (e.g. as shown in Fig. 2.35), the following steps are used:

(a) Starting with a polished piece of intrinsic CVD diamond, laser cut into it (or otherwise etch) the electrode pattern desired.
(b) Clean the etched pattern to remove any non-diamond carbon.
(c) Return to CVD reactor and grow b-doped diamond over the etched surface.
(d) Polish back the b-doped layer until the intrinsic base layer is revealed, leaving b-doped diamond in the etched features.

In this way a whole variety of electrode structures can be manufactured in CVD diamond; the advantage of the coplanar electrode is that it is all diamond and thus chemically and biologically inert, and the conducting b-doped diamond is electrically isolated in such a way that the electrode surface area is well defined.

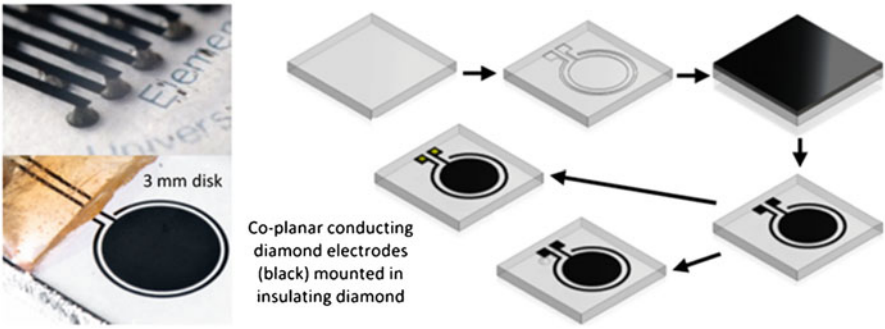

Fig. 2.35 Typical contacting options for coplanar b-doped diamond sensors that can be optimised to sense: conductivity of solutions, PH level, dissolved gases and undesirable impurities in water (ranging from heavy metals to explosives) (courtesy of Warwick University)

9.8 Water Treatment

Electrolytic Ozone Inc. (EOI) has developed and commercialised a revolutionary platform for generating ozone in water. Ozone kills nearly every known pathogen and is one of the most effective deodorisers known to man. Synthetic diamond anodes enable ozone to be produced on a scale that is suitable for homes, restaurants, hotels and hospitals more efficiently and more reliably than any other technology currently available (www.e6.com; www.eoi-oxygen.com).

Figure 2.36 schematically shows the EOI ozone generation cell. An ion-permeable membrane separates two electrodes, the anode is made of boron-doped diamond, and the cathode can also be boron-doped diamond or a suitable metal. The anode is highly perforated (by cutting slots or holes into the diamond plate) to give as many 'triple points' (where diamond, water and membrane are in contact) as possible. When driven by a small voltage, ozone is generated at the triple point on the anode side, with a proton being exchanged through the membrane to the cathode side, where hydrogen is generated. Dissolved ozone remains in the water for many minutes, depending upon concentration and water temperature, and is available in a safe form for sanitisation applications. Figure 2.37 shows an EOI battery operated spray bottle for dispensing the ozonated water.

Boron-doped synthetic diamond has unique physical, chemical and electrochemical properties enabling efficient oxidation of organic and inorganic compounds, via the production of highly oxidising radicals within the water to be treated or at the diamond electrode surface in contact with the water.

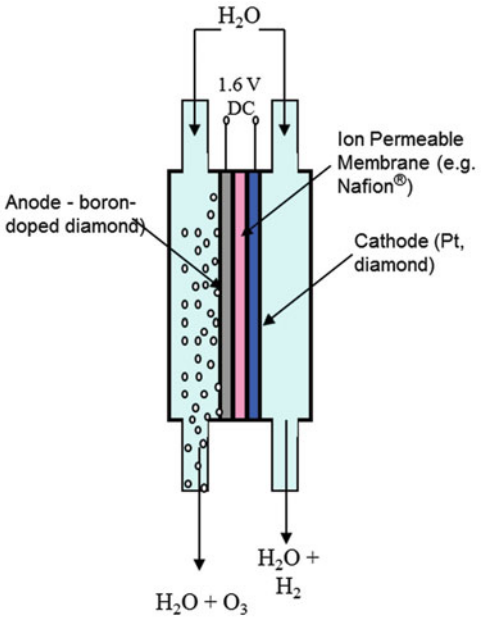

Fig. 2.36 Schematically shows the EOI ozone generation cell (www.eoi.oxygen.com)

Fig. 2.37 A prototype EOI dispenser (courtesy of EOI Inc)

Table 2.5 Showing the oxidation potential for oxidants

Oxidant	Oxidation potential
Fluorine	3.0
Hydroxyl radical	**2.8**
Ozone	2.1
Hydrogen peroxide	1.8
Potassium permanganate	1.7
Chlorine dioxide	1.5
Chlorine	1.4

Table 2.5 shows that the highly oxidising hydroxyl radical can be generated at the diamond anode, along with many other useful oxidising species (including ozone). Referring back to Fig. 2.34, we can see that only high-quality CVD diamond is able to reach the +2.8 V necessary to generate the hydroxyl radical.

The hydroxyl radical is extremely short lived (around 10^{-9} s) and is thus only available for oxidation of organics at the diamond anode surface. Figure 2.38 shows an as-grown boron-doped CVD diamond electrode that is 130 mm in diameter and around 400 microns thick. In industrial applications (an example of which is shown in Fig. 2.39), many such electrodes are placed in parallel to give a very large surface area which, when driven with sufficient current density of 1000–5000 A/m^2 at voltages around 3 V, can produce sufficient quantities of oxidants to effectively 'electrochemically incinerate' most organic pollutants, chemical or biological.

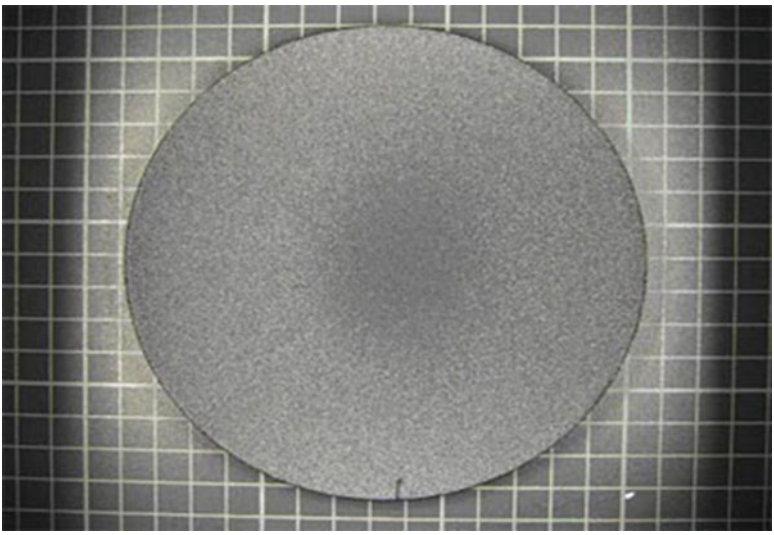

Fig. 2.38 Shows an as-grown boron-doped CVD diamond electrode that is 130 mm in diameter and around 400 microns thick (courtesy of E6)

Fig. 2.39 Showing two, multiplate diamond electrochemical reactors for industrial scale water treatment

Applications include removal of dyes; treating landfill leachants; destruction of formaldehyde; removing toxins, pesticides and solvents; converting ammonia to nitrogen without producing nitrates; and removing odours from sulphurous mercaptans. Electrolytic Ozone Inc. is also developing technologies to exploit synthetic diamond's superior characteristics for these applications (www.e6.com; www.eoi-oxygen.com).

Table 2.6 Comparing the electronic properties of various semiconductor materials (Wort and Balmer 2008)

	Si	SiC-4H	GaN	Diamond
Bandgap (eV)	1.1	3.2	3.44	5.47
Breakdown field (MV/cm)	0.3	3	5	20
Electron mobility (cm^2/Vs)	1450	900	440	4500
Hole mobility (cm^2/Vs)	480	120	200	3800
Thermal conductivity (W/cmK)	1.5	5	1.3	24
Johnson's figure of merit	1	410	280	8200
Keyes' figure of merit	1	5.1	1.8	32

9.9 Thermal Management Applications

The exceptionally high thermal conductivity (5× that of the next best thermal conductor) combined with electrical insulation makes diamond the heat spreader of choice for many high power density applications (Susmann et al. 2000). One such application is spreading the heat away from laser diode junctions. This was one of the earliest applications for CVD diamond and is covered well by Susmann (Susmann et al. 2000).

More recently, the integration of CVD diamond with GaN on a wafer scale has become possible, allowing higher power densities to be achieved at radio frequencies (Altman et al. 2014).

Table 2.6 compares the electronic properties of various semiconductor materials, and although it is apparent that diamond would excel as a semiconductor material, limitations imposed by the lack of a suitable dopant currently relegate diamond to uses where the intrinsic properties can be deployed.

SiC and GaN are very important wide bandgap materials showing great promise for both switching and RF power applications. The properties of both SiC and GaN materials are exciting to designers due to their ability to operate at higher voltages, higher power densities, higher temperatures and higher frequencies compared to their silicon counterparts. The high critical field of GaN compared to Si (3.5×10^6 cf 0.3×10^6 V/cm) is a property which allows GaN devices to operate at higher voltages and lower leakage currents. Having higher electron mobility and electron saturation velocity make GaN devices better suited than Si for higher frequency of operation. GaN's electron mobility is higher even than that of SiC, making GaN the best material for very high frequencies, where power transmission is required. However, as shown in Table 2.6, GaN's thermal conductivity is not high enough by itself to enable it to reach its full potential for power density, which makes heat management for GaN devices a challenge for system designers.

GaN epitaxial layers are typically grown on either a 'nonnative' Si or SiC substrate. In both cases, there are crystal lattice differences which need to be taken into consideration. One way to do reduce the stress induced by lattice mismatch is through the use of transition layers. These transition layers cause an

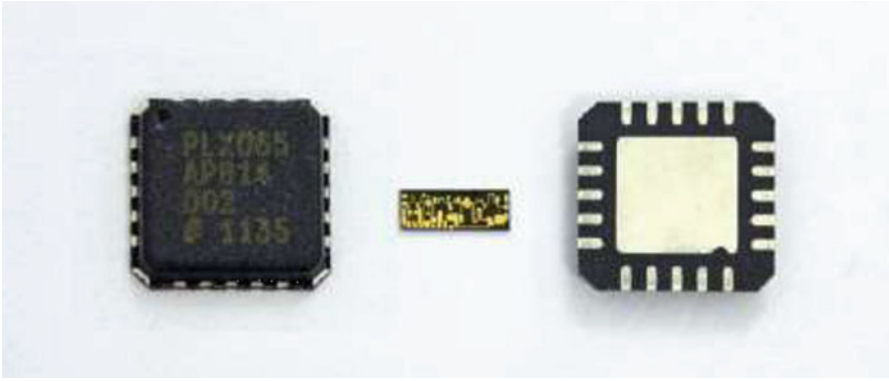

Fig. 2.40 GaN-on-diamond eliminates the need for performance-limiting transition layers (courtesy of E6)

important drawback for GaN devices because they have a higher density of defects and reduced thermal transport properties. To address this and improve the thermal performance, GaN-on-diamond technology is an attractive alternative.

9.10 GaN-on-Diamond's Advantages

High-quality GaN-on-diamond wafers have been demonstrated to have GaN epitaxy quality virtually identical to the original layers as grown on Si substrates. State-of-the-art HEMTs made with GaN-on-diamond technology show excellent electrical DC and RF properties. By eliminating the transition layers as shown in Fig. 2.40, it has been demonstrated that GaN-on-diamond transistors can also achieve power densities more than three times those of GaN-on-SiC devices (Dumka et al. 2013). And the thermal barrier resistance (TBR) between gate junction and substrate can be as much as 50 % less with GaN-on-diamond devices compared to GaN-on-SiC devices (Pomeroy et al. 2013) as shown in Fig. 2.41.

These two advantages can generate significant system-level benefits for defence applications (e.g. radar and EW) and commercial applications (e.g. cellular base stations and communications/weather satellites). By way of examples:

1. GaN-on-diamond RF power amplifiers can be used to reduce cooling complexity and cost in varying degrees whilst increasing lifetimes.
2. A threefold increase in power density means devices can be 1/3 the size—saving on weight and complexity.
3. Processing three times fewer GaN-on-diamond wafers than GaN-on-SiC to achieve the same RF output power means significant reductions in fab costs, some of which could be passed on to the system maker in a reduced power amplifier price per watt.

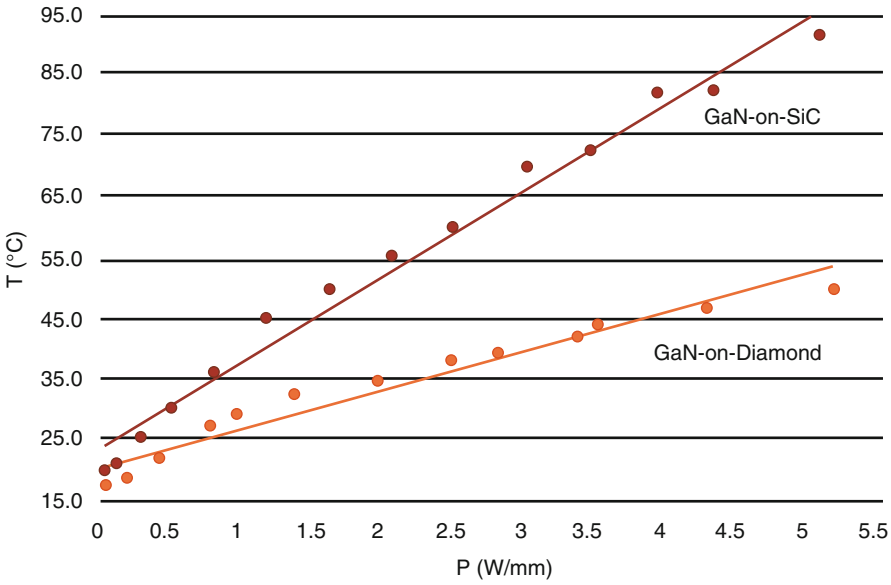

Fig. 2.41 GaN-on-diamond power devices run significantly cooler than GaN on SiC for a given power output due to the better heat spreading ability of CVD diamond (courtesy of E6)

4. System designers may be able to use fewer power amplifier devices by taking advantage of the higher power density to generate more power per device of the same size. Fewer power amplifiers would mean a reduction in peripheral circuitry, thereby lowering system cost.

Preliminary high-temperature operating life test data show a reliability improvement for GaN-on-diamond devices compared to the control GaN/Si devices produced from the same original GaN epitaxy. Most importantly, due to diamond being within a micron of the GaN epi, power densities of three times that of GaN/SiC and its thermal impedance is up to 50 % lower than GaN/SiC.

These GaN-on-diamond thermal advantages will lead to:

(a) Reduced $ per watt RF power amplifiers due to more devices per wafer
(b) Reduced RF system cooling costs—both fixed costs and operating expenses—due to a higher allowable ambient temperature
(c) Reduced size of the RF power amplifier and its related parts
(d) Reduced size and weight at the system level where cooling apparatuses are typically bulky and heavy

9.11 Future Applications in Diamond Quantum Technology

Synthetic diamond has recently emerged as a candidate material for a range of quantum-based applications including: secure quantum communication, quantum

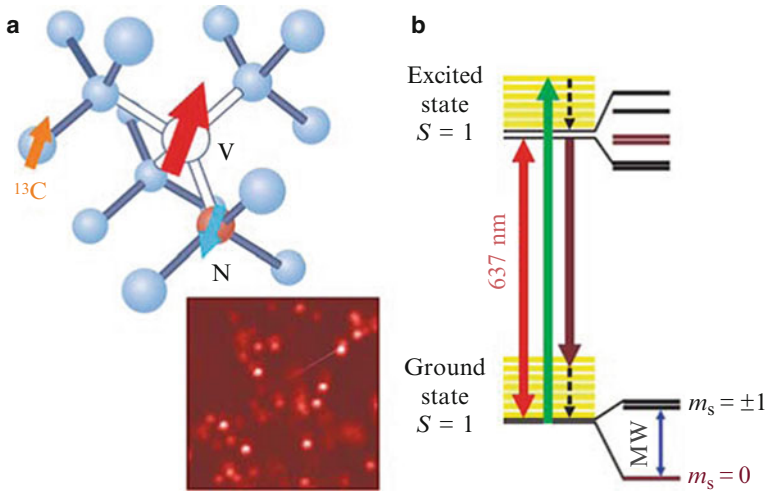

Fig. 2.42 Taken from *Physics Today*, article 67(10), 38 (2014) by Lilian Childress, Ronald Walsworth and Mikhail Lukin

computing and magnetic/electric field sensing. Quantum applications use the extreme world of quantum physics to perform operations that are not possible in systems following classical physics.

Diamond-based quantum technology offers potential solutions in two of the key challenges of the twenty-first century: that of biomedicine and the continual growth of the information economy. Diamond has the ability to do this using defects as a quantum resource. The specific diamond defect that can be used for these applications is the nitrogen-vacancy defect (NV), the unique properties of which allow its quantum states to be manipulated and read out using light, all at room temperature. In quantum-based applications, the synthetic diamond acts as a host for impurities or defects, acting like *a solid-state atom trap*. The quantum properties of these impurities, such as the nitrogen-vacancy defect, can be individually manipulated and made to interact, and photons of light emitted from these impurities can be used to read out their quantum information. A recent review article in *Physics Today* (Lilian et al. 2014) by Lilian Childress, Ronald Walsworth and Mikhail Lukin clearly very nicely explains (Fig. 2.42) the basic physics and processes used to realise diamond quantum devices (from the article Lilian et al. (2014)).

9.12 The Structure of the Nitrogen Vacancy

The NV centre, is a point defect made of a nitrogen atom substituted for carbon with an adjacent lattice vacancy. **(a)** In its negative charge configuration, the defect has a net electronic spin $S = 1$ (red arrow) on the vacancy V, with nearby nuclear spins

(blue and orange arrows) on nitrogen and carbon-13 impurities. In the confocal microscope image of diamond (inset), the fluorescence reveals individual NV centres. **(b)** The NV electronic state can be excited resonantly with 637-nm-wavelength light (red) or nonresonantly using shorter-wavelength light (green), after which the atom fluoresces at longer wavelengths (brown) following fast phonon relaxation. Black dashed arrows represent the relaxation through vibrational levels (yellow). Microwaves (MW) drive spin transitions between *m*s sublevels.

For biomedical applications, these quantum defects are used as magnetic field sensors which will enable 'cellular-MRI' capabilities; these have the ability to revolutionise medical diagnostics and drug design. For the information economy, the diamond defects can be used as qubits to form quantum repeaters for the backbone of ultra-secure quantum communication networks, quantum simulators and various roles in quantum computing. A lot of scientific development will be required to access these ambitious goals, but the key enabler to this is the diamond material and diamond processing. The high-purity diamond material has been developed and sold commercially by E6 for the advancement of these applications; the potential application markets are shown in Fig. 2.43.

Demonstrations of diamond-based magnetic field imaging have already been performed showing the ability to measure magnetic fields from bacteria, hard drive platens, tagged blood cells and even meteorites (Le Sage et al. 2013; Maletinsky et al. 2012). To move this technology from the academic laboratory to a widely used characterisation tool requires improvements in sensitivity and resolution, which in turn require improvements in diamond quantum device processing technologies.

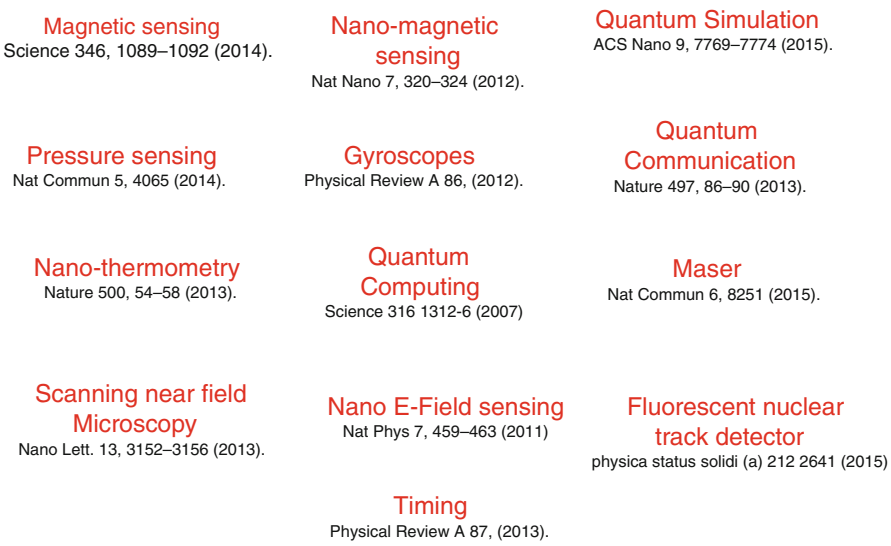

Fig. 2.43 Potential applications for diamond quantum devices with references to the application

9.13 Potential Markets for Diamond Quantum Devices

In quantum computing, synthetic diamond can be used as quantum bits or qubits (analogous to 1 and 0 in classical computers), which could potentially allow quantum computers to solve certain problems that would not be possible with standard computers.

For magnetic field sensing, synthetic diamond's quantum properties can be used to detect very small magnetic fields. Synthetic diamond-based magnetometers have a wide field of potential applications, such as detecting magnetic fields associated with the ion flow through membrane channels in cells, an application which has important implications for drug development.

A vast number of potential market applications exist for diamond quantum devices (Fig. 2.43). The size of these markets for this disruptive technology is huge, for example, in 2012 the high-performance computer market was $5.6 billion, and the market for laboratory equipment in 2013 was ~£137 billion. Diamond only addresses some of the issues in these areas and the diamond serviceable market will thus be a small percentage of these big markets; however, this is still considerable and estimated to be worth of order $1.3b.

9.14 Properties of Superhard Boron Nitride

The properties of cBN and wBN are homogeneous and isotropic. The cubic (sphalerite or zinc-blende structure) of boron nitride (cBN) is isostructural and isoelectronic to diamond, does not occur in nature and is produced from hexagonal BN using similar HPHT techniques and processes to those used to synthesise diamond from graphite. It possesses similar properties to diamond and in some respects has advantages over diamond as, unlike diamond, it is (a) chemically inert to ferrous materials at high temperature and (b) for electronic applications it can be doped to exhibit either n- or p-type semiconductivity. Its hardness is superior to all commercially available materials except diamond. The rare wurtzite (wBN) modification may even be harder than the cubic form (Pan et al. 2009). Figure 2.44 shows the structural differences between cBN and wBN.

Polycrystalline cBN with grain sizes on the order of 10 nm is also reported to have Vickers hardness comparable or higher than diamond (Tian et al. 2013). Because of much better stability to heat and metals, cBN surpasses diamond in many mechanical and abrasive machining applications (Engler 2007). The thermal conductivity of BN is among the highest of all electric insulators (see Table 2.7).

Boron nitride can be doped p-type with beryllium and n-type with boron, sulphur and silicon or co-doped with carbon and nitrogen. Both hexagonal and cubic BN are wide-gap semiconductors with a bandgap energy corresponding to the UV region. If voltage is applied to cBN (Kubota et al. 2007; Taniguchi et al. 2002), then it emits UV light in the range 215–250 nm and therefore can potentially be used as

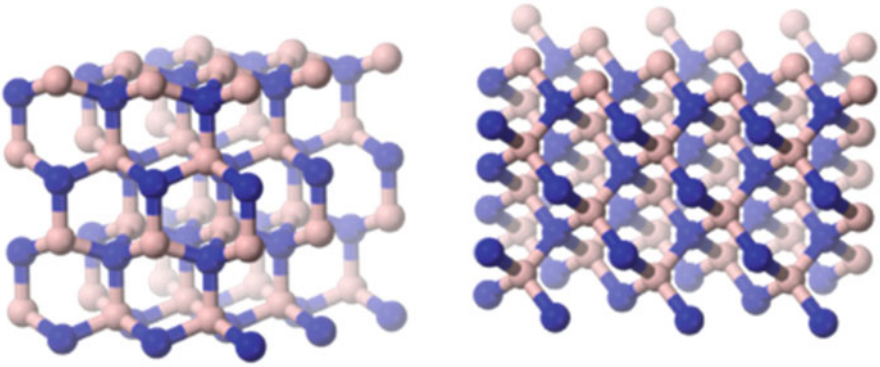

Fig. 2.44 Structural differences between sphalerite cBN (*Left*) and Wurtzite wBN (*right*)

Table 2.7 Showing the properties of cBN, wBN and diamond

Material	cBN	wBN	Diamond
Density (g/cm^3)	3.45	3.49	3.515
Mohs hardness	9.5–10	~10 (Carlomagno and Brebbia 2011)	10
Knoop hardness (GPa)	45	34	100
Bulk modulus (GPa)	400	400	440
Thermal conductivity (W/m.K)	740		600–2000
Thermal expansion (10^{-6}/°C)	1.2	2.7	0.8
Bandgap (eV)	6.4	4.5–5.5	5.5
Refractive index	2.1	2.05	2.4

Sources: Crystalline BN (Leichtfried et al. 2002; Ioffe 2014) diamond (Ioffe 2014)

light-emitting diodes (LEDs) or lasers. Cubic boron nitride is a III-V semiconducting material but has yet to be exploited in semiconducting applications due to the small size of crystals available and the lack of CVD synthesis processes.

Despite much research during the past 20+ years, films or plates of cBN, either polycrystalline or monocrystalline, have yet to be fully commercialised. Unlike diamond, where CVD techniques are able to produce highly pure bulk wafers of diamond, such techniques have yet to be realised for cBN equivalents. This is partly due to the lack of market need as there are other, 'almost as good', reasonably hard materials that are already readily available. These include silicon carbide (as an abrasive, electronic material and electronic substrate), silicon nitride (as a high-temperature tough ceramic), sapphire (as an electronic substrate, scratch-resistant infrared transmission window), zirconia (for bearings and medical implants) and so on (note: diamond on the other hand is a truly exceptional material being over twice as hard as the next (readily) available material (cBN) which, when combined with another from the large range of other truly exceptional and extreme properties of diamond, opens up its unique applications).

As a result of really being only available (at the time of writing) in submillimetre crystalline form, applications are limited to make use of its hardness combined with its chemical inertness in certain situations, i.e. abrasive and cutting tool applications.

Whilst fine powders of CBN can be used to machine ferrous components by grinding processes (and there are many very skilled tool makers who can optimise cBN grinding wheel design and lifetime for machining), cutting applications require the cBN to be present in a different format to manufacture cutting tools. To this end, polycrystalline CBN (or PCBN) materials have been developed to meet the market requirements to precision machine ferrous components. Unlike PCD, where the diamond component is sintered together (i.e. has contiguity), PCBN materials are compounds where a second phase bonds the CBN crystals together (i.e. not contiguous). The nature and properties of PCBN materials are thus dictated not only by the CBN component content but also the properties of the binder material and composite as a whole.

The following section separates the applications for superhard boron nitride materials into two. The first section deals with applications for monocrystalline CBN and the second is for applications for polycrystalline PCBN.

9.15 Physical Properties

The cubic form has the sphalerite crystal structure, the same as that of diamond, and is also called β-BN or cBN. The wurtzite BN form (wBN; point group = C_{6v}; space group = $P6_3mc$) has the same structure as lonsdaleite, a rare hexagonal polymorph of carbon. In both cBN and wBN, the boron and nitrogen atoms are grouped into tetrahedra, but the angles between neighbouring tetrahedra differ between the two (Silberberg 2009).

10 Applications of Superhard Boron Nitrides

10.1 Cubic Boron Nitride

Cubic boron nitride (CBN or cBN) is widely used as an abrasive (Todd et al. 1994; Jochen and Schwetz 2005; El Khakani and Chaker 1993). Its usefulness arises from its insolubility in iron, nickel and related alloys at high temperatures, whereas diamond is soluble in these metals to give carbides. Polycrystalline cBN (PCBN) abrasives are therefore used for machining steel, whereas diamond abrasives are preferred for aluminium alloys, ceramics and stone. When in contact with oxygen at high temperatures, BN forms a passivation layer of boron oxide. Boron nitride binds well with metals, due to the formation of interlayers of metal borides or nitrides. Materials with cubic boron nitride crystals are often used in the tool bits of

cutting tools. For grinding applications, softer binders, e.g. resin, porous ceramics and soft metals, are used. Ceramic binders can be used as well. Commercial products are known under names 'Borazon' (by Diamond Innovations), 'Elbor' or 'Cubonite' (by Russian vendors) and ABN by Element Six.

10.2 Abrasive Applications for cBN Crystals

The desirable characteristics of an abrasive include high hardness, strength, abrasion resistance, thermal and chemical resistance and an ability to maintain sharp cutting edges during use. These characteristics for cBN exceed the values of conventional abrasives, such as silicon carbide and aluminium oxide. In particular, the properties of high thermal stability and chemical resistance make it suitable for machining ferrous materials, an area where synthetic diamond abrasives are not normally employed.

Hardness is a crucial property of any abrasive. However, most abrasives suffer a loss in hardness at the elevated temperatures experienced during application. One of the physical advantages of CBN compared to conventional abrasives is that, in addition to being harder at ambient temperature, it maintains this hardness over a wide temperature range.

CBN abrasives provide higher productivity and dramatically longer tool lives compared to conventional abrasives (WC, SiC and Alumina) when grinding, honing and fine finishing hardened ferrous materials and difficult-to-machine alloys. CBN is firmly established in 'tool and cutter' grinding and in mass production grinding operations in the automotive, general engineering and aerospace industries. Application examples include:

- Camshafts
- Crankshafts
- Fuel injectors
- Transmission parts
- Gears
- CV joints
- Power steering pump parts and compressor parts
- Turbochargers
- Piston pins
- Valves and seats

CBN is specified for tools grinding ferrous metals and superalloys in Aerospace and land-based gas turbine components such as vanes, blades, nozzles and seats.

Some of the many advantages of CBN include improved surface finishes and the production of more favourable compressive residual surface stresses [E6web].

To provide the toolmaker with a choice of abrasives to enable optimisation of the tool for a specific application, cBN suppliers try to offer a range of abrasives. Each abrasive material range provides a unique combination of crystal strength, thermal

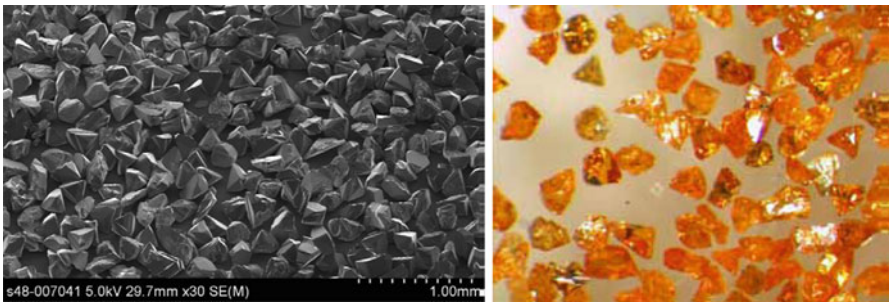

Fig. 2.45 Cubic boron nitride crystals produced by Element Six (ABN900 80/100 US mesh size)

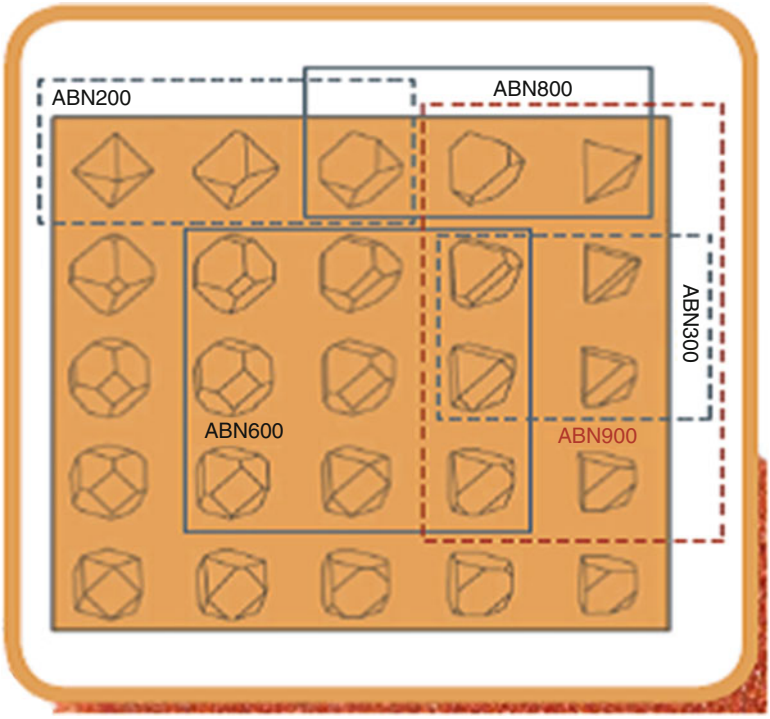

Fig. 2.46 Showing crystal morphologies engineered for specific grinding applications (www.e6.com)

stability and crystal morphology and size distribution. Examples of cBN crystals are shown in Fig. 2.45.

Crystalline cBN grit is engineered during its synthesis to produce crystals that are not only abrasive but wear and/or break down in a highly predictable manner. This enables tool to make design precision grinding wheels that perform reliably and consistently. A range of crystal morphologies is available in various cBN crystals as shown in Fig. 2.46.

10.3 Applications for Polycrystalline Boron Nitride (PCBN)

Polycrystalline cubic boron nitride (PCBN) composites are used for the production of precision cutting tools for machining ferrous materials such as hard steels, grey and hard cast irons and high-temperature superalloys. Different grades of PCBN are offered to meet specific application requirements. Low-CBN materials are most commonly used for the finishing of hardened steel components in the automotive industry and superalloys for land and air turbine engine components. High-CBN materials are used for rough and finish machining of cast irons and for extremely abrasive powder metallurgy parts, such as automotive valve seats [e6 web].

Polycrystalline cubic boron nitride (PCBN) composites are produced by sintering micron CBN (cubic boron nitride) powders with various ceramics, so as to produce extremely hard and thermally stable tooling materials. Most PCBN materials are integrally bonded to a cemented carbide substrate. CBN is the second hardest material known after synthetic diamond but has high thermal and chemical resistance properties. PCBN composites provide extreme resistance to deformation and wear at high temperatures—typically an order of magnitude better than the nearest ceramic materials.

Although PCBN is manufactured using similar HPHT sintering techniques, PCBN differs from PCD in that the cBN crystals are not congruent (i.e. not sintered together) but rather bonded together using either a metallic or ceramic matrix. The composite material properties are thus dictated by not only the cBN content but also the binder phase. Different binder phases are used in different applications where abrasive and chemical erosion can often occur. PCBN is available in various formats: discs of PCBN backed by WC/Co, free-standing PCBN, high PCBN content, low PCBN content, metallic binder or ceramic binder and coated versions of each. Figure 2.47 shows the classification of a variety of PCBN materials supplied by Element Six, their composition and material properties.

About two thirds of all PCBN tools are used for the machining of hardened steels, offering a viable, more cost-effective alternative to conventional grinding processes. Other applications are in the machining of hard, grey and high-strength cast iron and cold and hot-work tool steels. The machining of nickel and cobalt-based superalloys is a significant and rapidly growing application area for PCBN.

The chemical composition and microstructure of PCBN grades differ greatly depending on the application. Lower CBN content materials tend to be more resistant to chemical wear mechanisms prevalent when continuously turning hardened steels. Where there are interrupts in the workpiece—oil-holes in a shaft, for example—a medium content grade is preferred, as it offers the best combination of wear resistance and toughness.

For applications where abrasion resistance is dominant, as in the machining of grey and hard cast irons, a high CBN grade is the preferred choice. High-content PCBN (such as E6's AMB90) also exhibits excellent thermal properties and, being

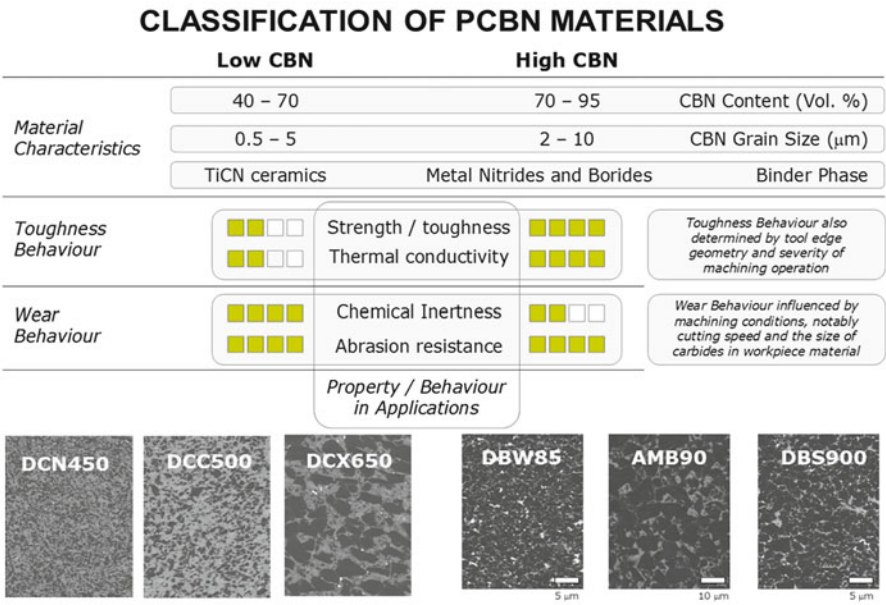

Fig. 2.47 Shows the classification of a variety of PCBN materials supplied by Element Six, their composition and material properties (courtesy of E6)

available as solid (unbacked) materials, provides additional economic benefits. Such a material is the workhorse grade for the roughing and finishing of brake discs and cast iron engine blocks, and typically outlasts ceramic tools by more than an order of magnitude, whilst operating at cutting speeds in excess of 2500 m/min. For extreme interrupted cutting applications, such as the milling of hardened steels, backed, high-content PCBNs are preferred because of their extreme strength and thermal shock resistance. These materials also have a fine-grain size, thereby ensuring a good workpiece surface finish, and they are used extensively in the fine finishing of cast irons and valve seats.

PCBN materials are used to machine materials that are either too hard for ceramic machine tools or interact with diamond (such as hard steels). The choice of which type of PCBN to use for any particular precision machining application is dictated by the interaction of the tool with the workpiece. Figure 2.48 shows where PCBN fits on the wear-resistance vs toughness diagram and the breakdown of PCBN usage as a function of cutting speed and severity of steel-hard part turning. Figure 2.49 shows in more detail which PCBN materials generally work best for a given application (courtesy of Element Six); however, this will always depend upon other factors such as machine and operational conditions.

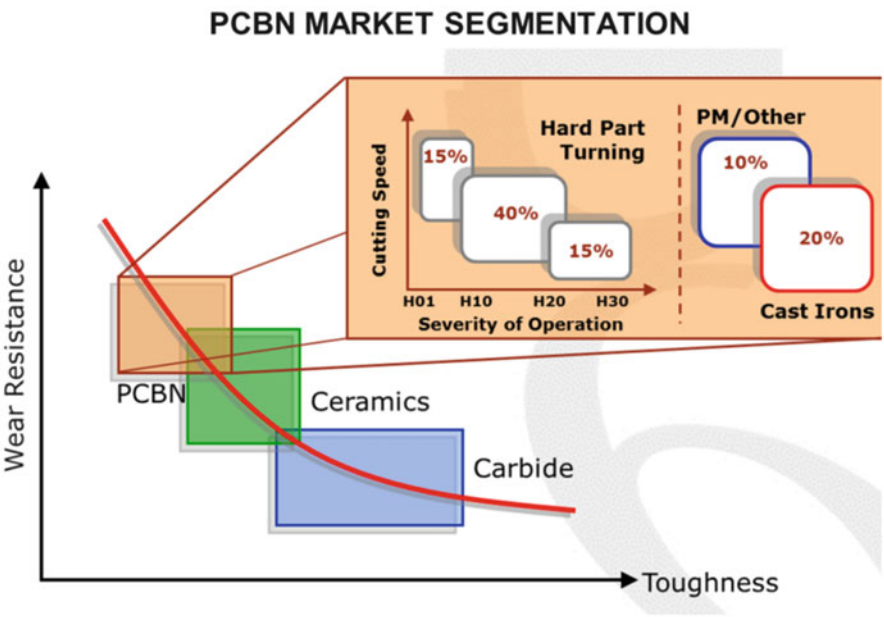

Fig. 2.48 PCBN fits on the wear-resistance vs. toughness diagram and the breakdown of PCBN usage as a function of cutting speed and severity of hard part turning (courtesy of E6)

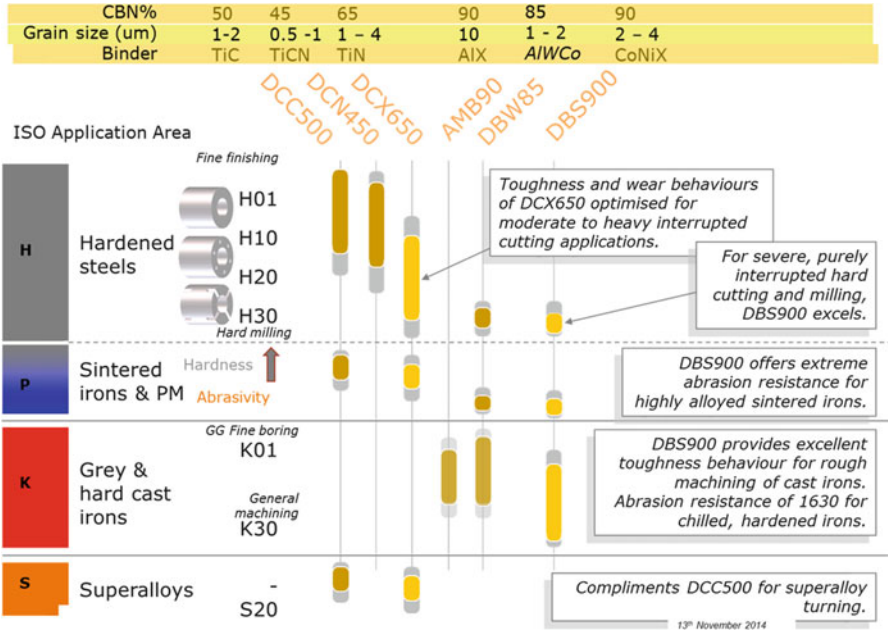

Fig. 2.49 Element Six' generalised recommendation on which PCBN materials work best for a given application

11 Summary

Diamond, in its various formats, is the only ultra-hard material currently used for a diverse range of industrial applications. The unique combination of extreme properties available in diamond, beyond its exceptional hardness, is what allows these applications to be realised. However, the largest current application is still in abrasives markets which are expanding as new, 'difficult-to-machine' materials (such as CFC and MMC materials) become more widely used. As a result, suppliers of diamond-based products for abrasive applications are continuously trying to improve the performance of their products through innovative synthesis and processing techniques which are best described as 'diamond engineering'.

The advent of CVD diamond technology has opened up a vast range of new applications beyond machining and wear parts, and CVD diamond is currently used in submarines (for sensors) to satellites (for windows and heat spreaders) and everywhere in between! New, quantum applications (based around specific N-V defects within highly perfect diamond structure that exhibit 'spin') are likely to lead to many new and exciting devices in the future.

Cubic BN, in its various formats, is truly a superhard material which currently compliments diamond in abrasive markets due to its ability to very effectively precision machine ferrous-based materials (unlike diamond). Currently, cBN and PCBN are only commercially produced by HPHT techniques for abrasive applications; however, it is highly likely that in the near future, CVD techniques to produce pure cBN layers and large monocrystals will be available. If this is the case, then cBN would find new applications in electronics (it could well prove to be the semiconductor of choice for high-power switching) and optical markets (e.g. for high-power LEDs).

In conclusion, I think it is fair to say that currently available super- and ultra-hard materials have a unique combination of extreme properties beyond simply their hardness, which are opening up many novel and exciting industrial applications.

References

Altman D, Tyhach M, McClymonds J, Kim S, Graham S, Cho J, Goodson K, Francis D, Faili F, Ejeckam F, Bernstein S (2014) Analysis and characterization of thermal transport in GaN HEMTs on diamond substrates. Submitted to I-THERM 2014 conference in Orlando

Andersson J, Hollman P, Jacobson S (1999) Abrasive technology: current development and applications I: the third international conference on abrasive technology: (ABTEC'99), Brisbane, 22–24 Nov 1999, pp 39–46

Bifano TG et al (1991) Ductile-regime grinding: a new technology for machining brittle materials. J Eng Ind Trans ASME 113(2):184–189

Carlomagno GM, Brebbia CA (2011) Computational methods and experimental measurements XV. WIT Press, Southampton

Dubrovinskaia N et al (2006) High-pressure/high-temperature synthesis and characterization of boron-doped diamond. Z Naturforsch B 61:1561–1565

Dumka DC, Chou TM, Francis D, Faili F, Ejeckam F (2013) AlGaN/GaN HEMTs on diamond substrate with over 7 W/mm output power density at 10GHz. Accepted to IET electronics letters (Issue #20, 2013)

El Khakani MA, Chaker M (1993) Physical properties of the x-ray membrane materials. J Vac Sci Technol B 11(6):2930–2937

Engler M (2007) Hexagonal boron nitride (hBN)—Applications from metallurgy to cosmetics

Granger MC, Xu J, Strojek JW, Swain GM (1999) Polycrystalline diamond electrodes: basic properties and applications as amperometric detectors in flow injection analysis and liquid chromatography. Anal Chim Acta 397:145

Haines J, Leger JM, Bocquillon G (2001) Synthesis and design of superhard materials. Annu Rev Mater Res 31:1–23

Hall HT (1960) Ultra-high pressure apparatus. Rev Sci Instr 31:125

Ioffe Database (2014) BN—boron nitride. Sankt Peterburg: FTI im. A. F. Ioffe, RAN

Isberg J, Hammersberg J, Johansson E, Wikström T, Twitchen DJ, Whitehead AJ, Coe SE, Scarsbrook GA (2002) High carrier mobility in single-crystal plasma-deposited diamond. Science 297(5587):1670–2

Jochen G, Schwetz KA (2005) Boron carbide, boron nitride, and metal borides, Ullmann's encyclopedia of industrial chemistry. Wiley, Weinheim

Klages CP (2000) Chemical vapour deposition of diamond films. In: Riedel R (ed) Handbook of ceramic hard materials. Wiley, Weinheim, pp 390–419

Koppang MD, Witek M, Blau J, Swain GM (1999) Electrochemical oxidation of polyamines at diamond thin-film electrodes. Anal Chem 71:1188

Kubota Y et al (2007) Deep ultraviolet light-emitting hexagonal boron nitride synthesized at atmospheric pressure. Science 317(5840):932–4

Leichtfried G et al (2002) 13.5 Properties of diamond and cubic boron nitride. In: Beiss P et al (eds) Landolt-Börnstein – Group VIII advanced materials and technologies, vol 2A2, Powder metallurgy data. Refractory, hard and intermetallic materials. Springer, Berlin, pp 118–139. doi:10.1007/b83029. ISBN 978-3-540-42961-6

Lilian C, Ronald W, Mikhail L (2014) Atom-like crystal defects: From quantum computers to biological sensors. Phys Today 67(10):38–43

Maletinsky P et al (2012) A robust scanning diamond sensor for nanoscale imaging with single nitrogen-vacancy centres. Nat Nanotechnol 7:320–324

Mollart Tim P, Wort Christopher JH, Pickles Charles SJ, McClymont Mark R, Perkins Neil , Lewis Keith L (2001) In: Proceedings of SPIE 4375, Window and Dome technologies and materials VII, 180, 7 Sept 2001

Nebel CE, Ristein J (eds) (2004) Thin film diamond II, semiconductors and semimetals, vol 77. Elsevier, London, p 121

Németh P, Garvie LAJ, Aoki T, Dubrovinskaia N, Dubrovinsky L, Buseck PR (2014) Lonsdaleite is faulted and twinned cubic diamond and does not exist as a discrete material. Nat Commun 5 Article 5447, 1–5

Pan Z et al (2009) Harder than diamond: superior indentation strength of wurtzite BN and lonsdaleite. Phys Rev Lett 102(5):055503

Pomeroy J, Bernardoni M, Sarua A, Manoi A, Dumka DC, Fanning DM, Kuball M (2013) Achieving the best thermal performance for GaN-on-diamond. In: 35th IEEE compound semiconductor IC symposium (CSICS) 13–16 Oct 2013, Monterey, Section H.4

Pope et al (2006) Prosthetic hip joint having polycrystalline diamond articulation surfaces and at least one solid polycrystalline diamond compact. Application number: 20080195220 Filed: 16 May 2006

Sage L et al (2013) Optical magnetic imaging of living cells. Nature 496:486–489

Silberberg MS (2009) Chemistry: the molecular nature of matter and change, 5th edn. McGraw-Hill, New York, p 483. ISBN 0073048593

Solozhenko VL, Andrault D, Fiquet G, Mezouar M, Rubie DC (2001) Synthesis of superhard cubic BC2N. Appl Phys Lett 78(10):1385

Soma T et al (1974) Characterization of wurtzite type boron nitride synthesized by shock compression. Mater Res Bull 9(6):755

Stoupin S, Terentyev SA, Blank VD, Shvyd'ko Yu V, Goetze K, Assoufid L et al (2014) All-diamond optical assemblies for a beam-multiplexing X-ray monochromator at the Linac Coherent Light Source. J Appl Crystallogr 47(Pt 4):1329–1336

Susmann R et al (2000) In: Riedel R (ed) Handbook of ceramic hard materials. Wiley, Weinheim

Taniguchi T et al (2002) Ultraviolet light emission from self-organized p–n domains in cubic boron nitride bulk single crystals grown under high pressure. Appl Phys Lett 81(22):4145

Tian Y et al (2013) Ultrahard nanotwinned cubic boron nitride. Nature 493(7432):385–8

Todd RH, Allen DK, Alting L (1994) Manufacturing processes reference guide. Industrial Press Inc., New York, pp 43–48

Vel L et al (1991) Cubic boron nitride: synthesis, physicochemical properties and applications. Mater Sci Eng: B 10(2):149

Venkatachalam S, Li X, Fergani O, Yang JG, Liang SY (2013) Crystallographic effects on microscale machining of polycrystalline brittle materials. ASME J Micro Nano Manuf 1:041001

Venkatachalam S, Li X, Fergani O, Yang JG, Liang SY (2015) Microstructure effects on cutting forces and flow stress in ultra-precision machining of polycrystalline brittle materials. ASME J Manuf Sci Eng 137(2):021020

Wentorf RH, Devries RC, Bundy FP (1980) Sintered superhard materials. Science 208 (4446):873–80

Wort CJH, Balmer RS (2008) Diamond as an electronic material. Mater Today 11(1–2):22–28

Chapter 3
Structure-Properties Relationships

Dr. Wallace Matizamhuka

Abstract This chapter explores the correlations between the microstructures of hard, superhard and ultrahard materials and resulting properties. Key microstructure features and their effect on mechanical properties (hardness, fracture toughness, strength, wear and thermal properties) are discussed. A number of analytical and empirical structure-properties-behaviour model(s) are proposed for a range of hard, super and ultrahard materials, extending from classical theories such as the Hall-Petch relationship, theory of critical distance and formation of Griffith cracks. The challenge in extending these theories to nanostructured materials is also discussed. Furthermore, the chapter addresses, the 'strength-toughness conflict' in hard, super and ultrahard materials and the effect of microstructure on crack growth behaviour. Some useful techniques that have been utilised to counteract the conflicts between strength and fracture toughness are also highlighted. The chapter also serves as an introduction to the later chapters where techniques for microstructure analysis and property testing are discussed in greater detail (Chap. 5). In Chap. 6 an in-depth discussion of nanostructured materials and the effect on material properties such as hardness, as well as their industrial applications, are presented.

1 Introduction

Hard, superhard and ultrahard materials display exceptional mechanical performance in hardness, toughness, incompressibility, thermal conductivity and wear resistance. This makes them suitable candidates in a wide range of applications such as mining industry drilling bits in rock cutting and petrochemical industry, polishing tools and machining tools for advanced aerospace alloys. A more detailed discussion of these and other applications of superhard and ultrahard materials is presented in Chap. 2. During operation, the tools are subjected to high-temperature

Dr. W. Matizamhuka (✉)
Senior Lecturer, Department of Metallurgical Engineering,
Vaal University of Technology, Vanderbijlpark, South Africa
e-mail: wallamatiza@yahoo.co.uk

V. Kanyanta (ed.), *Microstructure-Property Correlations for Hard, Superhard, and Ultrahard Materials*, DOI 10.1007/978-3-319-29291-5_3

wear and multiple interrupted impacts. Despite the superior mechanical properties, these materials are bound to fail mostly through chipping and fracture owing to their brittle behaviour, i.e. low fracture toughness. As in all materials, their performance is closely linked to the microstructure and obviously the operating conditions.

Although diamond has sufficed as the hardest material known to man, its interaction with iron-containing alloys at elevated temperatures limits its industrial application to machining of non-ferrous and non-metallic materials. In the 1960s a synthetic superabrasive cubic boron nitride (c-BN) was introduced in the market (Zheng et al. 1999; Solozhenko et al. 2005; Pierson 1994; Riedel 1992, 1994; Haines et al. 2001; Brazhkin 2007; Leger et al. 1994; Zerr and Riedel 2000; Badzian 1981; Nakano et al. 1994; Knittle et al. 1995; Nakano 1996; Zhao et al. 2002; Komatsu et al. 1996). The value of c-BN as a superabrasive lies in its much higher oxidation stability compared to diamond and its nobility to iron attack at elevated temperatures. However the hardness of c-BN is about half that of diamond. Over the years several attempts have been aimed at filling the hardness gap between the two traditional superabrasives (Matizamhuka 2010). This has been driven by the need to obtain an all-purpose, cost-effective superabrasive with a wider range of applications. A 'superhard' material by convention is one whose hardness exceeds 40 GPa on the Vickers scale of hardness. In this regard, only diamond and cubic boron nitride (c-BN, hereafter) qualify for this title.[1] However, over the years there have been tremendous efforts in the search for potential 'superhard' materials (Solozhenko et al. 2005; Pierson 1994; Riedel 1992, 1994; Haines et al. 2001; Brazhkin 2007; Leger et al. 1994; Zerr and Riedel 2000; Badzian 1981; Nakano et al. 1994; Knittle et al. 1995; Nakano 1996; Zhao et al. 2002; Komatsu et al. 1996). This has been stimulated by the need to design materials which not only approach diamond in hardness but are more useful and complimentary to the traditional superhard materials (Solozhenko et al. 2005; Pierson 1994; Riedel 1992, 1994; Haines et al. 2001; Brazhkin 2007; Leger et al. 1994; Zerr and Riedel 2000; Badzian 1981; Nakano et al. 1994; Knittle et al. 1995; Nakano 1996; Zhao et al. 2002; Komatsu et al. 1996). To design hard and superhard materials, it must be understood what makes these exceptional materials special. The link between structure and performance of these materials has been utilised to produce some of the most promising and important superhard materials. Thus it is imperative to understand such relationships in order to successfully develop future functional superhard materials. The review below is not meant to be completely exhaustive but to give an insight on the influence/role that microstructural features play on material performance. This chapter also serves as an introduction to the later chapters where techniques for microstructure analysis and property testing (Chaps. 4 and 5) and nanostructured materials and effect on

[1] Diamond can also be considered as ultrahard. Ultrahard materials are those whose hardness exceeds 80GPa on the Vickers scale of hardness.

materials properties as well as their industrial applications (Chap. 6) are discussed in greater detail.

2 Designing Superhard Materials

The synthesis of materials with hardness comparable to diamond has gained fundamental technological interest over the years (Zheng et al. 1999). This has emanated from the need of obtaining materials which are more useful rather than 'harder than diamond' as highlighted earlier (Solozhenko and Gregoryanz 2005). This may include materials that are expected to be chemically and thermally more stable than diamond and harder than c-BN. However to design new 'superhard' materials, it must be understood what makes diamond special. It is a well-known fact that the diamond crystal structure consists of tetrahedrally bonded sp^3-hybridised carbon atoms forming a rigid three-dimensional covalent network of high symmetry with extreme resistance to shear (Pierson 1994). There exist other carbon-based materials with shorter and stronger bonds than those in diamond (e.g. graphite), but these do not form a three-dimensional covalent network as in diamond, rather these carbon networks are associated with bonding which is heterodesmic in nature, in which layers are linked by strong covalent bonds and separated by weak interlayer forces (Van der Waals) (see Fig. 3.1) (Pierson 1994). A three-dimensional network composed of short, strong bonds is thus critical for hardness. The short bond length implies a high atomic and mass density comparable with diamond. Furthermore, a material is considered hard if it resists both elastic and plastic deformation (Riedel 1992; Haines et al. 2001). In principle, plastic deformation involves permanent and irreversible motion of atoms with respect to each other, often through the creation and movement of dislocations (Haines

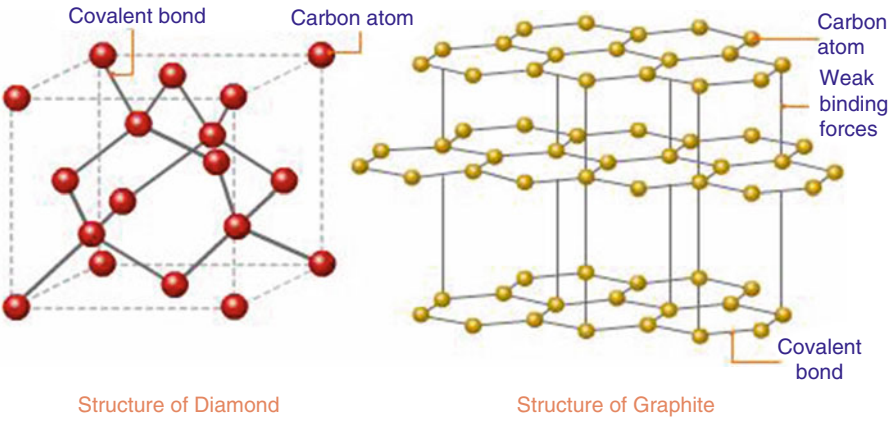

Fig. 3.1 Schematic representation of a diamond sp^3-hybridised bonds in comparison to the layered graphite structure (chemistry.tutorvista.com)

et al. 2001). This is in contrast with elastic deformation where atoms revert back to their initial positions after removal of load. Thus highly directional and strong bonding is of great importance in opposing or resisting such motions. However microscopic parameters (i.e. type of atom, structure and atomic forces) alone do not govern the mechanical characteristics of a material but also the morphology of the material constituents, defects in the sample, methods of measurement and temperature play crucial roles (Haines et al. 2001; Brazhkin 2007).

Furthermore, the strategic search for new superhard materials has also been directed towards modification of grain morphology and the state of defects to approach high hardness values (Haines et al. 2001; Brazhkin 2007). Another consideration in the designing of superhard materials is based on the stiffness of a material which is basically a measure of the resistance to volumetric compression (bulk modulus, B) (Riedel 1992; Haines et al. 2001). Often materials with high bulk moduli values are seen to possess high hardness values (Riedel 1992; Haines et al. 2001; Brazhkin 2007; Leger et al. 1994). This is based on the fact that such materials would resist deformation when subjected to high loads owing to their high stiffness values. However it is a source of substantial confusion that high bulk modulus and high hardness are discussed together and many a time omitting the contribution by the shear modulus. In reality there exists a better correlation, with reasonable scatter between hardness and shear modulus, G. Furthermore plastic deformation is initiated when the shear component of the applied stress exceeds the yield stress (Zerr and Riedel 2000).Thus the prediction of hardness values using the bulk moduli values alone may be misleading owing to this large scatter of the hardness-bulk modulus relationship. In view of this, these three main approaches have become the 'radar' to designing potential superhard materials. The first approach justifies the focus on the lighter elements boron, carbon, nitrogen and oxygen which form compounds with short covalent bonds. This has prompted research into three-dimensional boron-rich compounds (e.g. B_6O, $B_{22}O$, B_4C, $B_{25}N$ and $B_{53}N$) (Riedel 1994), boroncarbonitrides ($B_xC_yN_z$) (Badzian 1981; Nakano et al. 1994; Knittle et al. 1995; Nakano 1996; Zhao et al. 2002; Komatsu et al. 1996; Solozhenko et al. 2001; Mattesini and Matar 2001; Lambrecht and Segall 1993; Pan et al. 2005, 2006; Sun et al. 2001; Tateyama et al. 1997; Widany et al. 1998) and the hypothetical C_3N_4 (Riedel 1994; Teter et al. 1996; Malkow 2001). On the other hand, the hardness values of existing superhard materials have been enhanced by manipulating the grain morphologies through various techniques. This second approach has led to a hybrid of nano-grained superhard materials with improved mechanical properties (Haines et al. 2001; Brazhkin 2007).The third approach focuses on achieving the goal through high bulk modulus elements. In this case the elements do not possess high enough hardness values to be considered 'superhard'. Compounds have been tailored by alloying with small, covalent bond-forming atoms such as boron, carbon, nitrogen and oxygen structures with high-packing indexes (Brazhkin 2007).This has led to another hybrid of highly incompressible hard materials such as RuO_2 (Brazhkin 2007) WC and Co_6W_6C (Dubrovinskaia et al. 1999) transition metal borides (TiB_2,WB_4,WB_2 and WB) and BeB_2 (Brazhkin).

However despite the efforts, the first two approaches seem to have yielded materials with hardness values approaching that of diamond but not exceeding it. The progress in obtaining superhard materials using the third approach has somewhat been hindered by the fact that most of the compounds in this group possess some degree of ionicity (bonds not purely covalent) with low shear component values (Haines et al. 2001). Against this background, clearly it remains a challenge to experts in the materials science field to find substitute materials which fully complement diamond in this regard.

3 Influence of Microstructural Parameters on the Mechanical Properties

It is apparent that the majority of macroscopic properties of polycrystalline materials are directly influenced by the microstructure. There are a number of microstructural parameters of importance each of which has a certain influence on the specific property in question. This section will highlight those parameters that should be considered, and more detail will be found in the subsequent sections looking at the specific properties. One of the most important factors in a given microstructure is the grain size, grain size distribution and grain shape. These have a direct influence on the hardness, fracture toughness, strength, wear and thermal properties as discussed in subsequent sections. The microstructure can therefore be tailored to suit certain needs depending on the targeted performance level. The grain size distribution in some instances gives an indication of the packing index of the particles which is quite important especially for liquid infiltrated compacts.

Another parameter of importance is the contiguity in composite materials especially in the case where there is significant contrast in properties, e.g. WC/Co and polycrystalline diamond compacts. This effectively indicates the different volume fractions of the phases present and has a direct influence on performance. Lastly, interface composition is also a very important feature which affects almost all the mechanical properties and can be controlled to target certain performance levels.

4 Establishing Structure-Property Correlations of Superhard Materials

From the above discussion, it is a well-established fact that the mechanical characteristics of most materials depend on both microscopic properties (i.e. interatomic forces) and macroscopic properties (i.e. morphology, stress fields, defects, possible inhomogeneities, etc). As such it is imperative to establish a correlation between these properties with the behaviour of materials. In accordance with earlier

discussions, superhard materials can be classified into four groups as specified in the work of Brazhkin et al. (2002):

(i) Compounds formed by light elements from periods 2 and 3 of the periodic table. These normally form covalent and ionic-covalent bonds.
(ii) Crystalline and disordered carbon modifications with covalent bonds.
(iii) Partially covalent compounds between transition metals and light elements, e.g. borides, nitrides, oxides and carbides.
(iv) Nanostructured materials.

4.1 Group 1 Compounds

Typically superhard materials from this group are made from elements in the middle of period 2 and 3. These are capable of forming tight three-dimensional rigid lattices with short, non-polar covalent bonds. These bonds offer maximum resistance to atomic movement and are directional, and they would rather be broken than bent (Sung and Sung 1996). This includes compounds of boron, carbon, nitrogen and oxygen. The small atomic radii enable the formation of short interatomic distances and a high coordination number (C-N) (Sung and Sung 1996). This allows atoms to be surrounded by a large number of neighbours with a high degree of covalence. The combined effect is to basically concentrate the bond energy in a small volume thus a substantial amount of stress is required to deform such a crystal lattice (Sung and Sung 1996). Examples of compounds in this group include boron-rich compounds (B_6O, $B_{22}O$, B4C, $B_{25}N$, $B_{13}C_2$, and $B_{53}N$), boron carbonitrides $B_xC_yN_z$ and the hypothetical C_3N_4 (Brazhkin et al. 2002; Sung and Sung 1996; Kurakevych 2009).

Several modifications of boron compounds have been reported (Kurakevych 2009). The boron structure consists of an icosahedra B_{12} bonded with covalent bonds (Kurakevych 2009). Four allotropic modifications of boron have been reported, i.e. rhombohedral α-B_{12} (Decker and Kasper 1959), rhombohedral β-B_{106} (Hughes et al. 1963), tretragonal $\tau - B_{192}$ and orthorhombic $\gamma - B_{28}$ (Oganov et al. 2009). Two-element boron phases have been synthesised which include cubic boron nitride (c-BN), second to diamond in hardness. Also some subnitrides have been reported, i.e. $B_{50}N_2$, B_6N, B_4N and $B_{13}N_2$, characterised by high hardness values due to the short covalent bonds they possess. Boron carbides are known to possess remarkably higher oxidation resistance and interaction with iron group metals than other carbon-based materials (Kurakevych 2009). The B-O system has generated boron suboxides (e.g. B_6O) with typical hardness values close to that of superhard materials (~40 GPa). The C-N system still remains hypothetical with the C_3N_4 cubic phase predicted to have shorter covalent bonds than diamond and hence harder than diamond. However experimental data has shown that C_3N_4 is much less harder than diamond although the results are still debatable; this clearly indicates that hardness properties cannot be predicted from bond length alone (Brazhkin et al. 2002; Sung and Sung 1996; Kurakevych 2009).

4.2 Group 2: Carbon-Based Materials

This forms a special group of superhard materials due to the existence of a variety of chemical bonds between carbon atoms (Oganov et al. 2009). Diamond, the hardest material known to man to date, consists of sp^3-hybridised carbon bonds. Single crystals of diamond possess high values of elastic constants c_{11} and c_{44} as well as low Poisson's ratio ~0.07 (Frantsevic 1980; Novikovin 1987; Kurdumova et al. 1984). Lonsdaleite is another sp^3-hybridised modification of carbon possessing similar mechanical properties to diamond. There are a number of sp^2-hybridised hypothetical carbon structures which have been investigated theoretically (Liu et al. 1981). These however possess lower bulk moduli values (50–370 GPa) than diamond (Brazhkin et al. 2002). Fullerenes form a family of sp^2-hybridised superhard phases with extremely high bulk moduli values (800–900 GPa), twice as high as that of diamond (Ruoff and Li 1995). A typical example includes the C_{60} molecule, a naturally soft molecular crystal, which tends to harden under very high pressures (50–70 GPa) (Brazhkin et al. 2002).Worth mentioning is the amorphous diamond-like hard carbon (DLHC). What governs the high hardness and strength values for these phases is basically the small carbon atom radii capable of forming short bonds coupled with four-coordinated non-polar directional covalent bonds similar to what was discussed in group 1 above (Fig. 3.2).

4.3 Group 3: Transition Metal Compounds

A number of transition metals possess high bulk moduli values but do not possess high enough hardness values to be considered *superhard*. In principle, the transition metals could introduce a high valence electron density to resist elastic deformation whereas the light metals can introduce short and strong covalent bonds with high resistance to slipping under stress. Superhard compounds have been tailored by alloying with small, covalent-forming atoms such as boron, carbon, nitrogen and oxygen to form structures with high-packing indexes (Brazhkin et al. 2002; Matizamhuka 2010). The leaders in this class are the borides, e.g. WB_4, WB_2 and WB, with approximate hardnesses of 36–40 GPa (Brazhkin et al. 2002). Other highly incompressible compounds have been reported in this group which include RuO_2 (Leger et al. 1994), Co_6W_6C (Dubrovinskaia et al. 1999), BeB_2 (Brazhkin et al. 2007), ReB_2, OsB_2, WB_4,IrN_2, PtN_2 and TiB_2 (Brazhkin et al. 2002; Veprek 2013); however carbides and nitrides are inferior in hardness to borides (Brazhkin et al. 2002). It should be noted that some of the compounds formed in this group are not purely covalent and in some instances possess some degree of ionicity thus limiting the hardness/strength properties.

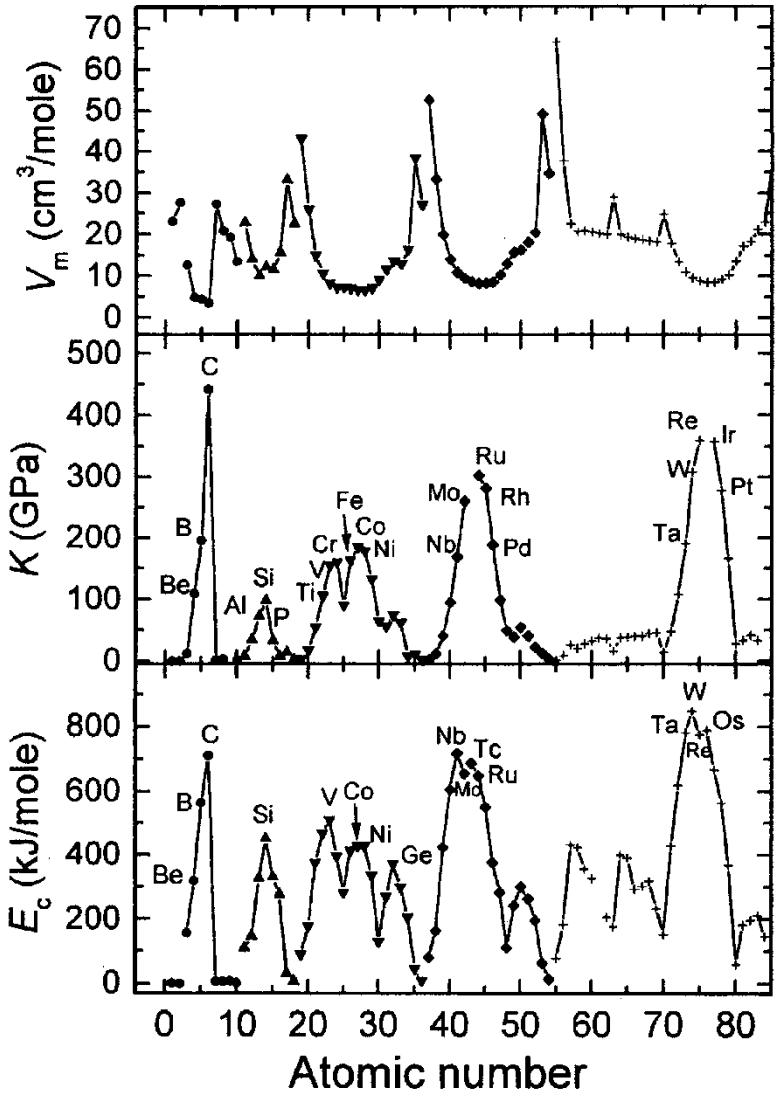

Fig. 3.2 Schematic representation of the dependency of certain physical properties on the atomic number, i.e. molar volume V_m, bulk modulus K and cohesive energy E_c (Brazhkin et al. 2002)

4.4 Group 4: Nanocrystalline and Superlattice Structures

The above discussions highlight the possibility of obtaining superhard structures through microscopic property interactions. However limitations arise owing to deviations from ideality, e.g. non-uniform distribution of electron density may arise and distortion in the four-coordinated structure may also arise. This introduces

differences between the real and ideal hardnesses of most of the covalent compounds in the preceding groups. However, it is possible to reduce this difference by tailoring the morphology/inhomogeneity of these compounds (Brazhkin et al. 2002; Veprek 2013). There are two limiting cases in which the real hardness can be substantially improved:

(i) In the ideal defect-free crystal where dislocations are absent
(ii) In the amorphous or nanocrystalline state where there is maximum hindrance to dislocation motion

Obviously defect-free crystals cannot be easily obtained for several thermodynamic reasons (e.g. thermal activation of point defects) (Brazhkin et al. 2002). On the other hand, amorphous solids may contain some defects within the network which effectively introduce deviations from 'ideal' ordering of the amorphous networks thus introducing deviation from ideal hardness (Davis 1976; Mott and Davis 1979). It is clear from the practical standpoint that the properties of superhard materials can be enhanced through grain refinement into the nano-range. This is discussed in much further details in Chap. 6.

In a number of cases, the practically achievable mechanical properties of most engineering materials are orders of magnitude lower than theoretical ones owing to the presence of flaws/defects in structures. Most of these defects (e.g. dislocations, microcracks, grain boundaries) are quite prone to shearing and can easily grow under stresses much lower than the ideal strength, thus limiting the material strength and hardness values (Veprek 2013). By reducing the grain size, the flaw/defect size is decimated which in turn strengthens grain boundaries by hindering dislocation multiplication and motion (Liu and Cohen 1989). Traditionally strengthening of materials has been achieved by well-known metallurgical principles such as solution hardening, work hardening and grain boundary hardening (Veprek 1999; Hertzberg 1989; Kelly and MacMillan 1986; Inoue et al. 1994). It must be noted that solution and work hardening do not operate in small nanocrystals of ≤ 10 nm due to solute atoms segregating at grain boundaries where there are no dislocations (Veprek 1999). Thus the grain boundary hardening concept would be more relevant to superhard materials. To get a more in-depth understanding of the property-size effect, a look into the Hall-Petch relation is vital at this point. The Hall-Petch relation correlates the material's ideal properties (hardness, strength, critical fracture stress) to the crystallite size. This relation has traditionally been used to explain the strengthening effect of a wide range of materials as a function of crystallite/grain size. Thus the Hall-Petch relation can be rewritten as follows:

$$\sigma_c = \sigma_0 + \frac{k_{gb}}{\sqrt{d}} \tag{3.1}$$

Here σ_c is the critical fracture stress, d the crystallite size and σ_0 and k_{gb} are constants. However at smaller crystallite sizes, i.e. below 10 nm, reverse Hall-Petch dependence occurs due to various mechanisms described and reviewed in Refs (Veprek 1999; Veprek and Argon 2001; Ashby 1972; Luthy et al. 1979;

Mohamed and Langdon 1974; Crampon and Escaig 1980) and also later on in Chap. 6. Computer simulation studies have shown that the reverse Hall-Petch dependence in nanocrystalline metals is due to the grain boundary sliding as a result of small sliding events of atomic plains at the grain boundary without thermal activation (Veprek 1999; Schiotz et al. 1998). In principle, a further increase in strength and hardness with decreasing grain size can be achieved by blocking grain boundary sliding (grain boundary hardening) (Veprek 1999). Grain boundary hardening can be affected by the use of nanocrystalline/amorphous grain boundary filler as suggested by Veprek (1999). It is important that such nano-phases should be refractory and stable at high temperatures and possess high structural flexibility in order to accommodate coherency strain without forming dangling bonds (discontinuity), voids or other flaws (Veprek 1999).

Alternatively, the relation can be understood through the general Griffith formula relating the critical stress causing growth of microcracks of size to the flaw size a_0:

$$\sigma_c = k_{\text{crack}} \sqrt{\frac{2E\gamma_s}{\pi a_0}} \propto \frac{1}{\sqrt{d}} \tag{3.2}$$

Here E is the Young's modulus, γ_s is the surface cohesive energy and k_{crack} is a constant dependent on the nature and shape of the microcrack and type of stress applied. In principle, the flaw size a_0 in a well-compacted material is always smaller than the crystallite size, i.e. $a_0 \leq d$ (Veprek 1999). Thus a reduction in grain size will effectively reduce the size of flaws and at much smaller sizes will in turn decimate or even eliminate most flaws. This is further discussed in Chap. 5 which looks at fracture toughness, methods of measuring it and their limitations.

Another design concept is depositing epitaxial multilayers having different elastic constants but similar thermal expansion and strong bonds as proposed by Koehler (1970). These multilayers are referred to as heterostructures or superlattices (Veprek 1999). Superhard epitaxial nano-polycrystalline superlattices of nitrides and oxides have been reported, e.g. TiN/VN (Helmersson 1987) and TiN/NbN (Shinn et al. 1992; Chu et al. 1992; Larsson et al. 1996). A hardness increase by a factor of 2–4 was achieved when the lattice period decreased to about 5–7 nm, e.g. for TiN/NbN a hardness of ~50 GPa was reported with a lattice period of 4 nm (Shinn et al. 1992). The question here is 'What really makes superlattices superhard?' If one considers the separate layers making up superlattices, they possess hardnesses lower than 40 GPa, but in the combined state, there is substantial enhancement of hardness values to reach or even exceed 40 GPa. This can be explained by how effective these structures are capable of hindering dislocation motion. Normally, the thicknesses of these layers are kept small to avoid dislocation operating within the layers (Veprek 1999). Under an applied stress, a dislocation may form in the softer layer, and as it moves towards the interface, elastic strain induced in the second layer (with higher elastic modulus) would case a repulsing force that would hinder dislocation from crossing the interface (Veprek 1999). This

basically enhances the strength/hardness of the layers. For further reading on the theories of superlattice properties, the reader is referred to the reviews by Barnett (1993) and Anderson and Li (1995). At this point it would be appropriate to introduce the most prominent mechanical properties of superhard materials and relate them to the respective structures. The word 'most prominent' is used here to highlight the properties that we are putting more emphasis on. What really qualifies most of the superhard materials in most of the industrial applications is their ability to withstand extreme conditions during, for example, cutting applications. Here high hardness, good wear, fracture toughness and thermal properties are most important. Thus what follows below is an insight into the relations between these specific properties with the material properties.

5 The Hardness Paradigm

Hardness can be defined as the resistance of a material to elastic and plastic deformation (Veprek 1999, 2013). This deformation begins when the shear component of the applied stress exceeds the yield stress (Matizamhuka 2010; Veprek 1999, 2013; Davis 1976; Mott and Davis 1979; Liu and Cohen 1989). Hardness is strongly influenced by residual stresses, toughening phases, microstructural textures, grain size, applied load, porosity and structure and composition of grain boundaries (Veprek 1999, 2013; Cottrell 1967). The hardness value is given by a ratio of the applied load to the area of surface contact of a hard indenter, usually diamond, loaded perpendicular to a planar surface of the material under test. The measured hardness value of any material depends on parameters associated with the test method and indenter geometry (Matizamhuka 2010; Veprek 1999, 2013; Cottrell 1967). It varies with the applied load, indenter shape and dimensions, microstructure and prior history of the material, loading rate, the environment and the test temperature (Matizamhuka 2010; Veprek 1999, 2013; Cottrell 1967). Thus in order to compare hardness values of different materials, the specific test method and test conditions have to be described carefully (Matizamhuka 2010; Veprek 1999, 2013; Cottrell 1967).

Theoretical attempts to describe hardness in terms of the elastic bulk or shear moduli of an ideal solid are not uncommon. The elastic moduli are an intrinsic mechanical property of a material dominated by the strength of the chemical bonds between the atoms (Matizamhuka 2010; Veprek 1999, 2013; Cottrell 1967). The high elastic moduli of superhard materials reflect the strong chemical bonds between the atoms. These bonds are predominately covalent in nature. In general, ionic/covalent bonds deform less than metallic bonds under a given external force (Matizamhuka 2010; Veprek 1999, 2013; Cottrell 1967). Thus the theoretical hardness assumes higher values at greater elastic moduli values. This 'theoretical' hardness is proportional to the reciprocal value of the bulk modulus, B (Matizamhuka 2010; Veprek 1999, 2013; Cottrell 1967).

There is a relationship between the bulk modulus B, the applied stress ψ and ε the elastic strain from Hooke's law,

$$B = \frac{d\psi}{d\varepsilon} \tag{3.3}$$

and from the binding energy E_b, bond length and stress relation,

$$\psi = \frac{dE_b}{da} \tag{3.4}$$

Clearly there is a direct relationship between the bulk modulus, B, and the binding energy, E_b, and the interatomic bond distance, a, which is described by the equation below:

$$B = \frac{d^2E_b}{da^2} \tag{3.5}$$

Thus high bond energy means high electron density between the atoms as in non-polar covalent bonds formed between atoms of small radii of the first period which explains the high hardness values attained by compounds of these elements (Matizamhuka 2010; Veprek 1999, 2013). A more common bulk modulus-bond length relationship which has been used to predict the theoretical hardness values of most existing and potential superhard materials is given by the equation below (Matizamhuka 2010; Veprek 1999, 2013; Cottrell 1967):

$$B(GPa) = \left(\frac{N_c}{4}\right)\left(\frac{1971 - 220\lambda}{d^{3.5}}\right) \tag{3.6}$$

where, N_c is the coordination number, d is the bond length *(Å)* and λ is an empirical parameter measuring the polarity of the bond. For non-polar covalent bonds such as in diamond, $\lambda = 0$, in other compounds such as c-BN, Si_3N_4 and SiC, $\lambda > 0$, hence the lower bulk moduli and hardness values for these compounds compared to diamond (Fig. 3.3).

Clearly, a high coordination number is required in order to maximise the value of B. Also a high bond energy as found for non-polar covalent bond between atoms of small radii results in high theoretical hardness. This explains the reason why carbon in its metastable fourfold-coordinated sp^3 hybridisation in diamond forms the hardest known material followed by c-BN. Also the expected high theoretical hardness of C_3N_4 is based on this prediction, i.e. a small C-N bond distance and relatively small polarity.

However it has been argued that materials deform plastically only when subjected to a shear stress (Cottrell 1967). Thus the shear stress needed for dislocation motion and multiplication to cause plastic deformation is proportional to the elastic shear stress of a deformed material (Cottrell 1967). Thus the

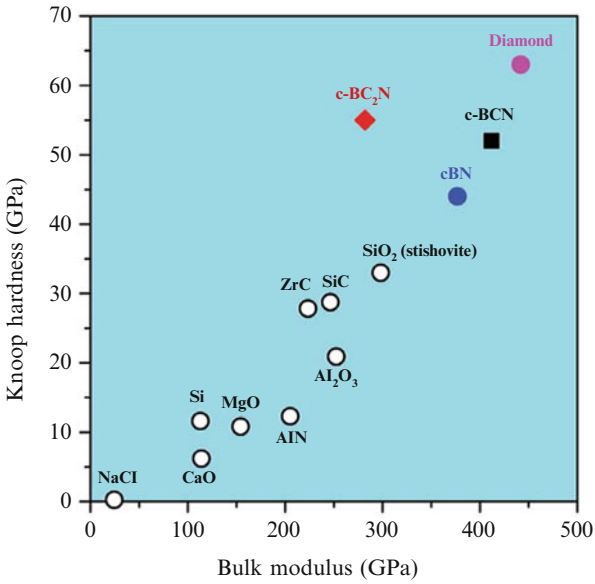

Fig. 3.3 A schematic representation of the Knoop hardness as a function of bulk modulus of some hard and superhard materials (Solozhenko and Gregoryanz 2005)

prediction of hardness using the bulk modulus value may be misleading owing to the greater scatter of hardness-bulk modulus relationship. Gilman (1973) and Liu and Cohen (1989) established a linear correlation between hardness and bulk modulus. This was subsequently followed by an improved correlation between hardness and shear modulus proposed by Teter and Hemeley (1996). Most pre-2012 publications have been based on these empirical correlations to predict the hardness of potential/new superhard materials (Tian 2012). In recent years, the use of these simple linear correlations has increasingly become questionable. This is due to the fact that the bulk modulus which is a measure of a material incompressibility depends largely on the valence electron density. Thus the greater the electrons involved, the greater the repulsions within a structure implying a higher value of B. On the other hand, the shear modulus which measures the resistance to shape change at a constant volume gives an indication of the material's ability to resist shearing forces. Clearly, both bulk and shear moduli are elastic in nature and correspond to reversible elastic deformation. It should be noted that with hardness, a permanent plastic deformation occurs, and this basically makes the predictions made earlier by Cohen and Gilman unreliable for predicting the hardness values of materials.

A more reliable relationship was proposed by Chen et al. (2011) which incorporates both the elastic and plastic properties of pure polycrystalline metals. Chen et al. proposed a ratio referred to as the Pugh's modulus ratio $k = G/B$ which relates the brittleness, G, to the ductility B of materials. Thus brittle materials are bound to possess a larger k value compared to ductile ones. The Pugh's ratio is related to the Vickers hardness, H_V, through the correlation:

$$H_V = 2\left(k^2 G\right)^{0.585} - 3 \tag{3.7}$$

This agrees well with experimental data. G/B depends monotonically on Poisson's ratio according to the relationship:

$$\upsilon = \frac{\left(3 - 2\frac{G}{B}\right)}{\left(6 + 2\frac{G}{K}\right)} \tag{3.8}$$

The Poisson's ratio correlates the bond stiffness and hardness of a material. It formally takes values between –1 and 0.5; thus the lower limit generally corresponds to a material that does not change its shape and the upper limit to the unchanged volume (Brazhkin et al. 2002). For systems with predominantly ionic and van der Waals-type bonds, υ is close to 0.25 corresponding to $G/B = 0.6$. For metallic structures υ lies between 0.3 and 0.4 with G/B in the range $0.2 < G/B < 0.5$. Most covalent compounds $\upsilon < 0.25$ and $G/B > 0.6$. Very few covalent compounds have a shear modulus exceeding the bulk modulus, $G > B$ ($\upsilon < 0.125$) (Brazhkin et al. 2002).The only such compounds include diamond, c-BN, quartz (α-SiO_2), lonsdaleite, B_6O, HfB_2, ZrB_2 and TiB_2 (Brazhkin et al. 2002). The high G/B ratios in most covalent compounds are associated with high angular stiffness of directional covalent bonds (Brazhkin et al. 2002). This stiffness plays quite an important role especially when coordination decreases from four towards lower values (Brazhkin et al. 2002). At higher coordination numbers (>4), there is normally loss of directionality in covalent compounds and hence decrease in bond-bending forces (Brazhkin et al. 2002).

These predictions are based on macroscopic concepts which make it difficult to relate hardness to the microstructure of a material (Tian 2012). To understand the fundamental parameters controlling hardness, one needs to find a correlation between hardness and microscopic parameters (Tian 2012). In principle, at microscopic level, hardness measures the combined resistance of chemical bonds to indentation (Tian 2012). This implies that the greater the number of bonds in a region of the surface, the harder the material. Thus, it would be scientifically correct to correlate hardness to bond resistance, bond strength and electronegativity of a material. This simply implies that harder crystals are characterised by short and strong chemical bonds, high valence electron density/ high bond density and strongly directional bonds.

Another important aspect that plays a crucial role in hardness enhancement is grain refinement into the nano-range as described in the above sections. Conventionally, the enhancement can be explained through the hardening effect of grain boundaries as expressed by the Hall-Petch equation:

$$H = H_0 + \frac{k_{HP}}{\sqrt{D}} \tag{3.9}$$

Here K_{HP} is Hall-Petch hardening coefficient (sample dependant), D grain size (nm) and H_0 hardness of bulk single crystal.

This concept is based on the fact that reducing crystallite size results in strengthening and hardening due to a more effective impediment of plasticity by the increased number of grain boundaries (Veprek 2013). However, this has been observed to be limited to a crystallite size down to 10–15 nm, and below this range, softening arises as grain boundary shear dominates (Veprek 1999, 2013). The reader can also refer to Chap. 6 where this is discussed in greater detail. It is interesting to note that larger enhancement of the hardness can be achieved even at finer crystallite size (3–4 nm) if low energy grain boundary or a strong interfacial layer is formed. At finer crystallite sizes, the number of defects decreases such as dislocations, twins, microcracks and others. These defects easily shear and grow upon a stress much lower than the ideal strength thus limiting the strength and hardness values (Veprek 1999, 2013).

Macrohardness testing of ceramic materials normally results in considerable cracking which may disguise the corners of the impression (Matizamhuka 2010; Veprek 1999, 2013). The extent of cracking is related to grain size and fracture toughness, and acceptable measurements are feasible below 5 kg in most cases (Matizamhuka 2010; Veprek 1999, 2013). Recommended practice is that a quoted number for a material should be the average from 5 to 10 randomly positioned macrohardness tests and preferably more than 20 randomly positioned microhardness tests (Matizamhuka 2010; Veprek 1999, 2013). This is done owing to the scatter of results normally obtained on ceramics as a result of their multiphase nature, their generally non-cubic symmetry and porosity that exists below the surface of the test piece (Matizamhuka 2010; Veprek 1999, 2013). It is therefore not uncommon to obtain coefficients of variation of 10 % in macrohardness measurements and 20 % in microhardness measurements (Matizamhuka 2010; Veprek 1999, 2013). Chapter 4 discusses the various techniques for hardness measurements and their limitations. The chapter also proposes ways in which such difficulties can be overcome in order to obtain accurate values of hardness.

5.1 Factors Affecting Hardness

The hardness of brittle materials has a strong dependence on the flaws present which act as stress concentration sites incapable of relaxing plastic deformation (Teter and Hemeley 1996). These flaws are present in many forms in most hard materials, the most prominent being residual stresses, microstructural textures, grain size, porosity and the structure of grain boundaries (Evans and Lange 1975). In practice sintered specimens usually have a relative density below 99 % (Evans and Lange 1975). This leaves some residual porosity which has been found to affect the hardness in a negative sense (Evans and Lange 1975). Pores are less resistant to indent penetration thus they present regions of low hardness in the material. It has been observed that small porosity levels of 1–2 % can affect the hardness more than an increase in the grain size from 0.5 μm to 2 μm (Evans and Lange 1975).

It has been observed that any polycrystal exhibits a hardness like the single crystal if the load is small enough, i.e. if only a few grains are affected (Evans and Lange 1975). At higher loads the indentation size becomes much larger than the grains, and in polycrystals, this size effect is partly offset by the hindrance of dislocation activity due to close spacing of grain boundaries, in the case of fine-grained microstructures (Evans and Lange 1975). On the other hand, with coarse-grained microstructures, there is less resistance to plastic deformation because of lower hindrance to dislocation activity. This in itself explains why fine-grained materials are found to be harder than their coarse-grained counterparts. This is also highlighted in the Hall-Petch relationship which shows an inverse relationship between the hardness and the grain diameter, d (Evans and Lange 1975).

Hardness has also been found to be affected by the structure of grain boundaries typically in liquid-phase sintered materials (Brazhkin et al. 2004). Theoretically Si_3N_4 has a Vickers hardness in the region of ~17–18 GPa, but the liquid-phase sintered counterpart has a reduced hardness (Brazhkin et al. 2004). This reduction in hardness is thought to be due to lowered resistance to indent penetration by the binder material present at the grain boundaries.

The factors discussed above are all related to the material properties. There are also factors related to the environment such as temperature and moisture present and those related to the equipment used such as geometry of the indent and magnitude of the applied load. Detailed discussions of these factors are dealt with thoroughly in various other publications (Brazhkin et al. 2004; Lawn et al. 1975).

6 Fracture Mechanics of Superhard Materials

Superhard components in most cases fail by unstable propagation of cracks initiated at flaws which are present due to manufacture or surface treatment (Evans and Lange 1975). These flaws are usually in the form of pores, cracks and inclusions. The brittle behaviour of superhard materials is attributed to low resistance to crack propagation (Brazhkin et al. 2004; Lawn et al. 1975). There are two main methods used for characterising the crack propagation behaviour of materials. The more commonly used method is the evaluation of the fracture toughness K_{IC}. K_{IC} is a critical value of the stress intensity factor K_I. The latter quantity serves as a scale factor to define the magnitude of the crack tip stress field (Lawn et al. 1975). K_I is dependent on the applied load, initial size of crack and geometry of the component (Lawn et al. 1975) and has been found to increase until unstable crack propagation occurs at some critical value, i.e. $K_I = K_{IC}$ (Niihara et al. 1982). There are basically three loading modes which result in high stresses at the crack tip, namely:

(i) Mode 1: tension normal to the crack plane
(ii) Mode 2: shear loading in crack direction
(iii) Mode 3: out of plane shear loading

Mode 1 has been found to be the most important (Niihara et al. 1982).

An alternative method is based on energy considerations in crack propagation described by the crack resistance factor G_{IC}. This idea is referred to as the Griffith criterion (Lawn et al. 1975; Niihara et al. 1982). The criterion compares the magnitude of the strain energy released to that consumed by a crack increment, the so-called R, representing the resistance to cracking (Niihara et al. 1982). An equilibrium condition occurs when the difference, $G–R = 0$, and crack growth is favoured if $G–R > 0$ and healed when $G–R < 0$. This forms the basis of the Griffith criterion (Niihara et al. 1982).

It has been observed that the most problematic part of toughness determination is to create a crack and to measure its size (Lawn et al. 1975). There are several methods in use for fracture toughness determination, detailed discussion of which is presented in a number of publications (Evans and Lange 1975; Brazhkin et al. 2004; Lawn et al. 1975; Niihara et al. 1982) and in Chap. 5.

6.1 Vickers Indentation Cracks

Fracture toughness determination with Vickers hardness indentations was proposed by Evans et al. (1976) and later extended by Niihara et al. (1982) and Anstis et al. (1981). The fracture toughness is calculated from the length of cracks which develop during a Vickers indentation test and can be measured optically at the specimen surface (Niihara et al. 1982; Evans and Charles 1976; Anstis et al. 1981). The basic procedure for fracture toughness determination consists of three main steps, namely (Brazhkin et al. 2004):

(i) Generation of a crack in a test specimen
(ii) Measurement of load of failure
(iii) Calculation of K_{IC} from failure load, failure stress and crack depth using relations dependent on crack length, specimen dimensions and yield stress

The fracture toughness value can be obtained from the relation (3.10):

$$K_{IC} = 0.032H\sqrt{a}\left(\frac{E}{H}\right)^{\frac{1}{2}}\left(\frac{c}{a}\right)^{-\frac{3}{2}} \tag{3.10}$$

H is the hardness, E is the Young's modulus, a is half the indent diagonal and c is the length of crack (Brazhkin et al. 2004).

In the development of new superhard or composite materials, the Young's modulus value, E, is usually unknown. It is common practice to adopt relations independent of E; Shetty et al. (1981) developed a relationship based on the Palmqvist radial cracks found on the specimen surface shown below (Anstis et al. 1981; Shetty et al. 1985):

$$K_{IC} = 0.0889\sqrt{\left(\frac{H \times P}{4l}\right)} \tag{3.11}$$

H is the Vickers hardness, P is the indent load, $l = c–a$ where $2a$ is the indent diagonal and $2c$ is the length of full crack.

The development of cracks in brittle materials occurs in a sequence of steps. Under the indentation load, the elastic limits of most ceramic materials are exceeded, and a zone of plastic deformation develops beneath the pyramidal indenter (Evans 1974a, b; Munz and Fett 1999; Olagnon et al. 2006; Elssner et al. 1999). The indenter acts as a wedge and induces tensile stresses in the surrounding material (Evans 1974; Munz and Fett 1999; Olagnon et al. 2006; Elssner et al. 1999). During the loading phase, these tensile stresses overlap with compressive stresses caused by the applied indentation load. There is development of cracks but with restricted mobility. When the load is removed from the indenter, the compressive stress component ceases to exist, and cracks formed assume their final length (Evans 1974a, b; Munz and Fett 1999; Olagnon et al. 2006; Elssner et al. 1999). The cracks will grow to a point at which the stress intensity falls below its critical value (Evans 1974a, b; Munz and Fett 1999; Olagnon et al. 2006; Elssner et al. 1999).

Given the variety of cracking mechanisms associated with ceramic materials, both the stress field underload and the residual stress are clearly very complex (Evans 1974; Munz and Fett 1999; Olagnon et al. 2006; Elssner et al. 1999). Additionally in materials with large grain size and single crystals, irregular cracks and lateral cracks which proceed parallel to the surface causing chipping may develop (Evans 1974; Munz and Fett 1999; Olagnon et al. 2006; Elssner et al. 1999). The presence of residual stresses in the vicinity of the crack also results in subcritical crack growth in air. All these lead to an underestimation of the fracture toughness value. It is common practice to create indentation cracks in oil to avert subcritical crack growth in air and to measure the crack size immediately after indentation (Evans 1974; Munz and Fett 1999; Olagnon et al. 2006; Elssner et al. 1999).

6.2 *Influence of Microstructural Parameters on Toughening*

To improve the fracture toughness of superhard materials, it is imperative to accurately analyse the failure mechanisms and the structure-property relationship between fracture initiation and microstructure (Evans 1974). Over the years, the enhancement of toughness properties of advanced materials has been achieved by tailoring their microstructures to provide toughening mechanisms. In principle, toughening mechanisms can be categorised into two types: intrinsic and extrinsic. Intrinsic mechanisms operate ahead of a crack tip and are primarily related to plasticity, i.e. enlargement of the plastic zone which is effective against both

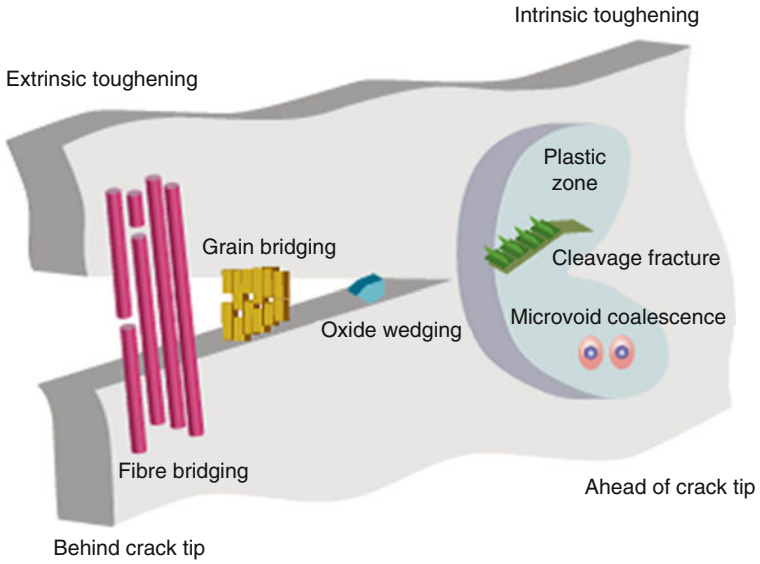

Fig. 3.4 Schematic representation of extrinsic and intrinsic toughening mechanisms (Ritchie 2011)

crack initiation and propagation (Mcnamara et al. 2015; Zhu et al. 2015; Ritchie 2011; Krstic 1988). This is the primary source of toughening in ductile materials and is ineffective with brittle materials (Mcnamara et al. 2015; Zhu et al. 2015; Ritchie 2011; Gomez and Elices 2006; Krstic 1988). Conversely, extrinsic toughening acts primarily on the wake of the crack to shield local stresses and strains at the crack tip (Ritchie 2011). Effectively extrinsic toughening is usually associated with processes behind a crack tip[2], and there has to be a crack for them to operate; thus they have no effect on crack initiation (Ritchie 2011). There are a variety of microstructural mechanisms utilised to effect extrinsic toughening which include crack bridging by unbroken fibres or ductile phase in composites, friction interlocking of grains during intergranular fracture in monolithic ceramics, meandering and crack surface sliding and shielding and microcracking in transformation-toughened ceramics (Launey 2009) (Fig. 3.4).

A classic example is the use of nanoscale glassy films along grain boundaries to promote boundary cracking and grain bridging in SiC. The fracture toughness of SiC is ~2–3 $MPam^{1/2}$ when it fractures transgranularly and can approach 10 $MPam^{1/2}$ for intergranular fracture (Ritchie 2008, 2011). This is attributed to the greater crack-stopping power when the crack has to negotiate round the grains as opposed to propagating through the grains.

[2] Extrinsic toughening can also be caused by crack shielding, crack deflection from hard particles or along weak interfaces and crack branching as shown in the Appendix Fig. A1.

As discussed above the most important toughening mechanisms in polycrystalline brittle materials are the extrinsic type such as grain bridging and transformation toughening. It is thus imperative to understand how microstructural features affect the effectiveness of these mechanisms during design of new or prediction of toughness properties of old superhard materials. In grain bridging, frictional bridging occurs behind the crack tip when a reinforcement-matrix interface debonds and the reinforcement is further pulled out. This effectively acts to reduce the crack opening and provides a shielding effect. Thus the shielding effect depends on the reinforcement strength, volume fraction, size, the Young's modulus and the interface properties (Fantozzi and Saadaoui 2014). The relation between bridging stress, σ_b, and crack opening displacement, δ, has been modelled and the more dominant bridging stress can be expressed as: (Launey et al. 2010)

$$\sigma_b = \sigma_m \left(1 - \frac{\delta}{\delta_c}\right)^n \tag{3.12}$$

Here σ_m is the bridging stress, δ_c is the crack opening displacement at which grain bridging disappears and the exponent n describes the stress decrease.

In view of the above, it is apparent that the magnitude of grain bridging is a function of the expansion anisotropy, interfacial roughness, grain size and morphology (aspect ratio), which can be controlled by additives or heat treatments (Fantozzi and Saadaoui 2014) . Thus grain coarsening and elongating the microstructure enhances the frictional bridging and pull-out resulting in greater stress intensity factor (Fantozzi and Saadaoui 2014). Classical examples include coarse grain alumina and the so-called self-reinforced Si_3N_4 (Fantozzi and Saadaoui 2014). It must be noted however that there exists a critical grain size above which a low intensity factor is observed due to appearance of transgranular fracture which reduces the grain-bridging effect (Fantozzi and Saadaoui 2014). In a recent study on leached polycrystalline diamond (PCD) compacts, the effect of a decreasing grain size shows a decrease in fracture toughness (Mcnamara et al. 2015). In principle, the finer the grain sizes have lower aspect ratios between adjacent grains thus presenting lower resistance to crack propagation compared to a coarse grain. In the case of a coarse grain size, a propagating crack will experience more resistance as it must negotiate around larger grains, thus increasing the energy required for fracture over the entire process. Transformation toughening is synonymous with ZrO_2-based ceramics. This occurs as a result a volumetric increase (~5 %) accompanying transformation which creates compressive stresses that shield the crack tip from the applied stress (Fantozzi and Saadaoui 2014; Launey et al. 2010; Nalla et al. 2003; Weiner and Wagner 1998). In essence, the magnitude of transformation toughening is controlled by the stability of the transforming phase which is influenced by the microstructure, i.e. grain size, morphology and location (along grain boundaries or inside the grains) ((Fantozzi and Saadaoui 2014)).

7 Strength of Brittle Materials

In principle the strength of a brittle material is not an intrinsic material property but more of a *conditional* property quite useful for design and comparison/ranking purposes (Kelly 1995). Thus strength values are strongly dependent on the material microstructure, processing history, testing methodology and environment and failure mechanisms. Griffith et al. (1920) pioneered the work on the strength behaviour of brittle materials using glass. He showed that strength is sensitive to microcrack-like defects and drew up a relationship between the fracture strength and flaw size.

In principle, Griffith showed that crack extension occurs in brittle materials when the stored elastic energy (mechanical energy) released during extension just exceeds the energy required to form new surfaces (surface energy) (Lawn et al. 1994). Under equilibrium conditions, we have the famous Griffith strength equation where the total system's internal energy (mechanical + surface energy) is unchanged with incremental crack extension (Kelly 1995; Griffith 1920; Lawn et al. 1994):

$$\sigma_f = \left(\frac{2E'\gamma}{\pi a_0}\right)^{1/2} \tag{3.13}$$

Here σ_f is the fracture strength in uniform tension, E' is the plain structure elastic modulus, γ is the surface energy per unit area and a_0 is the starter flaw/crack size.

The classical Griffith relation links the material strength and toughness to a critical flaw size (Griffith 1921). Over the years a number of authors have demonstrated the relationship of the critical length scale to the material grain size in the presence of thermoelastic stresses (Macnamara et al. 2015; Evans 1974; Krstic 1984). However in most of these analyses, the critical grain size was often not equal to the actual grain size (Manamara et al. 2015). A number of researchers have investigated the effect of a microstructure on the experimentally measured fracture toughness (Mcnamara et al. 2015; Taylor 1996, 1999, 2004, 2006; Taylor et al. 2005). They have demonstrated that for a number of engineering materials, the characteristic length scale can be related back to the microstructure. This is known as the *theory of critical distances (TCD)*. In principle, this theory uses the characteristic material length to predict the fracture toughness for notched specimen (Mcnamara et al. 2015).

From a conceptual point of view, the theory predicts that once an effective stress (σ_{eff}) is reached across a grain length, that grain will fail and a crack will grow (Mcnamara et al. 2015). The TCD theory demonstrates that failure occurs when a distance-dependent effective stress exceeds the ultimate tensile strength/flexural strength, σ_0 of a material (Mcnamara et al. 2015). The effective stress can be determined by a number of methodologies which include point method (PM), line method (LM) and area method (AM) which all use a characteristic length parameter calculated as follows (Mcnamara et al. 2015):

$$L = \frac{1}{\pi}\left(\frac{K_{IC}}{\sigma_0}\right)^2 \tag{3.14}$$

Here σ_0 is the characteristic material strength. The most widely used methodologies are the LM and PM. The LM postulates that a material reaches its failure limit when the stress averaged over a line, starting from the notch equals the inherent material strength σ_0 (Mcnamara et al. 2015).

In practice, the critical distance r_c is taken as the smallest microstructural feature and in the case of brittle polycrystalline materials is taken as the nominal grain size (Mcnamara et al. 2015). It must be noted that there exist errors associated with this whole approach; the reader is referred to references in Mcnamara et al. 2015 and the references therein for further reading (Mcnamara et al. 2015). This is also discussed in Chap. 5 as the authors evaluate the commonly used fracture measurement methods and their limitations when applied to hard, superhard and ultrahard materials.

7.1 Factors Affecting Strength

In practice most of the strength-controlling defects are introduced into materials during processing. These include porosity regions, agglomerates, inclusions and large-grained zones (Kelly 1995; Lange 1984). Furthermore, surface flaws are introduced by machining and grinding operations a material may be subjected to. Such defects act as weakness points/stress concentration sites yielding a range of 'strength values' for a given material. Secondly many practical aspects of testing can alter strength results which include specimen size effects, stress concentrations and failure mode (failure location, flaw type) (Kelly 1995). For instance, some materials will show lower strength when tested under humid or in the presence of moisture due to slow crack growth rate (Kelly 1995). Creyke et al. 1982 showed that strength is exponentially sensitive to slow crack growth parameter n by comparing time to failure (t_1, t_2) under different static stresses (σ_1, σ_2):

$$\left(\frac{t_1}{t_2}\right) = \left(\frac{\sigma_1}{\sigma_2}\right)^n \tag{3.15}$$

Although ASTM testing standards exist, there are problems that arise during testing that can produce inaccurate results such as alignment problems between specimen and test fixtures, specimen to support ratio dimensions, processing flaws and specimen thickness. In essence, strength values give an indication of the stress a specific material will support for a given flaw size distribution and failure mode (Kelly 1995). There are however complications that arise in determining strength values which are associated with the material structure, flaw size distribution and

failure mode. A widely accepted model for material and structural evaluation is the Weibull risk-of-rapture analysis given by the probability of failure below:

$$P_f = 1 - \exp\left\{-\frac{(\sigma - \sigma_n)^m}{\sigma_0}\right\} \tag{3.16}$$

Here σ_0 represents a location parameter of Weibull distribution strength at 63.2 % failure probability (mean value in the Weibull normal distribution), and σ_n is the minimum strength and normally taken as zero. Note the exponent expression, which is evaluated over either a surface/volume from which failure can originate. An important assumption is that failure is a result of a single 'failure type' (structural inhomogeneity) (Frischholz 2004). In principle the Weibull modulus *(m)* is a direct measure of the distribution of strengths. Thus the higher the Weibull modulus means the more uniform defects distribution and the more consistent the material. Put differently the material behaviour will be more consistent and the probability curve is narrower. Typical values in the range $10 < m < 20$ have been achieved using four-point bending method (Frischholz 2004). It must be noted here that since the number of defects is dependent on the sample volume, the strength of larger parts is normally less than what is measured on the sample (Frischholz 2004).

7.2 The Conflicts Between Strength and Toughness

The quest for engineering materials that possess both high strength and toughness (damage tolerant) remains elusive. This emanates from the fact that the two properties are mutually exclusive. It is important to note that the mechanisms that promote high strength tend to oppose/conflict with those mechanisms that promote higher toughness. Strength sometimes represents a material resistance to nonrecoverable deformation (e.g. plastic deformation). On the other hand, toughness is a measure of the material's resistance to fracture and, as such, requires a material's ability to dissipate local high stress by enduring deformation (Zhu et al. 2015; Ritchie 2008, 2011). This explains the reason why hard materials tend to be brittle and lower strength materials (mostly metals), which can deform more readily, tend to be tougher (Ritchie 2011). It is interesting to note that much research efforts on hard and superhard materials have focused on pursuing higher strength with rather limited corresponding regard for toughness (Veprek 2013; Zhu et al. 2015).

The drive towards damage-tolerant materials is to be able to utilise the lightweight hard and superhard materials for vital, safety-critical applications such as in aerospace, transportation and power generation industries (Ritchie 2011). Although the conflicts between strength and toughness are very real, it has been proven that there exist ways to attain both properties in a single material through the presence of multiple plasticity and toughening mechanisms acting on differing length scales

(Ritchie 2011). A successful example is the development of bulk metallic glass (BMG)-based composites which are composed of a crystalline dendrite second phase in a BMG matrix which essentially promotes the formation of multiple shear bands leading to a strong and tough material (Ritchie 2011). Nature-inspired toughening mechanisms which involve both intrinsic and extrinsic toughening have been utilised to design and synthesise biomimetic structural materials (Zhu et al. 2015). Despite these efforts, there still exists rather limited success in attaining both strength and toughness in superhard materials which often require material-specific complicated and expensive processing routes hardly applicable to other materials (Zhu et al. 2015).

8 Wear of Superhard Materials

Superhard materials find use in tribological applications due to their high hardness, high-temperature stability and chemical inertness relative to metals (Olagnon et al. 2006). However during operations chipping by interrupted impacting increases wear thus higher toughness is required for these materials to survive greater wear. Wear of superhard ceramic materials is highly dependent on both operating conditions (normal load, velocity and temperature) and material properties (grain size, mechanical and thermal properties) (Shetty et al. 1985; Morrell 1985; Cohen 1985). Previous and ongoing studies have shown that wear of ceramics depends to a large extent on the 'wear mode' occurring at the machining onset (Olagnon et al. 2006). At low loads and relatively low temperatures, the wear mode is to a large extent controlled by the tribochemical reactions. On the other hand, at higher loads and higher temperatures, the dominant wear mode is mechanical wear occurring by propagation of cracks along grain boundaries resulting in microfracture within the material (Olagnon et al. 2006). In the latter case, the microstructure of the material is expected to play a more significant role than its chemical stability (Olagnon et al. 2006). This clearly highlights the interlink between the fracture toughness, rapture strength, hot hardness and materials' tribological properties.

As highlighted before, hardness alone does not guarantee good wear or tribological properties in any material. It is clear that the trend now is towards development of newer materials possessing high toughness and hot hardness which implies good wear properties.

9 Thermal Shock

Most ceramic materials have low thermal conductivity thus making them prone to thermal shock which occurs as a result of a sudden change in temperature especially during cooling. This basically introduces transient thermal stresses which can

become large enough to induce damage such as microcracking or complete fracture (Fantozzi and Saadaoui 2014). Thermal shock can be quantified using the equation below:

$$\Delta T_c = \sigma_f \frac{(1-\upsilon)}{E\alpha} \tag{3.17}$$

The value ΔT_c is the applied temperature difference in quenching experiments often used as a thermal shock parameter indicating resistance to crack initiation. Here σ_f is the strength, υ the Poisson's ratio, E is the Young's modulus and α coefficient of thermal expansion.

Thus the thermal shock resistance is influenced in addition to specimen properties by material properties such as Young's modulus, thermal expansion coefficient, tensile strength and fracture toughness. It is thus apparent that increasing the crack resistance generally increases the material shock resistance. Typically, coarse grains induce a high crack growth resistance, thus maintaining a high initial strength which gradually decreases after thermal shock compared to the catastrophic strength loss observed in fine grain material (Fantozzi and Saadaoui 2014). The behaviour observed in fine grain materials is however not well understood and is open to debate. Thermal shock resistance of Si_3N_4 ceramics has been enhanced by using SiC whisker reinforcement or by coarsening and elongating the microstructure (Lawn et al. 1994).

10 Concluding Remarks and Future Trends

In this chapter, the behaviour of hard, superhard and ultrahard materials has been analysed in relation with their microstructures. It has been shown that the development of superhard materials with hardness values approaching that of diamond can be elucidated through microstructural control. It is clear that the progress of these materials has been hindered owing to their inferior fracture toughness properties which basically limit their range of applications. A number of fracture enhancement techniques have been utilised such as grain bridging and transformation toughening through tailoring the microstructures. However there is still potential to create damage-tolerant superhard and ultrahard materials that can be utilised in safety-critical applications. The strength-fracture toughness conflict still remains elusive as these properties are mutually exclusive. Although efforts have been made to produce strong and tough materials (e.g. BMGs), there still remains scepticism whether the techniques utilised can be applied to other materials. The thermal and wear properties of hard, superhard and ultrahard materials form an important aspect as they directly affect the performance owing to their operating conditions (high temperature and interrupted impact). It has been shown that coarse-grained/elongated microstructures with greater resistance to crack initiation and propagation give the best performance at higher temperatures and impact. However this

happens at the expense of hardness. Thus there is a need to strike a balance between the two properties and hence form the future trends towards achieving more useful superhard materials rather than only superhardness. The present review is not meant to be completely exhaustive but to shed some light on the more important microstructural aspects which have a direct influence on a materials' performance.

References

Anderson PM, Li C (1995) Hall–Petch relations for multilayered materials. Nanostruct Mater 5:349
Anstis GR et al (1981) J Am Ceram Soc 64:533–538
Ashby MF (1972) Acta Metall 20:887
Badzian AR (1981) Cubic boron nitride–diamond mixed crystals. Mater Res Bull 16 (11):1385–1393
Barnett SA (1993) Physics of thin films. In: Francombe MH, Vossen JL (eds) Mechanics and dielectric properties, vol 17. Academic, Boston
Brazhkin VV (2007) High pressure synthesized materials: treasure and hints. High Pressure Res 27 (3):333–351
Brazhkin VV, Lyapin AG, Hemley RJ (2002) Harder than diamond: dreams and reality. Philos Mag A82(2):231–253
Brazhkin V et al (2004) From our readers: What does 'harder than diamond' mean? Nat Mater 3:576–577
Chen XQ et al (2011) Intrinsic correlation between hardness and elasticity in polycrystalline materials and bulk metallic glasses. Intermetallics 19:1275–1281
Chu X et al (1992) Deposition and properties of polycrystalline TiN/NbN superlattice coatings. J Vac Sci Technol A 10:1604
Cohen ML (1985) Calculation of bulk moduli of diamond and zinc-blende solids. Phys Rev B32 (12):7988–7991
Cottrell AH (1967) An introduction to metallurgy. Edward Arnold publishers, London, p 192
Crampon J, Escaig BJ (1980) Am Ceram Soc 63:680
Creyke WEC, Sainsbury IEJ, Morrell R (1982) Design with nonductile materials. Applied Science, London, pp 68–101, 115–133
Davis L (1976) Metallic glasses. In: Gilman JJ, Leamy HJ (eds) Fundamental Aspects of Structural Alloy Design. Springer, US NY, p 431–450
Decker BF, Kasper JS (1959) The crystal structure of a simple rhombohedral form boron. Acta Crystallogr 12:503–506
Dubrovinskaia NA et al (1999) Thermal expansion and compressibility of Co W C. J Alloys Compd 285:242–245
Elssner G et al (1999) Ceramics and ceramic composites: materialographic preparation. Elsevier, Amsterdam/New York, pp 144–158
Evans AG (1974a) Fracture mechanics of ceramics, vol 1. Plenum Press, New York, p 17
Evans AG (1974b) The role of inclusions in the fracture of ceramic materials. J Mater Sci 9:1145–1152
Evans AG, Charles EA (1976) J Am Ceram Soc 59:371
Evans AG, Lange FF (1975) J Mater Sci 10:1659–1664
Fantozzi G, Saadaoui M (2014) Toughness, fatigue and thermal shock of ceramics: microstructural effects. Compr Hard Mater 2:299–319
Frantsevic NH (1980) Superhard materials. Naukova Dumka: Kiev, Ukraine, 620
Frischholz (2004) Breviary Technical Ceramics. Verband der Keramischen Industry e.V., Germany

Gilman JJ (1973) Hardness – a strength microprobe. In: Westbrook JH, Conrad H (eds) The science of hardness testing and its research applications. American Society for Metals, Metals Park
Gomez FJ, Elices M (2006) Fracture loads for ceramic samples with rounded notches. Eng Fract Mech 73(7):880–894
Griffith AA (1920) Phenomena of rupture and flow in solids. Philos Trans R Soc Lond A224:163–198
Haines J et al (2001) Synthesis and design of superhard materials. Annu Rev Mater Res 31:1–23
Helmersson U (1987) J Appl Phys 62:481
Hertzberg RW (1989) Deformation and fracture mechanics of engineering materials, 3rd edn. Wiley, New York
Hughes RE et al (1963) Structure of beta-rhombohedral boron. J Am Chem Soc 28(3):289–301
Inoue A et al (1994) Jpn Inst Met Mater Trans 35:85
Kelly JR (1995) Perspectives on strength. Dent Mater 11:103–110
Kelly A, MacMillan NH (1986) Strong solids, 3rd edn. Clarendon, Oxford
Knittle E et al (1995) High-pressure synthesis, characterization, and equation of state of cubic C-BN solid solutions. Phys Rev B 51(18):12149
Koehler JS (1970) Phys Rev B.2:547
Komatsu T et al (1996) Synthesis and characterization of a shock-synthesized cubic B–C–N solid solution of composition BC2.5N. J Mater Chem 6(11):1799–1803
Krstic VD (1984) Fracture of brittle solids in the presence of thermoelastic stresses. J Am Ceram Soc 67(9):589–593
Krstic VD (1988) Grain-size dependence of fracture stress in anisotropic brittle solids. J Mater Sci 23:259–266
Kurakevych OO (2009) Superhard phases and simple substances and binary compounds of the B-C-N-O system: from diamond to the latest results. J Superhard Mater 31(3):139–157
Kurdumova V et al (1984) Polymorphous modifications of carbon and boron nitride. Naukova Dumka, Kiev
Lambrecht WRL, Segall B (1993) Anomalous band-gap behaviour and phase stability of c-BN–diamond alloy. Phys Rev B 17(15):9289–9296
Lange FF (1984) Structural ceramics: a question of fabrication reliability. J Mater Eng Syst 6:107–113
Larsson M et al (1996) Surf Coat Technol 86/87:351
Launey ME (2009) Fracture toughness and crack resistance curve behaviour in metallic glass matrix composites. Appl Phys Lett 94:241910–241913
Launey ME, Buehler MJ, Ritchie RO (2010) On the mechanistic origins of toughness in bone. Annu Rev Mater Res 40:25–53
Lawn BR, Swain MV, Phillips K (1975) J Mater Sci Lett 10:1236–1239
Lawn BR et al (1994) Making ceramics ductile. Science 263:1114
Leger JM et al (1994) Materials potentially harder than diamond: quenchable high-pressure phases of transition metal dioxides. J Mater Sci Lett 13:1688–1690
Liu AY, Cohen ML (1989) Prediction of new compressibility solids. Science 245:841
Liu A et al (1981) Phys Rev B 43:6742
Lüthy H, White RA, Sherby OD (1979) Mater Sci Eng 39:211
Malkow T (2001) Critical observations in the research of carbon nitride. Mater Sci Eng 302 (2):311–324
Matizamhuka WR (2010) A Study on the synthesis of ultrahard cubic BC_2N heterodiamond. PhD Thesis, University of the Witwatersrand
Mattesini M, Matar SF (2001) Search for ultra-hard materials: theoretical characterisation of novel orthorhombic BC_2 N crystals. Int J Inorg Mater 3:943–957
Mcnamara D et al (2015) Fracture toughness evaluation of polycrystalline diamond as a function of microstructure. Eng Fract Mech 143:1–16
Mohamed FA, Langdon TG (1974) Metal Trans A5:2339

Morrell R (1985) Handbook of properties of technical engineering ceramics part 1: an introduction for the engineer and designer. H.M.S.O, London, pp 92–93
Mott N, Davis E (1979) Electron processes in non-crystalline materials. Clarendon Press, Oxford
Munz D, Fett T (1999) Ceramics: mechanical properties, failure behaviour, materials selection, vol 36. Springer, Berlin, Heidelberg
Nakano S (1996) Advanced materials '96: new trends in high pressure research. In: Proceedings of the 3rd NIRIM international symposium for advanced materials, National Institute for Research in Inorganic Materials, Japan, p 287
Nakano S et al (1994) Segregate crystallisation of several diamond like phases from the graphitic BC_2N without additive at 7.7GPa. Chem Mater 6(12):2246–2251
Nalla RK, Kinney JH, Ritchie RO (2003) Mechanistic fracture criteria for the failure of human cortical bone. Nat Mater 2(3):164–168
Niihara K et al (1982) J Mater Sci Lett 1:13–16
Novikovin V (1987) Physical properties of diamond. Naukova Dumka, Kiev. Kosolapova
Oganov AR et al (2009) Ionic high pressure form of elemental boron. Nature 457:863–867
Olagnon C, Chevalier J, Panchard V (2006) Global description of crack propagation in ceramics. J Eur Ceram Soc:1–9
Pan Z et al (2005) Ab initio pseudopotential studies of cubic BC_2N under high pressure. J Phys Condens Mater 17:3211–3220
Pan Z et al (2006) *Ab initio* structural identification of high density cubic BC_2N. Phys Rev B 73:214111–214114
Pierson H (1994) Handbook of carbon, graphite, diamond and fullerenes: properties, processing and applications. Noyes Publications, New Jersey, pp 30–39
Riedel R (1992) Materials harder than diamond? Adv Mater 4(11):759–761
Riedel R (1994) Novel ultrahard materials. Adv Mater 6(7/8):549–560
Ritchie RO (2008) Mechanisms of fatigue crack-propagation in metals, ceramics and composites: role of crack tip shielding. Mater Sci Eng A 103(1):15–28
Ritchie RO (2011) The conflicts between strength and toughness. Nat Mater 10:817–822
Ruoff A, Li TA (1995) Rev Muter Sci 25:249
Schiotz J, Di Tolla ED, Jacobsen KW (1998) Nature 391:561
Shetty DK et al (1981) Baxial fracture studies of a glass-ceramic. J Am Ceram Soc 64(1):1–4
Shetty DK et al (1985) J Mater Sci 20:1873–1882
Shinn M, Hultman L, Barnett SA (1992) J Mater Res 7:901
Solozhenko VL, Gregoryanz E (2005) Synthesis of superhard materials. Mater Today 8:44–51
Solozhenko VL et al (2001) Synthesis of superhard cubic BC_2N. Appl Phys Lett 78(10):1385.17
Sun H et al (2001) Structural forms of cubic BC_2N. Phys Rev B 64:094108-6
Sung C-M, Sung M (1996) Carbon nitride and other speculative superhard materials. Mater Chem Phys 43:1–18
Tateyama Y et al (1997) Proposed synthesis path for heterodiamond BC_2N. Phys Rev B 55(16): R10161-4
Taylor D (1996) Crack modelling: a technique for the fatigue design of components. Eng Fract Mech 3(2):129–136
Taylor D (1999) Geometrical effects in fatigue: a unifying theoretical model. Int J Fract 21 (5):413–420
Taylor D (2004) Predicting the fracture strength of ceramic materials using the theory of critical distances. Eng Fract Mech 71(16–17):2407–2416
Taylor D (2006) The theory of critical distances applied to the prediction of brittle fracture in metallic materials. Struct Integr Durab 1(2):145–154
Taylor D, Cornetti P, Pugno N (2005) The fracture mechanics of finite crack extension. Eng Fract Mech 72(7):1021–1038
Teter DM, Hemeley RJ (1996) Low compressibility carbon nitrides. Science 271:1161
Tian Y (2012) Microscopic theory of hardness and design of novel superhard crystals. Int J Refract Met Hard Mater 33:93–106

Veprek S (1999) The search for novel, superhard materials. J Vac Sci Technol A 17(5):2401–2420
Veprek S (2013) Recent search for new superhard materials: go nano. J Vac Sci Technol A 5 (050822):1–33
Veprek S, Argon AS (2001) Mechanical Properties of superhard nanocomposites. Surf Coat Technol 146–147:175–182
Weiner S, Wagner HD (1998) The material bone: structural-mechanical functional relations. Annu Rev Mater Sci 28:271–298
Widany J et al (1998) Density-functional based tight-binding calculations on zinc-blende type BC_2N-crystals. Diam Relat Mater 7:1633–1638
Zerr A, Riedel R (2000) In: Riedel R (ed) Handbook of ceramic hard materials, vol 1. Wiley-VCH, Weinheim
Zhao Y et al (2002) Superhard B–C–N materials synthesized in nanostructured bulks. J Mater Res 17(12):3139–3145
Zheng JC et al (1999) Ground-state properties of cubic C–BN solid solutions. J Phys Condens Mater 11:927–935
Zhu H et al (2015) Anomalous scaling law of strength and toughness of cellulose nanopaper. Proc Natl Acad Sci USA 112:1–6

Chapter 4
Measurements of Hardness and Other Mechanical Properties of Hard and Superhard Materials and Coatings

Dr. Maritza G.J. Veprek-Heijman
and Prof. Dr. Prof. h.c. Dr. h.c. Stan Veprek

Abstract We discuss the methods and problems associated with a reliable measurements of mechanical properties of superhard ($H \geq 40$ GPa) and ultrahard ($H \geq 80$ GPa) materials and coatings. It is shown that the "nanoindentation" can yield incorrect results of hardness and elastic moduli when applied to super- and ultrahard materials. Therefore, the classical two-step method, where, after the indentation with a given load, the size of remnant indentation is measured by a microscope, is recommended for the verification of the results obtained from the "nanoindentation." We further discuss methods for the determination of elastic moduli, tensile yield strength, and internal friction. Special attention is devoted to the measurement of the mechanical properties of super- and ultrahard thin films on softer substrates. It is shown that the Bückle's rule, according to which the indentation depth should not exceed 10 % of the film thickness of a hard film on soft substrate, does not apply for hard and superhard materials.

1 Introduction

Experimental determination of the mechanical properties of hard and superhard materials is usually not an easy task. In many cases, a large load of several newtons (N) has to be applied during the hardness measurement to achieve the load-invariant value of the hardness. Also the compliance of the testing systems used may be higher than that of the sample being tested. This makes the accurate determination

Dr. M.G.J. Veprek-Heijman (✉)
Department of Chemistry, Technical University Munich, Munich, Germany
e-mail: Maritza.Veprekheijman@lrz.tum.de

Prof. Dr. Prof. h.c. Dr. h.c. S. Veprek
Professor Emeritus, Department of Chemistry, Technical University Munich, Munich, Germany
e-mail: Stan.Veprek@lrz.tum.de

V. Kanyanta (ed.), *Microstructure-Property Correlations for Hard, Superhard, and Ultrahard Materials*, DOI 10.1007/978-3-319-29291-5_4

of the deformations in the sample very difficult, particularly when using the modern automated load-depth sensing techniques with instruments called "nanoindentometers." The properties of the materials are often affected by the residual stress in the structure due to the manufacturing route used. This is particularly important for hard and superhard coatings on softer substrates. These and other issues, challenges, and methods of overcoming them will be discussed in this chapter with focus on the correct measurements of hardness of bulk materials as well as of thin films on softer substrates and wear protection coatings on tools for machining. Because the measurements of fracture toughness, which is also an important property of hard (hardness $H \geq 10$ GPa), superhard ($H \geq 40$ GPa), and ultrahard ($H \geq 80$ GPa) materials, will be discussed in Chap. 5, we limit our discussion of this topic only to a short remark. Also the coefficient of friction, μ, will be mentioned only briefly. Special attention is devoted to the measurement of elastic moduli, yield strength, and the thickness of the hard, superhard, and ultrahard thin films on softer substrate that is needed for correct measurement. It is shown that for the correct hardness measurements, the required thickness of the hard, superhard, and ultrahard thin film on a soft substrate must be much larger than what the Bückle's rule of 10 % suggests.

The fracture toughness, expressed in terms of stress intensity factor K_I given by Eq. 4.1 (here, σ is the stress needed to propagate a crack of a size $2a$, and *Const*. is a factor that takes into account the flaw shape and geometry, as well as the loading mode configuration (Anderson 1995)), is the resistance of a material against the propagation of a preexisting (prefabricated) crack (McClintock and Argon 1966; Hertzberg 1989; Anderson 1995). It should be emphasized that one has to distinguish between fracture toughness defined in this way and the resistance against brittle fracture due to the absence of microcracks and other flaws in the material because of a high-threshold limit needed to initiate a crack in an optimally processed material. This can be easily understood by comparing the Griffith formula for critical stress σ_C needed for propagation of a penny-shaped crack of diameter $2a$ given in Eq. 4.2 (here, E_Y is the Young's modulus and γ_C is the surface energy) and the ideal decohesion strength σ_{Decoh} given by Eq. 4.3 (here a_0 is the interatomic distance; Kelly and Macmillan 1986).

$$K_I = \text{Const.} \cdot \sigma \cdot \sqrt{\pi \cdot a} \tag{4.1}$$

$$\sigma_C = \sqrt{\frac{2E_Y \cdot \gamma_S}{\pi \cdot a}} \tag{4.2}$$

$$\sigma_{\text{Decoh.}} = \sqrt{\frac{2E_Y \cdot \gamma_S}{\pi \cdot a_0}} \tag{4.3}$$

In an optimally processed polycrystalline material, the size of cracks resulting from the preparation scales approximately with the crystallite size d. Therefore, σ_C is relatively small in coarse-grained polycrystalline materials where a is of the order of tens microns, but it strongly increases for nanocrystalline materials where it can approach the ideal decohesion strength σ_{Decoh} (Veprek et al. 1996; Veprek 1999).

Such material can reach a high elastic limit of several percentage or more approaching that of an ideal flaw-free material (Veprek and Argon 2002; Veprek et al. 2003b). We shall discuss this point in Chap. 6. Whereas the measurement of the fracture toughness (Eq. 4.1) of bulk materials is well established and described in Chap. 5 and in a number of textbooks, the measurement of the threshold for the crack initiation is difficult because it depends on the statistics of the flaws formed during the preparation of the material. The statistical modeling and the probability of the cleavage fracture are calculated either by the relatively simple "weakest link" model or by the truncated Weibull distribution described, e.g., in Anderson (1995) to which we refer for further details.

The coefficient of friction, μ, of a material in a sliding contact with another one describes important property for many applications. It is the force F necessary to keep two surfaces, which are pressed together by a load L_N normal to the direction of the sliding, from sliding against each other (Feynman et al. 1966, p. 12–3 ff.).

$$F = \mu \cdot L_N \tag{4.4}$$

Thus, μ is a dimensionless scalar. The coefficient of friction depends on the asperities of the sliding surfaces, on the surface energy of the materials sliding against each other, on the sliding speed, and on humidity or other environmental effects which can act as lubricants (Bayer 2002). To initiate sliding between two surfaces which are in rest requires higher force F_0 than that in steady-state sliding conditions because the surface asperities are "locked in" at rest (F_0 is called "stiction"). For these and many other reasons, the coefficient of friction has to be measured under precisely defined conditions. Such conditions are usually specified in the user's manuals of tribometers on the market.

Friction may also be important during the measurement of the hardness of materials, because high friction coefficient between the indenter and the sample being measured may result in a falsified, apparently higher, hardness (Tabor 1951). However, because only diamond indenters are used for measuring the hardness of super- and ultrahard materials, and because diamond has a small coefficient of friction of about 0.1 toward the majority of materials (Tabor 1951), this effect is probably not too important. Nevertheless, it should be kept in mind and checked by comparing the value of the hardness measured without and with a lubricant. Friction may also be important when measuring "hot hardness," i.e., hardness at elevated temperature.

One of the important fields of application of super- and ultrahard materials is the machining of metallic alloys, wood, and ceramics. For these applications, bulk materials (c-BN, diamond, cermets) as well as wear protection coatings on tools made of high-speed steel (HSS) or cemented carbide (WC-Co) are used. Important are not only the high hardness, high fracture toughness, and low coefficient of friction, but also high oxidation and chemical resistance against the material being machined. For example, in spite of its high hardness of 70–100 GPa, diamond cannot be used for the machining of ferrous alloys or other materials which contain elements that form stable carbides, because in that case the chemical wear

dominates. Thus, not only purely "mechanical" properties are important in the applications. But these aspects are beyond the scope of this chapter. Therefore, here we shall focus on the measurement of the hardness and afterward discuss the measurements of elastic moduli and some other properties.

2 Hardness

2.1 The Meaning of Hardness

In general sense, hardness is the resistance of a material against plastic deformation under the applied load. Thus, the nature of the applied load defines different hardnesses, such as scratch hardness according to Mohs, impact hardness, or indentation hardness (Tabor 1951). Scratch hardness, being used by mineralogists because of its simplicity, particularly when working in the field, is not suitable for material scientists and engineers because it is strongly nonlinear (see, e.g., McClintock and Argon 1966, p. 450). The dynamic impact hardness is important, e.g., in interrupted cutting, such as milling, for the lacquer on the front part of a vehicle exposed to impact of particles and the like. Because these materials are not superhard, we shall not discuss the impact hardness in any further details here. The definition of the impact hardness can be found in the book by Tabor (1951), and the more recent method of its testing is described by McClintock and Argon (1966), Knotek et al. (1992), and Bouzakis et al. (2007).

From the scientific point of view, most important is the indentation hardness with self-similar indenters, such as Vickers or other pyramidal or conical indenters, where the contact area between the indenter and the material being measured, A_C, is proportional to the square of the indentation depth, h^2. The indentation hardness is the average pressure beneath the indenter under the conditions of fully developed plasticity (Meyer 1908; Tabor 1951). Note that the pressure beneath the indenter is distributed very inhomogenously (see, e.g., Fig. 11 in Veprek et al. 2007). The correctly measured indentation hardness must be load invariant. Unfortunately, this condition is often neglected in many published papers which incorrectly report on "superhard materials" because the measurements have been done at a too small load, where the indentation size effect (ISE, see below) may falsify the hardness measurement (see Veprek-Heijman and Veprek (2015) and references therein).

2.2 Indentation Hardness

The most popular and reliable method of the hardness measured using the self-similar indenters has been the two-step indentation procedure with the Vickers indenter, which is a four-faced pyramid made of diamond with an angle of 136°

between the opposite faces. This angle has been chosen to make the Vickers hardness similar to the Brinell hardness as to yield the same values of hardness. Brinell hardness test uses a spherical indenter which is not self-similar, i.e., the indentation depth or the contact radius has to be specified (Tabor 1951, p. 98). The indenter is pressed into the material being tested with a given load, L, this load is applied for a defined period in order to check for possible creep. After unloading the projected area, A_P, of the remnant plastically deformed indent is measured with a microscope. The contact area, A_C, can be calculated from A_P using the known geometry of the Vickers indenter. Alternatively, the diagonal of the remnant indent is measured and A_C calculated. The Vickers hardness is

$$H_V = L/A_C. \tag{4.5}$$

The engineers use the so-called Vickers number in the units g/mm^2. We shall adhere to the units GPa (10,000 VH $\approx$ 10 GPa). One can also use the projected area of the indent, A_P, which yields the Meyers hardness $H_{Meyer} = L/A_P$. The Vickers and Meyers hardness are related by $H_V = 0.927 \cdot H_{Meyer}$ (Tabor 1951, p. 98), provided the indenter has a sharp tip or the indentation depth is sufficiently large so that the error of h due to the tip rounding can be neglected. It has to be kept in mind that when indenting into superhard materials, the sharp diamond tip is plastically (irreversibly) deformed up to a "radius" 0.5–0.7 μm (see below). Keeping the load applied for a sufficiently long time is necessary when the material being tested undergoes creep under the load.

For an ideal Vickers indenter, the contact area, A_C, and indentation depth, h, are related by Eq. 4.3. However, when the indenter tip is dull, the actual contact area is—for the same indentation depth—larger than that corresponding to Eq. 4.3. Neglecting this "tip rounding" results in incorrect, too high hardness value. This error can be neglected when the indentation depth is large, but it becomes serious when the indentation depth is about 100 nm or less, as is the case with the modern "nanoindentometers."

$$A_C = 26.43h^2 \tag{4.6}$$

Later on, the Berkovich indenter with three faces and cube-corner indenter with four faces have been introduced because they develop larger stress under the sharp tip to assure yielding of the material being tested at a low applied load. The relation between the indentation depth and contact area is similar to Eq. 4.3 with different proportionality constants that can be found, e.g., in Fischer-Cripps (2004). The larger stress that develops under the sharper indenter tips of Berkovich and cube-corner indenters is an important advantage when measuring the hardness of thin films using the automated load–depth-sensing technique called "nanoindentation," which has been introduced by Doerner and Nix (1986) and later on improved by Oliver and Pharr (1992, 2004).

However, the advantage of Berkovich and cube-corner indenters is less pronounced when measuring super- and ultrahard materials because, in that case, the

initially sharp indenter tip undergoes plastic deformation and rounding, as shown by experiment (see Fig. 8 in Veprek et al. 2003a) and by nonlinear finite element modeling (see Figs. 1 and 2 in Veprek-Heijman et al. 2009). Typically, a sharp indenter with a tip "radius"[1] of ≤ 0.1 μm is plastically deformed when indenting into a super- and ultrahard material so that after 2–3 indentations, the "radius" increases to about 0.3–0.5 μm. However, with increasing number of the subsequent indentations, the incremental increase of the tip "radius" is diminishing until it stabilizes at about 0.5–0.7 μm (Fig. 2 in Veprek-Heijman et al. 2009). Upon further indentations, the tip "radius" deforms mainly elastically.

For these reasons, hardness of super- and ultrahard materials can be reproducibly measured only with a dull indenter. This often (but not always, see below and Chap. 6) requires the use of large indentation depth of ≥ 400–600 nm and corresponding large load of up to several N. Such high loads cannot be provided by the majority of the modern "nanoindentometers." Therefore, one has to use the conventional two-step techniques.

As we shall discuss later, the measured apparent hardness increases when the applied load decreases under a certain value (Sect. 2.3). This so-called indentation size effect (ISE) can have a variety of origins, the not perfectly shaped and sharp indenter being only one of them. The ISE due to tip rounding has to be experimentally corrected for by a special procedure called "tip area correction" when using the automated load–depth-sensing technique ("nanoindentation"), which typically uses relatively small load. The early method of Doerner and Nix used the constant hardness method, where the apparent hardness of a reference material is measured as function of applied load up to sufficiently large load where ISE vanishes because the indentation depth is much larger than the error of the indentation depth due to the dull tip, and the correct hardness is measured. Then, a polynomial function is used to transform the measured dependence of the apparent hardness on the applied load as to obtain correct hardness for all points measured at different loads. In the method of Doerner and Nix, about 25 % of the initial part of the unloading indentation curve is linearly extrapolated to zero load, where the so-called corrected indentation depth, h_{Corr}, is obtained. From this value of h_{Corr}, the hardness is calculated according to Eq. 4.2. This procedure is a purely empirical calibration of the instrument, and the value of h_{Corr} is not any real indentation depth (Behncke 1993, Sect. 4.4).[2] Nevertheless, it can provide correct results when the calibration is carefully done as shown in Fig. 4.1. Figure 4.1a shows an example of repetitive measurement of the hardness of Si and sapphire wafers using the early version of the indentometer Fischerscope H100, which has been on the market several years before the paper of Oliver and Pharr has been published. Therefore, it used the

[1] We write "radius" within quotation marks because the tip is not exactly spherical (see Fig. 1 in Veprek-Heijman et al. (2009)).

[2] Doerner and Nix measured the shape of the diamond indenter using scanning electron microscope and used this for the tip area correction.

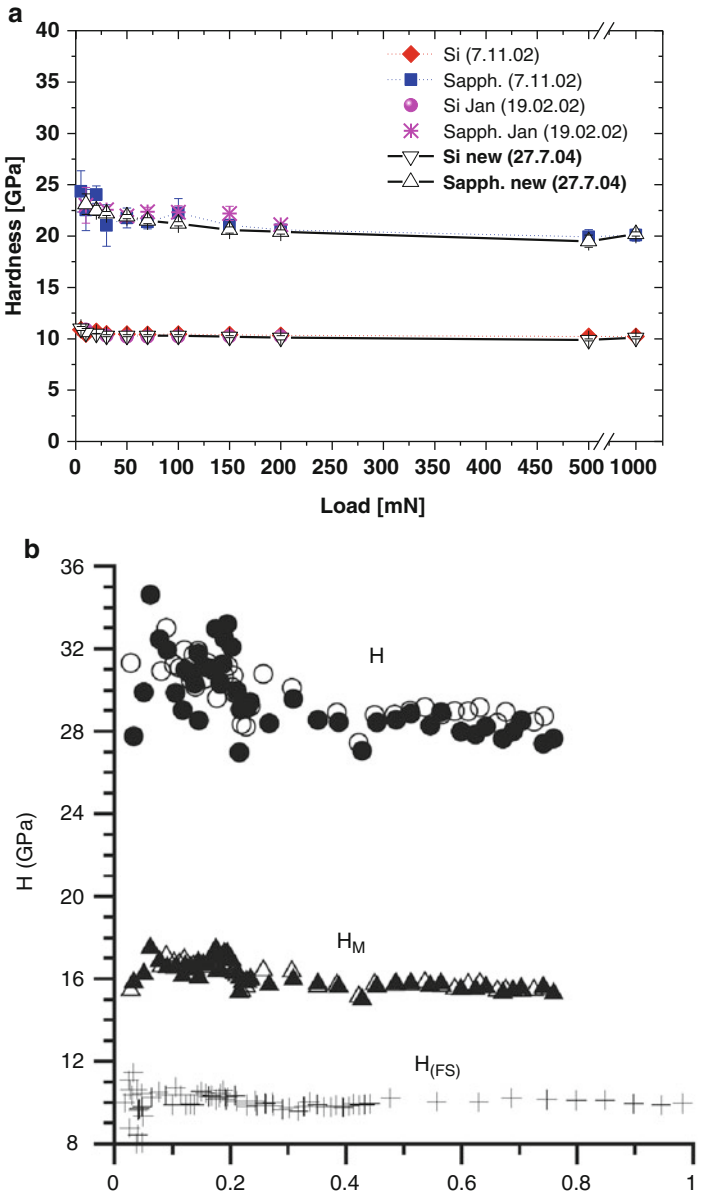

Fig. 4.1 (**a**) Hardness of silicon used for the calibration of the early version of Fischerscope H100 in the constant hardness mode and resultant hardness of sapphire (see also Veprek et al. 2003a). (**b**) Example of the measurement of the hardness, as function of indentation depth, of sapphire using a modern nanoindentometer that has been calibrated according to the Oliver and Pharr procedure using constant stiffness method (see text from Fischer-Cripps et al. 2006)

method of Doerner and Nix [similar results, measured by other coworkers of S. V., have been published in Veprek S et al. (2003a)].

The method of Oliver and Pharr uses for the "tip area correction" constant stiffness method and a power-law fit of the initial part of the unloading curve together with an "intercept factor" to determine the corrected indentation depth (Oliver and Pharr 1992, 2004; Fischer-Cripps 2004). Oliver and Pharr called their procedure "an improved technique for determining hardness. . .," and, after their first paper (Oliver and Pharr 1992), they published several critical papers analyzing possible artifacts which may occur when using this technique (e.g., Oliver and Pharr 2004). Also other researchers analyzed this techniques and suggested many corrections and improvements (e.g., Chaudhri 2001; Chaudhri and Lim 2007; Meza et al. 2007; Rodriguez et al. 2011; Keutenedjian Mady et al. 2012). We cannot review this issue here because the number of the relevant papers is too large. But we would like to emphasize that large care has to be taken when measuring hardness of superhard materials using the "nanoindentation" technique. Unfortunately, the original method of Oliver and Pharr (1992) is often used by the workers without any critical analysis. We would like to illustrate it here by only two examples.

Figure 4.1b shows an example of the hardness of sapphire (see points denoted H) measured with the "nanoindenter" UMIS that has been calibrated by means of the constant stiffness of fused silica using the Oliver and Pharr method (Fischer-Cripps et al. 2006). H_M is the Martens hardness, i.e., the hardness under applied load, H_{FS} is the hardness of the fused silica, and h_C is the corrected indentation depth (h_C of 0.8 μm corresponds to a load of about 200–300 mN). Obviously, the value of the hardness of sapphire obtained by Fischer-Cripps with this method of about 28–30 GPa is too high. There are many papers reporting the hardness of sapphire, measured by the conventional two-step techniques at large load of several N, to be 21 ± 1.5 GPa (e.g., Berg et al. 2000; Müller 1984; Holleck 1986; Kollenberg 1988, homepages of industrial companies producing sapphire such as Kyocera (2015) and others). The hardness of sapphire of about 21 GPa is almost independent of the crystallographic orientation of the surface being indented (Sinani et al. 2009). This value of the hardness agrees very well with the data in Fig. 4.1a that were measured with the original version of Fischerscope H100 using the simple method of Doerner and Nix.

The incorrect, too high value of the hardness of sapphire of 28–30 GPa obtained by the Oliver and Pharr method when the instrument is calibrated for a constant stiffness of fused silica, in contrast to the results of Fig. 4.1a, has been reported in several publications and books without any critical analysis (e.g., Fischer-Cripps 2004, Appendix 5; Dub et al. 2014). It is probably related to the fact that sapphire has different elastic–plastic behavior and higher Young's modulus as compared to its hardness than fused silica. No systematic study of this issue has been conducted so far, although some improvements, such as "variable intercept factor," have been discussed (Chudoba and Jennett 2008). The complex elastic–plastic transformation and pop-in phenomena that occur in sapphire upon indentation at small load of few mN and displacement < 100 nm will not be discussed here (see, e.g., Dub et al. 2014). With reference to Fig. 4.1a, we emphasize that these phenomena do

not occur at larger load where the correct, load-invariant hardness of about 21 GPa is found.

We shall not continue the discussion of the methods which should be used for the measurement with the automated load-depth sensing "nanoindentation" technique. We only emphasize that the example of sapphire should be a warning that much care should be taken when measuring hardness of super- and ultrahard materials using the "nanoindentation" technique. The so-called tip area correction is obviously a calibration of the instrument using a material with given elastic–plastic mechanical properties, and this calibration does not need to apply to a material with different elastic–plastic behavior.

In order to illustrate the problems which may happen when using the "nanoindentation" technique without a deeper analysis of the method, we show in Fig. 4.2 the mistakes which happen when the so-called corrected (in fact "transformed" by the polynomial fit according to Doerner and Nix as explained above) indentation curves are incorrectly taken as the true load–depth dependencies, as done in Fischer-Cripps et al. (2012). Figure 4.2a is Fig. 2 from Veprek et al. (2003c). One can see that the hardness of the nanocomposite coatings of 49.7 GPa obtained from the early version of Fischerscope H100 which used the Doerner and Nix method for calibration (Doerner and Nix 1986), that of 48.4 GPa obtained from the size of the remnant indent measured by scanning electron microscope, SEM, and those obtained by linear extrapolation of 20, 30, and 35 % of the initial part of the unloading curve, agrees with the average value of the 48.7 GPa within 1.6 %. In contrast, the value obtained by fitting this curve using the Oliver and Pharr method yields only 28.8 GPa, lower by a factor of 1.7. However, when the method of Oliver and Pharr is applied to the "as measured" curve, which is the actual load-depth dependence, hardness value of 52.3 GPa is obtained. This value is slightly higher than the correct one because of neglect of the tip rounding. This difference is relatively small because the indentation depth of about 0.6 μm was sufficiently large so that the neglect of the tip rounding causes only a relatively small error.

In order to emphasize this point, we show in Fig. 4.2b the hardness of a reference industrial diamond in dependence on the applied load. The results obtained from the early version of Fischerscope H100 are displayed as asterisks. When applying the Oliver and Pharr method to the "as measured" indentation curves and approximately accounting for the tip rounding, hardness of about 110 GPa is obtained. This is in a reasonable agreement with the values of about 104 GPa obtained by the early version of Fischerscope H100, which used the method of Doerner and Nix,[3] and with the value of 110 GPa measured on the same diamond by Fischer-Cripps et al. (2006) who used the method of Oliver and Pharr. However, when the method of Oliver and Pharr is applied to the "corrected" (i.e., transformed by the polynomial function) curve of the Fischerscope H100, an incorrect hardness of about

[3] One has to consider the fact that the values obtained from the individual measurements show relatively large scattering of up to 10 %.

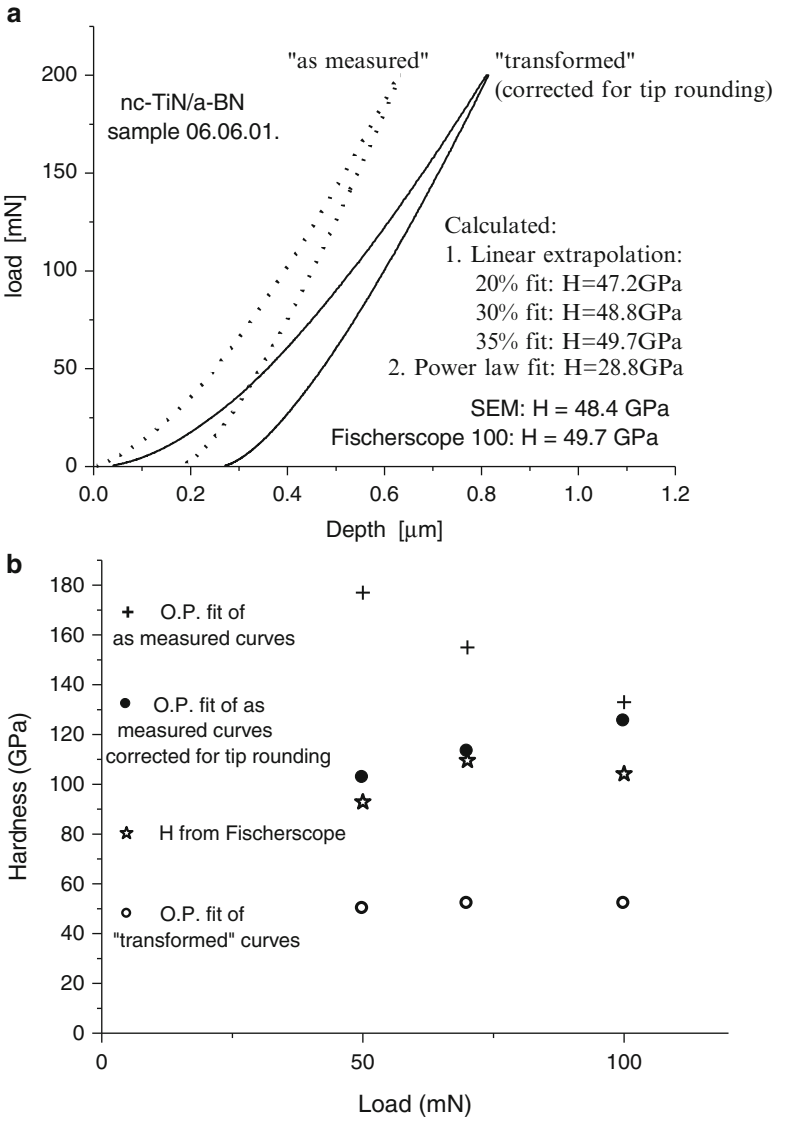

Fig. 4.2 (**a**) "As measured" and "calibrated" indentation curves into superhard nc-TiN/a-BN coatings. The apparent "hardness" obtained from the calibrated and as measured curve using Oliver and Pharr method (Oliver and Pharr 1992) is 28.8 and 52.3 GPa, respectively (reproduced from Fig. 2 in Veprek et al. 2003c with permission). (**b**) *Crosses*, hardness of diamond vs. maximum applied load calculated by means of Oliver and Pharr method from the "as measured" indentations curves without tip area corrections; *full circles*, after a simple tip correction assuming a tip radius of about 0.7 μm, roughly in agreement with the tip rounding reported earlier (Veprek-Heijman et al. 2009); *stars*, hardness obtained from Fischerscope H100; *open circles*, incorrect values of "hardness" obtained from the fit—using the Oliver and Pharr method—of the indentation curves which have been calibrated according to Doerner and Nix method (Doerner and Nix 1986)

50 GPa, lower by about a factor of two, is obtained. This has been shown by the authors already in 2003 (see Fig. 3 in Veprek 2003c). Exactly this mistake happened to Fischer-Cripps et al. in their paper where they claim that we measured the hardness of the ultrahard nanocomposite coatings incorrectly, "too high by a factor of two" (Fischer-Cripps et al. 2012).

Another effect, which may falsify the hardness measurement when using the automated load-depth sensing technique, is the pileup that often occurs during indentation into ductile materials. During the indentation, the ductile material flows up along the diamond indenter, thus decreasing the apparent indentation depth that is measured by the automated load-depth sensing techniques. As a result, the indentometer is sensing smaller indentation depth than the correct one, thus giving an incorrect, higher hardness. The only way to avoid this error is to measure the size of the remnant indentation by a microscope. Many modern "nanoindentometers" are equipped with atomic force microscope and thus enable this task. Because pileup is relatively unlikely to occur when indenting superhard materials, we don't discuss this issue here in any more detail and refer to the literature instead (Taljat et al. 1998; Bolshakov et al. 1997; Bolshakov and Pharr 1998).

From this short overview of possible artifacts that may occur when using the "nanoindentation," it should be clear that the ultimate test remains the classical two-step indentation method, where the size of the remnant plastic indent is measured by a microscope after unloading. This statement is further supported by the fact that many super- and ultrahard materials display ISE that is not related to the finite radius of the indenter tip (see next section) which makes it necessary to use large load of several N that many of the modern sophisticated "nanoindentometers" do not provide. We refer to the paper by Brazhkin et al. who emphasized these facts already in previous studies (Brazhkin et al. 2004).

2.3 *Indentation Size Effect and the Possible Errors of the Hardness Measurements*

As already mentioned, the indentation size effect (ISE) can have a variety of origins, including the rounding of the indenter tip. This can be compensated for by a careful calibration of the instrument ("tip area correction").

Another possible reason for the appearance of ISE is the incomplete development of the plastic deformation beneath the indenter at low applied load which leads to an apparently higher strength and hardness of materials when tested at nanoscale. When materials, such as aluminum or copper, are tested by "nanoindentation" with a load of a few 10 μN where the indentation depth amounts to only a few 10 nm, the plasticity cannot fully develop and the behavior of such materials corresponds to that of an ideal perfect single crystal (see, e.g., Gouldstone et al. 2001; Li et al. 2002; Van Vliet and Suresh 2002). Such a

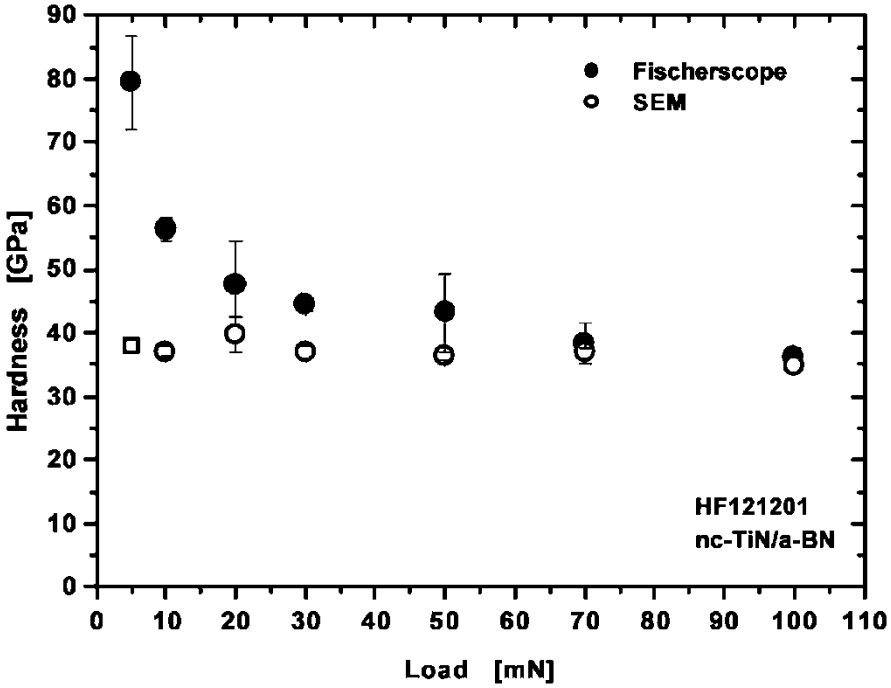

Fig. 4.3 Hardness of a 6 μm thick nc-TiN/BN nanocomposite coating vs. applied load obtained from indentometer Fischerscope H100 after tip area correction (*full symbols*) and from the area of remnant plastic deformation determined by calibrated scanning electron microscope (from Veprek et al. 2003a) with permission)

behavior resembles the strengthening of nano-sized materials (Zhu et al. 2008) although it is also found in large-grain polycrystals when indented at nanoscale. We refer to a recent review by Pharr et al. for further details regarding ISE (Pharr et al. 2010). Here we only emphasize that the hardness measurement by indentation has to be done at sufficiently high load to assure that the material operates in a regime of fully developed plasticity for which the criterion is that the hardness is load invariant as described by Meyer already some time ago (Meyer 1908).

Even if a sufficiently high load is used and the tip area correction carefully done, ISE may occur due to other artifacts. In Fig. 4.3 we show such an example: The hardness obtained from the area of the remnant plastic deformation by calibrated scanning electron microscope (SEM) is constant for all loads between 5 mN and 100 mN used, but the hardness values obtained from the indentometer show a pronounced ISE, approaching the correct value only at a load of 70 mN. As described in our earlier paper to which we refer for further details, this ISE was due to anelastic[4] deformation of the steel substrate (Veprek et al. 2003a).

[4] Anelasticity is a reversible, time delayed deformation described, e.g., in Gottstein (2004).

ISE which cannot be corrected for by the "tip area correction" routine has its origin in the mechanical properties of the material being tested. Figure 4.4a shows an example of strongly pronounced ISE in moissanite (6H-SiC—one of many modifications of silicon carbide) where a load of about 100 N is needed to reach the regime of load-invariant hardness (Brazhkin et al. 2004). Because these authors refer to an unpublished work, we cannot discuss the possible reason for such large ISE. Possibly, it can lay in the easy formation of stacking faults between the SiC double layers which are well known to occur in SiC. This easy formation of the stacking faults has, as a consequence, also the large number (more than 200) of different polymorphs of this material. Possibly, many of such polymorphs appear during the indentation into this material.

Another example of ISE is shown in Fig. 4.4b for ReB_2 which has "low compressibility" (large elastic moduli) and, therefore, has been suggested to be superhard (Chung et al. 2007). However, as seen in Fig. 4.4b by extrapolation of the measured data to larger load, the load-invariant hardness of ReB_2, which would be obtained at a larger loads than those used in this measurement, is less than 30 GPa. Obviously, ReB_2 is not superhard as incorrectly claimed in that paper (Chung et al. 2007) and in several follow-up papers which refer to the value of 48 GPa measured at the low load of 0.46 N. The reasons for the slow approach of the apparent hardness toward the correct load-invariant value are most probably electronic instabilities and concomitant structural transformations to other unstable and metastable structures with lower shear resistance than the original equilibrium structure that occur under a finite shear strain, as shown by Zhang et al. (2010). We refer to the paper of Zhang et al. and to the recent review (Veprek 2013) for further discussion of this problem.

Because electronic instabilities upon a final shear are likely to occur in materials with complex atomic valence orbitals, such as d-metals where electronic instabilities upon shear due to crystal field splitting are likely to occur (Zhang et al. 2010, 2014; Veprek 2013), measurement of the hardness as function of applied load has to be done to verify if the measured values are indeed load invariant. The data presented in Fig. 4.3 clearly show that the ISE is absent in the nanocomposites at loads of ≥ 5 mN because the 3 nm small TiN nanocrystals approach the ideal strength and therefore deform only elastically, whereas the interfaces are the carrier of the plastic flow (see below).

Also diamond transforms to graphite upon shear of > 0.3 in the (111)[11–2] slip system as shown by first-principles studies (e.g., Veprek et al. 2010a) and experimentally observed by Raman scattering of the indented area (Gogotsi et al. 1999). However, because of the relatively simple electronic structure of diamond, this transformation requires a very high shear stress. Therefore, diamond is ultrahard. Its correct, load-invariant hardness can be obtained already at relatively low load of ≤ 30 mN [see, e.g., Fig. 12a in Veprek et al. (2005)]. However, nanotwinned diamond with average distance between the twins of about 4 nm displays a pronounced ISE reaching the load-invariant hardness of about 200 GPa only

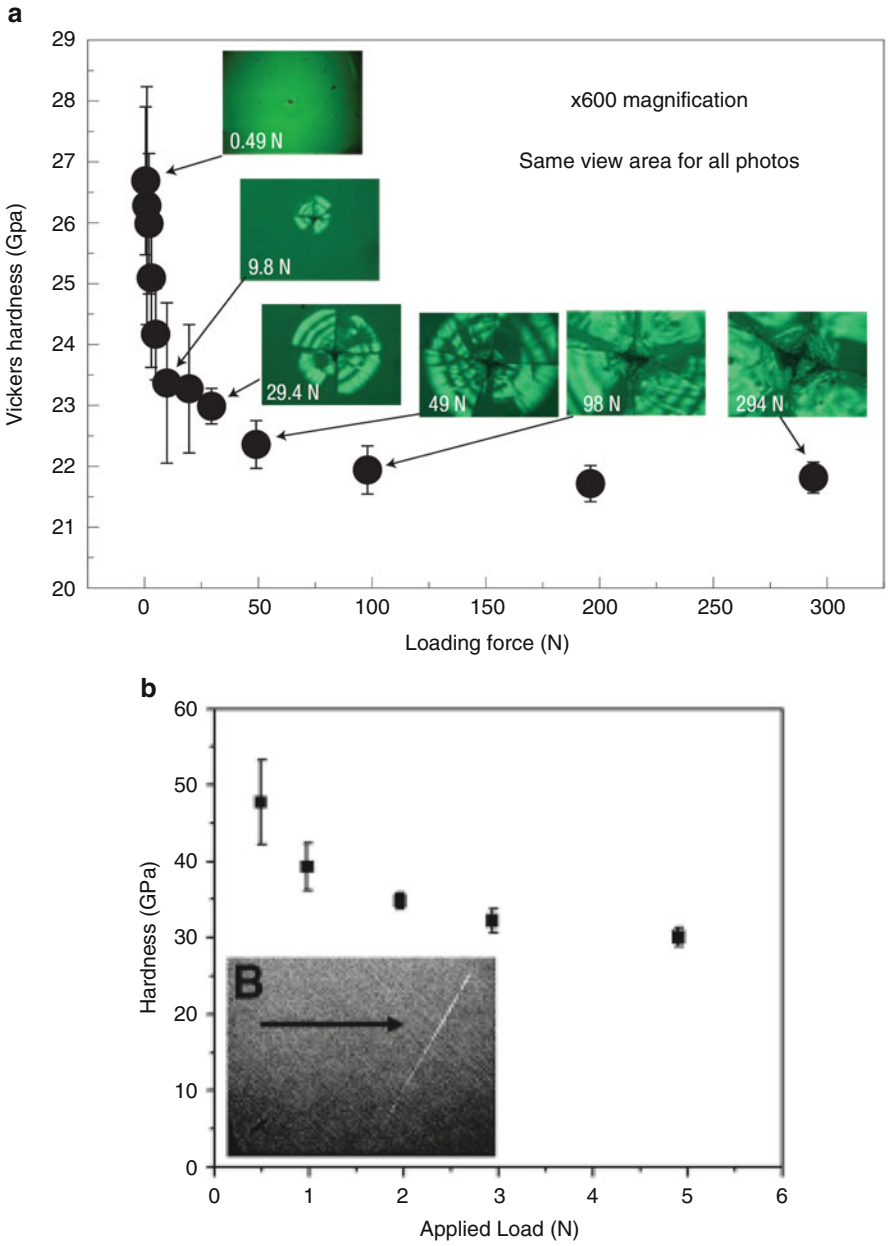

Fig. 4.4 (**a**) Vickers hardness of moissanite (6H-SiC) vs. the applied load together with the micrographs of the indents (from Brazhkin et al. 2004, with permission). (**b**) Hardness of ReB_2 vs. the applied load (from Chung et al. 2007, with permission)

at a load of 5 N [see Fig. 3a in Huang et al. (2014) and Fig. 4 in Xu and Tian (2015)].[5]

As already mentioned, there is no any unambiguous rule which could predict at what load the load-invariant value of hardness can be achieved in a given material. As a somewhat vague rule of thumb, we would suggest that only materials with simple electronic structure, such as diamond, or those where the regions of the plastic flow are well defined, such as the grain boundaries in the superhard nc-TiN/Si_3N_4 and related nanocomposites (Veprek et al. 2010a; Veprek 2013; Ivashchenko et al. 2015), the ISE is likely to be small, and the load-invariant hardness can be measured at relatively low load of few mN. For example, in the nc-TiN/Si_3N_4 nanocomposites with a thickness of 5–13 μm, the load-invariant superhardness has been achieved already at a small load of ≥ 5 mN [see Figs. 3 and 28a in Veprek (2013)]. In materials with a complex electronic structure, such as the borides of d-metals, a large load of up to several N is needed. This may be a limitation for the use of the modern instruments for "nanoindentation" to determine hardness of super- and ultrahard materials, because many of these instruments do not provide a sufficiently large load.

2.4 *Measurement on Hard and Superhard Coating on Softer Substrates*

Hard and superhard coatings are industrially used as wear protection coatings on tools for machining (drilling, milling, turning, etc.), injection molding, stamping, and the like (see, e.g., Inspektor and Salvador 2014; Mayrhofer et al. 2006; Veprek and Veprek-Heijman 2008). Cemented carbide (WC-Co) and high-speed steel (HSS) are used as materials of the tools. Hard coatings are used also in machine parts; in medicine, as decorative coatings; and in many other applications. In almost all these cases, the substrate is softer than the coating. Thus, the question arises as to what conditions must be met to make sure that the hardness is measured correctly in such a case. This problem has been discussed in some detail in the recent paper (Veprek-Heijman and Veprek 2015) and references quoted therein. Here, we shall give a short summary of this problem.

As we have seen in the previous section, the indentation load and concomitant indentation depth must be sufficiently high to assure that the material being

[5] One might doubt if it is possible to measure hardness of 200 GPa using diamond indenter because the diamond indenter has a hardness of only 80–100 GPa. This is possible because the diamond indenter is loaded mainly in compression, whereas the material being indented is loaded predominantly in shear (see, e.g., Fig. 13.8 in McClintock and Argon (1966), p. 454 and also Fig. 29 in Veprek (2013) that shows the flow of the material in the indenter due to the indentation into an ultrahard material). Diamond as well as the majority of intrinsically strong materials sustains up to eight times higher stress in compression than in shear. The recent estimate of the maximum pressure that diamond can sustain suggests a lower limit of about 420 GPa (Eremets et al. 2005).

measured operates in the regime of fully developed plasticity where the correct, load-invariant hardness is obtained. The corresponding "minimum indentation depth" may be as small as 100 nm for simple nitrides, carbides, or nanocomposites, but several μm may be needed for some materials that display a slow approach to the load-invariant value. The high elastic strain in the hard coatings may cause plastic deformation of the softer substrate even when the plastically deformed zone in the coatings beneath the indenter is relatively small and does not reach the interface to the substrate. In that case, the measured "compound hardness" of the coatings and softer substrates is obtained. When the hardness is measured, at sufficiently thick coatings, as function of the increasing applied load (or indentation depth), the obtained values change from that of the coatings to the compound hardness of the system coatings/substrate that continuously decreases toward the hardness of the substrate. Several models have been proposed to evaluate the correct hardness of the coatings from the compound measured hardness of the system coatings/substrate (e.g., Johnsson and Hogmark 1984; Korsunsky et al. 1998; Bull et al. 2004). However, the range of the load where these models work sufficiently well is relatively narrow, and high-quality experimental data are needed. Therefore, these models are of limited use and shall not be discussed here.

The linear FEM work of Sun et al. (1995a, b) showed the influence of the ratio of the yield strength of coatings and substrate and of the tip radius of a rigid indenter on the loading curve in the indentation experiment. However, these calculations were limited to linear FEM and to thin coatings of limited hardness. Here, we shall summarize the results of nonlinear finite element modeling (FEM) which has been recently conducted to determine the thickness of the coating of a given hardness on typical substrates used, such as steel, silicon wafer, and cemented carbide (Veprek-Heijman and Veprek 2015). He and Veprek (2003) conducted similar studies using the linear FEM, but limited in the study as regards the range of hardness of the coatings and the type of the substrates. Therefore, we shall not discuss them here.

The nonlinear FEM accounts for the pressure enhancement of elastic moduli[6] and concomitant increase of plastic flow resistance due to the pressure beneath the indenter that develops during the hardness measurement (Veprek et al. 2007). As shown in Veprek et al. (2007), the distribution of the volumetric strain (elastic deformation, Fig. 11 therein) and deviatoric strain (plastic deformation, Fig. 12) under the indenter differ significantly for the linear and nonlinear FEM. This emphasizes the need for using the nonlinear constitutive material model to calculate how the strains in the coatings are transferred into the substrate and when they may cause its plastic deformation.

[6] Under isostatic pressure the elastic moduli are enhanced. For example, the bulk modulus at pressure p is given by $B(p) = B_0 + b \cdot p$ where B_0 is the bulk modulus at zero pressure and b is the proportionality factor which is typically between 3 and 5 for the majority of materials (Rose et al. 1984).

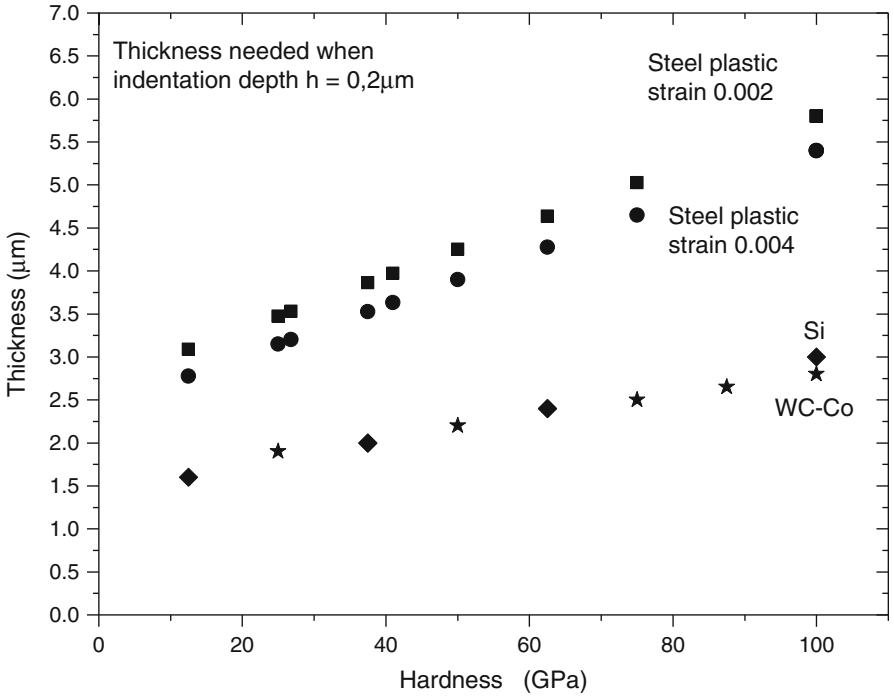

Fig. 4.5 Minimum thickness of the coatings of the given hardness that is needed for the correct measurement of the hardness of the coatings (see text). For steel substrate we show data for plastic strain of 0.002 and 0.004 to illustrate that this difference has only small effect on the t/h ratio. *Full squares*, steel substrate with plastic strain 0.002; *full circles*, steel substrate with plastic strain 0.004; *full diamonds*, substrate Si; *asterisks*, substrate WC-Co cemented carbide

In our nonlinear FEM, we calculated the thickness of the coatings of a given hardness that is needed to avoid plastic deformation of the given substrate when the minimum indentation depth is 0.2 µm, using a dull indenter as explained above (Veprek-Heijman and Veprek 2015). Figure 4.5 shows the minimum thickness of the coatings of different hardness on three different substrates, as indicated, that is needed to avoid plastic deformation of the substrate (i.e., plastic strain ≤ 0.002 or 0.2 %). For steel substrate we show also the results for somewhat larger onset of the plastic strain of 0.004 to illustrate that in this range of the strain, the difference is relatively small (Veprek-Heijman and Veprek 2015).

Usually, one refers to the "Bückle's rule" according to which the indentation depth should not exceed 10 % of the thickness of the coatings in order to avoid the plastic deformation of the softer substrate (Bückle 1965, 1973). In our recent paper (Veprek-Heijman and Veprek 2015), we presented the dependence of the ratio of thickness of the coatings to the indentation depth which is needed to avoid plastic deformation of the substrate. Obviously, this rule does not apply for coatings with hardness ≥ 10 GPa on steel and for coatings with hardness of ≥ 30 GPa on Si wafers and cemented carbide. Clearly, Bückle's rule does not apply when measuring the hardness of superhard materials.

Thus, the reader should use Fig. 4.5 of this paper as rough guideline to estimate which thickness of coatings with given hardness on a given substrate is needed for correct measurements. However, the reader has to consider that these data apply for indentation depth of only 0.2 μm. If large indentation depth is needed to achieve the load-invariant regime of the measured hardness, correspondingly thicker coatings are needed. This has been emphasized and followed in our papers on the superhard nanocomposites from the very beginning (Veprek and Reiprich 1995), but ignored in many papers of other researchers where "superhardness" of 40–60 GPa has been reported on 1–2 μm thick or even thinner coatings deposited on steel or Si substrates. For example, Zhang et al. reported "hardness" of up to 38 GPa for 0.16–0.41 μm thick Ti-Si-N coatings which is obviously incorrect (Zhang et al. 2004). Unfortunately, there are many other examples of reports on "superhard" coatings where the hardness has been incorrectly measured [see some examples quoted in Veprek-Heijman and Veprek (2015)].

When the hardness of ultrahard coatings is measured, the required thickness may be too large for unambiguous verification that the obtained hardness is really load invariant. For example, in the case of ultrahard coatings on steel or silicon, the required thickness would be several tens of micrometers. Such coatings are difficult or impossible to prepare because of biaxial compressive stress present in coatings deposited by plasma chemical or physical vapor deposition. In such case, one has to measure the compound hardness of the system coatings/substrate up to sufficiently large load of at least 500 mN. Afterward, one has to use the nonlinear FEM to verify the data obtained at large loads, where the plastic deformation of the softer substrate occurs or even dominates. Only when the measured curve can be reproduced using the nonlinear FEM with one constant value of the hardness of the coatings can the value of hardness be considered correct.

This is illustrated in Fig. 4.6 which shows the comparison between the measured hardness of 7.3 μm thick ultrahard quasi-ternary nc-TiN/Si_3N_4/$TiSi_2$ coatings on steel (with an additional interlayer of 3.4 μm TiN), determined from the scanning electron micrographs and calculated by the nonlinear FEM. With reference to Fig. 4.3, we note that the indentation size effect occurs at low load of less than 5 mN for the nc-TiN/BN coatings. In Fig. 28a of Veprek (2013), we have an example of 13.8 μm thick nc-TiN/Si_3N_4 coatings which show load-invariant hardness from the smallest load of 20 mN used, i.e., the indentation size effect occurs at smaller load. There are more examples which show that in the nanocomposites under discussion here, the ISE is limited to much smaller load because the plastic flow occurs in the grain boundaries (Ivashchenko et al. 2015). Therefore, also in the example shown in Fig. 4.6b, the indentation size effect is not seen because the lowest load used was 50 mN.

In the FEM calculations, the only adjustable parameter has been the yield strength of the coatings as described in Veprek-Heijman et al. (2009).[7] One can

[7] The reader should note that other parameters, such as elastic moduli of the materials of coatings and substrate as well as their dependence on pressure, the yield strengths, and hardness of the substrate, enter the FEM calculations as constant materials parameters.

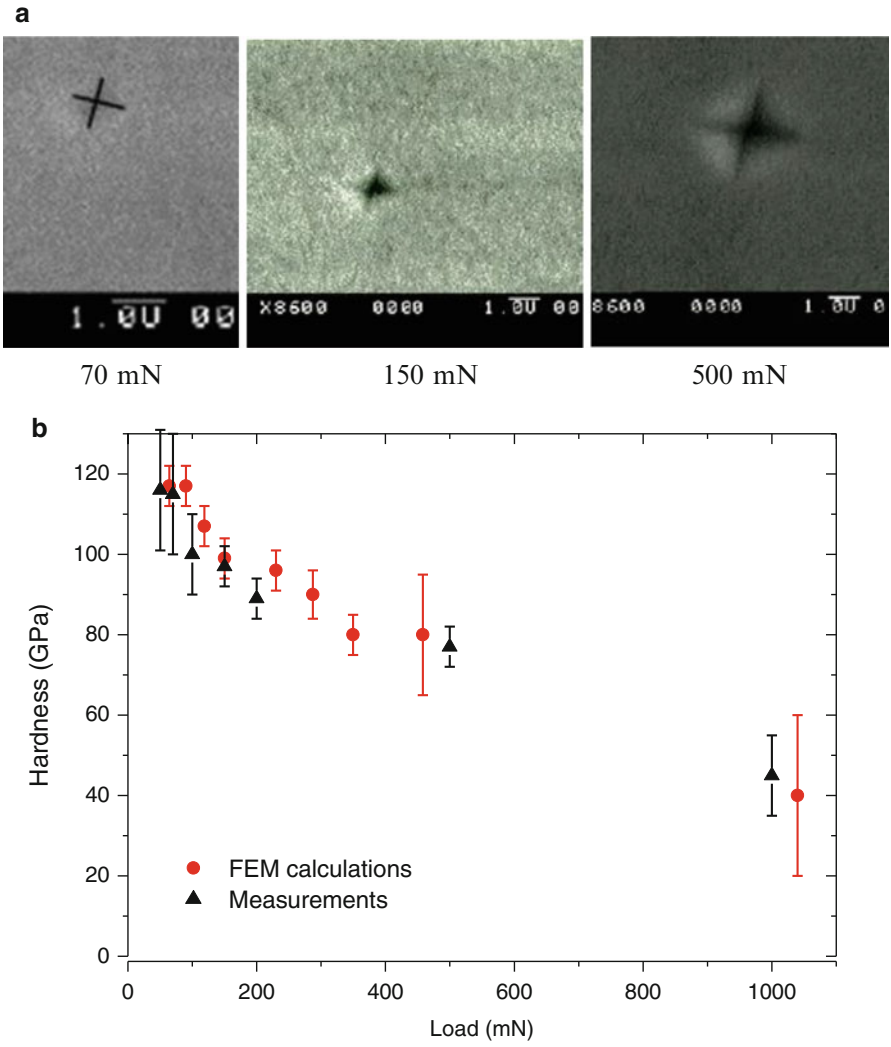

Fig. 4.6 (**a**) Examples of scanning electron micrographs of remnant indentations into the ultrahard nc-TiN/Si_3N_4/$TiSi_2$ nanocomposites at a given load as indicated, (**b**) hardness vs. maximum applied load: *crosses* are the experimental data from (Veprek and Veprek-Heijman 2012), and *open symbols* are the values calculated by the present nonlinear FEM (Veprek-Heijman and Veprek 2015)

see that the experimental data agree very well with the nonlinear FEM calculations up to high load of 1000 mN. Thus, the hardness of about 115 GPa measured at load of 50 and 70 mN is the correct hardness of the coatings because the nonlinear FEM reproduces very well the compound hardness of the system coatings/substrate up to the highest load of 1000 mN. We emphasize again that indentation size effect can be ruled out in these data. Note that at a load of 500 mN, the compound hardness is

still close to 80 GPa. As discussed in Chap. 6, in these nanocomposites the grain boundaries are the carrier of the plastic flow, whereas the 3–4 nm size TiN nanocrystals deform only elastically. For this reason the load-invariant hardness is measured already at the low load of 50–70 mN.

In conclusion to this subsection, we emphasize that the hardness of hard and superhard coatings can be correctly measured only when the coatings are sufficiently thick to avoid the plastic deformation of the substrate and to verify that the measured value of hardness is load invariant. In the case of ultrahard coatings, where the required thickness of the coatings would be too large, nonlinear FEM has to be used to verify if the compound hardness of the system coating/substrate yields a correct value of the hardness of the coating. Application of the Bückle's rule, according to which the indentation depth should not exceed 10 % of the thickness of the coatings, is not justified for superhard coatings on soft substrates.

3 Measurement of Elastic Moduli

The Young's modulus is conventionally determined in a classical tensile stress test. However, the preparation of the sample for such test is difficult or impossible when the measurement should be done with hard and superhard materials. Moreover, novel ultraincompressible materials, which are believed to be possibly superhard, are often prepared in very small quantities and as small grains which are not suitable for the classical measurements. Therefore, other methods for the determination of Young's and other moduli have to be used.

In principle, Young's modulus might be evaluated by the load–depth-sensing technique using the method of Oliver and Pharr that enables to determine the "reduced modulus," E_r, given by Eq. 4.2 (1992). Here, E is the Young's modulus and ν is the Poisson's ratio of the coatings and E_i and ν_i are the same parameters for the indenter (Oliver and Pharr 1992):

$$E_r = \frac{1-\nu^2}{E} + \frac{1-\nu_i}{E_i} \tag{4.7}$$

Although this method works reasonably well for softer materials, its application to superhard materials is not guaranteed because the analysis of the unloading part of the indentation curve is based on linear elastic–plastic behavior. This alone may cause errors of the evaluated Young's modulus at more than 20 % (Veprek RG et al. 2007). Moreover, the concept of the reduced modulus and applicability of the Sneddon's solution on which the concept of the measurement is based have been questioned by several researchers (e.g., Bolshakov and Pharr 1997; Hay et al. 1999; Chaudhri 2001; Chaudhri and Lim 2007; Rodriguez et al. 2011). We don't want to discuss this complex issue here. Instead we shall discuss other techniques which are suitable for the determination of elastic moduli of superhard materials. Because, as mentioned, the classical tensile stress–strain test, from which Young's modulus can

be determined, is difficult to conduct with superhard materials and coatings, we shall focus on other methods of the measurements which do not suffer from this difficulty.

The bulk modulus B can be determined from high-pressure X-ray diffraction (XRD), when small samples of the material are inserted into diamond anvil cell and exposed to high pressure and the change of the spacing of the crystallographic plains as function of applied pressure is determined from XRD. This method is described in a number of papers to which we refer for further details (e.g., Jayaraman 1983; Cynn et al. 2002). It has been also used to measure the bulk modulus of superhard nanocomposites (Veprek et al. 2010b). The sample preparation is simple because small quantity of powder of a grain size of > 10 μm is sufficient for such measurements. The only problem may be that synchrotron radiation is needed for such studies, but this should not be a serious problem nowadays. In such experiments, also the pressure dependence of the bulk modulus is obtained (e.g., Veprek et al. 2010b).

Young's modulus E of thin films can be measured by the vibrating reed method. In this case, the coatings are deposited on both sides of an elongated substrate strip made of an elastic metal that is subsequently fixed on one end, and its mechanical oscillations are excited by means of an appropriate actuator. The resonant frequency of the oscillating reed is measured, and the Young's modulus of the coating is calculated from a well-established formula (Li et al. 2004). This method can be simultaneously used to evaluate the internal friction of poly- or nanocrystalline coatings which provides an important information about the structural stability of the grain boundaries, segregation of the phases, and formation of stable poly- or nanocrystalline structure (see Li et al. 2004, 2005).

Probably the most convenient method for measuring elastic moduli is Brillouin surface scattering (BSS; see, e.g., Zinin et al. 1999; Abadias et al. 2014a, b) which allows to simultaneously determine the Young's modulus, E, and shear modulus, G, which also yield the Poisson's ratio ν due to the relationship $G = E/2(1 + \nu)$ (see, e.g., Kelly and Macmillan 1986). In such a way, all three moduli can be compared using the well-known relationships between them (Kelly and Macmillan 1986). Using the combination of high-pressure XRD, vibrating reed, and Brillouin surface scattering, all three moduli of the nc-TiN/Si_3N_4 nanocomposites have been determined with high accuracy and agreement between all three methods within less than 5 % as shown in Table 4.1 (Veprek et al. 2003c). Obviously, the vibrating reed, surface Brillouin scattering, and high-pressure XRD are the methods of choice for the measurements of the elastic moduli of superhard and ultrahard materials.

Table 4.1 Average values of Young's E, bulk B, and shear modulus G measured on TiN and on superhard nc-TiN/Si_3N_4 nanocomposites by vibrating reed, high-pressure XRD, and surface Brillouin scattering using a large number of samples (see Veprek et al. 2003c)

E (GPa)	B (GPa)	G (GPa)
445 ± 20	295 ± 15	195 ± 15

Ultrasonic interferometry can be used for the determination of second-order elastic constant of bulk samples from which elastic moduli B and G can be calculated using the well-known formulae (see review by Jacobsen et al. 2005). Thus, also the Poisson's ratio and Young's modulus can be obtained. The recent development of this technique into the gigahertz range allowed one to measure elastic moduli with high precision of about 0.1 and 1 % for samples of 1 and 0.1 mm size, respectively (Chang et al. 2014). The measurements can also be done on samples placed in diamond culets and exposed to high pressure. As far as we know, this method has not been used so far for measurement of elastic properties of thin films on a substrate. Most probably, the usually small thickness of the coatings and the presence of the substrate will make it difficult.

4 Measurement of Stress in the Films Deposited on a Substrate

Because optimally processed superhard bulk materials should be free of noticeable stresses, we shall concentrate on the measurement of stress in polycrystalline thin films on a substrate. One has to distinguish between the random stress which originates from the grain boundaries and biaxial stress of the coatings that may have a variety of origins. However, we have to keep in mind that random strain and concomitant stress are likely to appear in the recently prepared nanocrystalline diamond (Chang et al. 2014) and in nano-twinned c-BN (Tian et al. 2013) and diamond (Huang et al. 2014; Xu and Tian 2015). No such studies have been done so far.

The random stress has its origin in dislocations or in strain within the grain boundaries of polycrystalline material that causes random dilatation and compression of the crystallites, which contributes to broadening of the Bragg reflection in XRD. The most reliable determination of the random strain provides the integral method of Warren and Averbach, which uses the Fourier transform to distinguish between the broadening of the Bragg reflections due to the random strain and broadening due to finite crystallite size (Warren and Averbach 1952; Klug and Alexander 1974; Mittemeijer and Welzel 2008). The frequently used method of Williamson and Hall (Williamson and Hall 1953; Hall 1949; Hall and Williamson 1951; Pelleg et al. 2005) assumes additive contribution of the broadening due to finite crystallite size and random strain to the experimentally measured peak width that is however valid only if the peaks have Cauchy profiles (Klug and Alexander 1974, p. 635). This is generally not the case. Therefore, the integral method of Warren and Averbach has to be used. The random strain and concomitant stress within the grain boundaries in the superhard nc-TiN/Si_3N_4 nanocomposites with 3–4 nm size TiN nanocrystals can reach high values of ≥ 7 GPa [see Fig. 5 in

Niederhofer et al. (1999)] which may—in long terms—destabilize some metastable phases within the grain boundaries [see Veprek (2013) and references therein].

Biaxial stress in thin films may be due to mismatch of the coefficient of thermal expansion, or to ion bombardment during the film growth, or to a variety of other effects. The stress may also change with the depth in the film and in particular during the film growth. Because the discussion of the different type of the stress is beyond the scope of this chapter, we limit our discussion only to the compressive biaxial stress that is caused in the films by energetic ion bombardment during growth in plasma chemical and physical vapor deposition and is important for, e.g., the adherence of coatings on tools.

A medium compressive stress of 1–3 GPa, which is obtained by bombardment of the growing film with low-energy ions [see, e.g., Fig. 1 in Veprek et al. (1987)], is beneficial because it makes the film dense which avoids incorporation of impurities when the film is—after the deposition—exposed to air. However, a too large compressive stress causes undesirable delamination. For these reasons the measurement of the stress is needed. This can be done by measurement of the shifts of the Bragg peaks in XRD using the so-called $\sin^2\varphi$ method (Noyan and Cohen 1987). However, there are several assumptions behind this method which are not always met in the praxis. Therefore, the simple method of the measurement of the curvature of the film/substrate system after the deposition of the film is, according to the experience of the present authors, much easier and reliable. The measurement can be done after the deposition, but the evolution of the stress during the growth, which may be quite complicated, can be also done in situ during the film growth (see, e.g., Fillon et al. 2010; Chason 2012; Abadias et al. 2008, 2011, 2013, 2014c). The stress in the film is evaluated from the bending of the system film/substrate using the Stoney's formula (Stoney 1909; Janssen et al. 2009). The multiple laser beam reflection from the surface of the film (or from the substrate) is a more elaborate technique to measure the bending of the system substrate/film (Chason 2012), but for the "daily" deposition experiments, the determination of the stress from the bending measured by optical microscope is in most cases sufficient.

Stress in the coatings may also influence the measurement of the mechanical properties of the thin films, in particular by "nanoindentation." We refer to the published papers for further details (e.g., Bolshakov et al. 1996; Tsui et al. 1996; Keutenedjian Mady et al. 2012). The hardness of transition metal nitrides deposited by reactive sputtering under ion bombardment at relatively low temperature can reach very high values [e.g., up to almost 80 GPa for TiN (Musil et al. 1988) and more than 40 GPa for a variety of nanocomposites consisting of hard transition metal nitride and ductile metal that does not form nitride (Musil 2000)], but upon annealing to ≥ 500 °C, the hardness decreases to its usual value (Karvankova et al. 2001). These coatings are discussed in Chap. 6.

5 Tensile Yield Strength

Tensile yield strength is the applied tensile stress where—after unloading—the remnant plastic deformation amounts to 0.2 %, i.e., plastic strain 0.002 (Gottstein 2004, p. 203). It can be exactly measured only in a tensile test, which—as already discussed—is not an easy task to conduct with superhard materials. Moreover, special sample preparation is required for the tensile test, which is very difficult to do when the material is available only as small species. Eremets et al. (2005) determined the yield strength of diamond of about 130–140 GPa by measuring the pressure distribution over the diamond anvils and by using the theory of elasticity. This method can be applied to other superhard materials.

As a very rough estimate, one may use the relation between the hardness H and tensile yield strength Y, $H = C \cdot Y$ with the constraint factor $C \approx 2.6$–2.8 that has been calculated by several researchers and more recently also by means of nonlinear FEM (Veprek-Heijman et al. 2009). A detailed discussion of the meaning of the constraint factor can be found in Veprek (2013), Appendix B.[8] When the hardness is measured correctly, the uncertainty of the yield stress should not be more than about 20 %. But, as mentioned, the reliability of such values is limited.

6 Summary

A correct measurement of hardness of super- and ultrahard materials must assure that the reported value is load invariant. In many cases of intrinsically super- and ultrahard materials, this can be achieved only at very large load of several N. Because the majority of the modern automatic load–depth-sensing instruments ("nanoindenters") do not allow one to apply high loads of several N, and because of many other possible artifacts that may occur when using this technique, the most reliable way to measure the hardness is the classical two-step method, where after unloading, the size of the remnant plastic indentation is measured with a microscope. In this case one also avoids the problem arising from different elastic–plastic behavior of different materials used for the calibration of the "nanoindentometer" and materials being measured. We have shown several examples of possible artifacts which can occur when the "nanoindentometers" are used.

[8] It has been claimed that for extrinsically superhard materials, the expanding cavity model (Hill 1950) should be used that yields a much smaller value of the constraint factor (Fischer-Cripps et al. 2012). However, in the expanding cavity model, only radial flow of material occurs, whereas in the superhard nanocomposites, the flow resembles that of the slip-line fields (Hill 1950; McClintock and Argon 1966) that yields the constraint factor of 2.7–3 [see Veprek (2013), Appendix B, and Fig. 29 therein]. The expanding cavity model is useful for elastomers, some polymers, and materials that plastically deform by densification, such as silicate glasses, but not for superhard ceramic materials.

When measuring on super- and ultrahard materials, an initially sharp diamond indenter undergoes plastic deformation which finishes at a "radius" of about 0.5–0.7 μm. Therefore, the hardness measurement on super- and ultrahard materials can be done only with a dull indenter. This requires relatively high applied load to develop full plasticity in the material being tested.

A particular problem is the measurement on super- and ultrahard coatings deposited on a softer substrate. We have shown that the Bückle's rule does not apply, and therefore very thick coatings are needed. This problem may be solved by a combination of the measurement of the compound hardness of the coating/substrate system as function of the applied load and nonlinear finite element modeling.

We briefly discuss also the measurement of elastic moduli, stress in the coatings, and tensile yield strength.

Acknowledgment We would like to thank the company SHM s.r.o. for the financial support of our work and the Department of Chemistry of the Technical University of Munich for providing us with the infrastructure needed for this work.

References

Abadias G, Guerin P (2008) *In situ* stress evolution during magnetron sputtering of transition metal nitride thin films. Appl Phys Lett 93:111908-1-3

Abadias G, Koutsokeras LE, Patsalas PA, Leroy W, Depla D, Zlotsi SV, Uglov VV (2011) In situ stress evolution during growth of transition metal nitride films and nanocomposites. In: Nanomaterials: applications & properties. Proceedings of the 1-st international conference, Crimea, 1:355–364

Abadias G, Koutsokeras LE, Siozios A, Patsalas P (2013) Stress, phase stability and oxidation resistance of ternary Ti–Me–N (Me = Zr, Ta) hard coatings. Thin Solid Films 538:56–70

Abadias G, Djema P, Belliard L (2014a) Alloying effects on the structure and elastic properties of hard coatings based on ternary transition metal (M = Ti, Zr or Ta) nitrides. Surf Coat Technol 257:129–137

Abadias G, Kanoun MB, Goumri-Said S, Koutsokeras L, Dub SN, Djemas P (2014b) Electronic structure and mechanical properties of ternary ZrTaN alloys studied by *ab initio* calculations and thin-film growth experiments. Phys Rev B 90:144107-1-18

Abadias G, Fillon A, Colin JJ, Michel A, Jaouen C (2014c) Real-time stress evolution during early growth stages of sputter-deposited metal films: influence of adatom mobility. Vacuum 100:36–40

Anderson TL (1995) Fracture mechanics, fundamentals and applications, 2nd edn. CRC Press, Boca Raton

Bayer RG (2002) Wear analysis for engineers. NHB Publishing, New York

Behncke H-H (1993) Bestimmung der Universalhärte und anderer Kennwerte an dünnen Schichten, insbesondere Hartstoffschichten. Härterei-Technische Mitteilungen 48:3–10

Berg G, Friedrich C, Broszeit E, Berger C (2000) Data collection of properties of hard materials. In: Riedel R (ed) Handbook of ceramic hard materials, vol 2. Wiley-VCH, Weinheim

Bolshakov A, Oliver WC, Pharr GM (1996) Influences of stress on the measurement of mechanical properties using nanoindentation: part II. Finite element simulations. J Mater Res 11:760–768

Bolshakov A, Pharr GM (1997) Inaccuracies in Sneddon's solution for elastic indentation by a rigid cone and their implications for nanoindentation data analysis. Mater Res Soc Symp Proc 436:189–194
Bolshakov A, Oliver WC, Pharr GM (1997) Finite element studies of the influence of pile-up on the analysis of nanoindentation data. Mat Res Soc Symp Proc 436:141–146
Bolshakov A, Pharr MG (1998) Influences of pileup on the measurement of mechanical properties by load and depth sensing indentation techniques. J Mater Res 13:1049–1058
Bouzakis K-D, Mirisidis I, Michailidis N, Lili N, Sampris A, Erkens G, Cremer R (2007) Wear of tools coated with various PVD films: correlation with impact test results by means of FEM simulations. Plasma Processes Polym 4:301–310
Brazhkin V, Dubrovinskaia N, Nicol M, Novikov N, Riedel R, Solozhenko V, Zhao Y (2004) What does 'harder than diamond' mean? Nat Mater 3:576–577
Bückle H (1965) Mikrohärteprüfung und ihre Anwendungen, Berliner Union, Waiblinger Kreiszeitung, Stuttgart 1965. German translation from L'Essai de Microdurete et ses Applications, Publications Scientific et Techniques du Ministère de L'Air, 1960
Bückle H (1973) In: Westbrook JH, Conrad H (eds) The science of hardness testing and its research applications. American Society for Metals, Metals Park, Ohio, pp 453–494
Bull SJ, Berasetegui EG, Page TF (2004) Modelling of indentation response of coatings and surface treatments. Wear 256:857–866
Chang YY, Jacobsen SD, Kimura M, Irifune T, Ohno I (2014) Elastic properties of transparent nano-polycrystalline diamond measured by GHz-ultrasonic interferometry and resonant sphere methods. Phys Earth Planet In 228:47–55
Chason E (2012) A kinetic analysis of residual stress evolution in polycrystalline thin films. Thin Solid Films 526:1–14
Chaudhri MM (2001) A note on a common mistake in the analysis of nanoindentation data. J Mater Res 16:336–339
Chaudhri MM, Lim YY (2007) Nanoindentation techniques: a critical assessment of the current methods of data analysis. Key Eng Mater 345–346:1107–1114
Chudoba T, Jennett NM (2008) Higher accuracy analysis of instrumented indentation data obtained with pointed indenters. J Phys D Appl Phys 41:215407-1-16
Chung H-Y, Weinberger MB, Levine JB, Kavner A, Yang J-M, Tolbert SH, Kaner RB (2007) Synthesis of ultra-incompressible superhard rhenium diboride at ambient pressure. Science 316:436–439
Cynn H, Klepeis JE, Yoo CS, Young DA (2002) Osmium has the lowest experimentally determined compressibility. Phys Rev Lett 88:135701-1-4
Doerner MF, Nix WD (1986) A method for interpreting the data from depth-sensing indentation instrument. J Mater Res 1:601–609
Dub SN, Brazhkin VV, Belous VA, Tolmacheva GN, Konevskii PV (2014) Comparative nanoindentation of single crystals of hard and superhard oxides. J Superhard Mater 36:217–230
Eremets MI, Trojan IA, Gwaze P, Huth J, Boehler R, Blank VD (2005) The strength of diamond. Appl Phys Lett 87:141902-1-3
Feynman RP, Leighton RB, Sands M (1966) The Feynman lectures on physics, I. Addison-Wesley, Reading, p 12-3-5
Fillon A, Abadias G, Michel A, Jaouen C, Villechaise P (2010) Influence of phase transformation on stress evolution during growth of metal thin films on silicon. Phys Rev Lett 104:096101-1-4
Fischer-Cripps AC (2004) Nanoindentation, 2nd edn. Springer, New York
Fischer-Cripps AC, Karvankova P, Veprek S (2006) On the measurement of hardness of superhard coatings. Surf Coat Technol 200:5645–5654
Fischer-Cripps AC, Bull SJ, Schwarzer N (2012) Critical review of claims for ultra-hardness in nanocomposite coatings. Philos Mag 92:1601–1630
Gottstein G (2004) Physical foundations of material science. Springer, Berlin
Gogotsi YG, Kailer A, Nickel KG (1999) Transformation of diamond to graphite. Nature 401:663–664

Gouldstone A, VanVliet KJ, Suresh S (2001) Simulation of defect nucleation in a crystal. Nature 411:656

Hall WH (1949) X-ray line broadening in metals. Proc Phys Soc (Lond) A 62:741–743

Hall WH, Williamson GK (1951) The diffraction pattern of cold worked metals: I the nature of extinction. Proc Phys Soc 64(B):937–946

Hay JC, Bolshakov A, Pharr GM (1999) A critical examination of the fundamental relations used in the analysis of nanoindentation data. J Mater Res 14:2296–2305

He JL, Veprek S (2003) Finite element modeling of indentation into superhard coatings. Surf Coat Technol 163–164:374–379

Hertzberg RW (1989) Deformation and fracture mechanics of engineering materials, 3rd edn. John Wiley, New York

Hill R (1950) The mathematical theory of plasticity. Oxford University Press, Oxford

Holleck H (1986) Material selection for hard coatings. J Vac Sci Technol A 4:2661–2669

Huang Q, Yu D, Xu B, Hu W, Ma Y, Wang Y, Zhao Z, Wen B, He J, Liu Z, Tian Y (2014) Nanotwinned diamond with unprecedented hardness and stability. Nature 510:250–253

Inspektor A, Salvador PA (2014) Architecture of PVD coatings for metalcutting applications: a review. Surf Coat Technol 257:138–153

Ivashchenko VI, Veprek S, Argon AS, Turchi PEA, Gorb L, Hill F, Leszczynski J (2015) First-principles quantum molecular calculations of structural and mechanical properties of TiN/SiNx heterostructures, and the achievable hardness of the nc-TiN/SiNx nanocomposites. Thin Solid Films 578:83–92

Jacobsen SD, Reichmann HJ, Kantor A, Spetzler HA (2005) A gigahertz ultrasonic interferometer for the diamond anvil cell and high-pressure elasticity of some iron-oxide minerals. In: Chen A, Wang Y, Duffy TS, Shen G, Dobrzhinetskaya LF (eds) Advances in high-pressure technology for geophysical applications. Elsevier, Amsterdam, pp 25–48

Janssen GCAM, Abdalla MM, van Keulen F, Pujada BR, van Venrooy B (2009) Celebrating the 100th anniversary of the Stoney equation for film stress: developments from polycrystalline steel strips to single crystal silicon wafers. Thin Solid Films 517:1858–1867

Jayaraman A (1983) Diamond anvil cell and high-pressure physical investigations. Rev Mod Phys 55:65–108

Johnsson B, Hogmark S (1984) Hardness measurements of thin films. Thin Solid Films 114:257–269

Karvankova P, Männling HD, Eggs C, Veprek S (2001) Thermal stability of ZrN–Ni and CrN–Ni superhard nanocomposite coatings. Surf Coat Technol 146–147:280–285

Kelly A, Macmillan NH (1986) Strong solids, 3rd edn. Clarendon, Oxford

Keutenedjian Mady CE, Rodriguez SA, Gomez AG, Souza RM (2012) Numerical analysis of different methods to calculate residual stresses in thin films based on instrumental indentation data. J Mater Res 27:1732–1741

Klug HP, Alexander LE (1974) X-ray diffraction procedures for polycrystalline and amorphous materials, 2nd edn. John Wiley, New York

Knotek O, Bosserhoff B, Schrey A, Leyendecker T, Lemmer O, Esser S (1992) A new technique for testing the impact load of thin films: the coating impact test. Surf Coat Technol 54/55:102–107

Kollenberg W (1988) Plastic deformation of Al_2O_3 single crystals by indentation at temperatures up to 750 °C. J Mater Sci 23(1988):3321–3325

Korsunsky AM, McGurk MR, Bull SJ, Page TF (1998) On the hardness of coated systems. Surf Coat Technol 99:171–183

Kyocera (2015) company, Kyoto Japan: http://global.kyocera.com/prdct/fc/product/pdf/s_c_sapphire.pdf downloaded 2015

Li J, VanVliet KJ, Zhu T, Yip S, Suresh S (2002) Atomistic mechanism governing elastic limit and incipient plasticity in crystals. Nature 418:307–310

Li ZS, Fang QF, Veprek S, Li SZ (2004) Evaluation of the internal friction and elastic modulus of the superhard films. Mater Sci Eng A 370:186–190

Li SZ, Fang QF, Liu Q, Li ZS, Gao J, Nesladek P, Prochazka J, Veprek-Heijman MGJ, Veprek S (2005) Thermally activated relaxation processes in superhard nc-TiN/a-Si_3N_4 and nc-$(Ti_{1-x}Al_x)$N/a-Si_3N_4 nanocomposites studied by means of internal friction measurements. Compos Sci Technol 65:735–774

Mayrhofer PH, Mitterer C, Hultman L, Clemens H (2006) Microstructural design of hard coatings. Prog Mater Sci 51:1032–1114

McClintock FA, Argon SA (1966) Mechanical behavior of materials. Addison-Wesley, Reading

Meyer E (1908) Untersuchungen über Härteprüfung und Härte. Zt Vereins Deutsch Ing 53:645–654

Meza JM, More Farias MC, De Souza RM, Cruz Riano LJ (2007) Using the ratio: maximum load over unload stiffness squared, P_m/S_u. On the evaluation of machine stiffness and area function of blunt indenters on depth-sensing indentation equipment. J Mater Res 10:437–447

Mittemeijer EJ, Welzel U (2008) The "State of the Art" of the diffraction analysis of crystallite size and strain. Z Krist 223:552–560

Müller B, Grau P, Kluge G (1984) The hardness of chromium- and titanium-doped sapphire crystals. Phys Status Solidi 83:499–506

Musil J (2000) Hard and superhard nanocomposite coatings. Surf Coat Technol 125:322–330

Musil J, Kadlec S, Vyskocil J, Valvoda V (1988) New results in D.C. Reactive magnetron deposition of TiN films. Thin Solid Films 167:107–119

Niederhofer A, Nesladek P, Männling HD, Moto K, Veprek S, Jilek M (1999) Structural properties, internal stress and thermal stability of nc-TiN/a-Si_3N_4, nc-TiN/$TiSi_x$ and nc-$(Ti_{1-y}Al_ySi_x)$N superhard nanocomposite coatings reaching the hardness of diamond. Surf Coat Technol 120–121:173–178

Noyan IC, Cohen JB (1987) Residual stress measurement by diffraction and interpretation. Springer, New York

Oliver WC, Pharr GM (1992) An improved technique for determining hardness and elastic modulus using load and displacement sensing indentation experiment. J Mater Res 7:1564–1583

Oliver WC, Pharr GM (2004) Measurement of hardness and elastic modulus by instrumented indentation: advances in understanding and refinements to methodology. J Mater Res 19:3–20

Pelleg J, Elish E, Mogilyanski D (2005) Evaluation of average domain size and microstrain in a silicide film by the Williamson–Hall method. Metall Mater Trans A 36:3187–3194

Pharr GM, Herbert EG, Gao Y (2010) The indentation size effect: a critical examination of experimental observations and mechanistic interpretations. Annu Rev Mater Res 40:271–292

Rodrigez SA, Souza RM, Alcala J (2011) A critical assessment of elastic unloading in sharp instrumented indentation experiments and the extraction of mechanical properties. Philos Mag 91:1409–1423

Rose JH, Smith AR, Guinea F, Ferrante J (1984) Universal features of the equation of state of metals. Phys Rev B 29:2963–2969

Sinani AB, Dynkin NK, Konevskiy PV, Lytvynov LA (2009) Dependence of sapphire hardness on loading type and orientation. Bull Russ Acad Sci Phys 73:456–459

Stoney GG (1909) The tension of metallic films deposited by electrolysis. Proc R Soc Lond A 82:172–175

Sun Y, Bell T, Zheng S (1995a) Finite element analysis of the critical ratio of coating thickness to indentation depth for coating property nanoindentation measurements. Thin Solid Films 258:198–204

Sun Y, Bloyce A, Bell T (1995b) Finite element analysis of plastic deformation of various TiN coating-substrate systems under normal contact with a rigid sphere. Thin Solid Films 271:122–131

Tabor D (1951) The hardness of metals. At the Clarendon Press, Oxford

Taljat B, Zacharia T, Pharr GM (1998) Pile-Up behavior of spherical indentations in engineering materials. Mater Res Soc Symp Proc 522:33–38

Tian Y, Xu B, Yu D, Ma Y, Wang Y, Hang Y, Hu W, Tang C, Gao Y, Luo K, Zhao Z, Wang LM, Weng B, He J, Liu Z (2013) Ultrahard nanotwinned cubic boron nitride. Nature 493:385–388

Tsui TY, Oliver WC, Pharr GM (1996) Influence of stress on the measurement of mechanical properties using nanoindentation: part I. Experimental studies in an aluminum alloy. J Mater Res 11:752–759

VanVliet KJ, Suresh S (2002) Simulation of cyclic normal indentation of crystal surfaces using the bubble-raft model. Philos Mag 82:1993–2001

Veprek RG, Parks DM, Argon AS, Veprek S (2007) Non-linear finite element constitutive modeling of mechanical properties of hard and superhard materials studied by indentation. Mater Sci Eng A 448:366–378

Veprek S, Sarott FA, Iqbal Z (1987) Effect of grain boundaries in the Raman spectra, optical absorption, and elastic light scattering in nanometer-sized crystalline silicon. Phys Rev B 36:3344–3350

Veprek S, Reiprich S (1995) A concept for the design of novel superhard coatings. Thin Solid Films 268:64–71

Veprek S, Haussmann M, Reiprich S (1996) Superhard nanocrystalline W_2N/amorphous Si_3N_4 composite materials. J Vac Sci Technol A 14:46–51

Veprek S (1999) The search for novel, superhard materials. J Vac Sci Technol A 17:2401–2420

Veprek S, Argon AS (2002) Towards the understanding of mechanical properties of super- and ultrahard nanocomposites. J Vac Sci Technol B 20:650–664

Veprek S, Mukherjee S, Karvankova P, Männling H-D, He JL, Moto K, Prochazka J, Argon AS (2003a) Hertzian analysis of the self-consistency and reliability of the indentation hardness measurements on superhard nanocomposite coatings. Thin Solid Films 436:220–231

Veprek S, Mukherjee S, Karvankova P, Männling H-D, He JL, Moto K, Prochazka J, Argon AS (2003b) Limits to the strength of super- and ultrahard nanocomposite coatings. J Vac Sci Technol A 21:532–544

Veprek S, Mukherjee S, Karvankova P, Männling H-D, He JL, Xu J, Prochazka J, Argon AS, Li AS, Fang QF, Li SZ, Manghnani MH, Tkachev S, Zinin P (2003c) Possible artefacts in the measurement of hardness and elastic modulus on superhard coatings and the verification of the correctness of the data. Mater Res Soc Symp Proc 750:9–15

Veprek S, Veprek-Heijman MGJ, Karvankova P, Prochazka J (2005) Different approaches to superhard coatings and nanocomposites. Thin Solid Films 476:1–29

Veprek S, Veprek-Heijman MGJ (2008) Industrial applications of superhard nanocomposite coatings. Surf Coat Technol 202:5063–5073

Veprek S, Argon AS, Zhang RF (2010a) Design of ultrahard materials: Go nano! Philos Mag 90:4101–4115

Veprek S, Prilliman SG, Clark AM (2010b) Elastic moduli of nc-TiN/a-Si_3N_4 nanocomposites: compressible, yet superhard. J Phys Chem Solids 71:1175–1178

Veprek S (2013) The search for new superhard materials: Go nano! J Vac Sci Technol A 31:050822-1-33

Veprek-Heijman MGJ, Veprek RG, Argon AS, Parks DM, Veprek S (2009) Non-linear finite element constitutive modeling of indentation into super- and ultrahard materials: the plastic deformation of the diamond tip and the ratio of hardness to tensile yield strength of super- and ultrahard nanocomposites. Surf Coat Technol 203:3385–3391

Veprek S, Veprek-Heijman MGJ (2012) Limits to the preparation of superhard nanocomposites: impurities, deposition and annealing temperature. Thin Solid Films 522:274–282

Veprek-Heijman MGJ, Veprek S (2015) The deformation of the substrate during indentation into superhard coatings: Bückle's rule revised. Surf Coat Technol 284:206–214

Warren BE, Averbach BL (1952) The separation of cold-work distortion and particle size broadening in X-Ray patterns. J Appl Phys 23:497–498

Williamson GK, Hall WH (1953) X-ray line broadening from filed aluminium and wolfram. Acta Metall 1:22–31

Xu B, Tian Y (2015) Ultrahardness: measurement and enhancement. J Phys Chem C 119:5633–5638

Zhang RF, Legut D, Niewa R, Argon AS, Veprek S (2010) Shear-induced structural transformation and plasticity in ultraincompressible ReB2 limit its hardness. Phys Rev B 82:104104-1-7

Zhang RF, Legut D, Wen XD, Veprek S, Rajan K, Lookman T, Mao HK, Zhao YS (2014) Bond deformation paths and electronic instabilities of ultraincompressible transition metal diborides: case study of OsB_2 and IrB_2. Phys Rev B 90:094115-1-6

Zhang XD, Meng WJ, Wang W, Rehn LE, Baldo PM, Evans RD (2004) Temperature dependence of structure and mechanical properties of Ti-Si-N coatings. Surf Coat Technol 177 (178):325–333

Zhu T, Li J, Ogata S, Yip S (2008) Mechanics of ultra-strength materials. MRS Bull 34:167–172

Zinin P, Manghnani MH, Tkacev S, Askarpour V, Lefeuvre O, Every A (1999) Brillouin spectroscopy of surface modes in thin-film Si_3N_4 on GaAs. Phys Rev B 60:2844–2850

Chapter 5
Fracture Toughness of Hard and Superhard Materials: Testing Methods and Limitations

Dr. Declan Carolan and Prof. Alojz Ivankovic

Abstract This chapter reviews the most important testing techniques for determination of fracture toughness in use today. A discussion of the merits and demerits of each technique is provided. A brief introduction into Linear Elastic Fracture Mechanics is provided. Finally a brief discussion of the statistical nature of the strength of superhard materials is introduced.

1 Introduction

Hard and superhard materials are promising engineering materials possessing very high strength and hardness in comparison to many metals and steels. In addition they typically possess very high melting points and, with the notable exception of diamond-based materials, maintain excellent chemical stability at elevated temperatures. However, their low resistance to fracture limits their reliability as an engineering material. Typical values for the fracture toughness of superhard materials are in the range of 1–12 MPa $m^{½}$.

Fracture toughness is a measure of a material's ability to resist crack initiation and propagation from a pre-existing flaw. Largely unheard of before World War II, it is now a fundamental topic of study for mechanical engineers. The brittle nature of ceramics and hard materials results from their mixed ionic–covalent bonding, which provides only a limited number of independent slip systems that are necessary to achieve the homogeneous plastic deformation observed in metallic materials (Kingery et al. 1976; Sakai and Bradt 1993). As a result of this inherent brittleness,

Dr. D. Carolan (✉)
ELEVATE Marie Curie Research Fellow, Department of Mechanical Engineering, Imperial College London, London, UK
e-mail: d.carolan@imperial.ac.uk

Prof. A. Ivankovic
Professor of Engineering Mechanics, School of Mechanical and Materials Engineering, University College Dublin, Dublin, Ireland
e-mail: alojz.ivankovic@ucd.ie

V. Kanyanta (ed.), *Microstructure-Property Correlations for Hard, Superhard, and Ultrahard Materials*, DOI 10.1007/978-3-319-29291-5_5

a crack in a brittle material is usually considered to extend through a stepwise bond rupture process (Lawn 1983). Brittle fracture is defined by Knott as the onset of unstable crack growth when the applied stress is below the yield stress of a material (Knott 1973). In reality, however, even the most brittle materials undergo some small-scale yielding close to the crack tip.

There are two main types of fracture in polycrystalline superhard materials, transgranular and intergranular. In transgranular fracture, as the name suggests, the crack travels through the grain of the material. The fracture can change direction from grain to grain due to the difference in orientation of the preferential slip planes of the individual crystals. Intergranular fracture occurs when the crack travels along the grain boundaries.

Brittle fracture is associated with small deformation. Consequently LEFM is usually appropriate without the need for recourse to the more computationally demanding theories of elastic plastic fracture mechanics.

1.1 Energy Balance Approach to Fracture

The first breakthrough in fracture mechanics came from A.A. Griffith with his classic paper in 1921 (Griffith 1921). Griffith considered a single crack in an infinite medium based on the earlier solution of Inglis (1913). He showed that the dichotomy between the theoretically predicted strength of a material based on a direct calculation of the cohesive forces between the atoms or molecules of a material and the experimentally measured strengths (which are orders of magnitudes lower) could be explained by the presence of microscopic cracks and flaws, which act as stress concentrators.

The 1913 paper of Inglis studied the stress concentration effect of an elliptical hole, with semimajor axis, a, and semiminor axis, b, in an infinite flat plate subject to a remote tensile loading (Fig. 5.1). He developed an expression relating the stress distribution at the tip of the major axis to the remote stress, σ, as

$$\sigma_y = \sigma\left(1 + \frac{2a}{b}\right) \tag{5.1}$$

As the semiminor axis, b, approaches zero, the hole begins to approximate a sharp crack and Eq. (5.1) is more conveniently represented in terms of the radius of curvature $r = b^2/a$:

$$\sigma_y = \sigma\left(1 + 2\sqrt{\frac{a}{\rho}}\right) \tag{5.2}$$

It can be clearly seen that as r approaches 0, the predicted stress at the tip of the crack becomes infinite. This is clearly a concerning result and motivated Griffith to develop his theory based on energy rather than stress.

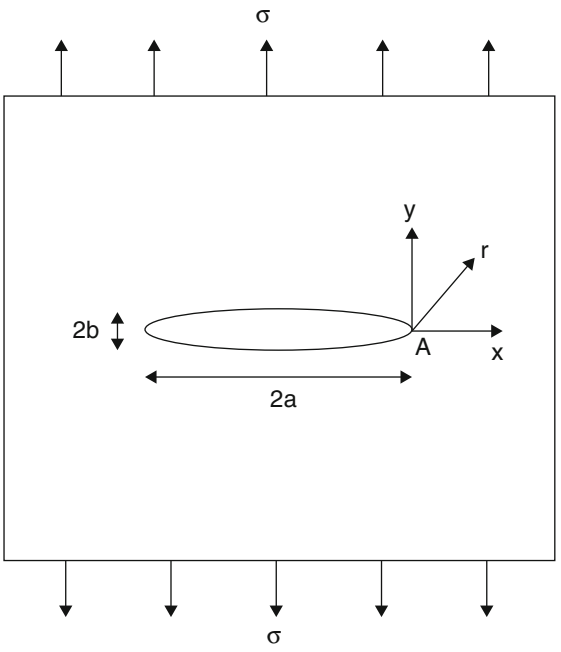

Fig. 5.1 Inglis' solution for the stress distribution around an elliptical hole in an infinite plate

The Griffith and later Orowan (1948) criterion for fracture states that crack growth can only occur if the energy required to extend a crack of length a in a system by an infinitesimal length da can just be delivered to the system. Applying the conservation of energy to an arbitrary control volume,

$$\mathrm{d}U_e = \mathrm{d}U_d + \mathrm{d}U_s + \mathrm{d}U_k \tag{5.3}$$

Note that in Eq. (5.3), $\mathrm{d}U_e$ represents the external energy supplied to the control volume, $\mathrm{d}U_d$ represents the energy that is irreversibly dissipated at the crack tip including the surface energy of the newly formed crack and plastic work, $\mathrm{d}U_s$ represents the change in elastic potential energy and $\mathrm{d}U_k$ represents the change in kinetic energy. If the crack then grows by an infinitesimal area dA, then we can write

$$\frac{\mathrm{d}U_e}{\mathrm{d}A} = \frac{\mathrm{d}U_d}{\mathrm{d}A} + \frac{\mathrm{d}U_s}{\mathrm{d}A} + \frac{\mathrm{d}U_k}{\mathrm{d}A} \tag{5.4}$$

where $\mathrm{d}U_d/\mathrm{d}A$ is defined as the fracture resistance of the material, R_f. The reduction in elastic potential energy due to this crack growth is defined as the strain energy release rate, G_I. Upon crack initiation $U_k = 0$ and $\mathrm{d}U_k/\mathrm{d}A = 0$ for a quasi-static crack (for a dynamic crack, $\mathrm{d}U_k/\mathrm{d}A \geq 0$), and so for fracture to occur, we require $G_I - R_f \geq 0$. Therefore, fracture occurs when $G_I \geq R_f$. This is termed the critical strain energy release rate, G_{Ic}, and is a material property at a given loading rate and temperature.

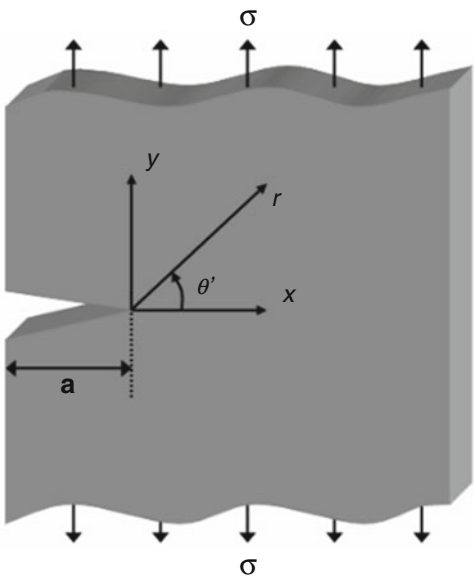

Fig. 5.2 Edge crack in a semi-infinite plate subject to a remote tensile stress

1.2 Stress-Intensity Factor Approach

An alternative approach to fracture assuming linear elastic was proposed by Irwin in 1956 (Irwin 1956) and considers the stress field associated with the crack tip. A semi-infinite plate with a crack subject to a remote mode I (opening) tensile loading is considered as shown in Fig. 5.2. The stress fields in the immediate vicinity of the crack tip can be expressed as

$$\sigma_{ij} = \frac{K_I}{\sqrt{2\pi r}} f_{ij}(\theta) \tag{5.5}$$

where σ_{ij} are the components of the stress tensor at the point of interest, r and θ are the polar coordinates of the point and f_{ij} is a function of θ. K_I is termed the mode I stress-intensity factor and is a parameter which gives the magnitude of the elastic stress field at the crack tip. Westergaard (1939) has previously shown that for a plate of thickness W containing a sharp crack under an applied remote stress σ_0, the stress function that relates σ_0 to the local field in the vicinity of the crack tip is of the form

$$\sigma_{ij} = \sigma_0 \left(\frac{a}{2r}\right)^{1/2} f_{ij}(\theta) \tag{5.6}$$

Combining Eqs. (5.5) and (5.6), it can be seen that

$$K_I = \sigma_0 \sqrt{\pi a} \tag{5.7}$$

A more general expression to account for the effect of finite geometries can be derived as

$$K_I = \sigma_0 \sqrt{\pi a} f\left(\frac{a}{W}\right) \tag{5.8}$$

where $f\left(\frac{a}{W}\right)$ is a dimensionless parameter that depends on the geometry of the test piece, W, and of the crack, a. Closer examination of Eq. (5.6) reveals that the stress is proportional to $1/\sqrt{r}$ and as r.

Following the above analysis, it can be shown that the stress-intensity factor approach to fracture mechanics is equivalent to the energy-based approach outlined in Sect. 1.1 For a cracked body under mode I loading, the relationship can be expressed as

$$G_{Ic} = \frac{K_{Ic}^2}{E^*} \tag{5.9}$$

where $E^* = E$ for plane stress and $E^* = E/(1 - \upsilon^2)$ for plane strain.

2 Standard Fracture Toughness Test Methods for Hard Materials

In comparison with other materials such as metals and polymers, ceramics and hard materials are rather brittle. This coupled with their high stiffness makes them difficult to obtain reliable data. Fracture toughness is usually the limiting factor in the use of superhard materials.

Several experimental test methods exist for the determination of fracture toughness of hard materials. These methods vary as to ease of use, costliness, reproducibility and appropriateness of the calculated fracture toughness. The basic procedure for the measurement of fracture toughness involves three steps:

- Generation of a precrack in a test specimen
- Measurement of the failure load
- Calculation of the critical stress-intensity factor, K_{Ic}

In order to help standardise the measurement of fracture toughness for ceramics and hard materials, the European Structural Integrity Society's Technical Committee for ceramics recently carried out a round robin (Primas and Gstrein 1997). They found that large variations existed between the different test methods, and furthermore, significant variations existed between laboratories for similar tests. This discrepancy was ascribed to the number of uncontrolled parameters during testing.

The round robin found that the most reproducible results were obtained via the chevron-notched beam method (with the proviso of stable crack growth), the surface crack in flexure method and the single-edge notched beam method (provided the notch width is below a critical notch width).

Moreover, the ASTM standard for determining the fracture toughness of ceramics suggests the use of the single-edge precracked beam, chevron-notched beam and the surface crack in flexure methods in either three- or four-point bending. Interestingly, it is also explicitly stated in this standard that the reported fracture toughness values would differ depending on the method used.

Finally Morell (2006) reviewed the progress in fracture toughness testing methods for ceramics widely reported in the literature. He concludes that only the single-edge precracked beam, chevron-notched beam, surface crack in flexure and single-edge V-notched beam are appropriate for standardisation. A number of other test geometries, e.g. double cantilever beam (Nicholson 1990; Sørenson et al. 1996), short rod chevron notch (Bubsey et al. 1982) and double torsion (Lin et al. 1994), which although satisfactory from a fracture mechanics point of view, are excluded due to the difficulty and expense in producing satisfactory test specimens.

It is therefore clear that there is still some uncertainty regarding the most appropriate method of establishing the fracture toughness of a superhard material. The rest of this chapter critically reviews the most promising methods.

2.1 Single-Edge Precracked Beam (SEPB)

The single-edge precracked beam is based on a flexural strength test piece in which a sharp precrack has been introduced at the midspan. Generation of the precrack is key, and there are four main methods in the literature to do this: bridge loading, stiff loop precracking, fatigue precracking and wedge precracking.

2.1.1 Bridge Precracking

The bridge precracking technique was originally developed in Japan (Nunomura and Jitsukawa 1978) and has since been widely adopted by a number of researchers (Nose and Fujii 1988; Warren and Johannsen 1984; Bar-On et al. 1990). In this method a small notch or line of indentations introduced by a Vickers indenter is placed on one face of a rectangular prism flexural strength specimen as shown in Fig. 5.3. The specimen is then compressed between two anvils. The top anvil is flat, while the bottom anvil has a small gap under the prenotch. Upon compressing a local tensile stress is induced in the specimen ahead of the prenotch. At a certain critical load, a crack develops ahead of the prenotch. The constraining global

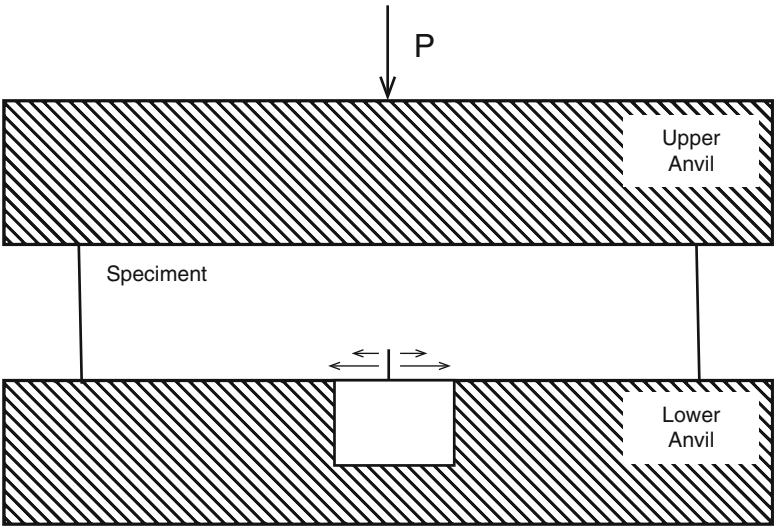

Fig. 5.3 Schematic of bridge indentation precracking method (adapted from Nose and Fujii (1988))

compressive stress field permits the crack to 'pop' and then stop before completely fracturing the specimen. Detection of this crack is usually achieved with an acoustic sensor.

The introduction of a straight crack is the main difficulty with this method as any slight misalignment can result in angled cracks. A variation of this technique that involves axial compressive loading combined with flexural impact has been reported successfully for tool steels (Eriksson 1975; Wronski et al. 1988) although it has not been reported for hard materials yet.

2.1.2 Stiff Loop Precracking

The stiff loop precracking method, as the name suggests, involves careful bending of the sample in a mechanically stiff system such as the one suggested by Morell and Parfitt (2005) or Fett et al. (1995). Their system had a frame compliance of 3 mm/kN at a compressive load of 5 kN. They successfully applied the method to both chevron and V-notched ceramics although they note that it was unsuccessful in introducing precracks in the stiffer hard metals. However, they suggest that either a redesign of the facility or a modification of the test piece geometry may lead to a further reduction in compliance of the precracking system.

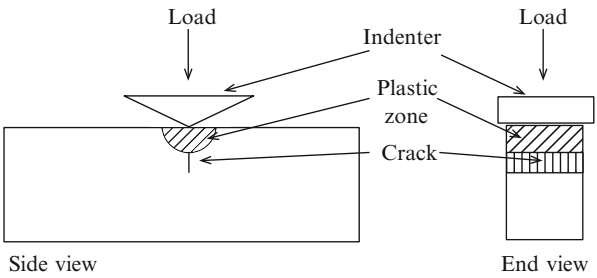

Fig. 5.4 Precracking via wedge indentation after Almond and Roebuck (1978)

2.1.3 Fatigue Precracking

Routinely used for metals and polymers, fatigue precracking has had limited success when applied to ceramics. Suresh et al. (1987) have successfully applied a pulsating compressive load to introduce a precrack into coarse and fine-grained alumina. Achilles (2007) points out the difficulties when this method is applied to stiffer ultrahard materials such as polycrystalline diamond. The closeness of ΔK_{th} to K_{Ic} means that extremely precise control of the test machine is required in order to avoid complete failure and loss of the specimen.

2.1.4 Wedge Precracking

Precracking of hard metals via wedge indentation has been suggested by Almond and Roebuck (1978). This method is similar to the introduction of surface cracks via Vickers indentation, the difference being that the wedge indenter introduces a planar crack extending from the indented face of the specimen. This is clearly shown in Fig. 5.4.

Upon preparing a batch of precracked specimen, they can then be tested to failure using the conventional three- or four-point bending fracture toughness test.

2.2 Chevron-Notched Bend (CNB) Test

The chevron-notched bend specimen is a well-established method to measure the fracture toughness of brittle ceramic materials (Reddy et al. 1988, more refs here). The chevron-notched bend test has been adopted as both an ASTM standard (ASTM 2001) and an ISO standard (ISO 2005). The chevron notch is a V-shaped ligament as shown in Fig. 5.5.

One of the main advantages of the CNB specimen is that they require no precracking. The specimen produces the sharp crack during loading. Furthermore, the extremely high stress concentration at the tip of the chevron notch ensures that the crack initiates at a low applied load, and the profile of the chevron notch dictates

that the stress-intensity factor passes through a minimum as the crack grows. The fracture toughness can be directly measured from the maximum test load, and a complete record of load and displacement or crack length is not strictly required.

Typical load–displacement curves resulting from an experimental test are shown in Fig. 5.6. In order for a test to be valid, the load–displacement curve must exhibit a smooth maximum (Fig. 5.6a); crack pop-in and subsequent stable crack growth as shown in Fig. 5.6b are also considered valid tests. A sharp drop-in load however is indicative of an invalid test, and fracture toughness calculations made using this data will overestimate the fracture toughness.

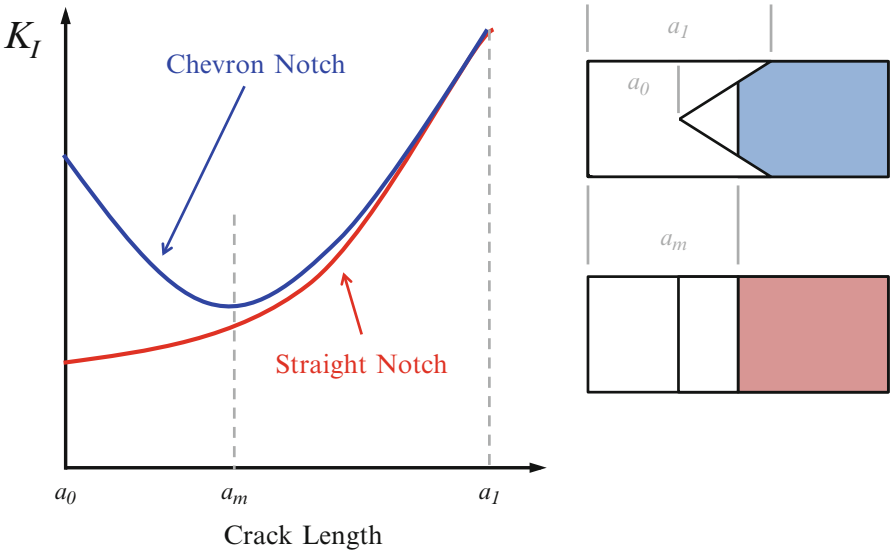

Fig. 5.5 Comparison of stress-intensity factor with crack length for chevron- and straight-notched specimens. Note the minimum KI for the chevron-notched specimens (adapted from Anderson 2005)

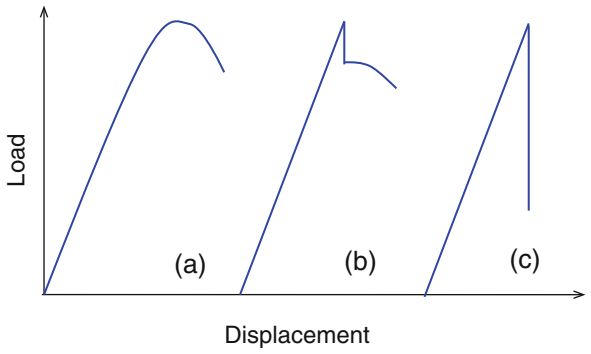

Fig. 5.6 Typical load–displacement curves obtained during chevron-notched bend tests

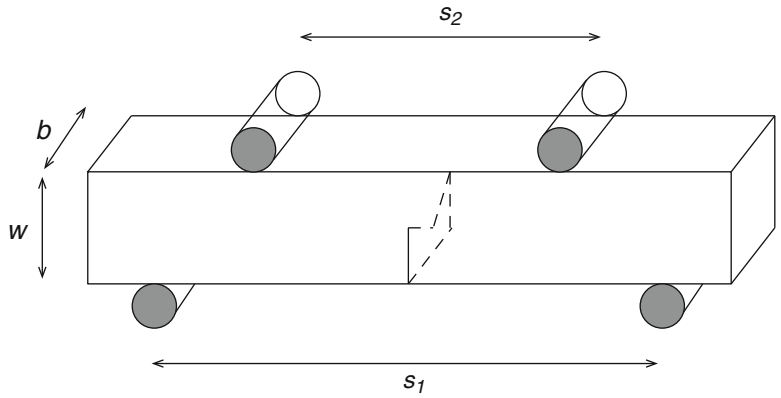

Fig. 5.7 Four-point bending specimen with chevron notch

The non-linearity in the load–displacement curve is caused by the crack propagation along the chevron notch. The fracture toughness can be calculated via

$$K_{Ic} = \frac{F}{b\sqrt{w}} Y^* \tag{5.10}$$

where F is the load to failure, b is the width of the specimen and w is the height. Y^* is a geometric function known as the minimum stress-intensity coefficient which depends on the precise specimen and notch geometry used in the experiment. Munz et al. (1980) have determined the following for the four-point bending specimen shown in Fig. 5.7:

$$Y^* = \left(3.08 - 5.00\alpha_0 + 8.33\alpha_0^2\right)\left(1 + 0.007\sqrt{\frac{s_1 s_2}{w^2}}\right)\frac{\alpha_1 - \alpha_0}{1 - \alpha_0}\frac{s_1 - s_2}{w} \tag{5.11}$$

where s_1 and s_2 are the inner and outer roller distance, $a_0 = a_0/w$ and $a_1 = a_1/w$. Equation 5.11 is valid for $0.12 \leq a_0 \leq 0.24$ and $0.9 \leq a_1 \leq 1$.

2.3 Indentation Fracture (IF)

Chantikul et al. (1981) and Anstis et al. (1981) proposed an indentation fracture toughness measurement method for ceramic materials. Two different methods were proposed by these authors—(i) a direct crack measurement and (ii) an indirect method. The indirect method uses an indenter to initiate a small crack in a sample and then submit it to three- or four- point bending. K_{Ic} is computed from indentation

load, P, and the bending strength σ_c of the indented specimen. Chantikul et al. (1981) give the following empirical formula:

$$K_{Ic} = 0.59\left(\frac{E}{H}\right)^{1/8}\left(\sigma_c P^{1/3}\right)^{3/4} \tag{5.12}$$

The product $\left(\sigma_c P^{\frac{1}{3}}\right)$ should be independent of P. The indirect indentation fracture test is similar to the surface crack in flexure test discussed in Sect. 2.4. However in the SCF test, the stress field due to the indentation is removed, whereas in the indirect indentation test, it is accounted for in the mathematics of the K_{Ic} equation.

Chantikul and co-worker's direct method, also called simply the Vickers indentation fracture (VIF) test (Quinn and Bradt 2007), has been widely used to estimate the fracture toughness of ceramics and hard materials over the last 40 years. Palmqvist (1957) was the first to advocate the cracks formed via indentation. Palmqvist's concept was later developed into a fracture toughness test by Evans and Charles (1976). The original equation was first refined by Marshall and Evans (1981) and then by Anstis et al. (1981). Niihara (1983, 1983a) has published an alternative equation designed to specifically address the issue of Palmqvist cracks. In this chapter we concentrate on the equation presented by the group of Chantikul and Anstis as it appears to be the most widely adopted in the literature.

The direct method calculates the hardness, H, from the shape of the indents shown in Fig. 5.8 and uses this value to calculate the fracture toughness:

$$H = \frac{P}{\alpha a^2} \tag{5.13}$$

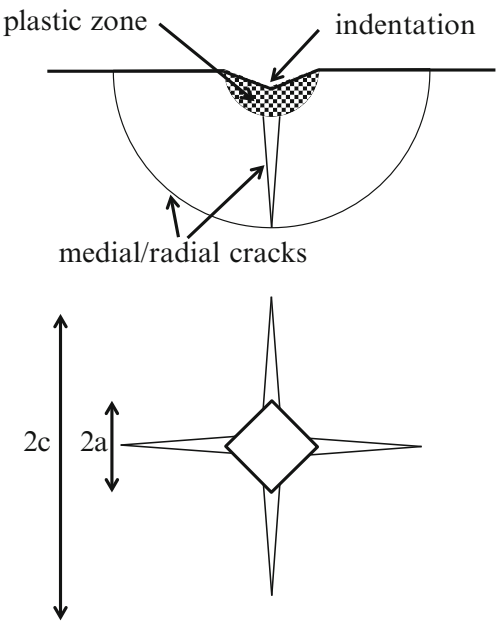

Fig. 5.8 Cracking around a hardness indentation. After Wachtman et al. (2009)

where a is a numerical factor, equal to 2 for a Vickers indent, and P is the applied load. The fracture toughness is then calculated via

$$K_{Ic} = \frac{\zeta\left(\frac{E}{H}\right)^{1/2} P}{c^{3/2}} \tag{5.14}$$

where ζ is a dimensionless constant, E is the Young's modulus and P is the indentation load. Primas and Gstrein (1997) note that the accuracy of crack length measurements using this technique is highly dependent on both the equipment and the subjectivity of the scientist carrying out the test. Hence, this method is particularly susceptible to error. Furthermore, following the work of Carolan (2011), it was found that the indentation fracture method was particularly unsuitable for superhard materials specifically PcBN. In a recent review, Quinn and Bradt (2007) conclude that there is no one equation that can satisfy the expected fracture results for a number of materials. They definitively conclude 'the VIF method should not be used for fracture toughness testing, even if just for a comparative basis'. Nevertheless, the simplicity of the technique means that it continues to be widely used in the literature despite the mounting evidence that it is unsuitable as a fracture toughness test method.

2.4 Surface Crack in Flexure

The surface crack in flexure was first suggested by Petrovic and Mendiratta (1979). It provides a flaw that is closest to the size of flaws commonly found in components. The precracks can be introduced using preferably a Knoop indenter, although a Vickers indenter can also be used. The long axis of the Knoop indenter should be aligned across the sample test piece. Sufficient force should be applied so as to ensure that a halfpenny crack is formed.

The indentation procedure produces a compressive residual stress field around the indent. This is removed by surface grinding. It is recommended that the surface layer to be removed be typically between 4.5 and 5 times the depth of the indent (ISO 2003).

The sample is then fractured in four-point bending. Identification of the initial crack size is conducted post mortem and can require some skill and experience on the part of the individual. Quinn et al. (1994) suggest that angling the indenter at a small angle (~1/2°) to the specimen surface can significantly improve the detection of the initial crack. A typical initial crack is shown in Fig. 5.9 (Quinn 2007).

The fracture toughness in four-point bending is calculated via the following expression:

$$K_{Ic} = Y\left(\frac{3P_{\max}(s_0 - s_1)}{2bw^2}\right)\sqrt{a} \tag{5.15}$$

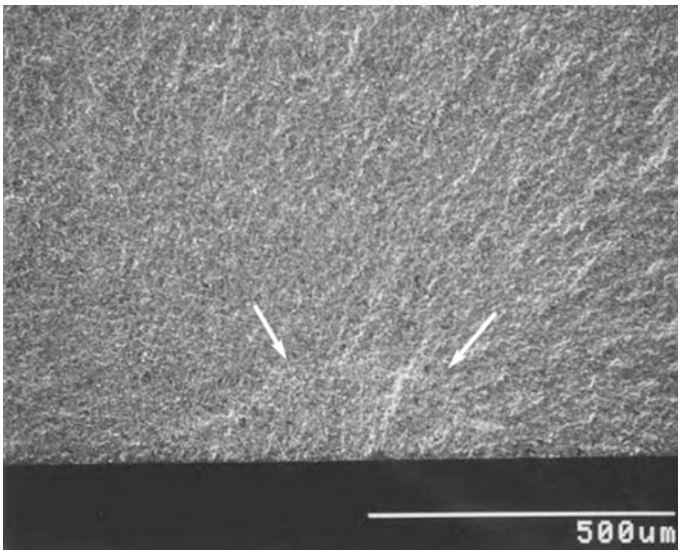

Fig. 5.9 Surface crack in flexure in silicon nitride (taken from Quinn 2007). The *arrows* indicate the extent of the initial crack

where $P_{\max}$ is the maximum load during the test, a is the initial crack depth and b and w are the width and depth, respectively. s_0 and s_1 are the outer and inner spans of the four-point bend test. The stress-intensity coefficient Y varies around the crack. In general Y is calculated at the surface of the crack and at the maximum depth of the crack and the larger of these two values is used in Eq. (5.15). Newman and Raju (1981) provide the equations to calculate Y.

At the specimen surface,

$$Y = \sqrt{\pi}\frac{M}{\phi}H_1\sqrt{\left(\frac{a}{c}\right)(1.1 + 3.5\alpha^2)} \tag{5.16}$$

At the maximum depth of the crack,

$$Y = \sqrt{\pi}\frac{M}{\phi}H_2 \tag{5.17}$$

The quantities H_1, H_2, M and ϕ are given by

$$H_1 = 1 - \left[0.34 + 0.11\left(\frac{a}{c}\right)\right]\alpha \tag{5.18}$$

$$H_2 = 1 - \left[1.22 + 0.12\left(\frac{a}{c}\right)\right]\alpha + \left[0.55 - 1.05\left(\frac{a}{c}\right)^{\frac{3}{4}} + 0.75\left(\frac{a}{c}\right)^{\frac{3}{2}}\right]\alpha^2. \tag{5.19}$$

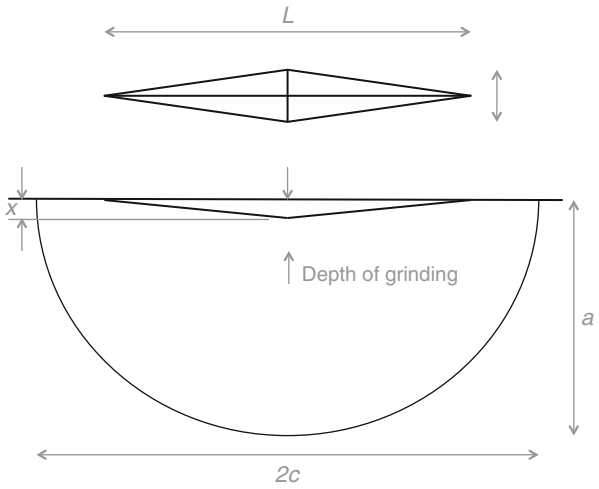

Fig. 5.10 Geometrical data for a Knoop indentation with halfpenny crack

$$M = 1.13 - 0.09\left(\frac{a}{c}\right) + \left[-0.54 + \frac{0.89}{0.2 + \frac{a}{c}}\right]\alpha^2 + \left[0.5 - \frac{1}{0.65 + \left(\frac{a}{c}\right)} + 14\left(1 - \left(\frac{a}{c}\right)^{24}\right)\right]\alpha^4. \tag{5.20}$$

$$\phi \cong \left[1 + 1.464\left(\frac{a}{c}\right)^{1.65}\right]^{\frac{1}{2}} \tag{5.21}$$

The geometrical terms in the above equations are as shown in Fig. 5.10. a has its usual meaning, $a = a/W$.

The surface crack in flexure with Knoop indentation has also been used by a number of researchers to investigate mixed mode fracture (Petrovic and Mendiratta 1976; Marshall 1984; Petrovic 1985; Gopalakrishnan and Mecholsky 2013). In this test the Knoop surface flaw is placed on the tensile surface at an angle α.

2.5 *Double-Torsion Test*

The double-torsion specimen was first proposed by Outwater et al. (Outwater and Austin 1969; Outwater et al. 1974) for epoxy materials. It is a popular choice for measuring the subcritical crack growth of ceramic and superhard materials, e.g. alumina (Venikis et al. 1990; Ebrahimi et al. 2000), zirconia (Gremillard et al. 2000), silicon carbide (Govila 1980) and polycrystalline diamond (Lin et al. 1994). It has the advantage of simple and low-cost specimen geometry (Fuller 1979). The measurement of K_{Ic} is crack length independent; the crack extension is

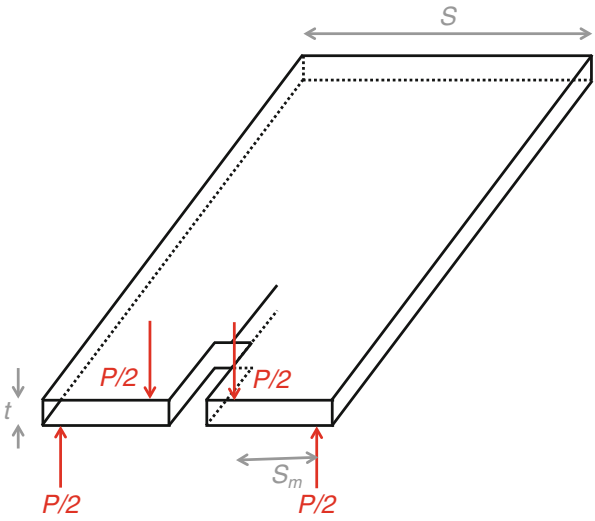

Fig. 5.11 Schematic of double-torsion specimen

monitored in terms of changes in compliance. Moreover, the simplicity of the test allows for scaling up of the test, meaning that it has also found use in the field of concrete and rock mechanics research (Hillerborg 1983; Kim and Partl 2012; Ciccotti et al. 2000, 2001).

A schematic of the double-torsion test is given in Fig. 5.11 (Freiman and Mecholsky 2012; Shyam and Lara-Curzio 2006). The elastic strain energy as the crack propagates, G_I, is given by

$$G_I = \frac{3P^2S_m^2}{2St^4G_s\varphi} \tag{5.22}$$

where G_s is the shear modulus, P is the load and S_m, S and t are as defined in Fig. 5.11. φ is a function determined by Fuller (1979) and is given by

$$\varphi = 1 - 0.6302\left(\frac{2t}{S}\right) + 1.20\exp\left(\frac{-\pi S}{2t}\right) \tag{5.23}$$

Finally assuming plane strain, the mode I critical stress-intensity factor can be written as

$$K_I = PS_m\left[\frac{3(1+\upsilon)}{St^4\varphi}\right]^{1/2} \tag{5.24}$$

2.6 Diametral Compression Test

The cracked Brazilian disc test or diametral compression test first found application in the area of rock mechanics (Carniero and Barcellos 1953; Yarema and Krestin 1966) and has subsequently been applied to ceramics (Awaji and Sato 1978; Shetty et al. 1985) and even polymers (Zhou et al. 2006). One of the principal advantages of this test is that it can be used to find the fracture toughness for a range of mode mixities.

The typical loading arrangement is given in Fig. 5.12. It consists of a cylindrical specimen with radius, R, with a crack of length $2a$ passing through the central diameter of the specimen. The angle of the precrack with reference to the loading direction dictates the mode mixity. The methods of introducing a precrack are the same as for the various flexural specimens although a chevron notch is usually preferred. The fracture toughness is given by

$$K_{I,II} = Y_{I,II}\sqrt{a}\frac{P}{\pi R b} \tag{5.25}$$

where K_I and K_{II} are the mode I and mode II stress-intensity factors, respectively, and b is the thickness of the cylindrical specimen. A number of authors (Awaji and Sato 1978; Atkinson et al. 1982; Xu 1995) have computed the stress-intensity factors, Y_I and Y_{II}, for an extensive range of $a/R$and crack inclination angles. They demonstrate that pure mode II results can be obtained for a small crack inclined at an angle of 30 to the loading direction. Pure mode I can be obtained at a crack inclination angle of 0 as shown in Fig. 5.12.

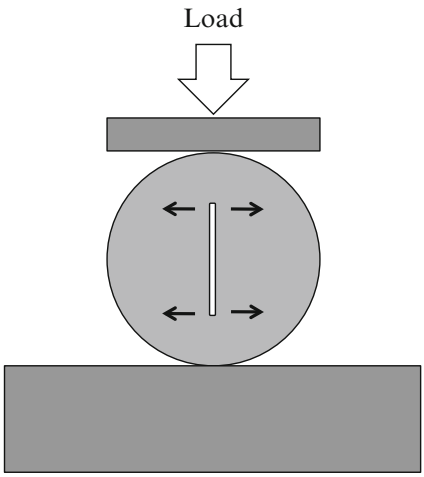

Fig. 5.12 Geometry of diametral compression test

2.7 *Single-Edge Notched Bend (SENB) and Single-Edge (V-) Notched Bend (SE(V)NB) Tests*

Due to the extreme hardness of PCD and PCBN, it is often difficult to introduce a sharp precrack into a specimen without completely fracturing the specimen.

A number of researchers have proposed a single-edge V-notched bend with a sharpened crack introduced via a honing procedure (Damani et al. 1996; Gogotsi 2000; Rocha and daCosta 2006; Carolan et al. 2011). This technique consists of introducing a relatively blunt notch via a conventional machining process such as milling or electro-discharge machining and subsequently sharpening and extending the notch with a razor blade embedded in a paste of diamond grit to produce a much finer notch with a very sharp root radius (Lammer 1988). An example of such a honing apparatus is given in Fig. 5.13, while an example of a notch produced by this honing procedure in a fine-grained polycrystalline cubic boron nitride is given in Fig. 5.14.

Early works by Damani et al. (1996) and Nishida et al. (1994) have shown that for a polycrystalline ceramic, a notch root radius of less than 10 μm can simulate a sharp crack. Kübler (2002) empirically demonstrated that the measured fracture toughness values in an SEVNB test are true fracture toughness values if the notch root radius is less than twice the characteristic length of a major microstructural feature. For values above this critical notch root radius, the measured fracture

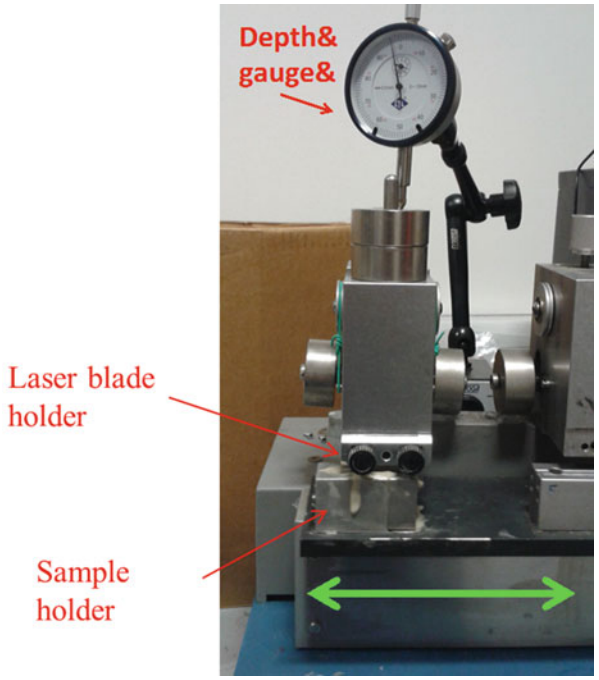

Fig. 5.13 Diamond slurry honing apparatus (image courtesy Element Six Ltd.)

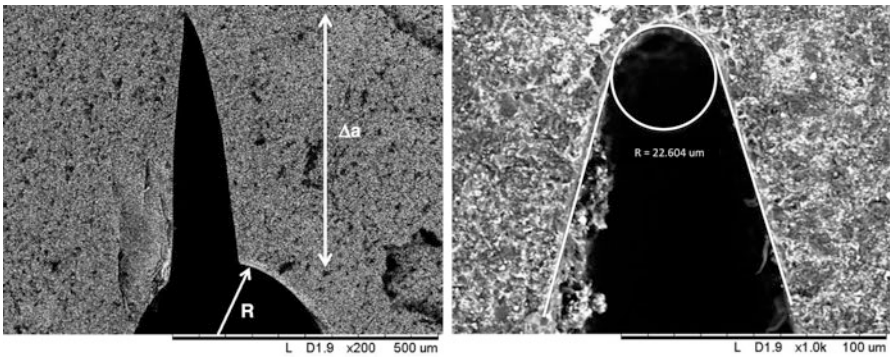

Fig. 5.14 SEM micrograph of honed notch in polycrystalline cubic boron nitride showing the original notch at the bottom of the figure (*left*). A close up of the honed notch tip can be seen on the *right*. The notch root radius of the honed was 22.6 μm (Carolan et al. 2011)

toughness was observed to increase linearly with the square root of the notch root radius, R_c. Mathematically this is expressed as

$$K_b = K_{Ic} \qquad R \leq 2d \tag{5.26}$$

$$K_b = K_{Ic} + m(R_c - 2d)^{1/2} \qquad R > 2d \tag{5.27}$$

where K_b is the experimentally measured (or apparent) fracture toughness. K_{Ic} is the true material fracture toughness, R is the radius of the notch tip and d is the characteristic microstructural length suggested by Kübler. The slope m can be interpreted as the sensitivity of the material to the overestimation of fracture toughness with increasing notch bluntness.

The systematic overestimation of fracture toughness above the critical notch root radius led researchers to explore the role of the length scale in fracture of blunt-notched materials. The theory of critical distances is one such fracture theory. The TCD is a modification of conventional LEFM, in which the mechanics at the microstructural level are represented by the introduction of a material length scale (Taylor 1996).

2.7.1 Theory of Critical Distances

Neuber (1958) and Peterson (1959) first formulated the fundamental ideas upon which the theory of critical distances is based. They applied the theory to predict the fatigue failure of metallic components. The theory is notable for having been 'discovered' numerous times since this early work. For example, Whitney and Nuismer (1974) proposed an equivalent method to TCD to predict the effect of circular holes on the failure strength of fibre-reinforced composite laminates.

Later Taylor and co-workers developed these relationships and successfully applied them to a number of different materials (Taylor 1996, 1999, 2004, 2006;

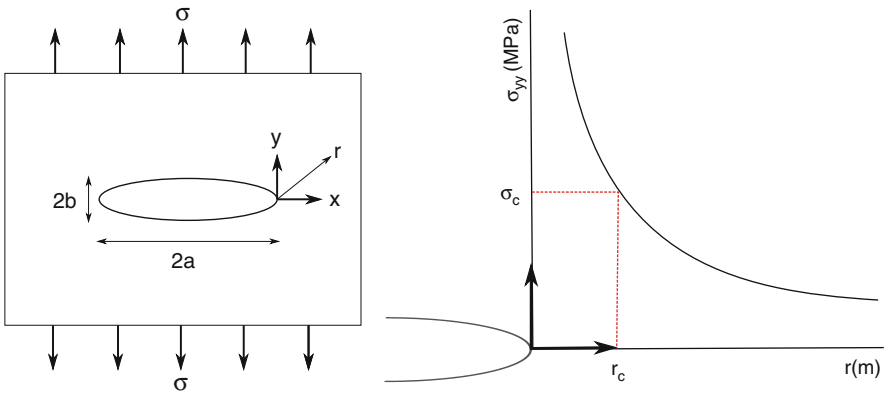

Fig. 5.15 Elliptical hole in a plate and typical stress distribution ahead of the notch

Taylor et al. 2005). Taylor's group coined the term 'theory of critical distances' as an umbrella term for all the 'stress at a distance' approaches in the literature.

The theory of critical distances essentially states that failure occurs when some critical stress is exceeded at some critical distance. For brittle superhard materials, where failure usually occurs in a brittle manner, this critical stress can be assumed to be equal to the ultimate tensile or flexural strength of the material. There are a number of methods used for calculating the critical distance, including the point method, line method, area method and volume method.

As discussed previously, we expect that our measure of fracture toughness will be systematically overestimated due to the large notch root radius in an SENB test. The effect of this notch on the measured fracture toughness can be quantified using a critical distance approach. Returning to Inglis' classical analysis of an elliptical hole in a plate as shown in Fig. 5.15, we consider the local elastic stress, σ_{yy}, a small distance, r, from the tip of the notch. As before, the radius of curvature is $R = b^2/2a$. The local stress can then be written as

$$\sigma_{yy} = \sigma a^{1/2} \frac{2R + 2r}{(R + 2r)^{3/2}} \tag{5.28}$$

where σ is the applied normal stress removed from the notch and r is the distance ahead of the notch tip as shown in Fig. 5.15. For an infinitely sharp notch, $R = 0$ and Eq. (5.28) reduces to

$$\sigma_{yy}(2\pi r)^{1/2} = \sigma(a)^{1/2} \tag{5.29}$$

and the stress intensity at the crack tip is

$$K_I = \sigma_{yy}(2\pi r)^{1/2} = \sigma(a)^{1/2},\ R = 0 \tag{5.30}$$

The interpretation of the fracture criterion is that $\sigma_{yy} = \sigma_c$ and $r = r_c$ at fracture, i.e. fracture will occur when the stress at a some characteristic distance ahead of the crack tip exceeds the intrinsic strength of the material. The value of $= \sigma_c$ and $r = r_c$ should be independent of the geometry of the system (Susmel and Taylor 2010). We can then write the fracture criterion

$$K_{Ic} = \sigma_c (2\pi r_c)^{1/2}, \quad R = 0 \tag{5.31}$$

Now returning to the fracture of an SENB sample with a notch root radius, $R > R_c$, and incorporating Eq. (5.28), we have

$$K_{Ic} = \sigma_c (2\pi r_c)^{1/2} = \sigma(a)^{1/2} \frac{1 + \frac{R}{r_c}}{\left(1 + \frac{R}{2r_c}\right)^{3/2}} \tag{5.32}$$

Equation gives the relationship between toughness, notch root radius and a characteristic length of a material, where the characteristic length, r_c, appears explicitly with the geometric quantity R.

Now experimentally the fracture toughness of a blunt-notched sample, K_b, is measured as

$$K_b = \sigma(a)^{1/2} \tag{5.33}$$

and the real fracture toughness can be expressed as the product of Kb and a function containing both geometric, R, and material information, r_c:

$$K_{Ic} = K_b \frac{1 + \frac{R}{r_c}}{\left(1 + \frac{R}{2r_c}\right)^{3/2}} \tag{5.34}$$

Carolan et al. (2011) have proposed a method to estimate the critical fracture toughness of superhard materials based on the measurement of blunt-notched fracture toughness from a number of specimens with different notch root radii. This is particularly useful in the case of PCBN and PCD materials where the time and cost effort required to hone a sharpened notch are often prohibitive. For softer ceramic materials, honing a sharpened notch is not so difficult, and the blunt-notched procedure is overly complicated in this case and testing with a honed notch is recommended.

Figure 5.16 depicts the relationship between the measured fracture toughness of a number of three-point bend samples with varying notch root radii (Carolan et al. 2011). It is clearly noted that the fracture toughness of fine-grained PcBN is highly dependent on the notch root radius, while only a small effect of notch root radius is noted for the coarser grained PcBN. In each case the plotted line is the analytical solution from Eq. (5.34), and the critical distance, r_c, is taken to be equal to the given pre-sintered PcBN grain size.

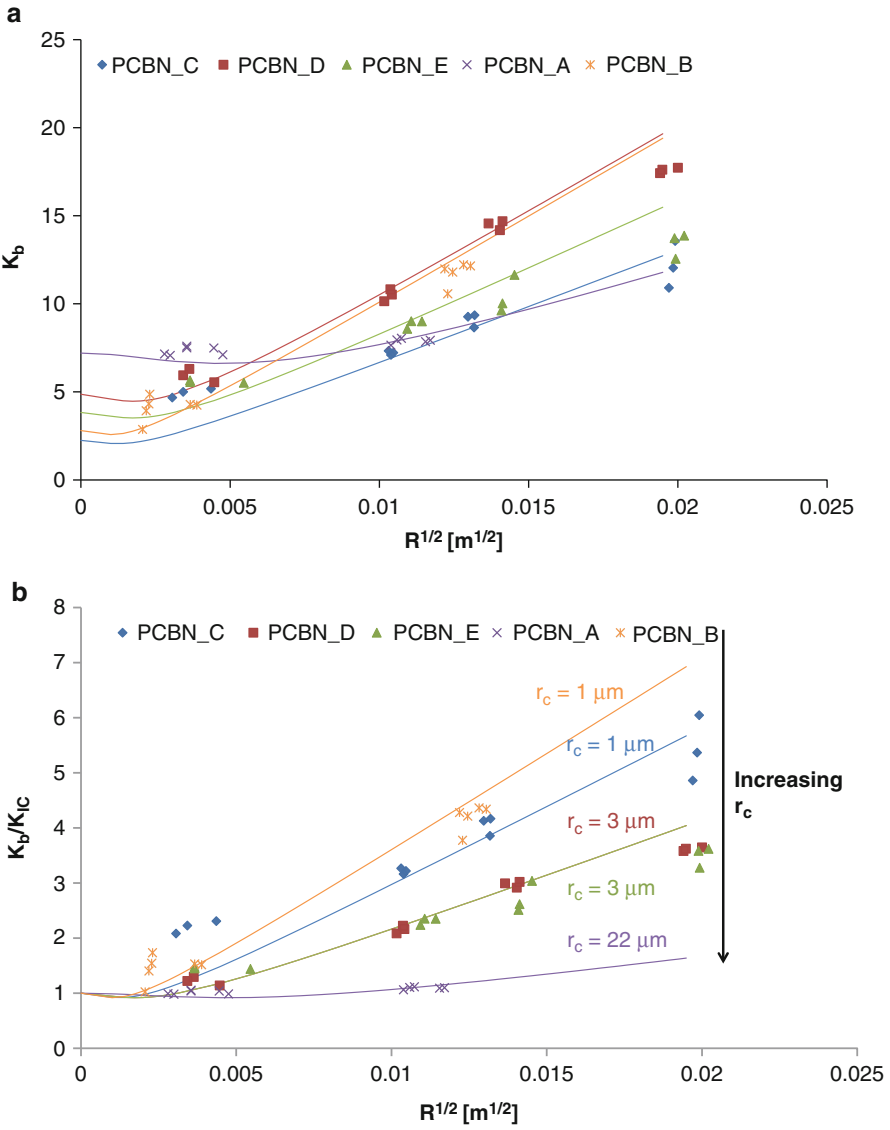

Fig. 5.16 (**a**) Fracture toughness of PCBN as a function of the square root of the notch root radius and (**b**) normalised fracture toughness of PCBN as a function of the square root of the notch root radius (Carolan et al. 2011)

In light of these results, Carolan et al. (2011) proposed that the fracture toughness of an ultrahard material could be measured directly from blunt-notched cracks and prior knowledge of the underlying microstructure. Further works by this group, detailed by Mc Namara et al. (2015), have subsequently suggested in a detailed experimental study on leached and unleached PcD that the choice of grain size as

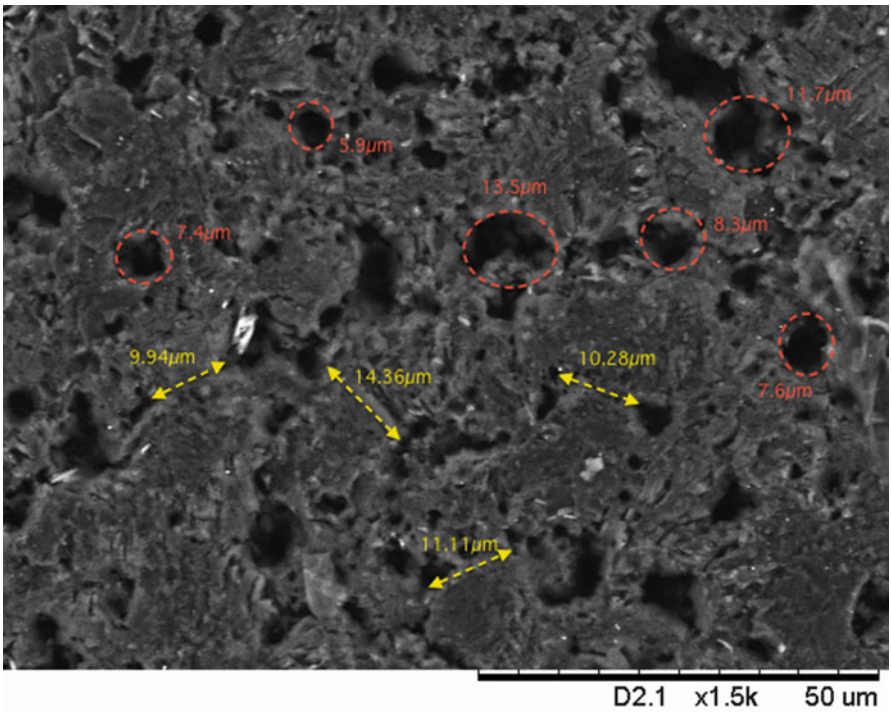

Fig. 5.17 Scanning electron micrograph showing characteristic microstructural length scales for a nominal pre-sintered grain size of 30 µm (McNamara et al. 2015)

the characteristic length is not always the correct choice. They attribute this to the particle crushing, which occurs during the early stage of sintering for large grain sizes, thus making a physical interpretation of r_c difficult to identify. Figure 5.17 shows the variation in possible microstructural length scales for a PcD material with a pre-sintered grain size of 30 µm (McNamara et al. 2015). Furthermore, they show that when the second-phase cobalt material is chemically removed, the dependence of the measured toughness, K_b, on the notch root radius is greatly reduced.

Therefore the blunt notch approach to determining fracture toughness should be applied with care. While it offers a good estimate of fracture toughness for ultrahard materials where the production of a sufficiently sharp crack or notch becomes prohibitively difficult, it is not suggested as a substitute for a properly prepared test specimen as discussed in this chapter. In any case, it is recommended that the user evaluate the measured toughness at a number of different radii and calculate the fracture toughness via a best-fit procedure either analytically or numerically (Carolan et al. 2013).

3 Strength of Superhard Materials

The strength of brittle superhard materials is generally measured in flexure (Lu et al. 2004; Basu et al. 2009) using the three- or four-point bend tests. Strength measurements arising from a series of such tests of nominally identical specimens typically produce a considerable degree of scatter in the results (Weibull 1951). This behaviour can be directly linked to the presence of inherent flaws in the material. These flaws can vary in size position and orientation and can qualitatively explain the observed variation in strength (Lawn 1998; Danzer 2006).

Clearly the large scatter in material strength data has implications for design using superhard materials as the design safe strength is often much less than the average measured strength. Engineers have typically resorted to characterising these strength distributions via statistical means. The Gaussian (or normal), log-normal and Weibull (Weibull 1951) distributions are three commonly used distributions to characterise the scatter in strength data.

3.1 Gaussian Distribution

The Gaussian distribution is a two-parameter model, described by the mean strength, σ_m, and the standard deviation of the measured strengths, σ, of the measured data. It is normalised and described by the probability density function:

$$f(\sigma) = \frac{1}{\sqrt{2\pi}\mu} \exp\left[-\frac{(\sigma - \sigma_m)^2}{2\sigma^2}\right] \tag{5.35}$$

It is a symmetrical distribution and is typically used when all the measured data lies close to the mean.

3.2 Lognormal Distribution

The lognormal distribution is related to the normal distribution, and a variable can be classified as lognormally distributed if the logarithm of the random variable is normally distributed. Unsurprisingly, the probability density function is similar to that of the normal distribution. It is characterised by two parameters, a shape parameter, μ, and a scale parameter σ_m.

$$f(\sigma) = \frac{1}{\sqrt{2\pi}\mu\sigma_m} e^{\left[-\frac{(\log(\sigma)-\sigma_m)^2}{2\sigma^2}\right]} \tag{5.36}$$

The mean m and variance v of a lognormal distribution can be directly calculated from the shape and scale parameters as

$$m = e^{\mu+\sigma^2/2}, \quad v = \left(e^2 - 1\right)e^{2\mu+\sigma^2}$$

3.3 Weibull Distribution

The Weibull distribution is based upon the weakest link hypothesis. This means that failure of any flaw will lead to complete failure of the structure and that there is no interaction between flaws prior to material failure. The Weibull distribution has been traditionally employed to describe the strength distribution of brittle materials (Weibull 1951; Trustrum and Jayatilaka 1983).

Consider a material divided into n equal volume elements δV_i under a uniform stress σ. $P_f(\sigma,\delta V_i)$ is defined as the probability of failure of the element i. Since the stress is the same for all volume elements and the specimen is assumed to be homogeneous, all $P_f(\sigma, \delta V_i)$ can be taken to be the same, i.e. the probability of failure of any volume element is identical, so we can write $P_f(\sigma)$. The probability of survival is then $1\text{-}P_f(\sigma, \delta V_i)$. The specimen will survive only if all of the volume elements survive. The total probability of survival, $1\text{-}P_f(\sigma, \delta V_i)$, of a specimen of volume $V = n\delta V$ under uniform stress is

$$1 - P_f(\sigma, V) = \left[1 - P_f(\sigma)\right]^n = \left[1 - \frac{V}{n}\frac{P_f(\sigma)}{\delta V}\right]^n = \left[1 - \frac{V\varphi(\sigma)}{n}\right]^n \tag{5.37}$$

Note that it is assumed that as δV decreases, $P_f(\sigma)/\delta V$ approaches the limit $\varphi(\sigma)$. In the limit as n becomes large, Eq. (5.37) becomes

$$1 - P_f(\sigma, V) = e^{(-V\varphi(\sigma))} \tag{5.38}$$

Weibull assumed the following form for $\varphi(\sigma)$:

$$\varphi(\sigma) = \left(\frac{\sigma - \sigma_u}{\sigma_0}\right)^m \tag{5.39}$$

where σ_u defines a failure below which failure will never occur. For ceramics and hard materials, this is taken to be zero (Lu et al. 2002). Finally for a two-parameter Weibull distribution, the cumulative probability of survival of a material subjected to a uniform stress is given by

$$P(\sigma) = 1 - \exp\left(-V\left[\frac{\sigma}{\sigma_0}\right]^m\right) \tag{5.40}$$

where σ_0 is the Weibull characteristic strength and m is the Weibull modulus. The Weibull modulus characterises the level of scatter in the strength data. A low Weibull modulus indicates a wide scatter in the strength data. A ceramic or superhard material would typically have a Weibull modulus between 5 and 20 (Braiden 1975; McNamara et al. 2014), while that of a metal is usually 100 or greater (Askeland et al. 2010).

The corresponding probability density function can then be written as

$$p(\sigma) = \frac{m}{\sigma_0}\left(\frac{\sigma}{\sigma_0}\right)^{m-1} \exp\left(-\left[\frac{\sigma}{\sigma_0}\right]^m\right) \tag{5.41}$$

The three-parameter form was also proposed by Weibull in which $s$is replaced by σ-σ_u *and* σ_0 represents some stress below which fracture will never occur. However the simpler two-parameter distribution has been adequate to fit the observed strength distribution of ceramic materials (Lu et al. 2002).

The fundamental assumption of the Weibull distribution is that of the weakest link, i.e. specimen failure is linked to failure of the weakest element in the specimen and there is no interaction between critical flaws. Some evidence has been presented recently to suggest that the Weibull distribution may not be the most appropriate choice of statistical tools to describe the experimentally measured strength data for brittle materials. Lu et al. (2002a, 2004) compared the strength data for three different ceramics and analysed them using the Weibull and normal distributions. They found that for ZnO, the strength data was best characterised by the normal rather than the Weibull distribution. McNamara et al. (2014) have compared the measured strength data for both polycrystalline diamond and polycrystalline cubic boron nitride against a Weibull, normal and lognormal distribution. Moreover, they investigated the effect of specimen size. They found that the fracture strength of polycrystalline cubic boron nitride was best described by a Weibull distribution, while that of polycrystalline diamond was best described by a lognormal distribution. A significant effect of specimen size was noted for polycrystalline cubic boron nitride, and the Weibull statistical model captured this effect.

3.3.1 Determining the Weibull Parameters

The Weibull parameters can be determined using a least-squares fitting of a linearized form of the distribution. The basic procedure is now discussed. Taking natural logarithms twice of n gives

$$\ln\left(\ln\left(\frac{1}{P_s}\right)\right) = \ln(V) + m\ln(\sigma) - mln(\sigma_0) \tag{5.42}$$

The Weibull parameters can be determined by fitting a straight line to $\ln(\ln(1/P_s))$ as a function of $\ln\sigma$. It is common when measuring samples with the same volume to take the unit volume and so $\ln V = 0$. Obviously if different volumes of materials are being tested, then this term cannot be so easily discounted. The Weibull modulus m is the slope of this plot, while σ_0 can be calculated by noting the intercept on the $\ln(\ln(1/P_s))$ axis at $\ln\sigma = 0$. σ_0 is then calculated by

$$\sigma_0 = \left[e^{-\text{intercept}}\right]^{m^{-1}} \tag{5.43}$$

The calculation of ln σ is trivial but there is some choice as to the calculation of P_s (Davidge 1979). Typically the measured strength values are placed in ascending order and assigned a rank from 1 to n. The survival probability for the i^{th} strength value is then

$$P_{si} = 1 - \frac{i - 0.5}{n} \tag{5.44}$$

A typical plot for determining these parameters is given in Fig. 5.18 (McNamara et al. 2015) for two grades of polycrystalline diamond material (denoted PCD30A

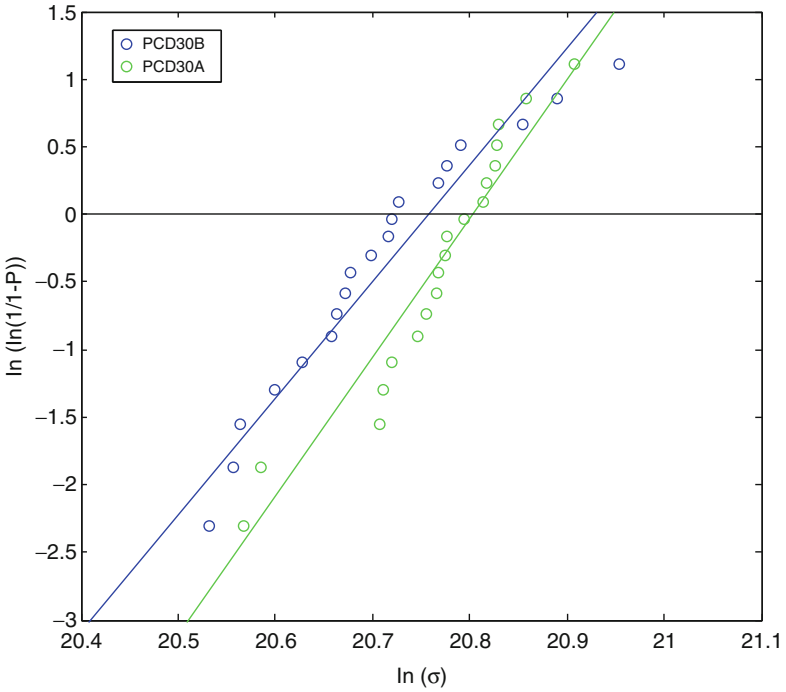

Fig. 5.18 Weibull plot of strength data for two grades of polycrystalline diamond denoted PCD30A and PCD 30B (McNamara et al. 2015)

and PCD 30B). The slope of the empirical data determines the Weibull modulus, m, while the intersection of the x-axis with the empirical line fit is the natural logarithm of the characteristic strength, σ_0. These samples both have a nominal diamond grain size of 30 μm, differing only in the percentage cobalt in the interstitial regions of the compact. PCD30A has the largest percentage cobalt and also has lower scatter in terms of strength data as indicated by the higher Weibull modulus, $m = 13.35$, with respect to PCD30B, $m = 8.26$. PCD30A also has a slightly higher characteristic strength, $\sigma_0 = 1075$ MPa versus $\sigma_0 = 1034$ MPa for PCD30B.

4 Conclusions

Despite the seemingly simple almost perfectly linear elastic behaviour of many hard and superhard materials, the fracture mechanisms of these systems are extremely complex and the correct determination of fracture toughness is by no means a trivial task. As a result there remains some disagreement in the community as to a consensus test method. This chapter has reviewed the most popular methods in the literature, with particular emphasis on those methods applicable to superhard materials such as PcBN and PcD.

It is noted that the calculation of a fracture toughness value is dependent on the experimental method used to obtain the data. These differences can be can be attributed to the different crack lengths employed, e.g. those arising from a macro-scale notch versus those arising from a flaw induced via indentation and also R-curve effects.

While research on this topic continues, it is vital that the user be aware of the limitations and advantages of each method. In particular, the commonly used indentation fracture method does not give correct fracture toughness values and should be avoided.

Specimens containing a machined notch can be used only if it can be ensured that the tip radius of the notch is sufficiently acute so that the true fracture toughness is measured. Failing the resources to produce such a small notch, an estimate of the fracture toughness can be made from testing a number of blunt notches given information about the underlying microstructure.

The chevron-notched beam is perhaps the most versatile of all the methods examined. However, preparation of the samples can be tricky, especially when the supply of material is limited.

Acknowledgements Financial support from the Irish Research Council and Marie Curie Actions under the ELEVATE programme is gratefully acknowledged.

References

Achilles RD (2007) Development of a procedure for fatigue crack growth in PDC. In: 2nd international industrial diamond conference, Rome

Almond EA, Roebuck B (1978) Precracking of fracture-toughness specimens of hardmetals by wedge indentation. Metals Technol 5:92–99

Anderson TL (2005) Fracture mechanics; fundamental and application, 3rd edn. Taylor and Francis, Boca Raton, Florida

Anstis GR, Chantikul P, Lawn BR, Marshall DB (1981) A critical evaluation of indentation techniques for measuring fracture toughness: I direct crack measurements. J Am Ceram Soc 64(9):533–538

Askeland D, Fulay P, Wright W (2010) The science and engineering of materials. Cengage Learning, Stamford

ASTM (2001) Standard test methods for determination of fracture toughness of advanced ceramics at ambient temperatures (C 1421-01b). ASTM International. West Conshohocken, Pennsylvania, USA

Atkinson C, Smelser RE, Sanchez J (1982) Combined mode fracture via the cracked Brazilian test. Int J Fract 18:279–291

Awaji H, Sato S (1978) Combined mode fracture toughness measurement by the disk test. J Eng Mater Technol 100:175–182

Bar-On I, Beals JT, Leatherman GI, Murray CM (1990) Fracture toughness of ceramic precracked bend bars. J Am Ceram Soc 73:2519–2522

Basu B, Tiwari D, Kundu D, Prasad R (2009) Is Weibull distribution the most appropriate statistical strength distribution for brittle materials? Ceram Int 35:237–246

Braiden PM (1975) Introduction to Weibull statistics. United Kingdom Energy Authority

Bubsey RT, Munz D, Pierce WS, Shannon JL Jr (1982) Compliance calibration of the short rod chevron-notch specimen for fracture toughness testing of brittle materials. Int J Fract 18 (2):125–133

Carniero FLLB, Barcellos A (1953) Concrete tensile strength. Union of Testing and Research Laboratories for Materials and Structures, Paris

Carolan D (2011) Mechanical and fracture properties of PcBN as a function of rate and temperature. PhD thesis, University College Dublin, Dublin

Carolan D, Alveen P, Ivankovic A, Murphy N (2011) Effect of notch root radius on fracture toughness of polycrystalline cubic boron nitride. Eng Fract Mech 78:2885–2895

Carolan D, Ivankovic A, Murphy N (2013) A combined experimental-numerical investigation of fracture of polycrystalline cubic boron nitride. Eng Fract Mech 99:101–117

Chantikul P, Anstis GR, Lawn BR, Marshall DB (1981) A critical evaluation of indentation techniques for measuring fracture toughness: II. Strength method. J Am Ceram Soc 64 (9):539–543

Ciccotti M, Gonzato G, Mulargia F (2000) The double torsion loading configuration for fracture propagation: an improved methodology for the load-relaxation at constant displacement. Int J Rock Mech Mining Sci 37(7):1103–1113

Ciccotti M, Negri N, Gonzato G, Mulargia F (2001) Practical application of an improved methodology for the double torsion load relaxation method. Int J Rock Mech Mining Sci 38 (4):569–575

Damani R, Gstrein R, Danzer R (1996) Critical notch-root radius effect in SENB-S fracture toughness testing. J Eur Ceram Soc 16(7):695–702

Danzer R (2006) Some notes on the correlation between fracture and defect statistics: are Weibull statistics valid for very small specimens? J Eur Ceram Soc 26:3043–3049

Davidge RW (1979) Mechanical behaviour of ceramics. Cambridge University Press, New York

Ebrahimi ME, Chevalier J, Fantozzi G (2000) Slow crack-growth behavior of alumina cermaics. J Mater Res 15(1):142–147

Eriksson K (1975) Rapid method for precracking of brittle materials. Scandinavian J Metall 4 (4):182–184
Evans AG, Charles EA (1976) Fracture toughness determinations by indentation. J Am Ceram Soc 59(7–8):371–372
Fett T, Munz D, Thun G, Bahr H-A (1995) Evaluation of bridging parameters in aluminas from R-curves by use of the fracture mechanical weight function. J Am Ceram Soc 78:949–951
Freiman SW, Mecholsky JJ (2012) The fracture of brittle materials: testing and analysis. John Wiley and Sons, Hoboken
Fuller ER Jr (1979) An evaluation of bouble-torsions testing – analysis. In: Freiman SW (ed) Fracture mechanics applied to brittle materials – ASTM STP 678. American Society for Testing and Materials, Baltimore
Gogotsi GA (2000) Fracture toughness studies on v-notched ceramic specimens. Strength Mater 32:81–85
Gopalakrishnan K, Mecholsky JJ Jr (2013) Quantitative fractography of mixed-mode fracture in an R-curve material. J Mater Sci 48:7081–7087
Govila RK (1980) Indentation-precracking and double-torsion methods for measuring fracture mechanics parameters in hot-pressed Si_3N_4. J Am Ceram Soc 63(5–6):319–326
Gremillard L, Chevalier J, Epicier T, Fantozzi G (2000) Microstructural study of silica-doped zirconia ceramics. Acta Mater 48(18–19):4647–4652
Griffith AA (1921) The phenomena of rupture and flow in solids. Philos Trans Ser A 221:163–198
Hillerborg A (1983) Theoretical analysis of the double torsion test. Cem Concr Res 13(1):69–80
Inglis CE (1913) Stresses in a plate due to the presence of cracks and sharp corners. Trans Instit Naval Archit 55:219–241
International Standards Organisation (2003) ISO standard 18756, fine ceramics (advanced ceramics, advanced technical ceramics)—Test method for fracture toughness of monolithic ceramics at room temperature by the surface crack in flexure method. International Standards Organisation. Geneva, Switzerland
International Standards Organisation (2005) ISO Standard 24370, fine ceramics (advanced ceramics, advanced technical ceramics)—Test method for fracture toughness of monolithic ceramics at room temperature by chevron-notched beam (CNB) method. International Standards Organisation. Geneva, Switzerland
Irwin GR (1956) Onset of fast crack propagation in high strength steel and aluminum alloys. Sagamore Res Conf Proc 2:289–305
Kingery WD, Bowen HK, Uhlmann DH (1976) Introduction to ceramics, 2nd edn. John Wiley and Sons, New York
Knott JF (1973) Fundamentals of fracture mechanics. Butterworth, London
Kim H, Partl MN (2012) Development of a double torsion fracture test to predict channelized behaviours of asphalt concrete. Construct Build Mater 26(1):694–700
Kübler JJ (2002) Fracture toughness of ceramics using the SEVNB method: from a preliminary study to a test method. In: Salem JA, Quinn G, Jenkins M (eds) Fracture resistance testing of monolithic and composite brittle materials. ASTM International, West Conshohocken, pp 93–106
Lammer A (1988) Mechanical properties of polycrystalline diamonds. Mater Sci Technol 4:949–955
Lawn BR (1983) Physics of fracture. J Am Ceram Soc 66:83–91
Lawn BR (1998) Fracture of brittle solids. Cambridge University Press, Cambridge
Lin T-P, Cooper GA, Hood M (1994) Measurement of the fracture toughness of polycrystalline diamond using the double torsion test. J Mater Sci 29:4750–4756
Lu C, Danzer R, Fischer FD (2002) Influence of threshold stress on the estimation of the Weibull statistics. J Am Ceram Soc 85:1640–1642
Lu C, Danzer R, Fischer FD (2004) Scaling of fracture strengths in ZnO: effects of pore/grain/size interaction and porosity. J Eur Ceram Soc 24:3643–3651
Marshall DB (1984) Mechanisms of failure from surface flaws in mixed-mode loading. J Am Ceram Soc 67:110–116

Marshall DB, Evans AG (1981) Reply to 'comment on elastic/plastic indentation damage in ceramics: the median/radial crack system'. Commun Am Ceram Soc 64(12C):182–183
McNamara D, Alveen P, Carolan D, Murphy N, Ivankovic A (2014) The influence of microstructure on the fracture statistics of polycrystalline diamond and polycrystalline cubic boron nitride. Ceram Int 40(8A):11543–11549
McNamara D, Alveen P, Carolan D, Murphy N, Ivankovic A (2015) Fracture toughness evaluation of polycrystalline diamond as a function of microstructure. Eng Fract Mech 143:1–16
Morell R (2006) Fracture toughness testing for advanced technical ceramics: internationally agreed good practice. Adv Appl Ceram 105(2):88–98
Morell R, Parfitt M (2005) A stiff facility for controlled pre-cracking in fracture toughness test, NPL Measurement Note DEPC (MN)034
Munz D, Shannon JL, Bubsey RT (1980) Fracture toughness calculation from maximum load in four point bend tests of Chevron notch specimens. Int J Fract 16:R137–R141
Neuber H (1958) Theory of notch stresses: principles for exact calculation of strength with reference to structural form and material, Materials science and engineering series. Springer, Berlin
Newman JC Jr, Raju IS (1981) An empirical stress intensity factor equation for the surface crack. Eng Fract Mech 15:185–192
Nicholson PS (1990) Constant-KI double cantilever beam test for ceramics materials. J Am Ceram Soc 73(6):1800–1802
Niihara K (1983) A fracture mechanics analysis of indentation-induced Palmqvist crack in ceramics. J Mater Sci Lett 2:221–223
Nishida T, Hanaki Y, Pezzotti G (1994) Effect of notch root radius on the fracture toughness of a fine grained alumina. J Am Ceram Soc 77:606–608
Nose T, Fujii T (1988) Evaluation of fracture toughness for ceramic materials by a single-edge-precracked-beam method. J Am Ceram Soc 71:328–333
Nunomura S, Jitsukawa S (1978) Fracture toughness of bearing steels by indentation cracking under multiaxial stress. Tetsu to Hagane 64 (in Japanese)
Orowan E (1948) Fracture and strength of solids. Reports on Progress in Physics, XII, pp 16–18
Outwater JO, Austin LE (1969) On the fatigue of epoxy. J Adhes 1:290–298
Outwater JO, Murphy MC, Kumble RG, Berry JT (1974) Double torsion technique as a universal fracture toughness test method. ASTM STP 559:127–138
Palmqvist S (1957) Method attBestammaSegheten hos spread material. SarskiltHardmetaller, JernkortoretsAnnaler 141:300–307
Peterson RE (1959) Notch-sensitivity. In: Sines G, Waisman JL (eds) Metal fatigue. McGraw-Hill, New York
Petrovic JJ (1985) Mixed-mode fracture of hot pressed Si_3N_4. J Am Ceram Soc 68:348–355
Petrovic JJ, Mendiratta PK (1976) Mixed-mode fracture from controlled surface flaws in hot pressed Si_3N_4. J Am Ceram Soc 59:163–167
Petrovic JJ, Mendiratta PK (1979) Fracture from controlled surface flaws. In: Fracture mechanics applied to brittle materials. STP 678, American Society for Testing and Materials, pp 73–82
Primas RJ, Gstrein R (1997) ESIS TC 6 round robin on fracture toughness. Fatigue Fract Eng Mater Struct 20:513–532
Quinn GD (2007) Fractography of ceramics and glasses, NIST special publication 960–16. National Institute of Standards and Technology, Washington, DC
Quinn GD, Kübler JJ, Gettings RJ (1994) Fracture toughness of advanced ceramics by the surface crack in flexure (SCF) method: a VAMAS round robin. Vamas report 17, Gaithersburg, Maryland
Quinn GD, Bradt RC (2007) On the Vickers fracture toughness test. J Am Ceram Soc 90 (3):673–680
Reddy KPR, Fontana EH, Helfinstine JH (1988) Fracture toughness of glass and ceramic materials using chevron-notched specimens. J Am Ceram Soc 71(6):C310–C313

Rocha CV, daCosta CA (2006) Effect of notch root radius on the fracture toughness of composite Si_3N_4 ceramics. J Mater Eng Perform 15(5):591–595
Sakai M, Bradt RC (1993) Fracture toughness testing of brittle materials. Int Mater Rev 38:53–78
Shetty DK, Rosenfield AR, Duckworth WH (1985) Fracture toughness of ceramics measured by a chevron notch diametral compression test. J Am Ceram Soc 68(12):C325–C327
Shyam A, Lara-Curzio E (2006) The double torsion testing technique for determination of fracture toughness and slow crack growth behaviour of materials: a review. J Mater Sci 41:4093–4104
Sørenson BF, Brethe P, Skov-Hansen P (1996) Controlled crack growth in ceramics: the DCB specimen loaded with pure moments. J Eur Ceram Soc 16(9):1021–1025
Suresh S, Ewart L, Maden M, Slaughter WS, Nguyen M (1987) Fracture toughness measurements in ceramics: pre-cracking in cyclic compression. J Mater Sci 22:1271–1276
Susmel L, Taylor D (2010) The theory of critical distances as an alternative experimental strategy for the determination of K_{Ic} and ΔK_{th}. Eng Fract Mech 77:1492–1501
Taylor D (1996) Crack modelling: a technique for the fatigue design of components. Eng Fract Mech 3:129–136
Taylor D (1999) Geometrical effects in fatigue: a unifying theoretical model. Int J Fract 21:413–420
Taylor D (2004) Predicting the fracture strength of ceramic materials using the theory of critical distances. Eng Fract Mech 71:2407–2416
Taylor D, Cornetti P, Pugno N (2005) The fracture mechanics of finite crack extension. Eng Fract Mech 72:1021–1038
Taylor D (2006) The theory of critical distances applied to the prediction of brittle fracture in metallic materials. Struct Integr Durab 1:145–154
Trustrum K, Jayatilaka AD (1983) Applicability of Weibull analysis for brittle materials. J Mater Sci 18(9):2570–2765
Venikis G, Ashby MF, Beaumont PWR (1990) R-curve behaviour of alumina ceramics. Acta Metall Mater 38:1151–1162
Wachtman JB, Cannon WR, Matthewson MJ (2009) Mechanical properties of ceramics, 2nd edn. John Wiley and Sons, New York
Warren R, Johannsen B (1984) Creation of stable cracks in hard metals using 'bridge' indentation. Powder Metall 27:25–29
Weibull W (1951) A statistical distribution function of wide applicability. J Appl Mech 18 (3):293–297
Westergaard HM (1939) Bearing pressure and cracks. J Appl Mech 6:A49–A53
Whitney JM, Nuismer RJ (1974) Stress fracture criteria for laminated composites containing stress concentrations. J Compos Mater 8:253–265
Wronski AS, Rebbeck MM, Amen SA (1988) Fracture mechanisms of an 18-4-1 high speed steel. J Mater Sci 23:2213–2219
Xu YL (1995) Green's function for general disk-crack problems. Int J Solids Struct 32:63–77
Yarema SY, Krestin GS (1966) Determination of the modulus of cohesion of brittle materials by compression testing of disks with a crack. Fiziko-KhimicheskayaMekhankiaMaterialov 2(1):10–14
Zhou J, Wang Y, Xia Y (2006) Mode-I fracture toughness measurement of PMMA with the Brazilian disk test. J Mater Sci 41(17):5778–5781

Chapter 6
Superhard and Ultrahard Nanostructured Materials and Coatings

Prof. Dr. Prof. h.c. Dr. h.c. Stan Veprek
and Dr. Maritza G.J. Veprek-Heijman

Abstract The recent search for new super- and ultrahard materials is briefly summarized. It is shown that many materials with high elastic moduli cannot be superhard because, upon finite shear, electronic instabilities and transformations to softer phases occur, particularly in materials which contain metals with d-electrons or non-binding electron pairs. Hardness enhancement can be achieved in nanostructured materials, but it is limited by grain-boundary shear when the crystallite size decreases to 10–15 nm called the "strongest size." When however, low-energy grain boundaries, such as stacking faults and twins, or one-monolayer thin sharp grain boundaries of silicon nitride strengthened by valence charge transfer are introduced, the grain-boundary shear can be reduced and the "strongest size" shifted to a few nanometers. This results in a significantly increased hardness enhancement. In such a way, extrinsically ultrahard materials, such as nanotwinned nt-c-BN and nt-diamond, and nanocomposites consisting of 3–4 nm small transition metal nitride with about one monolayer silicon nitride interfacial layer with hardness exceeding 100 GPa have been prepared. We discuss the conditions which have to be met for such nanocomposites to be super- and ultrahard and show that not all such systems can be superhard. Impurities, mainly oxygen content of more than a few hundred ppm, are critical limitation for achieving the high hardness. The superhard nanocomposites, such as nc-$(Ti_{1-x}Al_x)N/Si_3N_4$ and nc-$(Cr_{1-x}Al_x)N/Si_3N_4$, find important applications as wear-protection coatings on tools for machining, stamping, injection molding, and the like.

Prof. Dr. Prof. h.c. Dr. h.c. S. Veprek (✉)
Professor Emeritus, Department of Chemistry, Technical University Munich, Munich, Germany
e-mail: Stan.Veprek@lrz.tum.de

Dr. M.G.J. Veprek-Heijman
Department of Chemistry, Technical University Munich, Munich, Germany
e-mail: Maritza.Veprekheijman@lrz.tum.de

V. Kanyanta (ed.), *Microstructure-Property Correlations for Hard, Superhard, and Ultrahard Materials*, DOI 10.1007/978-3-319-29291-5_6

1 Introduction

Many efforts have been conducted recently to design new superhard (hardness $H \geq 40$ GPa, c-BN ≈ 48 GPa) and ultrahard ($H \geq 80$ GPa) comparable to diamond (80–100 GPa) materials. The majority of the papers focused on materials with large elastic moduli ("ultra-incompressibility") which are believed to be "intrinsically" superhard. However, large elastic moduli do not guarantee high hardness, because the moduli describe only the resistance of a material against elastic (reversible) infinitesimal distortion near the equilibrium positions, whereas plastic deformation occurs by shear at large strain at the atomic level. The apparent correlation of the hardness of some material with the shear modulus, G, which however displays large scatter [see Fig. 1 in (Teter 1998)], is due to the fact that the plastic flow, which occurs mainly by multiplication and movement of dislocations, is impeded by a variety of mechanisms (grain boundaries, precipitates, dispersed particles, and the like) that are dependent on G.

One has to keep in mind that the indentation hardness is the average pressure beneath the indenter under conditions of fully developed plasticity, where no single crystal exists anymore, and thus the material is full of flaws (Argon 2008). Therefore the recent theories of "hardness of an ideal crystal" (e.g., Gao et al. 2003; Simunek and Vackar 2006; Simunek 2009) calculate by first principles only the elastic stiffness of the crystals but not their plastic hardness under the condition of fully developed plasticity.

Sufficiently high elastic moduli are of course needed but not sufficient for achieving high hardness, because upon finite shear that occurs at atomic level upon plastic deformation, many materials undergo electronics instabilities and structural transformations into softer phases. For example, C_3N_4, which has elastic moduli, calculated by first principles, higher than c-BN and close to those of diamond (Cohen 1994; Liu and Cohen 1989; Zhang Y et al. 2006), has hardness less than 30 GPa (Veprek et al. 1995) because upon a shear of 0.24 in the (111) (Argon 2008) slip system, the non-binding electron pairs on nitrogen interact with atomic orbitals of carbon forming double bonds, and the system transforms into a softer, graphite-like phase (Zhang Y et al. 2006).

Rhenium diboride, ReB_2, like other diborides of 5d metals, has also large elastic moduli but hardness less than 30 GPa (see Chap. 4) because upon shear within the (0001) (Christiansen et al. 1998) slip system, it undergoes a number of electronic instabilities and transformation to instable and metastable phases with lower shear resistance [see Fig. 1 in (Zhang et al. 2010a)]. The formation of a variety of softer phases beneath the indenter is probably also the reason for the slow approach of the measured hardness to the load-invariant value which requires large load of more than 6 newtons (N) [see Fig. 2a in (Chung et al. 2007)]. The valence orbitals of osmium and iridium atoms differ only by one electron in the 5d shell (Os, $4f^{14}5d^{6}6s^{2}$; Ir, $4f^{14}5d^{7}6s^{2}$), yet their diborides OsB_2 and IrB_2 display very different plastic deformation paths and hardness (OsB_2, 30 GPa; IrB_2, 18 GPa) because of different crystal field splitting instabilities (Zhang et al. 2014). Diamond transforms to graphite

upon shear of > 0.3 in the (111) (Argon 2008) slip system as shown by first-principle calculations (e.g., Veprek et al. 2010) and as experimentally observed by Raman scattering of the indented area (Gogotsi et al. 1999). However, because of the relatively simple electronic structure of carbon, this transformation requires a very high shear stress. Therefore, diamond is intrinsically ultrahard. The electronic instabilities of the 5d orbitals due to the crystal field splitting and instabilities due to non-binding electron pairs upon finite shear are probably general phenomena limiting the hardness of many materials with high elastic moduli.

Boron suboxide, B_6O, has high hardness of 40–45 GPa in spite of its lower elastic moduli as compared with OsB_2 and ReB_2 because it has an electronically stable three-dimensional network of covalent bonds (Zhang et al. 2011). These few examples should be sufficient to illustrate that the search for new intrinsically superhard materials should not focus only on materials with high elastic moduli. Instead, much deeper insight into the electronic structure and its stabilities upon finite shear and into the deformation paths are needed (Veprek 2013).

Interesting is the case of heavily boron-doped diamond BC_5 for which load-invariant Vickers hardness of 71 GPa, higher than that of c-BN, has been reported (Solozhenko et al. 2009), although the ideal shear strength of BC_5, calculated by means of density functional theory, DFT, was significantly lower than that of c-BN (Zhang et al. 2009). The answer to this puzzle was identified in the small crystallite size of the material of 10–15 nm (Solozhenko et al. 2009) that is in the range of the so-called strongest size (Argon and Yip 2006). Also the high Vickers hardness of c-BC_2N of about 76 GPa (Solozhenko et al. 2001) has been explained by the small size of the nanocrystals (Zhang Y et al. 2004).

With decreasing crystallite size, the strength and hardness of a material increase because the grain boundaries impede the plastic deformation, by the well-known Hall-Petch mechanism for dislocations and by twinning, slip, and other mechanisms of plasticity (Argon 2008). The thickness of the large-angle grain boundaries extends usually over a distance of about 3–4 interatomic bonds. Therefore, below a crystallite size, d, of 10–15 nm, the fraction of the atoms in the grain boundaries strongly increases as $1/d$. The grain boundaries are weaker than the crystals because of density deficit and disorder therein. Therefore, with crystallite size decreasing below about 10 nm, the strengthening is replaced by the grain-boundary shear (also called "sliding" of "inverse Hall-Petch") below the "strongest size," and the material softens (Fig. 6.1). This transition from strengthening to softening has been found in many nanosized materials, such as metals (e.g., Argon and Yip 2006; Schiøtz et al. 1998; Schiøtz and Jacobsen 2003; Siegel and Fougere 1995) and ceramics (Skrovanek and Bradt 1979). The crystallite size where the strengthening changes to softening has been called by Yip "the strongest size" (Yip 1998). This strengthening with crystallite size decreasing to about 10–15 nm is found in almost any system when, for example, some elements or impurities are added leading to decomposition of a solid solution into two or more phases and concomitant grain refinement. However, the amount of such strengthening is limited by the grain-boundary shear as shown in Fig. 6.1. The "strongest size" can be slightly shifted to a smaller crystallite size, and the strength and hardness increased when

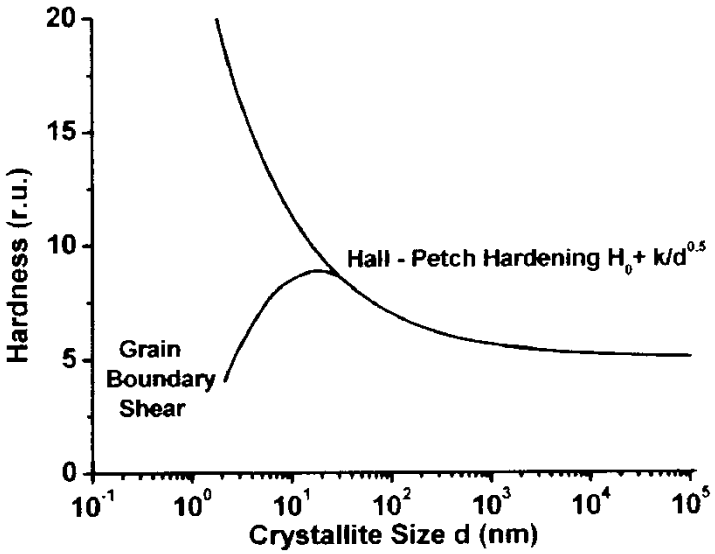

Fig. 6.1 Increase of the strength and hardness due to grain-boundary strengthening with decreasing crystallite size and its weakening due to grain-boundary shear below about 10–20 nm (From Veprek and Veprek-Heijman (2012) with permission)

the grain boundaries are made dense by thermal treatment. However there is a principal limitation to such treatment because the majority of nanosized materials coarsen upon annealing.

The question arises as if this "strongest size" could be shifted to a lower crystallite size by the formation of "strengthened" interfaces so that the "grain-boundary strengthening" would work even at a lower grain size of few nm. This has been the basic idea in the "concept for the design of novel superhard coatings" (Veprek and Reiprich 1995): to choose a quasi-binary or ternary system that will strongly segregate into two or more phases of which the one should form nanocrystals smaller than 10 nm, whereas the other one should form a very thin and sharp interfacial layer. We shall show that this is indeed possible in systems, such as Ti-Si-N, where the solid solution decompose spinodally with large de-mixing energy (Veprek and Veprek-Heijman 2012; Zhang and Veprek 2006). In recent years, this idea has been extended to low-energy interfaces, such as stacking faults (Jian et al. 2013) and twins (Huang et al. 2014; Tian et al. 2013; Xu and Tian 2015). The twins are of a particular interest because there is some evidence that in nanocrystals the dislocation activity upon plastic deformation is replaced by twinning (Zhu et al. 2009).

Of course one will ask what is the smallest crystallite size that can be prepared, and what maximum strength and hardness can be achieved. There is probably no universal answer to it, but some indications can be found in our earlier work on nanocrystalline silicon (nc-Si). It has been shown that there is a lower limit to the crystallite size of about 3 nm, because the tensile strain energy, originating from the

grain boundaries, thermodynamically destabilizes the nc-Si. Therefore amorphous silicon (a-Si) is preferred below that crystallite size because there are no grain boundaries in a-Si (Veprek et al. 1982). Because a similar strain was found in the superhard nc-TiN/Si_3N_4 nanocomposites, a similar effect may explain why the strongest nanocomposites have the size of TiN nanocrystals about 3 nm. We shall discuss this point in Sect. 2.5.

2 Concepts for the Design of New Nanostructured Superhard Materials

2.1 Heterostructures and Nanolaminates

Koehler was the first scientist who suggested to design new strong materials on the basis of nanolayered heterostructures (Koehler 1970). The idea was to form alternating layers of different materials with sufficiently different shear moduli but similar lattice constant to form coherent interfaces. The thickness of the individual layers should be small to make sure that the dislocation multiplication source cannot operate. Under stress, a dislocation present in the softer layer with a small shear modulus G_1 would move toward the interface with the stronger material where the elastic mirror force would be hindering it to pass. In such a way, the dislocation activity should be impeded by the coherent or semi-coherent interfaces. In a note added in proof, Koehler stated "The ideas described in this note are also valid if one of the materials is amorphous." Indeed, it has been found later on that the Koehler mechanism of strengthening operates also in polycrystalline nanolaminates and when one of the materials forms amorphous layers (e.g., Hilz and Holleck 1996; Holleck and Schier 1995; Sproul 1994, 1996; Yashar et al. 1999; Yashar and Sproul 1999).

Lehoczky was the first researcher who verified the idea of Koehler experimentally by depositing heterostructures of soft metals (e.g., Al-Cu) and conducting tensile tests. He has shown that, when the thickness of the layers decreased to a few 10 nm, the tensile yield strength of the laminates strongly increased. Although these metallic nanolaminates were not superhard, it is worth mentioning this pioneering work, because this was the first and to the best of our knowledge the only experimental proof of the concept of Koehler in tensile test (Lehoczky 1978a, b). In all following work, only the hardness has been measured.

Superhard heterostructures with hardness exceeding 40 GPa have been prepared when the concept of Koehler has been applied to hard transition metal nitrides. We cannot review here all the papers which have been published on the heterostructures and nanolaminates. Therefore we quote only the first papers from the University of Linköping (Sweden) and Northwestern University (USA) whose scientists pioneered this field (e.g., Helmersson et al. 1987; Mirkarimi et al. 1990, 1994; Hubbard et al. 1992; Shin et al. 1992) and refer to several review articles (Barnett 1993; Yashar and Sproul 1999; Barnett and Madan 1998) for further details.

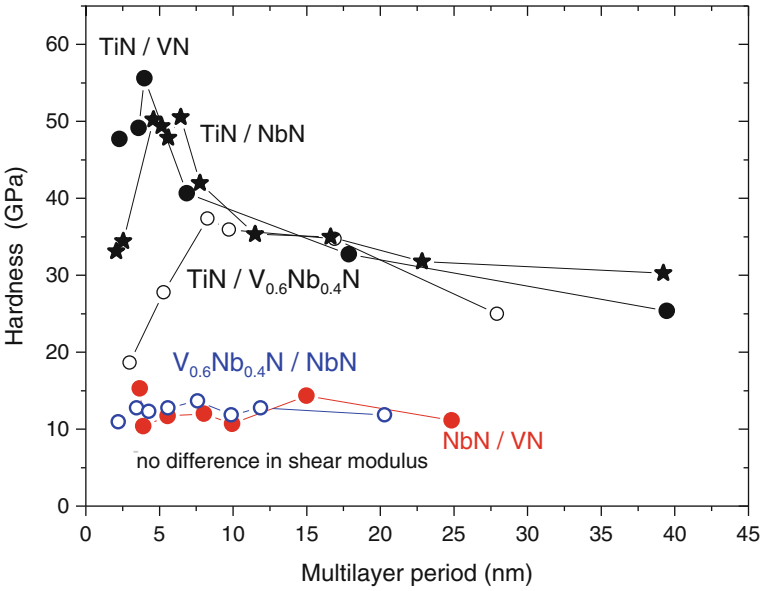

Fig. 6.2 Examples of hardness enhancement in heterostructures with different shear moduli of the pairs (TiN/VN, TiN/NbN, TiN/$V_{0.6}Nb_{0.4}N$) and with no significant difference in the moduli (NbN/VN, $V_{0.6}Nb_{0.4}N$)

In Fig. 6.2, we summarize several examples collected from these papers. Heterostructures with pairs of nitrides having different elastic moduli but similar lattice constant (single-crystalline TiN/VN and TiN/$V_{0.6}Nb_{0.4}N$, polycrystalline TiN/NbN) show pronounced hardness enhancement, whereas heterostructures which have only small difference in elastic moduli (NbN/VN, $V_{0.6}Nb_{0.4}N$) show no observable hardness enhancement. The decrease of the hardness at smaller multilayer period is due to roughness of the interface (Chu and Barnett 1995). Here we see the importance of sharp interface; we shall come to this point later in Sects. 2.4 and 2.5.

These heterostructures have been deposited by magnetron sputtering from two targets, and the composition has been changed by opening and closing shutters between the targets and the substrate (Barnett 1993). This provided fairly sudden changes from one composition to the other with interfaces whose sharpness has been limited only by ion-impact or thermally induced mixing.

The requirement for a sharp interface might appear a problem when the heterostructures and nanolaminate coatings should be used as wear protection on tools for machining. This is due to the fact that in the industrial coating system, the deposition of the individual layers from different targets occurs continuously, while the tools being coated are fixed on a rotating turntable. Nevertheless, Münz et al. were able to demonstrate that tools such as drills, mills, forming tools, and knives coated with nanolaminates deposited in an industrial coating equipment with large planar targets showed significantly improved cutting performance (Münz et al. 2001).

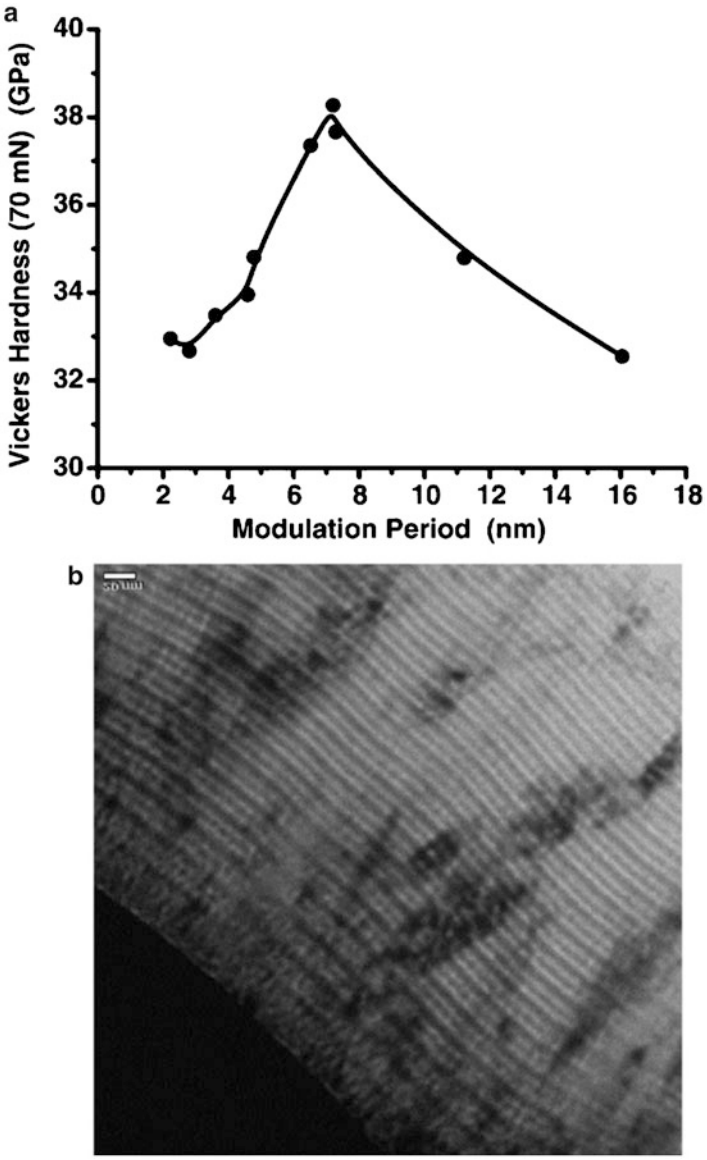

Fig. 6.3 (**a**) Hardness of the nc-$(Ti_{1-x}Al_x)N/Si_3N_4$ nanolayered nanocomposite coatings as the function of the period of the compositional modulation, (**b**) transmission electron micrograph showing the compositional modulation (From Veprek and Veprek-Heijman (2008) with permission)

Since this early development, the hard and superhard heterostructure and nanolaminate coatings are finding many applications, as illustrated, for example, in Fig. 6.3. The nc-$(Ti_{1-x}Al_x)N/Si_3N_4$ nanocomposite coatings (see Sect. 2.5) are deposited from two cylindrical vacuum arc cathodes consisting of titanium and

Al-Si alloy, which are placed in the center of the industrial coating chamber (for more detail, see www.shm-cz.cz). When the tools being coated are rotating around these cathodes, their composition is modulated being more Ti-rich on the side close to the Ti cathode and more Al + Si-rich on the opposite side. Although in this case no "heterostructures" but only coatings with modulated compositions were deposited, the effect of the hardness enhancement is clearly seen. Moreover, because the modulation of the composition results also in modulation of the elastic moduli, it results in enhancement of the fraction toughness. Coatings with modulated elastic moduli are much more resistant to crack propagation than bulk materials (Matthews et al. 2001).

2.2 *Hardness Enhancement Due to Refinement of the Grain Size*

As discussed in Sect. 1, the enhancement of strength and hardness due to the refinement of the grain size occurs in almost any system, but the hardness enhancement is limited to that corresponding to the "strongest size" of about 10–15 nm. This refinement can be obtained by a variety of means. For example, Barna et al. reported strong refinement of Al films when the aluminum has been deposited by evaporation in poor vacuum so that the films were contaminated by oxygen (Barna and Adamik 1998; Petrov et al. 2003). Depending on the Al:O flux ratio during the deposition, thin or thick Al_2O_3 layer is formed around the Al grains whose size decreased with increasing amount of oxygen down to a few tens of nanometers. Of course this is not a method for the preparation of superhard nanocomposites. This example should only illustrate that grain size refinement occurs in many cases when two immiscible materials form during the deposition.

Many papers have been published during the last 20 years about the preparation of nc-TmN/SiN_x (Tm = Ti, W, V, and many other transition metals) and other nanocomposites where a hardness enhancement has been found. Although, in many cases, these papers provide broad characterization, a systematic study of the hardness enhancement as function of the grain size is missing. However, the present authors found that, whenever enough data is available to extract the information from the papers, the maximum hardness enhancement correlates with the grain size of about 10–15 nm, i.e., with the "strongest size." For example, in the AlN/SiN_x nanocomposites, the maximum hardness of about 30 GPa [see Fig. 5 in Pélisson et al. (2007)] is achieved at Si content of about 7–13 at.% that corresponds to "AlN" grain size between of about 20 and 5 nm [see Fig. 3 in Pélisson et al. (2007)]. Such nanocomposites are not superhard as those with one monolayer Si_3N_4 interfacial layer which is strengthened by valence charge transfer, to be discussed in Sect. 2.5. Unfortunately, this important difference is neglected in many papers.

Also in the "high-entropy alloys" (Tsai and Yeh 2014), hardness enhancement is often found which might be related to the grain refinement (e.g., Hsieh et al. 2013;

Huang and Yeh 2009). As pointed out recently, high configuration ("mixing") entropy provides a way to rationalize why a homogeneous solid solution forms (if it forms) in these systems, but it is not a useful a priori predictor if the so-called high-entropy alloy will form thermodynamically stable single-phase solid solutions (Otto et al. 2013). In many cases, positive (destabilizing) mixing enthalpy dominates over the mixing entropy, and the system segregates forming a nanosized composite material. Therefore, much more detailed studies are needed to make sure which effects dominate in a given system.

As mentioned, hardness enhancement by refinement of the grain size is limited to about 30–35 GPa in all the cases where the necessary information is available. Therefore, superhard materials can be formed by the simple grain refinement only when the terminal phases are already very hard, as in the case of nanocrystalline c-BN and c- and wurtzite w-BN nanocomposites reported by Dubrovinskaia et al. (Dubrovinskaia et al. 2007). These researchers prepared the c- and w-BN nanocomposites by high-temperature, high-pressure (HTHP) synthesis and reported high hardness of about 85 GPa, close to the hardness of diamond as shown in Fig. 6.4. One notices that the large increase of the load-invariant hardness of the nanocomposite occurs at crystallite site 13–15 nm, the "strongest size." Single-phase c-BN shows also an enhancement of hardness at a crystallite size of about 40 nm. Using monomodal pyrolytic graphite with an ideal turbostratic structure, Solozhenko et al. (2012) succeeded to suppress the formation of w-BN and prepare single-phase nanocrystalline c-BN with load-invariant hardness of 85 GPa at crystallite size of 20 nm [see Fig. 3b in (Solozhenko et al. 2012)]. These materials

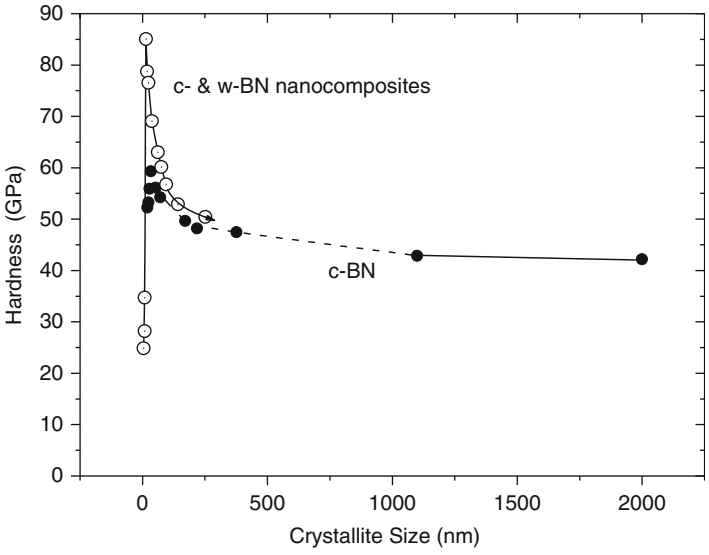

Fig. 6.4 Dependence of the load-invariant hardness on crystallite size in a single-phase c-BN and in nanocomposites consisting of cubic and wurtzite BN (From Dubrovinskaia et al. (2007) with permission)

have been prepared by means of HTHP synthesis that is suitable for the preparation of single crystals and polycrystals, but not coatings on, e.g., tools for machining, which is one of the important areas of applications of superhard materials.

Worth mentioning is the ultra-nanocrystalline diamond deposited by plasma-induced chemical vapor deposition (P-CVD) from hydrocarbons strongly diluted by hydrogen (Erdemir et al. 2005; Gruen 1999). This material consists of 3–4 nm size diamond nanocrystals connected by C = C double bonds. Because the deposited films were only few μm thick, reliable data about their load-invariant hardness are not available. Nevertheless the hardness of 1 μm thick coatings has been 100 GPa (see Fig. 4 in Veprek 1999). Besides high hardness, this material has also high corrosion resistance in acidic and basic environment and is biocompatible. Therefore it finds many applications not only as hard coatings on tools from machining of nonferrous materials but also in medicine as protection coatings on implants and the like (Auciello 2010; Auciello and Shi 2010).

2.3 *Hardness Enhancement by Ion Bombardment During Thin-Film Deposition*

When thin films of ceramic materials are deposited under energetic ion bombardment during the deposition at relatively low homologous temperature of less than about 30 % of the melting point, many defects due to displacement damage, formation of vacancies, implantation of interstitial, increase of biaxial compressive stress, and the like are formed. These complex synergistic effects result in an increase of the hardness. For example, Musil et al. (1988) reported hardness of TiN deposited by magnetron sputtering at relatively low temperature of more than 70 GPa (hardness of bulk TiN is about 21 GPa) and that of (TiAlV)N of more than 90 GPa. In another paper, hardness of 47 GPa has been reported for $(Ti_{1-x}Al_x)N$ coatings deposited with the same techniques (Musil and Hruby 2000). These researchers reported also a number of superhard nanocomposites consisting of hard transition nitride and soft, ductile metal that does not form stable nitrides [for a summary, see (Musil 2000)].

There are also papers of other groups reporting enhanced hardness in ceramic coatings deposited under energetic ion bombardment at relatively low homologous temperature which we shall not discuss here because such coatings suffer from two problems: (a) the high biaxial compressive stress that develops as a result of the ion bombardment causing delamination of the coatings from the substrate and (b) the fact that the hardness enhancement is lost when such coatings are annealed to 450–550 °C as illustrated in Fig. 6.5. In that figure, ZrN/Cu, ZrN/Ni, and Cr_2N/Ni are the nanocomposites deposited in the laboratory of Musil and annealed in pure nitrogen in the institute of S.V. (Karvankova et al. 2001). As one can see, upon annealing, the hardness decreases to the usual values of the hardness of the nitrides.

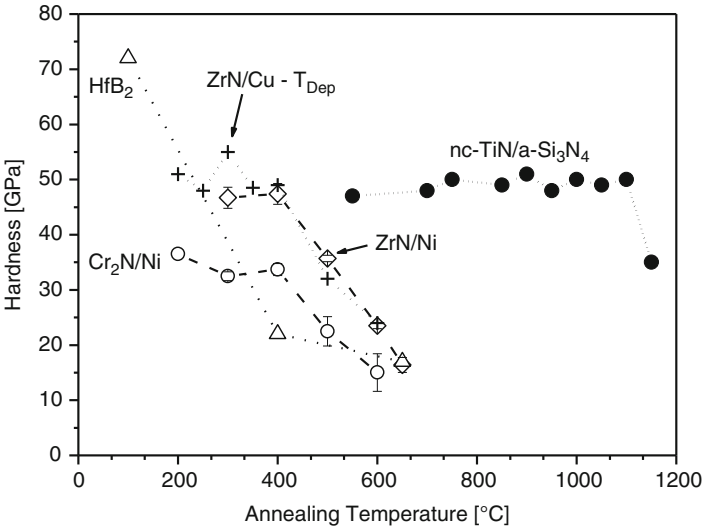

Fig. 6.5 Dependence of the hardness of HfB_2 (Herr and Broszeit 1997), Cr_2N/Ni, and ZrN/Ni (Karvankova et al. 2001) coatings hardened by energetic ion bombardment and stable superhard nc-TiN/a-Si_3N_4 nanocomposites on the temperature of isochronal annealing in pure nitrogen. The hardness was measured at room temperature after each annealing step. The crosses show the dependence of the hardness of the ZrN/Cu coatings on their deposition temperature (Zeman et al. 2000) (From Veprek et al. (2005a) with permission)

Also the HfB_2 coatings deposited by Herr and Broszeit (Herr and Broszeit 1997) lose the hardness enhancement upon annealing.

In contrast, the hardness of the nc-TiN/Si_3N_4 and nc-$(Ti_{1-x}Al_x)N/Si_3N_4$ nanocomposites formed by spinodal decomposition and deposited without energetic ion bombardment remains stable up to 1100–1200 °C, i.e., of about 65–70 % of the decomposition temperature of Si_3N_4. [For the thermal stability of nc-$(Ti_{1-x}Al_x)N/Si_3N_4$ nanocomposites up to 1200 °C, see Fig. 2 in Veprek et al. 2004b.] In conventional nanosized or nanostructured materials, the recrystallization and coarsening (Ostwald ripening) occur upon annealing to a homologous temperature of about $T_h = T/T_{\text{Decomp.}} \approx 0.4$. In contrast, the nanocomposites formed by spinodal decomposition with strengthened interfacial Si_4N_4 layer, to be discussed in Sect. 2.5, coarsen only above 1100–1200 °C, and then the hardness, measured after the annealing at room temperature, decreases. This result illustrates the remarkable stabilization of nanostructured material against coarsening. We shall discuss the latter nanocomposites in Sect. 2.5.

These examples show that hardness enhancement by energetic ion bombardment during deposition at relatively low temperature can be achieved in many (probably all) hard ceramic materials. However, the large compressive stress in the coatings and loss of the hardness enhancement upon annealing to relatively modest temperatures are severe obstacles for their application.

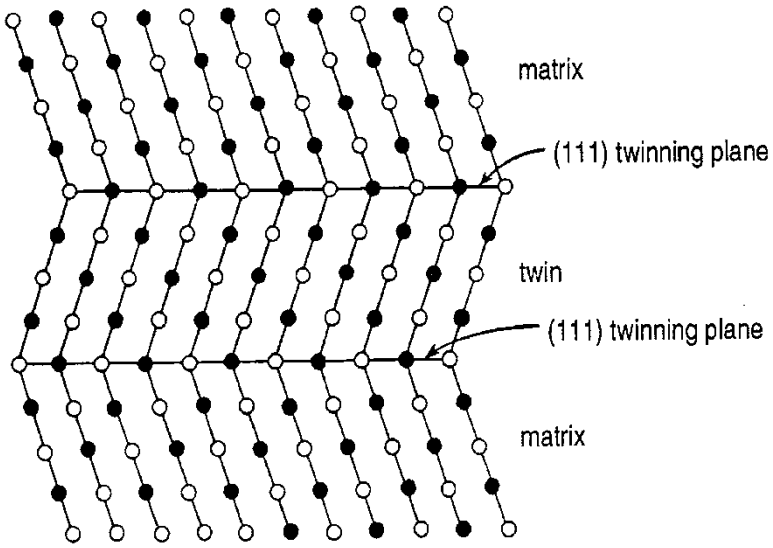

Fig. 6.6 Example of a twin and twinning boundary in an fcc lattice (Reproduced from Gottstein (2004) with permission)

2.4 Hardness Enhancement by Low-Energy Interfaces

Stacking faults and twins are low-energy, coherent grain boundaries (Gottstein 2004), whose "destabilizing" energy is less than about 10 % of the energy of common large-angle grain boundaries. Because the low-energy grain boundaries are only one monolayer thin (see Fig. 6.6), whereas the large-angle grain boundaries are 3–4 crystal planes thick, the fraction of the atoms within the low-energy grain boundaries is—for a given grain size—much smaller. Thus, one expects that the "strongest size" should be shifted to smaller crystallite size as compared to the case of common large-angle grain boundaries. With reference to Fig. 6.1, one logically expects that the strengthening due to smaller crystallite size should continue to increase following the "Hall-Petch" curve with crystallite size decreasing down to a few nm small nanocrystals, because the weakening due to grain-boundary shear will be much less (Huang et al. 2014; Tian et al. 2013; Xu and Tian 2015). Therefore, one expects large strengthening and hardening in nanosized materials with low-energy grain boundaries. Indeed, Mg alloys with a large density of stacking faults achieved the highest strength ever reported in these materials (Jian et al. 2013). The high density of the stacking faults has been achieved by severe plastic deformation of Mg alloy sheets upon a repeated rolling. Although these strong Mg alloys are not superhard, we mention them here to underline the general nature of this strengthening mechanism.

The recently synthesized nanotwinned c-BN (Tian et al. 2013) and diamond (Huang et al. 2014; Xu and Tian 2015) provide an important support to this

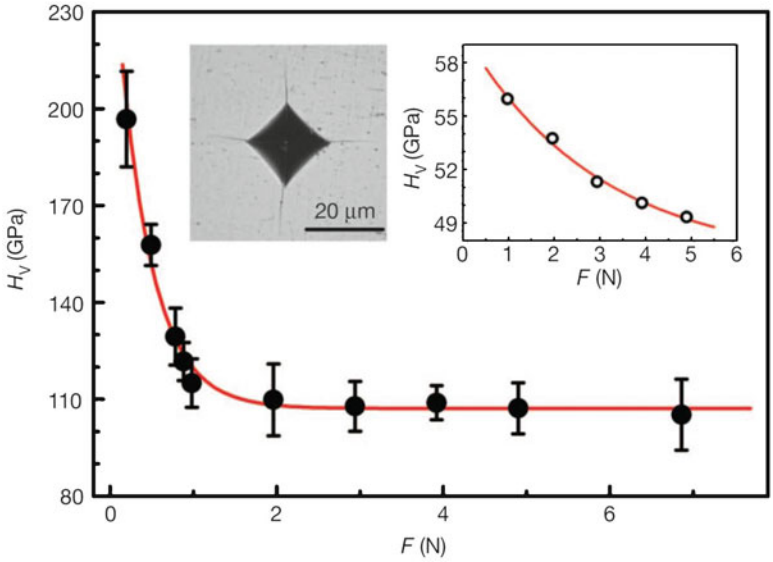

Fig. 6.7 Vickers hardness of nanotwinned c-BN vs. applied load and SE micrograph of an indent at a large load of 19.6 N. The *inset* on the *right* shows the hardness of bulk c-BN vs. applied load (From Tian et al. (2013) with permission)

hypothesis. In the nt-c-BN, the average distance between the twins was about 3.8 nm, and the hardness reached load-invariant value of 108 GPa at a load of$\geq$ 1.5 N. The material has been prepared by HTHP treatment of a special turbostratic onion-like BN nanoparticle precursor material. The usual HTHP synthesis of c-BN from the hexagonal "graphite-like" boron nitride yields nanocrystalline material with grain size$\geq$ 10 nm (Sumiya et al. 2000; Dub and Petrusha 2006; Dubrovinskaia et al. 2007; Solozhenko et al. 2012). These nanograins c-BN and c- and w-BN nanocomposites reach hardness of "only"$\leq$ 85 GPa because they have large-angle grain boundaries.

Figure 6.7 shows the Vickers hardness of nt-c-BN vs. the applied load and a scanning electron micrograph (SEM) image of an indent at a large load of 19.6 N. Obviously, the load-invariant hardness is reached already at a relatively low load of 1–1.5 N, whereas for bulk c-BN, the hardness continues to decrease even at a load of 5 N (see inset on the upper right-hand side of Fig. 6.7). The nanotwinned c-BN has also high toughness of $\geq$ 12 MPa $\cdot$ m$^{0.5}$ which is much higher than that of bulk c-BN of about 2.8 MPa $\cdot$ m$^{0.5}$ and higher oxidation resistance than c-BN. We refer to the paper of Tian et al. for further details.

The ultrahard nanotwinned diamond has been prepared from onion-like carbon by HTHP synthesis in a similar way as the nt-c-BN (Huang et al. 2014). Figure 6.8a shows the distribution of the twin thickness measured by high-resolution transmission electron microscopy (HRTEM), and Fig. 6.8b shows the hardness vs. the applied load. The average thickness of the twins of 5 nm is close to that of nt-c-BN, but the load-invariant hardness of about 200 GPa is much higher than that of nt-c-BN and of natural diamond.

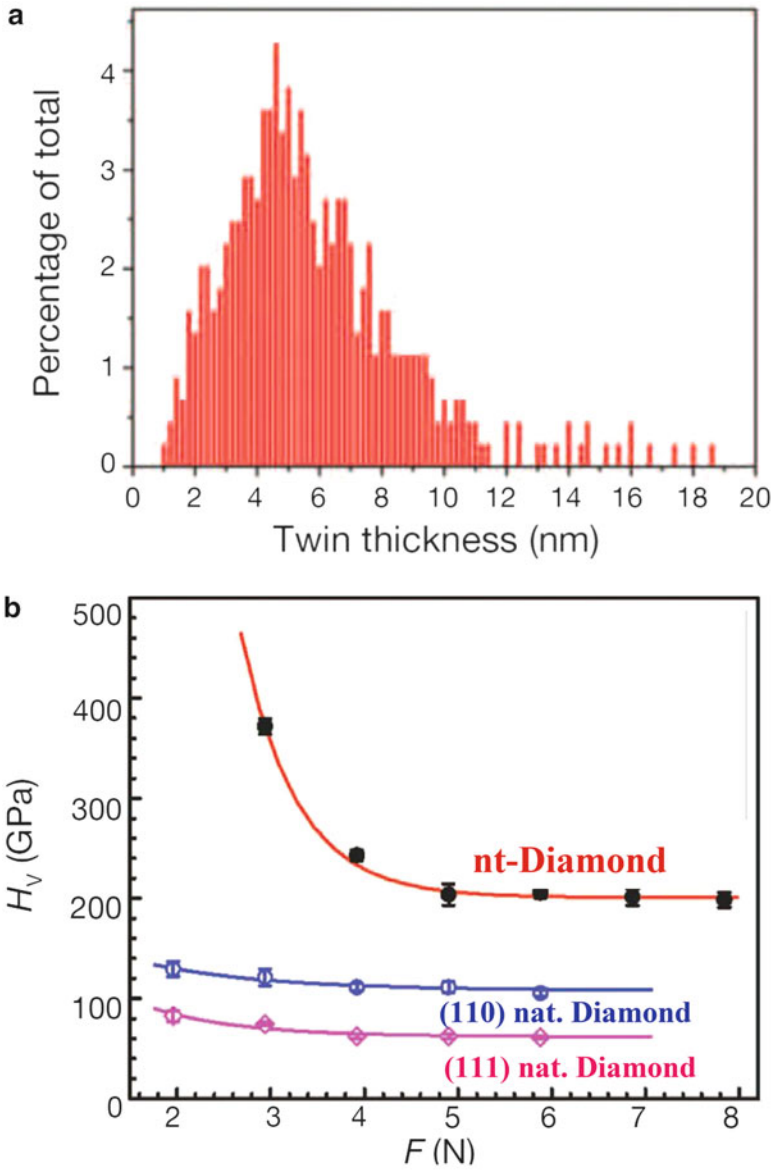

Fig. 6.8 (**a**) Distribution of the thickness of the nanotwins measured by HRTEM yielding an average value of about 5 nm, (**b**) Vickers hardness of nt-diamond (*red*), (110) (*blue*), and (111) face of natural diamond vs. applied load (From Huang et al. (2014) with permission)

A critical reader will ask how it is possible to measure such a high hardness using diamond indenter with a lower hardness of 70–100 GPa. This is indeed possible because the indenter is loaded mainly in compression, whereas the material being indented is loaded in shear, as shown by the slip-line field theory (Hill 1950) and

illustrated in Fig. 13.8 in McClintock and Argon (1966) to which we refer for further details. Figure 29 in Veprek (2013) shows that the materials flow in the diamond indenter under the load and within the contact with the material being indented occurs directed into the indenter, as expected under a pressure loading. Diamond, like other materials with cubic structure, sustains up to eight times larger load in compression than in shear (Eremets et al. 2005; Field 1992). We emphasize this point here, because the work of Tian and Huang has been criticized in a harsh manner using incompetent arguments that "one cannot measure hardness higher than diamond using diamond indenter" (Saxonian 2015).

We believe that these three examples strongly support the concept for the design of extrinsically superhard, nanostructured material with low-energy grain boundaries. As shown by the example of the Mg alloy, this concept is not limited to superhard materials only, but it applies generally for the design of strong and tough materials. The disadvantage of the HTHP synthesis is so far the small size of the samples which can be prepared. The Mg alloys with the nanosized stacking faults have been prepared by severe plastic deformation using repeated rolling, which is a technique applied on industrial scale to produce large metal sheets. Nevertheless, there is some hope that the HTHP techniques for the synthesis of nt-c-BN and nt-diamond can be further developed and scaled for industrial production.

2.5 *Superhard Nanocomposites with Strengthened Interfacial Layer*

In this section, we shall discuss the superhard nanocomposites consisting of nanocrystals of certain transition metal nitrides embedded in a thin interfacial layer of silicon nitride. These materials can reach a very high hardness of more than 100 GPa when correctly prepared and sufficiently free of impurities, mainly oxygen. They are produced by plasma chemical or physical vapor deposition (P-CVD or PVD) as thin films and can be applied as wear-protection coatings on tools for machining, forming, stamping, injection molding, and the like. The Czech company SHM has pioneered the industrialization of these coatings since 1996 when tools for machining coated with the nc-$(Ti_{1-x}Al_x)N/Si_3N_4$ nanocomposites were offered on the market for the first time. We shall discuss the generic concept for their design, the properties of the nanocomposites, and their limitations as regards the choice of the system and purity. It will be shown that not all systems meet the conditions needed to reach superhardness, and those which do meet them can reach high hardness only when carefully prepared and free of impurities. We shall start with the nc-TiN/Si_3N_4 nanocomposites because majority of the information is available for this system. Afterward, we shall discuss which of the other TmN/Si_3N_4 and TmN/XY systems (Tm, transition metal; XY another covalent compound instead of Si_3N_4) can meet the requirements to be superhard, and we shall finish with a brief summary of the industrial application.

A short remark: Attempts to prepare the nc-TiN/Si_3N_4 nanocomposites as bulk ceramics by means of high-temperature high-pressure sintering have brought only limited yet important improvement in the hardness and fracture toughness to 25 GPa and 6 MPa $\cdot$ $m^{0.5}$, respectively. In this case, the grain size varied between 33 and 340 nm (Bläß et al. 2015).

2.5.1 Superhard nc-TiN/Si_3N_4 Nanocomposites as a Model System

The Role of the Interfaces

Figure 6.9a shows the hardness enhancement of nc-TiN/Si_3N_4, nc-W_2N/Si_3N_4, and nc-VN/Si_3N_4 superhard nanocomposites as function of the Si content (Veprek and Veprek-Heijman 2007), and Fig. 6.9b shows the dependence of the lattice dilatation of nanocrystalline silicon (nc-Si) and of the TiN nanocrystals in nc-TiN/Si_3N_4 superhard nanocomposites as function of the crystallite size. In Fig. 6.9b, the values for nc-Si have been extracted from Veprek et al. (1982), whereas those for the nc-TiN/Si_3N_4 nanocomposites were taken from Veprek and Reiprich (1995). The crystallite size of nc-Si has been controlled by the deposition temperature between about 80 °C and 300 °C. In the case of the nanocomposites, the deposition temperature has been kept constant at 550 °C, and the size of the TiN nanocrystals was dependent on the content of Si_3N_4 as seen in Fig. 6.9a.

The hardness enhancement by a factor of up to 3.6 is achieved when the thickness of the Si_3N_4 interfacial layer is about one monolayer (1 ML) at Si content of about 7 % in all three nanocomposites, but this enhancement is lost when the thickness reaches 2 ML, i.e., Si content of about 14 % (Fig. 6.9a). At the maximum hardness, the crystalline size decreases to about 3 nm, and upon further increase of the Si_3N_4 layer thickness, the crystallite size increases again. This increase has been found only when the nanocomposites were deposited by P-CVD in high-frequency glow discharge where the bombardment of the growing film by energetic ions was negligible (Veprek and Reiprich 1995). When the deposition has been done under condition of energetic ion bombardment, the crystallite size decreased with increasing Si_3N_4 content in a similar manner to about 3 nm but remained constant upon a further increase of Si_3N_4 because of the effect of ion bombardment. The strain seen in Fig. 6.9b increases with increasing Si_3N_4 content up to the maximum hardness and minimum crystallite size and decreases again upon a further increase of the Si_3N_4 content [see Fig. 3 in Veprek et al. (2000)].

In order to understand this behavior, we have to briefly discuss the nc-Si first (Veprek et al. 1982). There is a density deficit within the grain boundaries of polycrystalline materials which imposes a tensile strain on the Si nanocrystals. For a crystallite size of < 10 nm, this appears as dilatation of the lattice parameter of the Si nanocrystals that has been measured by X-ray diffraction (XRD). This dilatation increases with decreasing crystallite size because there are less Si atoms balancing the stress from the grain boundaries by elastic elongation of the Si-Si bonds. Therefore, also the elastic strain energy increases. When, at the

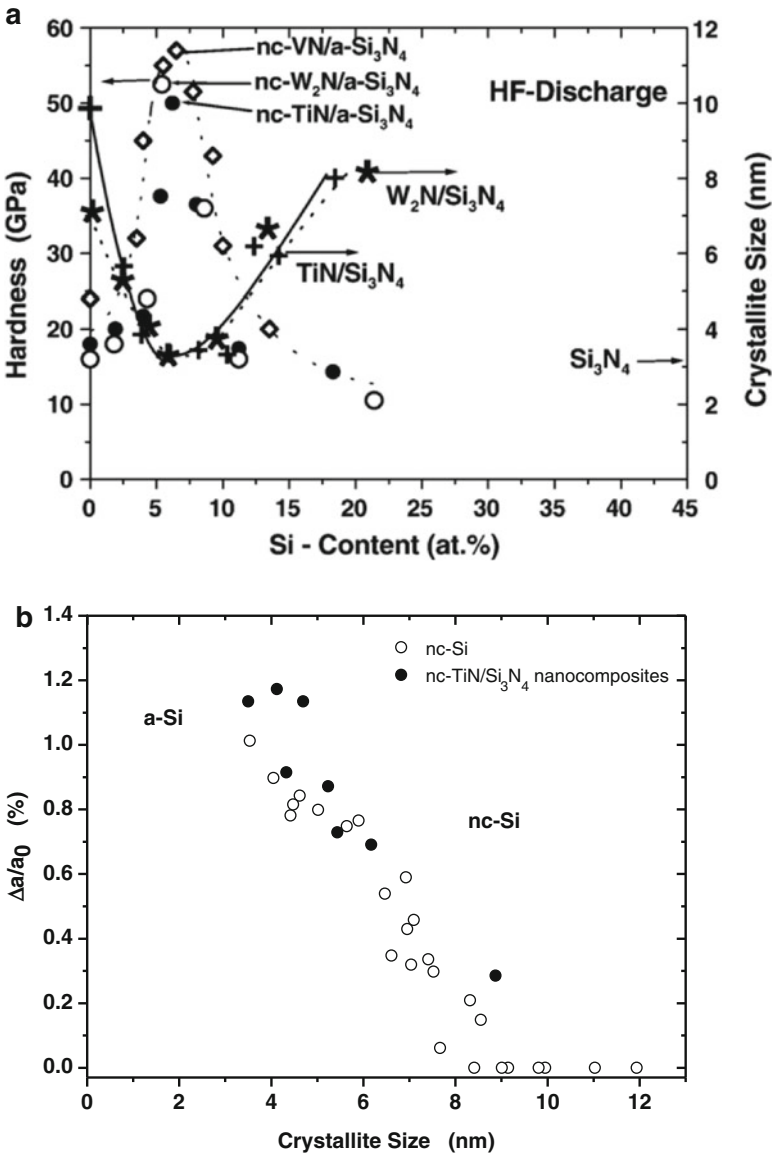

Fig. 6.9 (**a**) Hardness and crystallite size as function of silicon content for three nc-TmN/Si_3N_4 nanocomposites. Notice that all silicon was present as Si_3N_4, not dissolved in TiN (from Veprek and Veprek-Heijman (2007) with permission) and (**b**) lattice dilatation due to the tensile strain within the grain boundaries for nanocrystalline silicon nc-Si and superhard nc-TiN/Si_3N_4 nanocomposites

crystallite size of about 3.5 nm, the strain reaches $\geq 1\,\%$ (corresponding to a "negative pressure" of about 10 GPa), the elastic strain energy is equal to the excess energy of amorphous silicon (a-Si), i.e., nc-Si is unstable with respect to a-Si for a smaller crystallite size (for further details, see Veprek et al. 1982).

The situation is more complex in the nanocomposites because of several reasons: The lattice misfit between TiN and Si_3N_4 contributes to the measured lattice dilatation which reaches 1.2 % for the smallest crystallite size of about 3 nm. However, with a further increase of the silicon nitride content, the lattice dilatation of the TiN nanocrystals decreases because the thicker Si_3N_4 interfacial layer, which is weaker than the TiN, compensates the strain [see Fig. 5 in Veprek and Reiprich (1995)]. This explains why there is a minimum crystallite size of about 3 nm in the nanocomposites and why the TiN remains crystalline. It should be mentioned that due to the measured strain, there is a large random stress in the nanocomposites reaching a value of about 7–10 GPa for the smallest crystallite size [see Fig. 5 in Niederhofer et al. (1999)].

Strengthening of the Interfacial Si_3N_4 Layer. The question arises as to why the system chooses minimum crystallite size when the hardness reaches a maximum? The grain boundaries have excess energy and, therefore, destabilize any polycrystalline system. This is the general reason for recrystallization and coarsening of small-grain polycrystals upon annealing ("Ostwald ripening"). The only logical explanation of the behavior observed in the three nc-TmN/Si_3N_4 systems (Fig. 6.9a) was that the nc-TmN/1 ML-Si_3N_4/nc-TmN interface is somewhat stabilized as compared to conventional large-angle grain boundaries in polycrystalline TmN. This suggestion caused for many years controversial discussions with the specialists, until first-principle density functional theory (DFT) calculations confirmed it. We shall briefly summarize the understanding of the nc-TiN/Si_3N_4 nanocomposites that has been achieved so far.

Hao et al. conducted the first DFT investigations into the nc-TiN/Si_3N_4 nanocomposites (Hao et al. 2006a, b). These researchers have shown that the tensile strength of the 1 ML Si_3N_4-like[1] interfacial layer is larger than that of an ideal Si_3N_4 single crystal. More detailed DFT studies of this system by Zhang et al. have shown that the SiN_x interfacial layer is strengthened by valence charge transfer from the TiN nanocrystals (Zhang et al. 2009a, b). The valence charge transfer is a consequence of the fact that the electronegativity of Si (1.8) is larger than that of Ti (1.5). To illustrate this strengthening, we reproduce in Fig. 6.10 the valence charge density difference (VCDD) of the TiN(111)/1 ML-SiN/TiN(111) interface.

[1] The stoichiometry of 1 ML thick interfacial layer between TiN slabs deviates from that of the Si_3N_4 depending on the (hkl) nature of the interface. We write Si_3N_4-like because the X-ray photoelectron spectroscopic (XPS) studies have shown that silicon is fourfold coordinated to nitrogen like in Si_3N_4 crystal.

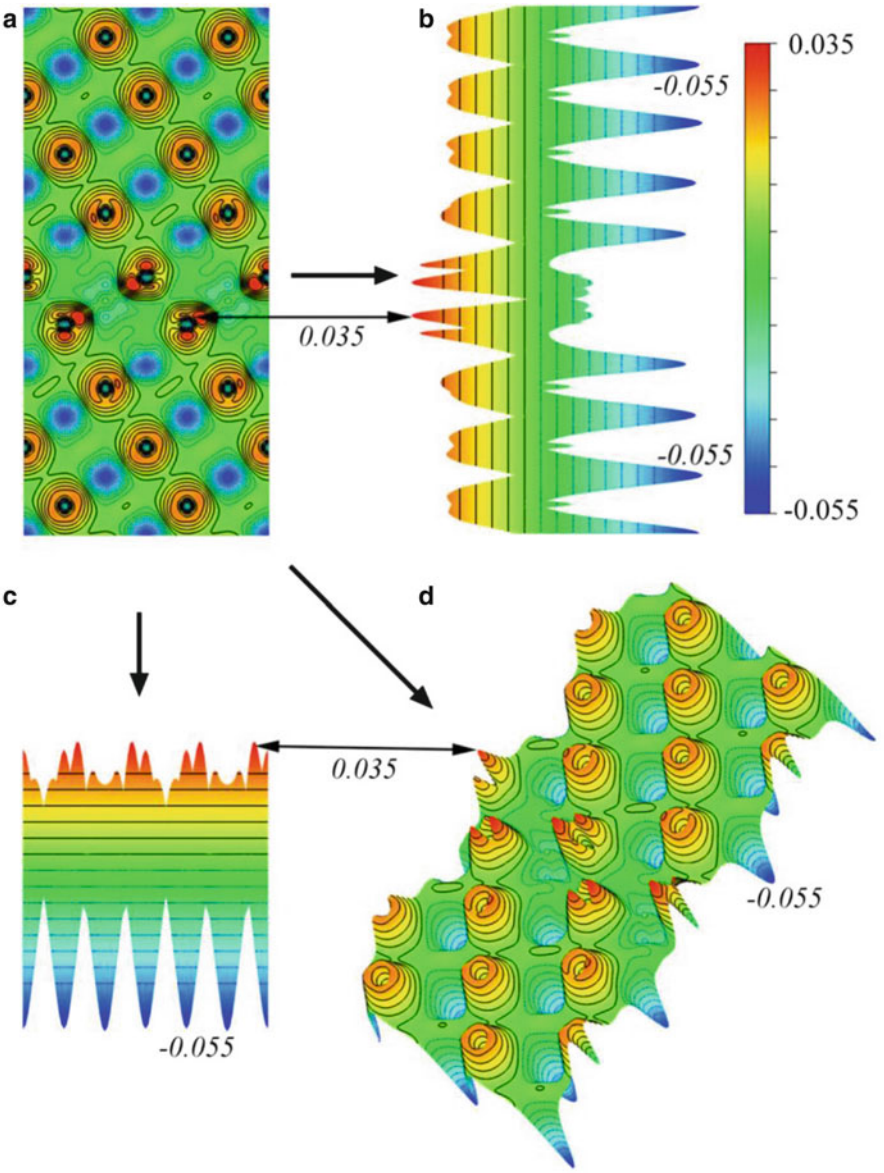

Fig. 6.10 (*Color online*) (**a**) Valence charge density difference of the TiN(111)/1 ML-SiN/TiN (111) interface and the corresponding bird's eye view profile seen from different directions marked by *arrows*: (**b**) *left view* and (**c**) *top view* and (**d**) *side view*. The color scale runs from −0.055 at *bottom blue* to 0.035 electrons/Bohr3 at *top red*. The small (*black*) *italic numbers* indicate the values of the valence charge density difference (From Zhang et al. (2009b) with permission)

Because the VCDD on nitrogen within the SiN layer is higher than that on nitrogen in the TiN and also the VCDD on Si is higher than the VCDD on Ti, it is clear that the 1 ML SiN interfacial layer is strengthened in agreement with the calculations of Hao et al. However, this does not mean that the whole TiN/1 ML-SiN/TiN interface is stronger than the ideal TiN single crystal. As a consequence of the valence charge transfer, the Ti-N bonds in the TiN nanocrystals close to the Si_3N_4 interface are weakened and thus represent the weak links in the system where, upon a tensile or shear load, the decohesion or shear occurs. For further details, we refer to the quoted papers (Zhang et al. 2009a, b).

Here we shall only explain the experimental observation seen in Fig. 6.9a that the hardness enhancement is lost when the Si_3N_4-like interfacial layer is 2 ML thick. In the case of 2 ML thick interfacial Si_3N_4 layer, the weakening of the Ti-N bonds due to the valence charge transfer to the 2 ML interfacial layer is too large and the whole system loses its strength enhancement. Upon a tensile load, the decohesion occurs at the interface between the SiN (or Si_3N_4) and TiN [for further details, see Zhang et al. (2010b); Ivashchenko et al. (2015)]. To summarize, because TiN is much stronger than Si_3N_4, the nanocomposites gain hardness when the interfacial Si_3N_4-like layer is one monolayer thin, but this enhancement is lost when the thickness is two monolayers or more, because too much valence charge density is transferred from TiN to the ≥ 2 ML SiN_x.

The limitation of the DFT is that it assumes a system with the atoms at rest, which means that the calculations are limited to 0 K. Therefore, Ivashchenko et al. conducted comparative studies by means of first-principle quantum molecular dynamics (QMD) that allows for thermal motions of the atoms (phonons) and conducts the DFT calculations in small time steps of this motion. Such calculations are very much computing time-consuming. Nevertheless, the calculations performed so far confirmed all essential results obtained in the earlier DFT studies by Zhang et al. which have been done for pseudomorphologically stabilized fcc-SiN that is unstable as bulk crystal. Ivashchenko et al. included in their calculations also Si_3N_4-like interfacial layers.

Interestingly, these researchers have found that the fcc-(111)-1 ML-SiN interfacial layer is stable also at very high temperatures although, according to the ordinary thermodynamics at macroscale, it should decompose according to the reaction $4SiN \rightarrow Si_3N_4 + Si$. This stability at nanoscale is probably due to the fact that for the decomposition reaction to occur, several atoms have to move simultaneously, i.e., the reaction requires a minimum volume for the "nucleation," which is difficult to occur in 1 ML layer. This example shows that also interfaces, which are unstable at macroscale, should not be ruled out at nanoscale. We still know very little about the nature of the interfaces in the nanocomposites. We refer to the relevant papers of Ivashchenko et al. for further details (Ivashchenko et al. 2012, 2015).

The Theoretically Achievable Hardness of the nc-TiN/Si_3N_4 Nanocomposites

The DFT and QMD studies enabled to calculate the shear resistance of the interfaces for a variety of (hkl) interfaces. These are of course lower than the ideal shear strengths of TiN single crystal. However, one has to remember that under the conditions of fully developed plasticity, where the correct, load-invariant hardness is measured, there is no ideal crystal but many defects, such as dislocations, grain boundaries, and in some cases metastable or unstable phases with much lower shear resistance as discussed above. Therefore, the values of shear resistance of a variety of (hkl) interfaces between about 11.5 and 22 GPa calculated by DFT (Veprek et al. 2007) and about 15–32 GPa calculated by QMD (Ivashchenko et al. 2015) can be used as shear resistances of the interfaces in the nanocomposites where the plastic flow occurs. We refer to these papers for further detail of the calculations. Here we only state that these calculations yielded an achievable hardness of the nanocomposites of 130–170 GPa, significantly above the hardness of natural diamond.

Therefore the experimental results published earlier by Veprek's group on the hardness of the nc-TiN/Si_3N_4 nanocomposites up to 70 GPa (see Fig. 6.11) and for the quasi-ternary nc-TiN/Si_3N_4/$TiSi_2$ nanocomposites above 100 GPa [see Fig. 5b in Veprek and Veprek-Heijman (2012) and Fig. 4.6b in Chap. 4 of this book] can be understood also from the theoretical point of view: There is no dislocation activity in 3 nm small nanocrystals whose strengths approach the ideal strength of a perfect single crystal. The high-pressure XRD studies of Prilliman et al. have shown that the TiN nanocrystals deform only elastically and the grain boundaries are the carrier of the plastic flow (Prilliman et al. 2006). Therefore, the plastic resistance of the grain boundaries determines the strength and hardness of the nanocomposites. And because the interfaces in the nc-TiN/Si_3N_4 nanocomposites are strengthened by the valence charge transfer, their plastic flow resistance is significantly higher than that of ordinary large-angle grain boundaries in highly deformed polycrystalline TiN.

Of course, there are still many open questions. The DFT and QMD calculations have been done for selected (hkl) interfaces in the TiN/SiN_x/TiN heterostructures, whereas the nanocomposites consist of an unknown variety of (hkl) interface which are only 1–2 nm small. Moreover, there are many boundaries between these small interfaces and also triple junctions whose role is difficult to estimate (see, e.g., Zhao et al. 2011, 2012). Therefore, it is difficult to know what exactly is happening in these nanosized grain boundaries upon a load. Nevertheless, the DFT and QMD calculations provide a solid basis for the understanding of the very high hardness in the nanocomposites.

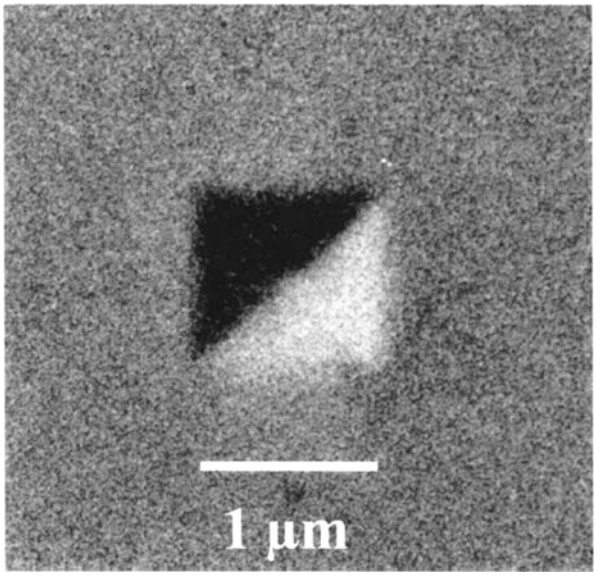

Fig. 6.11 SE micrograph of an indentation into 8 μm thick nc-TiN/a-Si_3N_4 nanocomposite coating with a Vickers diamond indenter at a load of 110 mN (From Veprek and Veprek-Heijman (2012) with permission)

The Mechanism of the Formation of the Nanocomposites

When the nc-TiN/Si_3N_4 (and related) nanocomposites are deposited by PVD or P-CVD, the individual atoms are arriving at the surface of the growing film randomly, i.e., a homogeneous solid Ti_x-Si_y-N_z solution is formed with composition given by the deposition parameters used. This solid solution has to decompose forming the nc-TiN/Si_3N_4 nanocomposite. In this system, the decomposition occurs by spinodal mechanism.[2] Figure 6.12 shows the Gibbs free energy for the Ti_x-Si_y-N_z system calculated by means of a semiempirical thermodynamics formula based on the sub-lattice model for different activities of nitrogen (Zhang and Veprek 2006). In later work, a combined DFT calculation and thermodynamical modeling have been used and very similar results have been obtained (Zhang and Veprek 2008). As one can see in Fig. 6.12, the system is chemically spinodal within the whole range of the composition even at the lowest nitrogen pressure used during PVD. At the composition corresponding to the 1 ML of interfacial Si_3N_4 (i.e., the maximum hardness), the de-mixing energy is more than 300 kJ/mol, about two orders of magnitude larger than in typical metallic alloys. This is a very high de-mixing energy. Therefore, the system is spinodal even if there is a certain lattice

[2] The term "spinodal" has been introduced by Van der Waals as a footnote in his Ph.D thesis, without any particular linguistic meaning, to assign the part of his isotherm between the binodal points where the second derivative is negative. Spinodal decompositions of a solid solution (or, e.g., copolymers) occur when the second derivative of the Gibbs free energy of that solution is negative, i.e., the system is inherently thermodynamically unstable [see Zhang and Veprek (2006) and references therein].

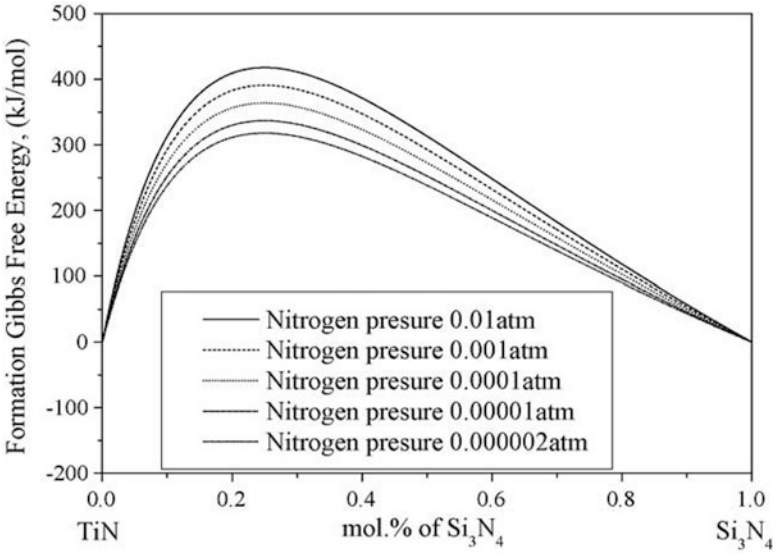

Fig. 6.12 Gibbs free energy of the formation of mixed TiN+ Si_3N_4 system at temperature of 873 K (corresponding to the *upper* limit of the deposition temperature used) for five different pressures of nitrogen used in the experimental work. TiN and Si_3N_4 have been taken as the reference phases (From Zhang and Veprek (2006) with permission)

mismatch between the TiN and Si_3N_4-like interfacial layer [for the details of the calculation, see Zhang and Veprek (2006)]. Because the spinodal decomposition yields a nanostructure with well-defined periodicity (Schmalzried 1995; Porter and Easterling 2001), there is a narrow size distribution of the TiN nanocrystals, as observed experimentally by means of HRTEM (Christiansen et al. 1998).

It should be emphasized that Christiansen et al. studied several nc-TiN/Si_3N_4 samples with different Si_3N_4 content up to 15 at.% of Si where the hardness enhancement is already lost (c.f. Fig. 6.9a). For each sample, several tens of HRTEM micrographs have been done and investigated. The nanostructures seen in the HRTEM micrographs were the same in plain as well as in cross-sectional view, and there was no indication of any columnar morphology, in contrast to many later reports of other groups (see later). The TiN nanocrystals were randomly oriented and of fairly regular shape with a narrow size distribution. (The random distribution of the TiN nanocrystals has also been confirmed by XRD [see Fig. 3 in Niederhofer et al. (1999)].) All the several hundred TiN nanocrystals investigated were without any defects, such as dissolved Si or oxygen. This is in agreement with the XPS studies mentioned above and with the fact that stoichiometric and pure transition metal nitrides and Si_3N_4 are immiscible (Rogl and Schuster 1992). As we shall show later, the "miscibility of Si in TiN" and columnar morphology reported in some later papers is due to oxygen impurities or other defects.

Conditions Needed to Assure that the Spinodal Decomposition Will Occur During the Deposition. The nitrogen activity (partial pressure) during the deposition is the thermodynamic driving force for the decomposition of an unstable Tm-Si-N solid solution. The rate of the decomposition is kinetically controlled by diffusion. Therefore, both the nitrogen pressure and the deposition temperature must be sufficiently high to assure that the spinodal decomposition and formation of stable nanostructure are completed during the deposition. Moreover, because the maximum hardness is achieved when the interfacial Si_3N_4 layer is about 1 ML thick, the Tm-Si-N system must be spinodal with a high de-mixing energy, because only in such a case the interfaces can be sharp (Veprek and Reiprich 1995). Figure 6.12 shows that even at the relatively low nitrogen pressure used in PVD, the Ti-Si-N system is spinodal. It has been found experimentally (Veprek and Reiprich 1995), and later on calculated from the known diffusion coefficients (Veprek et al. 2006), that a deposition temperature of ≥ 550 °C is needed to assure that the nanostructure will form during the deposition.

When these conditions are met, superhard nc-TiN/Si_3N_4 nanocomposites with hardness of about 70 GPa can be prepared as shown in Fig. 6.11 (Veprek and Veprek-Heijman 2012). The scanning electron micrograph (SEM) shows an indentation into 8 μm thick nc-TiN/Si_3N_4 nanocomposite coating with a Vickers diamond indenter at a load of 110 mN. One notices that a plastically deformed indentation area of 1 μm^2 ($=10^{-12}$ m^2) produced under a load of 100 mN corresponds to a Meyer hardness of 0.1 $N/10^{-12}$ $m^2 = 10^{11}$ $N/m^2 = 100$ GPa.[3] For a Vickers indenter of an ideal shape, the Meyer and Vickers hardness is related to as $H_{Vickers} = 0.927\ H_{Meyer's}$ (Tabor 1951). But because the diamond indenter deforms plastically upon indentation into superhard materials until the tip becomes dull with a radius of 0.5–0.7 μm (Veprek-Heijman et al. 2009), the Vickers and Meyer hardness is for a relatively small indentation shown in Fig. 6.11 almost identical.

In order to achieve such a high and long-term stable hardness, one must meet the conditions outlined above and the oxygen impurities must not exceed 100–200 ppm. Hardness in excess of 100 GPa has been obtained in the quasi-ternary nc-TiN/Si_3N_4/$TiSi_2$ nanocomposites [see Fig. 4.6 in Chap. 4 of this book and also Fig. 5 in Veprek and Veprek-Heijman (2012)] because the $TiSi_2$ is efficiently trapping the minor oxygen impurities. However, these nanocomposites lose the high hardness after 4–6 months because of degradation of the $TiSi_2$ as shown already in Veprek et al. (2005a) and discussed in some details recently (Veprek 2013). We refer to these papers for further details.

In conclusion to this section, long-term stable quasi-binary nc-TiN/Si_3N_4 nanocomposites with hardness of about 70 GPa have been prepared when the oxygen impurities were very low of about 100 ppm. Furthermore, many nc-TmN/

[3] Meyer's and Vickers hardness is the applied load divided by the projected and total contact area of the indent, respectively.

Si_3N_4 coatings with hardness ≥ 50 GPa have been prepared when the oxygen impurities did not exceed several 100 ppm (Veprek et al. 2000; Veprek and Veprek-Heijman 2012; Veprek 2013). We refer to these papers for further detail. On the basis of several papers published by other groups, it has been shown that when these conditions are not fulfilled, superhard nanocomposites cannot be obtained (Veprek et al. 2006). This will be the subject of the next session.

Impurities and Inappropriate Deposition Conditions Are Limiting the Achievable Hardness of the Nanocomposites

The failure of several groups to obtain the high hardness in the nc-TiN/Si_3N_4 nanocomposites has been either due to inappropriate deposition conditions used (mainly a too low temperature) or oxygen impurities as already discussed several years ago (Veprek et al. 2006; Veprek and Veprek-Heijman 2012). This is illustrated in Fig. 6.13 that shows the maximum achievable hardness in the nc-TiN/Si_3N_4 nanocomposite coatings as a function of oxygen impurities (Veprek et al. 2005b). It should be noted that there are results from five different P-CVD and PVD apparatuses from three different countries. Since writing that paper more than 10 years ago, many more results could be added in the range of oxygen impurity of > 0.5 % and hardness below 40 GPa, but we believe that the data in Fig. 6.13 are

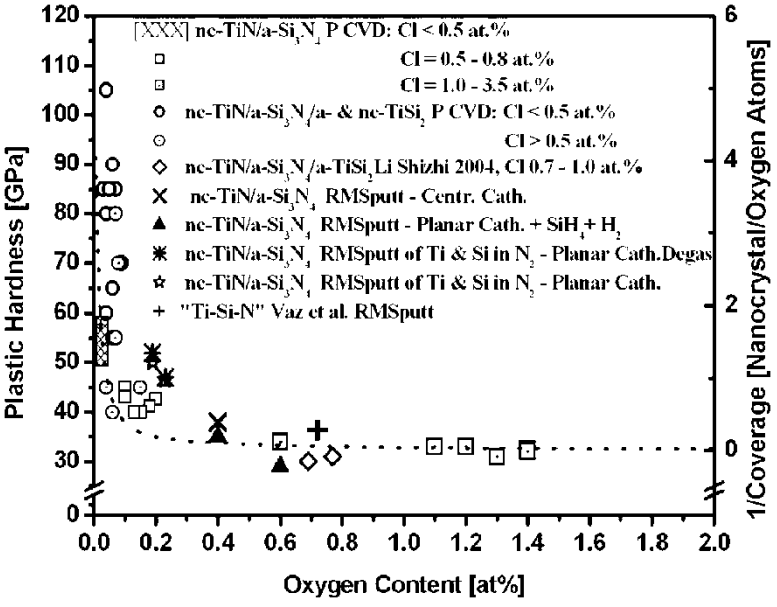

Fig. 6.13 Maximum achievable hardness in the nc-TiN/Si_3N_4 nanocomposite coatings vs. oxygen impurities. Note that there are results from five different P-CVD and PVD apparatuses from three different countries (From Veprek et al. (2005b) with permission)

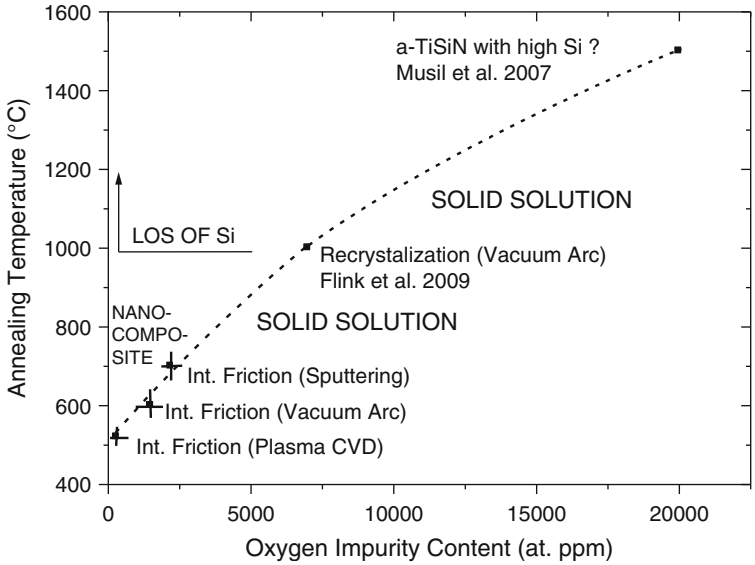

Fig. 6.14 Temperature needed for the decomposition of the Ti-Si-N solid solution and the formation of stable nc-TiN/Si_3N_4 nanostructure (the three points denoted "Int. Friction" on the *left*), the recrystallization of the solid solution, and the stability limit of Ti-Si-N coatings with high Si content (From Veprek and Veprek-Heijman (2012) with permission)

sufficient to show the critical role of oxygen impurities. The high hardness of $>$ 40–50 GPa can be achieved only when the oxygen impurity content is of few 100 ppm. The reason is that the Si-O bond is the strongest one within the whole Ti-Si-N (and other Tm-Si-N) system. Therefore, oxygen forms $\equiv$ Si-O-Si $\equiv$ clusters which degrade the interfacial Si_3N_4 layer [see Fig. 2 in Veprek et al. (2005b)] and hinder the diffusion and formation of the nanostructure as we shall discuss now. Other impurities, such as hydrogen and carbon, also degrade the mechanical properties of the nanocomposites (Veprek et al. 2004a), but oxygen is the most "dangerous" impurity because of its high electronegativity and strong Si-O bond.

The temperature needed for the decomposition of the solid solution and formation of the stable nanostructure increases with increasing impurity oxygen content, as shown in Fig. 6.14. The two points denoted "Int. Friction (Plasma CVD)" and "Int. Friction (Sputtering)" on the left lower part correspond to the formation of superhard nc-TiN/Si_3N_4 nanocomposites by P-CVD and reactive magnetron sputtering in the institute of S.V., whereas the point denoted "Int. Friction (Vacuum Arc)" corresponds to nc-($Ti_{1-x}Al_x$)N/Si_3N_4 nanocomposites deposited by vacuum arc in an industrial coating system of the SHM company (SHM). The point "recrystallization (vacuum arc)" corresponds to the "recrystallization" of the Ti-Si-N solid solution "stable" up to this point as reported by Flink et al. (2009), and the point "a-TiSiN with high Si" describes the stability limit of Ti-Si-N coatings with high Si content (Musil et al. 2007).

Flink et al. reported already in 2005 (Flink et al. 2005) about the high stability of the Ti-Si-N solid solution, but in that paper, the concentration of oxygen impurities has not been given. In a later paper, they confirmed the high stability of the solid solution up to 1000 °C and reported also the oxygen impurity content of about 0.7–0.8 % (7000–8000 ppm) for coatings with Si content of 7–9 % where the maximum hardness should be found. However, it is not possible to prepare superhard nanocomposites under such conditions because, as well known from silicon technology, silicon is lost by evaporation of SiO that is volatile above 900 °C. Indeed, using atom probe tomography, Tang et al. did not find any Si_3N_4-like interfacial layer in Ti-Si-N coatings with oxygen impurity content of about 1.2–1.4 at.% (Tang et al. 2010). According to the results shown in Fig. 6.14, the samples used by these researchers would have to be annealed at a high temperature of about 1200 °C to reach the "recrystallization." Flink et al. also reported very high density of dislocations of about $1 \cdot 10^{14}$ cm^{-2} in their Ti-Si-N films and stated that this "corresponds to values found for heavily cold work-hardened material" (Flink et al. 2009). Critical reader will realize that this value is the order of magnitude too high for cold work-hardened material (Argon 2008),[4] but it can be explained by the oxygen impurities: Taking the reported concentration of about 0.8 at.% and assuming that the thickness of the samples used for the TEM study was about 20–30 nm yield the areal density of the O-related defects of about 0.6 to 1×10^{14} cm^{-2}.

When, in a later work, the oxygen impurity has been decreased below the detection limit of 0.1 % (1000 ppm) of the analytic techniques used by this group, the homogeneous solid solution could be grown at 550 °C epitaxially on TiN up to a critical thickness of few tens of nm. The segregation of Si to the grain boundaries was seen for thicker layers, but it seems to be still incomplete (Eriksson et al. 2014). It remains an open question if the TiN and Si_3N_4 phases would segregate completely in these experiments when the oxygen impurity content would be only few 100 ppm. According to our results and those available in the literature (Rogl and Schuster 1992), the segregation will be completed if the impurity content will be sufficiently low.

There is a fundamental question regarding the nanostructure formation in the Ti-Si-N coatings deposited by PVD because all papers known to us reported columnar morphology. In our own studies using reactive magnetron sputtering, we have also observed dense morphology which appeared isotropic in the SEM [see Fig. 14 in Prochazka et al. (2004)], but columnar, although very dense morphology could be seen in HRTEM. However, the oxygen impurity of about 1000–1500 ppm was also much larger in our coatings deposited by reactive sputtering than in the nc-TiN/

[4] At a dislocation concentration of 10^{14} cm^{-2}, the long-range order is lost (Ninomiya 1978) and amorphization occurs (Nastasi et al. 1996). High dislocation density of 10^{14} cm^{-2} can be formed by a powerful 10 ps laser pulse, but the dislocation density quickly decays to 10^{13} cm^{-2} after only 140 ps (Bringa et al. 2006).

Si_3N_4 nanocomposites deposited by P-CVD, which had fully isotropic nature (see above). Nevertheless, the segregation of the TiN and Si_3N_4 has been clearly seen also in our coatings deposited by sputtering [see Fig. 9 in Veprek (2013)]. This question will remain open until someone succeeds to deposit these coatings by sputtering with impurity content of 100 ppm or less.

Coatings deposited by PVD should be also fully segregated nc-TiN/Si_3N_4 nanocomposites because the decomposition of the solid solution occurs by diffusion in the bulk of the growing film for the following reasons: Based on the published values of the diffusion coefficient of Si in TiN, it has been estimated that about 100 s are needed for Si to diffuse over a distance of about 5 nm, which is taken as an approximate criterion for the segregation of the phases, whereas several 1000 s are needed at 300 °C (Veprek et al. 2006; Zhang and Veprek 2006). With the deposition rate of $\geq$ 1.5 nm/s used in our sputtering system (Prochazka et al. 2004), a 5 nm thick layer of the solid solution is deposited within about 3 s, whereas the time needed for Si to diffuse such distance is about 100 s. Therefore, homogeneous solid solution is formed at the surface of the growing films initially during the deposition, and the decomposition of the solid solution and phase segregation occurs by diffusion in the bulk. One often finds a suggestion that the ion bombardment may enhance the diffusion and phase segregation. However, at the high deposition rates, the decomposition of the solid solution by diffusion occurs in the bulk where the ion bombardment does not play any role. Moreover, ion bombardment will enhance mixing.

In the case of the coatings deposited by P-CVD, the deposition rate of 0.5–0.7 nm/s was only slightly lower. Therefore, there seems to be no rational reason why the mechanism of the decomposition of the solid solution and formation of the nanostructure should be different in P-CVD and PVD coatings. All the discrepancies regarding the morphology and achievable hardness appear to be associated with the impurity content.

2.5.2 The Possibility of the Formation of Superhard Nanocomposites in Other Systems

Based on our present understanding of the mechanism of hardness enhancement in the nc-TiN/Si_3N_4 system, the following conditions are needed to achieve hardness enhancement by a factor of 3–5 as compared with the terminal phases which, of course, must be hard: (a) The system must be spinodal with a high de-mixing energy even if the segregated phases are not coherent, (b) the interfacial layer of the covalent XY compound must be stable between the surrounding TmN and another alternate hard material, (c) there must be some mechanism of strengthening of the interfacial XY layer similar to that in the nc-TiN/Si_3N_4 nanocomposites, and (d) the material must be prepared with a sufficiently high purity.

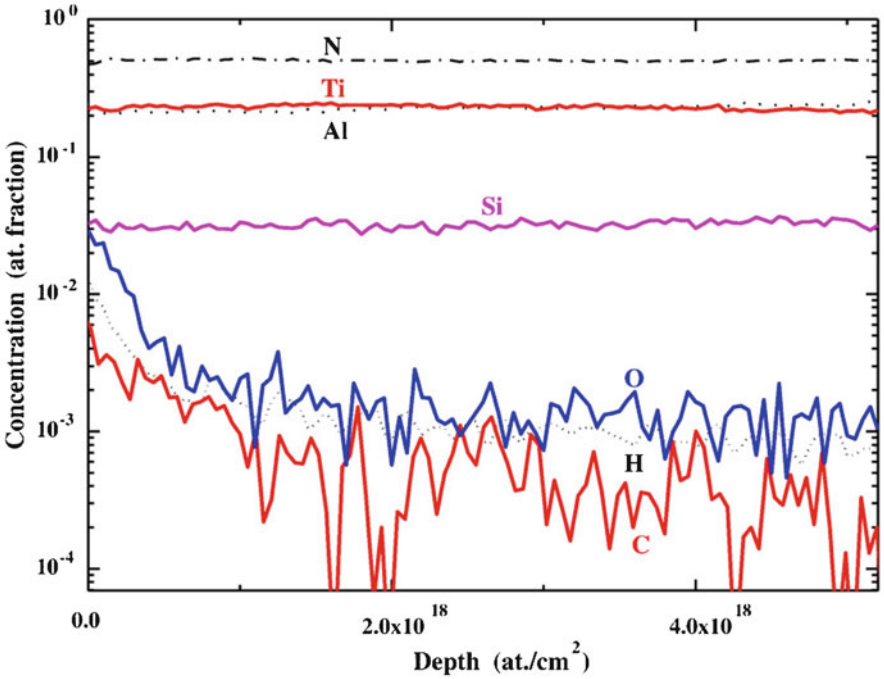

Fig. 6.15 Elastic recoil detection analysis (ERDA) of a typical nc-$(Ti_{1-x}Al_x)N/Si_3N_4$ coatings deposited by vacuum arc evaporation in an industrial coating system of the company SHM (SHM)

Thermodynamics

As shown in Fig. 6.9a, the superhard nc-TmN/Si_3N_4 nanocomposites have also been obtained with W_2N and VN. The company SHM is fabricating nc-$(Ti_{1-x}Al_x)N/Si_3N_4$ and nc-$(Cr_{1-x}Al_x)N/Si_3N_4$ nanocomposite coatings on tools that reach hardness of about 40 GPa when the oxygen impurity content is ≤ 1000 ppm (see Fig. 6.15). The lowest impurity content that has been achieved so far in such coatings deposited in an industrial coating equipment of the SHM company was about 700 ppm [see Fig. 21 in Veprek (2013)]. Thus, an improvement of the impurity by a factor of 3–4 is needed to reach the hardness of ≥ 50 GPa in the industrially produced coatings.

As mentioned, all transition metal nitrides and Si_3N_4 are immiscible, and they should probably decompose by spinodal mechanism, provided the lattice parameters of the TmN and Si_3N_4 do not differ too much. In such case, the only limitation is the stability of the interracial fcc-Si_3N_4-like layer. When the lattice mismatch between the transition metal nitride and Si_3N_4 is too large, the decomposition will not be coherently spinodal.

Using a combined first-principle DFT calculation and thermodynamic modeling, our group has studied a limited number of possible systems. The results are briefly summarized here:

- The Zr-Si-N (Sheng et al. 2008) and Al-Si-N (Sheng et al. 2013) systems are not coherently spinodal and, therefore, should decompose by nucleation and growth without the formation of a sharp interfacial Si_3N_4 layer. Therefore, the hardness enhancement observed in these systems is due to grain refinement only.
- Also the Zr-Al-N system should decompose by nucleation and growth (Sheng et al. 2008), and as we shall see, the fcc-AlN interfacial layer is unstable with ZrN.
- The $Ti_{1-x}B_xN$ system consisting of stoichiometric TiN and BN is chemically spinodal, and superhard nc-TiN/1 ML-BN nanocomposites have been prepared by P-CVD (Karvankova et al. 2006), whereas the frequently reported nitrogen-deficient TiB_xN_{1-x} ("$TiN + TiB_x$") system should decompose by nucleation and growth (Zhang et al. 2008). However, the large difference of the sizes of boron and titanium atoms makes a coherent or semi-coherent interfacial BN layer impossible to form [see Fig. 12a in Karvankova et al. (2006)]. Moreover, the 1 ML of fcc-BN between TiN slabs is unstable already at 0 K (Ivashchenko and Veprek 2013). Therefore, the hardness enhancement observed in the nc-TiN/BN nanocomposites is most probably due to the "strongest size," as seen in Fig. 6.16. The maximum hardness of about 50 GPa is achieved in this system when the surface coverage of the TiN nanocrystals by BN reaches about 1 ML as in the nc-TiN/S_3N_4 system. Moreover, the electronegativity of boron (2.0) is slightly larger than that of silicon (1.8). Therefore, one might believe that the mechanism of the hardness enhancement is similar in both systems. This is however not the case because due to the large misfit between TiN and BN, there are also some Ti-B bonds even at the maximum hardness and 1 ML coverage of TiN nanocrystals with BN (Karvankova et al. 2006). By careful observation (Fig. 6.16), one sees that the maximal hardness correlates with the size of the TiN nanocrystals around 10 nm, i.e., with "the strongest size." Therefore, the hardness enhancement in these nanocomposites is only due to the refinement of the grain size but not due to a "strengthened" interfacial layer.
- This example should be a warning that in many other systems, where a hardness enhancement up to 30–35 GPa has been found upon possible formation of nanocomposites, it was probably solely due to the grain refinement.
- One of the most promising systems is Zr-Al-O because it is chemically spinodal (Sheng et al. 2011a, b) and should have an "infinitive oxidation resistance" which is very important in many industrial applications. However, because the hard corundum α-Al_2O_3 modification forms only at high temperatures of ≥ 1000 °C, the mixed α-$(Al_{1-x}Cr_x)_2O_3$–ZrO_2 and in particular Cr_2O_3–ZrO_2 systems may be more suitable to form hard and superhard nanocomposites. The formation of "Cr-Zr-O" coatings with a pronounced hardness enhancement has been achieved by M. Jilek from the SHM company (Jilek 2012).

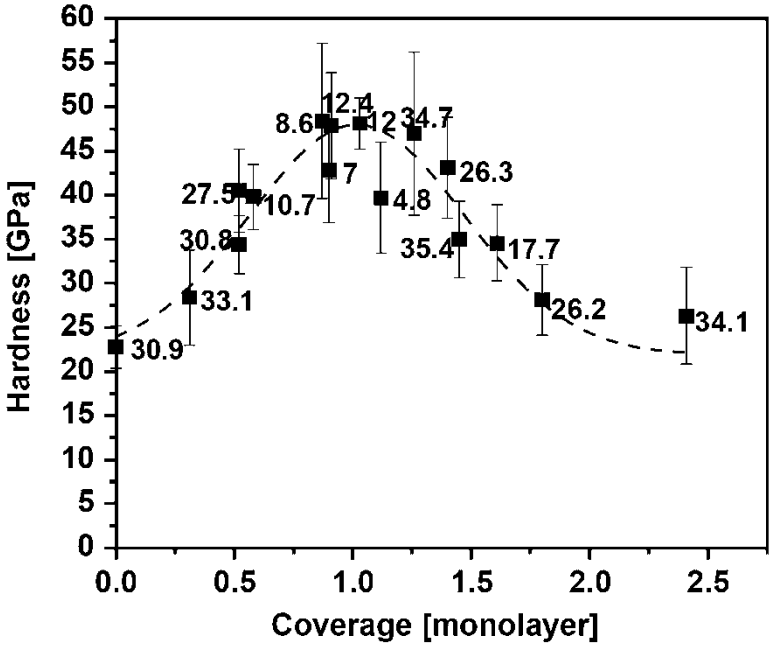

Fig. 6.16 Hardness of nc-TiN/BN nanocomposite coatings vs. surface coverage of the TiN nanocrystals with BN. The numbers are the corresponding size of the TiN nanocrystals (From Karvankova et al. (2006) with permission)

These limited examples clearly show that not all the systems can form superhard nanocomposites with hardness enhancement above 40–50 GPa because the interfacial covalent XY layer is not sharp and not strengthened. The most likely mechanism of the strengthening reported in many papers is due to refinement of the crystallite size. This is most probably valid also for papers reporting on nc-TmN/SiN_x nanocomposites with oxygen impurities of ≥ 0.3–$0.4\,\%$. The combined DFT and thermodynamics studies should be extended to other candidate systems because they are much faster and cheaper than the experimental trial and error approach.

Stability of the Interfacial Si_3N_4 and Alternate XY Layers

There are several ways of how to investigate the stability of the interfacial layer. The DFT method, which yields result at 0 K, does not guarantee that the structure obtained by structural relaxation until a minimum of the total energy has been achieved is really stable. Therefore, one has to study the dynamical phonon stability or artificially distort that structure and observe whether the total energy increases (the structure is stable or metastable in such a case) or decreases, in which case the

structure is unstable. Both approaches have been used to study the stability of the 1 ML-fcc-SiN layers pseudomorphically stabilized between TiN slabs. The artificial distortion approach has been used by Zhang et al. who showed that the fcc-(111)- and fcc-(110)-TiN interfacial monolayers are stable, but the fcc-(001)-SiN one is unstable. However, it has been stabilized by distortion of the Si atoms in (Veprek et al. 2004b) direction by 12 %, where the Si is essentially only fourfold coordinated (Zhang et al. 2009a, b). Marten et al. (2010) conducted the dynamic phonon studies of this system and confirmed the results of Zhang et al. More recently, Ivashchenko et al. used QMD to study this system at high temperatures and confirmed also these results (Ivashchenko et al. 2012). Interestingly, in the QMD calculations of Ivashchenko et al., the distortion of the Si atoms within the 1 ML SiN was random and not regular in the (Veprek et al. 2004b) direction as in the DFT studies of Zhang et al. This is due to the fact that the random distribution decreases the elastic lattice strain and concomitant elastic energy. This is seen as a decrease of the total energy after "annealing" the system to high temperature and "cooling" down to 300 K in a simulated "experiment."

The probably most efficient method is the phonon study of the soft modes, as recently done by Ivashchenko et al. [Ivashchenko et al. (2014); Ivashchenko and Veprek (2013)]. When the structure is stable with respect to a given phonon mode, its phonon vector is real, i.e., small distortions of the atoms from their equilibrium positions are damped. When, however, the structure is unstable upon an infinitesimal deformation corresponding to the given phonon mode that is driving the structural transformation, that phonon will be amplified which shows imaginary phonon vector (Dove 1993). Conventionally, this situation is represented by negative phonon frequencies.

Figure 6.17a shows the frequencies of soft phonon $\Lambda_3[2\pi/a(1/8,1/8,1/8)]$ and $\Delta_5[2\pi/a(1/4,0,0)]$ modes of the B1-AlN interfacial layer as the function of lattice parameters of the surrounding transition metal nitride slabs (Ivashchenko et al. 2014). The frequencies are positive for lattice parameters < 0.44 nm, i.e., an interfacial AlN layer should be stable between the slabs of corresponding nitrides such as TiN, VN, NbN, and the like but unstable, e.g., with ZrN whose lattice parameter is close to 0.47 nm.

However, it remains an open question if one could prepare superhard nanocomposites with a large hardness enhancement in the systems Ti-Al-N, V-Al-N, and Nb-Al-N because although some of them are chemically spinodal, the de-mixing energy is the order of magnitude smaller than that in the Ti-Si-N system, as shown, e.g., for the Ti-Al-N (Zhang and Veprek 2007a) and Cr-Al-N (Zhang and Veprek 2007b) systems. Furthermore, the electronegativity of Al (1.5) is similar or even lower than that of the transition metals mentioned (Ti-1.5, V-1.6, Nb-1.6). Thus, a strengthening of the fcc-AlN interfacial monolayer by valence charge transfer is ruled out. Therefore, superhard nc-TiN/AlN and related nanocomposites with a similar hardness enhancement mechanism as in the nc-TiN/Si_3N_4 system are unlikely to form.

In a similar way, it was shown that fcc-BN interfacial monolayer is unstable for lattice parameter of the TmN larger than about 0.32 nm [see Fig. 1 in Ivashchenko

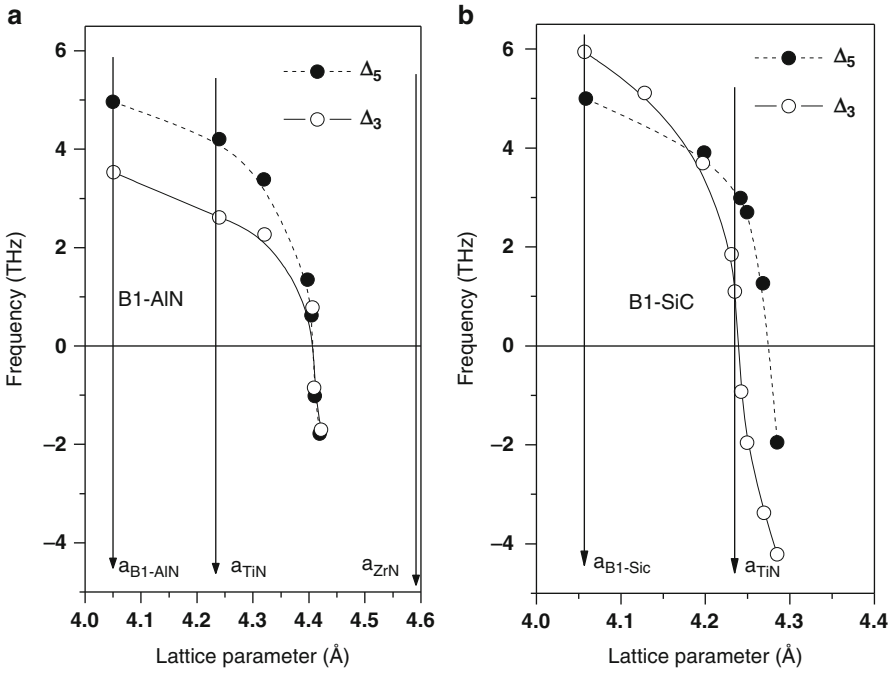

Fig. 6.17 (**a**) Frequencies of soft phonon $\Delta_3[2\pi/a(1/8,1/8,1/8)]$ and $\Delta_5[2\pi/a(1/4,0,0)]$ modes of B1-AlN interfacial layer and (**b**) for B1-SiC interfacial monolayer as function of lattice parameters of the surrounding transition metal nitride slabs (From Ivashchenko et al. (2014) and Ivashchenko and Veprek (2013) with permission)

and Veprek (2013)] which lends a further support to the fact that the hardness enhancement observed in the nc-TiN/BN nanocomposites is simply due to refinement of the grain sites of the TiN, as discussed above.

Interesting is the question if one could use SiC as the interfacial layer because Kong et al. reported significant hardness enhancement in TiN/SiC heterostructures deposited by magnetron sputtering at room temperature with TiN slabs of 4.3 nm and SiC layers of 0.6 nm thickness (Kong et al. 2007). Figure 6.17b shows the phonon frequencies of 1 ML fcc-SiC layer between TmN slabs of different lattice parameters. The lattice parameter of TiN of 0.423 nm is just close to the instability by the soft modes. Therefore, upon heating to 600 K, the fcc-SiC interfacial layer becomes unstable and converts to a disordered structure with broken bonds [see Fig. 3 in Ivashchenko and Veprek (2013)]. Moreover, $TiN_{1-x}C_x$ forms stable substitutional solid solution where carbon atoms replace nitrogen. In $TiN_{1-x}C_x$ deposited by P-CVD at temperature of 560 °C, with increasing fraction of carbon, the hardness increases from that of TiN to that of TiC following the rule of mixtures [see Fig. 8 in Veprek et al. (1996)]. Therefore, even when the TiN/SiC heterostructures deposited at room temperature have shown an interesting hardness enhancement, nc-TiN/SiC nanocomposites cannot be prepared because this system forms a stable solid solution.

In summary to this section, the understanding available to us now suggests that superhard nanocomposites with hardness enhancement by a factor of 3–5 can be formed only in the Tm-Si-N systems where the lattice parameter of the transition metal nitride does not differ too much from that of SiN_x, because only such systems are spinodal with large de-mixing energy, and the interfacial 1 ML SiN_x with silicon fourfold bonded to nitrogen is stable and strengthened by valence charge transfer. In majority of nanocomposites, where some hardness enhancement has been reported, this was due to a simple refinement of the grain size toward the "strongest size."

3 Industrial Applications

As already mentioned, the nc-$(Ti_{1-x}Al_x)N/Si_3N_4$ nanocomposites have been pioneered as wear-protection coatings on tools for machining by Czech company SHM since 1996, followed soon by many other companies. The advantage of the nanocomposites is not only the higher hardness which reduces the abrasion wear but also (an in many cases mainly) their higher oxidation resistance up to above 900 °C, which is about three times better than that of the $(Ti_{1-x}Al_x)N$ coatings, and therefore reduces the chemical wear by oxidation. The nc-$(Cr_{1-x}Al_x)N/Si_3N_4$ nanocomposites show even better oxidation resistance above 1000 °C [see Fig. 10 in Cselle (2005)]. We refer to our reviews for further details and information (Veprek and Veprek-Heijman 2008; Veprek 2013). Here we only emphasize several important points and give some examples of more recent achievements.

The high oxidation resistance is very important because in many machining operations, such as drilling, the cutting edge is running almost dry even when coolants are used. Thus, the number of holes being drilled by drills coated with the nc-$(Ti_{1-x}Al_x)N/Si_3N_4$ nanocomposites is more than factor of 3 larger than that with the conventional $(Ti_{1-x}Al_x)N$ coatings. Moreover, if one can reduce the amount of coolant or even eliminate them in dry machining, one can significantly reduce the overall costs of the machining by up to 30 %.

Besides the high hardness, the nanocomposites also show a very high elastic limit of almost 10 %, which means that they sustain large strain without formation of cracks [see Fig. 9 in Veprek et al. (2003)]. This is particularly important in interrupted cutting, such as milling. However, the "harder" machining and longer lifetime of tool coated with these coatings may result in fatigue of the material of which the tools are made as illustrated by curve 3 in Fig. 6.18. Because the mills coated with the nanocomposites allowed longer lifetime of the tools, fatigue in the cemented carbide of which the tool has been made of caused an unpredictable sudden wear. Such behavior cannot be tolerated because the operator must know when to change the tool to avoid damage to the part being machined. The solution was the TripleCoatings® with about 2 μm thick underlayer of $(Ti_{1-x}Al_x)N$ and about 1 μm top layer of the nc-$(Ti_{1-x}Al_x)N/Si_3N_4$ nanocomposites (Cselle 2008). In such a way, the wear became predictable and the lifetime of the tool has been

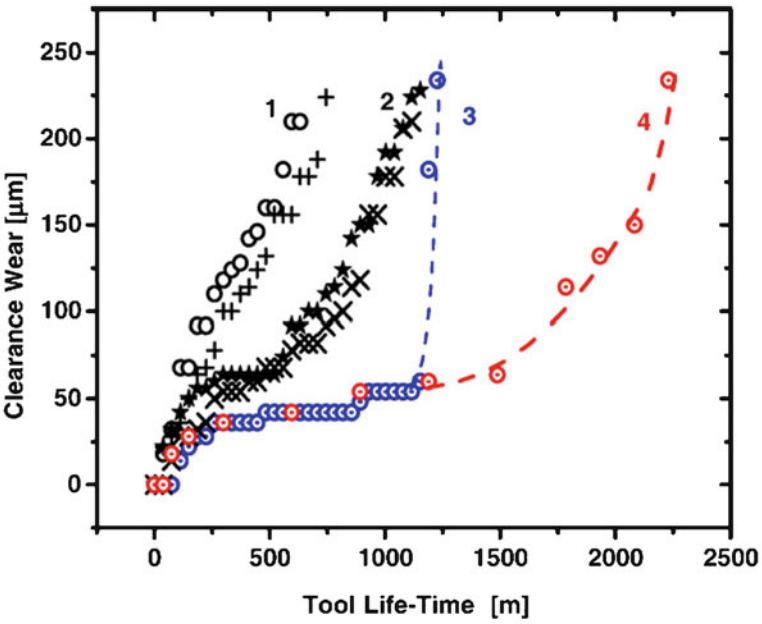

Fig. 6.18 Milling of 56 HRC hard steel using end mils made of cemented carbide coated with different coatings: 1, conventional $(Ti_{1-x}Al_x)N$ coatings from two different manufacturers; 2, "TiSiN" coatings from a foreign company; 3, nc-$(Ti_{1-x}Al_x)N/Si_3N_4$ nanocomposite coatings; and 4, "TripleCoatings®" consisting of about 2 µm thick $(Ti_{1-x}Al_x)N$ border layer and 1 µm thick nc-$(Ti_{1-x}Al_x)N/Si_3N_4$ nanocomposite *top* layer (From Cselle (2005) with permission)

increased by almost a factor of 5 as compared with the conventional $(Ti_{1-x}Al_x)N$ coatings (curve 4 in Fig. 6.18). One can also see that the nc-$(Ti_{1-x}Al_x)N/Si_3N_4$ nanocomposites are significantly better than the nc-TiN/Si_3N_4 ones (curve 2 in Fig. 6.18), probably because of higher oxidation resistance of the former.

The low thermal conductivity of the nanocomposites reduces the flow of heat released due to the machining into the cutting edge. The low thermal conductivity is caused by intense phonon scattering on the grain boundaries of the 3–4 nm small nanocrystals. In the case of "TiSiN" nanocomposite coatings, the thermal conductivity decreased from about 12 $W/m \cdot K$ for TiN to about 1.7 $W/m \cdot K$ for TiSiN nanocomposite coatings with high Si content. For the Al + Si content where the hardness of the coatings reached maximum, the thermal conductivity was about 3 $W/m \cdot K$ (Samani et al. 2013). The thermal conductivity increases with increasing temperature. The lowest thermal conductivity and its lowest increase with temperature have been found for the CrAlSiN nanocomposites (Martan and Benes 2012). A significant decrease of the thermal conductivity has been reported also for TiN/TiAlN multilayers (Samani et al. 2015). The low thermal conductivity of the nanocomposite coatings is of particular interest for tools made of HSS which must not be heated above 530 °C because above that temperature it softens.

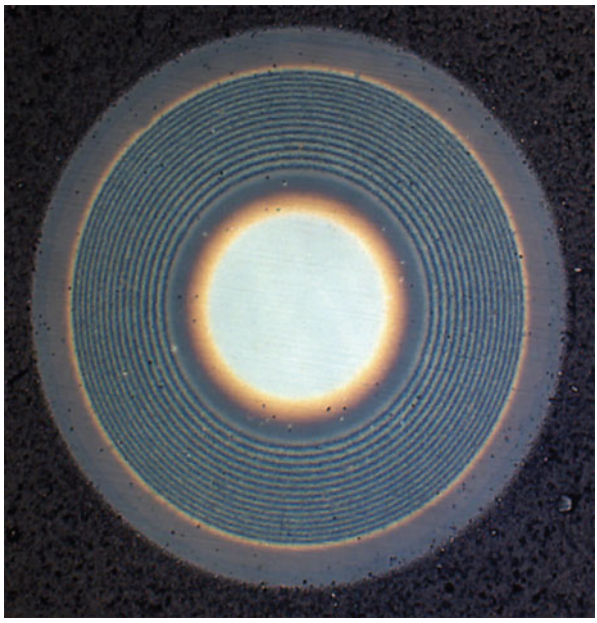

Fig. 6.19 Calotec in the coatings of the indexable inserts used for the milling of rails for fast trains showing the depth profile: substrate (cemented carbide) in the center and adhesion TiN layer (the first *red-yellow* layer), followed by a multilayers consisting of $(Ti_{1-x}Al_x)N$ (*dark*) and TiN (*red yellow*) with *top* layer of the nc-$(Ti_{1-x}Al_x)N/Si_3N_4$ nanocomposite (From Pramet SHM (2014) with permission)

Fast trains, such as Shinkansen in Japan, TGV in France, ICE in Germany, and others, are running at a speed of more than 300 km/h. In that case, the roughness of the rails must be less than 0.2 mm to avoid not only uncomfortable tremors and vibration of the train and noise but also to reduce the wear and possible crack formation in the rails. Therefore, the rails have to be periodically machined by milling. The tool has typically a diameter of about 60 cm and 22 teeth with many indexable inserts fixed there. It operates at 120–150 revolutions per minute with a surface speed of 220–280 m/min and feed of 700 m/h. The machining can be done only in the night when the fast trains do not operate. The company SHM in collaboration with the manufacturer of the indexable inserts Pramet developed special coatings shown in Fig. 6.19 (Pramet SHM 2014). The calotec ground section shows the depth profile of the coating: substrate (cemented carbide) in the center and adhesion TiN layer (the first red-yellow layer), followed by a multilayer consisting of $(Ti_{1-x}Al_x)N$ (dark) and TiN (red yellow) with top layer of the nc-$(Ti_{1-x}Al_x)N/Si_3N_4$ nanocomposite. This coating enabled to increase the lifetime of the expensive tool by more than 20 % and in such a way to extend the length of the rail that can be machined with one tool to more than 2 km.

As last example, we show in Fig. 6.20 tools made of steel for injection molding of Al alloys in fabrication of parts for automotive industry, after the fabrication of 15,000 parts. The tool treated in a conventional way by nitriding (left) shows a clear wear and had to be exchanged, whereas the tool coated with 2–3 μm thick nc-$(Cr_{1-x}Al_x)N/Si_3N_4$ coating does not show any noticeable wear. Obviously, the nanocomposites offer a great advantage also in operation where a combined abrasive and chemical wear occurs.

Fig. 6.20 Tools for injection molding of Al alloys in fabrication of parts for automotive industry, both after the fabrication of 15,000 parts. The length and diameter of the tools are about 200 and 20 mm, respectively. *Left tool* with conventional surface treatment by nitriding, *right tool* coated with 2–3 μm thick nc-$(Cr_{1-x}Al_x)N/Si_3N_4$ coating [From SHM, private communication (2013)]

4 Conclusions

The search for new intrinsically super- and ultrahard materials should not consider only the high values of elastic moduli, but it has to study in detail the electronic stability upon large shear and the deformation paths. The presently available results show that materials which contain d-metals or non-binding electron pairs are likely to undergo electronic instability and transformation to other phases with low plastic resistance. Thus, diamond will probably remain the intrinsically hardest material.

More promising are attempts to design extrinsically superhard nanostructured materials, such as heterostructures, nanosized materials with crystallite size close to 10–15 nm (the "strongest size") and in particular nanostructured materials with low-energy grain boundaries. The recently prepared nanotwinned nt-c-BN and t-diamond reached the load-invariant hardness of 109 and 200 GPa, respectively.

Super- and ultrahard nanocomposites with strengthened interfacial layer, such as nc-TiN/Si_3N_4 and nc-$TiN/Si_3N_4/TiSi_2$, can reach hardness in excess of

100 GPa provided they are correctly prepared with low impurity content. The nc-$(Ti_{1-x}Al_x)N/Si_3N_4$ and nc-$(Cr_{1-x}Al_x)N/Si_3N_4$ coatings are used as wear-protection coatings on tools for machining, stamping, forming, injection molding, and the like. Their advantage is not only the higher hardness but also high oxidation resistance and resistance against chemical corrosion as compared to their conventional counterparts $(Ti_{1-x}Al_x)N$ and $(Cr_{1-x}Al_x)N$.

We have also shown that not all "nanocomposites" reported in many publications during the last two decades can be superhard. In many cases, the observed, relatively small increase of the hardness was due to simple refinement of the grain size. The conditions needed for achieving the high hardness of ≥ 100 GPa in nanocomposite systems have been discussed in some detail, and some promising systems have been identified and others ruled out.

Acknowledgment We would like to thank Company SHM for the financial support of our work and the Department of Chemistry of the Technical University of Munich for providing us the space and access to the computer facilities.

References

Argon AS (2008) Strengthening mechanisms in crystal plasticity. Oxford University Press, Oxford

Argon AS, Yip S (2006) The strongest size. Philos Mag Lett 86:713–720

Auciello O (2010) Microchip-embedded capacitors for implantable neural stimulators. In: Zhou DD, Greenbaum E (eds) Implantable neural prostheses 2, Techniques and engineering approaches. Springer, New York

Auciello O, Shi B (2010) Science and technology of bio-inert thin films as hermetic-encapsulating coatings for implantable biomedical devices: application to implantable microchip in the eye for the artificial retina. In: Zhou DD, Greenbaum E (eds) Implantable neural prostheses 2, Techniques and engineering approaches. Springer, New York

Barna PB, Adamik M (1998) Fundamental structure forming phenomena of polycrystalline films and structure zone models. Thin Solid Films 317:27–33

Barnett SA (1993) Deposition and mechanical properties of superlattice thin films. In: Fracombe MH, Vossen JL (eds) Physics of thin films vol. 17 mechanic and dielectric properties. Academic, Boston

Barnett SA, Madan A (1998) Superhard superlattices. Phys World 11:45–48

Bläß UW, Baruskova T, Schwarz MR, Köhler A, Schimpf C, Petrusha IA, Mühle U, Rafaja D, Kroke E (2015) Bulk titanium nitride ceramics – significant enhancement of hardness by silicon nitride addition, nanostructuring and high pressure sintering. J Eur Ceram Soc 35:2733–2744

Bringa EM, Rosolankova K, Rudd RE, Remington BA, Wark JS, Duchaineau M, Kalantar DH, Hawreliak J, Belaket J (2006) Shock deformation of face-centred-cubic metals on subnanosecond timescales. Nat Mater 5:805–809

Christiansen S, Albrecht M, Strunk HP, Veprek S (1998) Microstructure of novel superhard nanocrystalline-amorphous composites as analyzed by high resolution transmission electron microscopy. J Vac Sci Technol B 16:19–22

Chu X, Barnett SA (1995) Model of superlattice yield stress and hardness enhancement. J Appl Phys 77:4403–4411

Chung H-Y, Weinberger MB, Levine JB, Kavner A, Yang JM, Tolbert SH, Kaner RB (2007) Synthesis of ultra-incompressible superhard rhenium diboride at ambient pressure. Science 316:436–439

Cohen ML (1994) Predicting properties and new materials. Solid State Commun 92:45–52

Cselle T (2005) Application of coatings for tooling: Quo Vadis 2005? Vacuum's Best, Special issue of the German journal: Vakuum in Forschung und Praxis. Wiley, Weinheim, p 33

Cselle T (2008) TripleCoatings® – a new generation of PVD-coatings for machining tools. In: Weinert K (ed) Spanende Fertigung, 5. Auflage. Vulkan-Verlag, Essen, pp 258–268, in German

Dove MT (1993) Introduction to lattice dynamics. Cambridge University Press, Cambridge

Dub SN, Petrusha IA (2006) Mechanical properties of polycrystalline c-BN obtained from pyrolytic g-BN by direct transformation technique. High Press Res 26:71–77

Dubrovinskaia N, Solozhenko VL, Miyajima N, Dimitriev V, Kurakevych OO, Dubrovinsky L (2007) Superhard nanocomposite of dense polymorphs of boron nitride: noncarbon material has reached diamond hardness. Appl Phys Lett 90:101912-1-3

Erdemir A, Eryilmaz OL, Urgen M, Kazmanli K, Mehta N, Prorok B (2005) Tribology of nanostructured materials and coatings. In: Gogotsi Y (ed) Handbook of nanomaterials. CRC Publication, Boca Ratton, pp 685–711

Eremets MI, Trojan IA, Gwaze P, Huth J, Boehler R, Blank VD (2005) The strength of diamond. Appl Phys Lett 87:141902-1-3

Eriksson AO, Tengstrand O, Lu J, Jensen J, Eklund P, Rosén J, Petrov I, Greene JE, Hultman L (2014) Si Incorporation in $Ti_{1-x}Si_xN$ films grown on TiN(001) and (001)-faceted TiN(111) columns. Surf Coat Technol 257:121–128

Field JE (ed) (1992) The properties of natural and synthetic diamond. Academic, San Diego

Flink A, Larsson T, Sjölen J, Kalrsson L, Hultman L (2005) Influence of Si on the microstructure of arc evaporated (Ti, Si)N thin films: evidence for cubic solid solutions and their thermal stability. Surf Coat Technol 200:1535–1542

Flink A, Beckers M, Sjölen J, Larsson M, Braun S, Karlsson L, Hultman L (2009) The location and effects of Si in $(Ti_{1-x}Si_x)N_y$ thin films. J Mater Res 24:2483–2498

Gao F, He J, Wu E, Liu S, Yu D, Li D, Zhang S, Tian Y (2003) Hardness of covalent crystals. Phys Rev Lett 91:015502-1-4

Gogotsi YG, Kailer A, Nickel KG (1999) Transformation of diamond to graphite. Nature 401:663–664

Gottstein G (2004) Physical foundations of material science. Springer, Berlin

Gruen DM (1999) Nanocrystalline diamond films. Annu Rev Mater Sci 29:211–259

Hao S, Delley B, Veprek S, Stampfl C (2006a) Superhard nitride-based nanocomposites: role of interfaces and effect of impurities. Phys Rev Lett 97:086102-1-4

Hao S, Delley B, Stampfl C (2006b) Structure and properties of TiN(111)/Si_xN_y /TiN(111) interfaces in superhard nanocomposites: first-principles investigations. Phys Rev B 74:035402-1-12

Helmersson U, Todorova S, Barnett SA, Sundgren JE (1987) Growth of single-crystal TiN/VN strained-layer superlattices with extremely high mechanical hardness. J Appl Phys 62:481–484

Herr W, Broszeit E (1997) The influence of a heat treatment on the microstructure and mechanical properties of sputtered coatings. Surf Coat Technol 97:335–340

Hill R (1950) The mathematical theory of plasticity. Oxford University Press, Oxford

Hilz G, Holleck H (1996) Structure and effect of interfaces in TiC-TiB_2-B_4C-SiC nanosized multilayer systems. Int J Refract Metals Hard Mater 14:97–104

Holleck H, Schier V (1995) Multilayer PVD coatings for wear protection. Surf Coat Technol 76–77:328–336

Hsieh MH, Tsai MH, Shen WJ, Yeh AW (2013) Structure and properties of two Al–Cr–Nb–Si–Ti high-entropy nitride coatings. Surf Coat Technol 221:118–123

Huang PK, Yeh JW (2009) Effect of substrate temperature and post-annealing on microstructure and properties of (AlCrNbSiTiV)N coatings. Thin Solid Films 518:180–184

Huang Q, Yu D, Xu B, Hu W, Ma Y, Wang Y, Zhao Z, Wen B, He J, Liu Z, Tian Y (2014) Nanotwinned diamond with unprecedented hardness and stability. Nature 510:250–253

Hubbard KM, Jervis TR, Mirkarimi PB, Barnett SA (1992) Mechanical properties of epitaxial TiN/($V_{0.5}Nb_{0.4}$)N superlattices measured by nanoindentation. J Appl Phys 72:4466–4468

Ivashchenko VI, Veprek S (2013) First-principles molecular dynamics study of the thermal stability of the BN, AlN, SiC and SiN interfacial layers in TiN-based heterostructures: comparison with experiments. Thin Solid Films 545:391–400

Ivashchenko VI, Veprek S, Turchi PEA, Shevchenko VI (2012) Comparative first-principles study of TiN/SiN_x/TiN interfaces. Phys Rev B 85:195403-1-15

Ivashchenko VI, Veprek S, Turchi PEA, Shevchenko VI, Leszczynski J, Gorb L, Hill F (2014) First-principles molecular dynamics investigation of thermal and mechanical stability of the TiN(001)/AlN and ZrN(001)/AlN heterostructures. Thin Solid Films 564:284–293

Ivashchenko VI, Veprek S, Argon AS, Turchi PEA, Gorb L, Hill F, Leszczynski J (2015) First-principles quantum molecular calculations of structural and mechanical properties of TiN/SiN_x heterostructures, and the achievable hardness of the nc-TiN/SiN_x nanocomposites. Thin Solid Films 578:83–92

Jian WW, Cheng GM, Xu WZ, Yuan H, Tsai MH, Wang QD, Koch CC, Zhu YT, Mathaudhu SN (2013) Ultrastrong Mg alloy via nano-spaced stacking faults. Mater Res Lett 1:61–67

Jilek M (2012) Private communication 2012, Unpublished

Karvankova P, Männling HD, Eggs CH, Veprek S (2001) Thermal stability of ZrN–Ni and CrN–Ni superhard nanocomposite coatings. Surf Coat Technol 146–147:280–285

Karvankova P, Veprek-Heijman MGJ, Azinovic D, Veprek S (2006) Properties of superhard nc-TiN/a-BN and nc-TiN/a-BN/a-TiB_2 nanocomposite coatings prepared by plasma induced chemical vapor deposition. Surf Coat Technol 200:2978–2989

Koehler JS (1970) Attempt to design a strong solid. Phys Rev B 2:547–551

Kong M, Dai J, Lao J, Li G (2007) Crystallization of amorphous SiC and superhardness effect in TiN/SiC nanomultilayers. Appl Surf Sci 253:4734–4739

Lehoczky SL (1978a) Retardation of dislocation generation and motion in thin-layered metal laminates. Phys Rev Lett 41:1814–1818

Lehoczky SL (1978b) Strength enhancement in thin-layered Al-Cu laminates. J Appl Phys 49:54795485

Liu AY, Cohen ML (1989) Prediction of new low compressibility solids. Science 245:841–842

Martan J, Benes P (2012) Thermal properties of cutting tool coatings at high temperatures. Thermochim Acta 539:51–55

Marten T, Isaev EI, Alling B, Hultman L, Abrikosov IA (2010) Single-monolayer SiN_x embedded in TiN: a first-principles study. Phys Rev B 81:212102-1-4

Matthews A, Jones R, Dowey S (2001) Modelling and deformation behaviour of multilayer coatings. Tribol Lett 11:103–106

McClintock FA, Argon AS (1966) Mechanical behavior of materials. Addison-Wesley, Reading

Mirkarimi PB, Hultman L, Barnett SA (1990) Enhanced hardness in lattice-matched single-crystal TiN/$V_{0.6}Nb_{0.4}$N superlattices. Appl Phys Lett 57:2654–2656

Mirkarimi PB, Barnett SA, Hubbard KM, Jervis TR, Hultman L (1994) Structure and mechanical properties of epitaxial TiN/$V_{0.3}Nb_{0.7}$N(100) superlattices. J Mater Res 9:1456–1466

Münz WD, Lewis DB, Hovsepian PE, Schönjahn C, Ehiasarian A, Smith IJ (2001) Industrial scale manufactured superlattice hard PVD coatings. Surf Eng 17:15–27

Musil J (2000) Hard and superhard nanocomposite coatings. Surf Coat Technol 125:322–330

Musil J, Hruby H (2000) Superhard nanocomposites $Ti_{1-x}Al_xN$ films prepared by magnetron sputtering. Thin Solid Films 365:104–109

Musil J, Kadlec S, Vyskocil J, Valvoda V (1988) New results in D.C. reactive magnetron deposition of TiN_x films. Thin Solid Films 167:107–119

Musil J, Zeman P, Dohnal P (2007) Ti-Si-N films with a high content of Si. Plasma Process Polym 4:S574–S578

Nastasi M, Mayer JW, Hirvonen J (1996) Ion-solid interaction. Cambridge University Press, Cambridge

Niederhofer A, Nesladek P, Männling HD, Moto K, Veprek S, Jilek M (1999) Structural properties, internal stress and thermal stability of nc-TiN/Si_3N_4, nc-TiN/$TiSi_x$ and nc-$(Ti_{1-x}Al_ySi_x)N$ superhard nanocomposite coatings reaching the hardness of diamond. Surf Coat Technol 120–121:173–178

Ninomiya T (1978) Theory of melting, dislocation model I & II. J Phys Soc Jpn 44:263–271

Otto F, Yang Y, Bei H, George EP (2013) Relative effect of enthalpy and entropy on the phase stability of equiatomic high-entropy alloys. Acta Mater 61:2628–2638

Pélisson A, Parlinska-Wojtan M, Hug HJ, Patscheider J (2007) Microstructure and mechanical properties of Al–Si–N transparent hard coatings deposited by magnetron sputtering. Surf Coat Technol 202:884–889

Petrov I, Barna PB, Hultman L, Greene JE (2003) Microstructural evolution during film growth. J Vac Sci Technol A 21:S117–S128

Porter DA, Easterling KE (2001) Phase transformations in metals and alloys, 2nd edn, reprinted by Nelson Thomes Ltd, Cheltenham

Pramet SHM (2014) Advanced PVD coatings for milling of rails. MM Prumyslove Spektrum 6:64–66 (in Czech)

Prilliman SG, Clark SM, Alivisatos AP, Karvankova P, Veprek S (2006) Strain and deformation in ultra-hard nanocomposites nc-TiN/a-BN under hydrostatic pressure. Mater Sci Eng A 437:379–387

Prochazka J, Karvankova P, Veprek-Heijman MGJ, Veprek S (2004) Conditions required for achieving superhardness of $\geq$45 GPa in nc-TiN/a-Si_3N_4 nanocomposites. Mater Sci Eng A 384:102–116

Rogl P, Schuster JC (1992) Phase diagrams of ternary boron nitride and silicon nitride, ASM The Materials Information Society. Material Parks, Ohio

Samani MK, Ding XZ, Amini S, Khosravian N, Cheong JY, Chen G, Tay BK (2013) Thermal conductivity of titanium aluminum silicon nitride coatings deposited by lateral rotating cathode arc. Thin Solid Films 537:108–112

Samani MK, Ding XD, Khosravian N, Amin-Ahmadi B, Yang Y, Chene G, Neyts EC, Bogaerts A, Tay BK (2015) Thermal conductivity of titanium nitride/titanium aluminum nitride multilayer coatings deposited by lateral rotating cathode arc. Thin Solid Films 578:133–138

Saxonian (2015) Homepage of the Saxonian Institute for surface mechanics http://www.siomec.de/en/113/Nanotwinned+diamond+with+unprecedented+hardness

Schiøtz J, Jacobsen KW (2003) A maximum in the strength of nanocrystalline copper. Science 301:1357–1359

Schiøtz J, Di Tolla FD, Jacobsen KW (1998) Softening of nanocrystalline metals at very small grain sizes. Nature 391:561–563

Schmalzried H (1995) Chemical kinetics of solids. WCH Verlag, Weinheim

Sheng SH, Zhang RF, Veprek S (2008) Phase stabilities and thermal decomposition in the $Zr_{1-x}Al_xN$ system studied by *ab initio* calculation and thermodynamic modeling. Acta Mater 56:968–976

Sheng SH, Zhang RF, Veprek S (2011a) Phase stabilities and decomposition mechanism in the Zr–Si–N system studied by combined *ab initio* DFT and thermodynamic calculation. Acta Mater 59:297–307

Sheng SH, Zhang RF, Veprek S (2011b) Study of spinodal decomposition and formation of nc-Al_2O_3/ZrO_2 nanocomposites by combined *ab initio* density functional theory and thermodynamic modeling. Acta Mater 59:3498–3509

Sheng SH, Zhang RF, Veprek S (2013) Decomposition mechanism of $Al_{1-x}Si_xN_y$ solid solution and possible mechanism of the formation of covalent nanocrystalline AlN/Si_3N_4 nanocomposites. Acta Mater 61:4226–4236

Shin M, Hultman L, Barnett SA (1992) Growth, structure and microhardness of epitaxial TiN/NbN superlattices. J Mater Res 7:901–911

SHM http://www.shm-cz.cz
Siegel RW, Fougere E (1995) Mechanical properties of nanophase metals. NanoStructured Mater 6:205–216
Simunek A (2009) Anisotropy of hardness from first principles: the cases of ReB_2 and OsB_2. Phys Rev B 80:060103(R)-1-4
Simunek A, Vackar J (2006) Hardness of covalent and ionic crystals: first-principle calculations. Phys Rev Lett 96:085501-1-4
Skrovanek SD, Bradt RC (1979) Microhardness of a fine-grain-size Al_2O_3. J Amer Ceram Soc 62:215–216
Solozhenko VL, Andrault D, Fiquet G, Mezouar M, Rubie DC (2001) Synthesis of superhard cubic BC_2N. Appl Phys Lett 78:1385–1387
Solozhenko VL, Kurakevych OO, Andrault D, Godec YL, Mezouar M (2009) Ultimate metastable solubility of boron in diamond: synthesis of superhard diamondlike BC_5. Phys Rev Lett 102:015506-1-4
Solozhenko VL, Kurakevych OO, Godec YL (2012) Creation of nanostructures by extreme conditions: high-pressure synthesis of ultrahard nanocrystalline cubic boron nitride. Adv Mater 24:1540–1544
Sproul WD (1994) Multilayer, multicomponent, and multiphase physical vapor deposition coatings for enhanced performance. J Vac Sci Technol A 12:1595–1601
Sproul WD (1996) Reactive sputter deposition of polycrystalline nitride and oxide superlattice coatings. Surf Coat Technol 86/87:170–176
Sumiya H, Uesaka S, Satoh S (2000) Mechanical properties of high purity polycrystalline c-BN synthesized by direct conversion sintering method. J Mater Sci 35:1181–1186
Tabor D (1951) The hardness of metals. At the Clarendon Press, Oxford
Tang F, Gault B, Ringer SP, Martin P, Bendavid A, Cairney JM (2010) Microstructural investigation of Ti–Si–N hard coatings. Scripta Mater 63:192–195
Teter MD (1998) Computational Alchemy: the search for new superhard materials. Mater Res Soc Bull 23:22–27
Tian Y, Xu B, Yu D, Ma Y, Wang Y, Hang Y, Hu W, Tang C, Gao Y, Luo K, Zhao Z, Wang LM, Weng B, He J, Liu Z (2013) Ultrahard nanotwinned cubic boron nitride. Nature 493:385–388
Tsai MH, Yeh JW (2014) High entropy alloys: a critical review. Mater Res Lett 2:107–123
Veprek S (1999) The search for novel superhard materials. J Vac Sci Technol A 17:2401–2420
Veprek S (2013) Recent search for new superhard materials: Go nano! J Vac Sci Technol A 31:050822-1-33
Veprek S, Reiprich S (1995) Concept for the design of novel superhard coatings. Thin Solid Films 268:64–71
Veprek S, Veprek-Heijman MGJ (2007) The formation and role of interfaces in superhard nc-Me_nN/a-Si_3N_4 nanocomposites. Surf Coat Technol 201:6064–6070
Veprek S, Veprek-Heijman MGJ (2008) Industrial applications of superhard nanocomposite coatings. Surf Coat Technol 202:5063–5073
Veprek S, Veprek-Heijman MGJ (2012) Limits to the preparation of superhard nanocomposites: impurities, deposition and annealing temperature. Thin Solid Films 522:274–282
Veprek S, Iqbal Z, Sarott FA (1982) A thermodynamic criterion of the crystalline-to-amorphous transition in silicon. Philos Mag 45:137–145
Veprek S, Weidmann J, Glatz F (1995) Plasma chemical vapor deposition and properties of hard C_3N_4 thin films. J Vac Sci Technol A 13:2914–2919
Veprek S, Haussmann M, Reiprich S, Li S, Dian J (1996) Novel thermodynamically stable and oxidation resistant superhard coating materials. Surf Coat Technol 86–87:394–401
Veprek S, Niederhofer A, Moto K, Bolom T, Männling HD, Nesladek P, Dollinger G, Bergmaier A (2000) Composition, nanostructure and origin of the ultrahardness in nc-TiN/Si_3N_4/$TiSi_2$ nanocomposites with $H = 80$ to ≥ 100 GPa. Surf Coat Technol 133–134:152–159

Veprek S, Mukherjee S, Karvankova P, Männling HD, He JL, Moto K, Prochazka J, Argon AS (2003) Limits to the strength of super- and ultrahard nanocomposite coatings. J Vac Sci Technol A 21:532–544

Veprek S, Männling H-D, Niederhofer A, Ma D, Mukherjee S (2004a) Degradation of superhard nanocomposites by built-in impurities. J Vac Sci Technol B 22:L6–L9

Veprek S, Männling HD, Jilek M, Holubar P (2004b) Avoiding the high-temperature decomposition and softening of $(Al_{1-x}Ti_x)N$ coatings by the formation of stable superhard nc-$(Al_{1-x}Ti_x)N$/a-Si_3N_4 nanocomposite. Mater Sci Eng A366:202–205

Veprek S, Veprek-Heijman MGJ, Karvankova P, Prochazka J (2005a) Different approaches to superhard coatings and nanocomposites. Thin Solid Films 476:1–29

Veprek S, Karvankova P, Veprek-Heijman MGJ (2005b) Possible role of oxygen impurities in degradation of nc-TiN/Si_3N_4 nanocomposites. J Vac Sci Technol B 23:L17–L21

Veprek S, Männling HD, Karvankova P, Prochazka J (2006) The issue of the reproducibility of deposition of superhard nanocomposites with hardness of ≥ 50 GPa. Surf Coat Technol 200:3876–3885

Veprek S, Argon AS, Zhang RF (2007) Origin of the hardness enhancement in superhard nc-TiN/a-Si_3N_4 and ultrahard nc-TiN/a-Si_3N_4/$TiSi_2$ nanocomposites. Philos Mag Lett 87:955–966

Veprek S, Argon AS, Zhang RF (2010) Design of ultrahard materials: Go nano! Philos Mag 90:4101–4115

Veprek-Heijman MGJ, Veprek RG, Argon AS, Parks DM, Veprek S (2009) Non-linear finite element constitutive modeling of indentation into super- and ultrahard materials: the plastic deformation of the diamond tip and the ratio of hardness to tensile yield strength of super- and ultrahard nanocomposites. Surf Coat Technol 203:3385–3391

Xu B, Tian Y (2015) Ultrahardness: measurement and enhancement. J Phys Chem 119:5633–5638

Yashar PC, Sproul WD (1999) Nanometer scale multilayered hard coatings. Vacuum 55:178–190

Yashar PC, Barnett SA, Hultman L, Sproul WD (1999) Deposition and mechanical properties of polycrystalline Y_2O_3/ZrO_2 superlattices. J Mater Res 9:3614–3622

Yip S (1998) The strongest size. Nature 391:532–533

Zeman P, Cerstvy R, Mayrhofer PH, Mitterer C, Musil J (2000) Structure and properties of hard and superhard Zr-Cu-N nanocomposite coatings. Mater Sci Eng A 289:189–197

Zhang RF, Veprek S (2006) On the spinodal nature of the phase segregation and formation of stable nanostructure in the Ti–Si–N system. Mater Sci Eng A 424:128–137

Zhang RF, Veprek S (2007a) Metastable phases and spinodal decomposition in $Ti_{1-x}Al_xN$ system studied by *ab initio* and thermodynamic modeling, a comparison with the TiN–Si_3N_4 system. Mater Sci Eng A 448:111–119

Zhang RF, Veprek S (2007b) Phase stabilities and spinodal decomposition in the $Cr_{1-x}Al_xN$ system studied by *ab initio* LDA and thermodynamic modeling: comparison with the $Ti_{1-x}Al_xN$ and TiN/Si_3N_4 systems. Acta Mater 55:4615–4624

Zhang RF, Veprek S (2008) Phase stabilities of self-organized nc-TiN/a-Si_3N_4 nanocomposites and of $Ti_{1-x}Si_xN_y$ solid solutions studied by ab initio calculation and thermodynamic modeling. Thin Solid Films 516:2264–2275

Zhang Y, Hong S, Chen C (2004) Superhard cubic BC_2N compared to diamond. Phys Rev Lett 93:195504-1-4

Zhang Y, Hong S, Chen C (2006) Strain dependent bonding in solid C_3N_4: high elastic moduli but low strength. Phys Rev B 73:064109-1-4

Zhang RF, Sheng SH, Veprek S (2008) Stability of Ti–B–N solid solutions and the formation of nc-TiN/a-BN nanocomposites studied by combined ab initio and thermodynamic calculations. Acta Mater 56:4440–4449

Zhang RF, Veprek S, Argon AS (2009a) Effect of nanometer-sized grains on the superhardness of *c*-BC_5: a first-principles study. Phys Rev B 80:233401-1-4

Zhang RF, Argon AS, Veprek S (2009b) Friedel oscillations are limiting the strength of superhard nanocomposites and heterostructures. Phys Rev Lett 102:015503-1-4

Zhang RF, Argon AS, Veprek S (2009c) Electronic structure, stability, and mechanism of the decohesion and shear of interfaces in superhard nanocomposites and heterostructures. Phys Rev B 79:245426-1-13

Zhang RF, Legut D, Niewa R, Argon AS, Veprek S (2010a) Shear-induced structural transformation and plasticity in ultraincompressible ReB_2 limit its hardness. Phys Rev B 82:104104-1-7

Zhang RF, Argon AS, Veprek S (2010b) Understanding why the thinnest SiN_x interface in transition-metal nitrides is stronger than the ideal bulk crystal. Phys Rev B 81:245418-1-7

Zhang RF, Lin ZJ, Zhao YS, Veprek S (2011) Superhard materials with low elastic moduli: three-dimensional covalent bonding as the origin of superhardness in B_6O. Phys Rev B 83:092101-1-4

Zhang RF, Legut D, Wen XD, Veprek S, Rajan K, Lookman T, Mao HK, Zhao YS (2014) Bond deformation paths and electronic instabilities of ultraincompressible transition metal diborides: case study of OsB_2 and IrB_2. Phys Rev B 90:094115-1-6

Zhao B, Gottstein G, Shvindlerman LS (2011) Triple junction effects in solids. Acta Mater 59:3510–3518

Zhao B, Ziemons A, Shvindlerman LS, Gottstein G (2012) Surface topology and energy of grain boundary triple junctions in copper tricrystals. Acta Mater 60:811–818

Zhu T, Li J, Ogata S, Yip S (2009) MRS Bull 34:167–172

Chapter 7
Future of Superhard Material Design, Processing and Manufacturing

Dr. Maweja Kasonde, CEng MIMMM
and Dr. Valentine Kanyanta, CEng MIMechE

Abstract Advancements in superhard and ultrahard material design will require a paradigm shift in the way we think about material design. It will need thinking outside the box and using unconventional technologies. The biggest challenges with superhard materials is their inherently lower fracture toughness, expensive to manufacture and difficult to process into final formats or geometries (such as for cutting tools) required by end users. These geometries are at times extremely complex 3D shapes with micron size features which are difficult to achieve via conventional processing methods. All these challenges limit the use of superhard and ultrahard materials in many drilling and machining applications. This chapter looks at firstly how the fracture toughness of superhard materials can be enhanced using concepts such as biomimicry, dispersing a tough phase in a superhard material matrix, engineering controlled defects, designing functionally graded structures, nanostructuring and imbedding a three-dimensionally interpenetrating network of a tough phase inside a brittle matrix. Secondly, the chapter briefly discusses additive manufacturing (e.g. 3D printing) as a route to reducing material waste/cost, increasing responsiveness to market needs for customised and complicated 3D shapes and eliminating the need for post-processing (i.e. moving towards a single-step manufacturing process).

1 Introduction

Superhard and ultrahard[1] materials such as cubic boron nitride and diamond have transformed the abrasive markets in terms of economics and productivity. Owing to their extremely high hardness, these materials are now widely used is industrial

[1] Diamond is the only intrinsically ultrahard material with a hardness of greater than 80 GPa, usually about 100 GPa. Superhard materials are defined as those with a load invariant Vickers hardness greater than 40GPa and ultrahard materials as having a hardness exceeding 80 GPa.

Dr. M. Kasonde, CEng MIMMM (✉)
Research Fellow, Element Six Limited, Oxfordshire, UK
e-mail: maweja.kasonde@e6.com

Dr. V. Kanyanta, CEng MIMechE
Principal Research Scientist, Element Six Limited, Oxfordshire, UK
e-mail: valentine.kanyanta@e6.com

V. Kanyanta (ed.), *Microstructure-Property Correlations for Hard, Superhard, and Ultrahard Materials*, DOI 10.1007/978-3-319-29291-5_7

applications requiring very high resistance to abrasion wear. They offer high material removal rates, superior surface finish and longer tool life. All these factors contribute to favourable economics of cutting, drilling and grinding operations. For example, the use of diamond-based cutting tools in oil and gas has resulted in significantly increased productivity and efficiency compared carbide and steel tools. The high penetration/drilling rates means drilling times can be significantly reduced. Long tool life also means less number of drill bit changes or trips (Scott 2006). These two factors have a significant impact on the cost per foot drilled, which includes both the direct and indirect overhead costs.

In cutting and machining operations, the ability to maintain a sharp cutting edge is extremely important in order to achieve superior surface finish of the work piece. This is made possible by the high resistance to abrasion wear of the cutting tool material. The tool also needs to be able to retain high hardness at elevated temperatures. At the cutting tip, temperatures can be extremely high especially in cases involving machining of super alloys such as INCONEL where temperatures are thought to be in excess of 1000 °C (Kennam et al. 2015). Diamond and cubic boron nitride have very good hot hardness and hence another reason why they are preferred in applications such as high speed turning of super alloys and case-hardened steels. The downside with these two superhard materials, especially in the case of diamond, is the low resistance to chemical wear when machining certain types of materials. Diamond-based cutting tools cannot be used to machine ferrous or iron-containing materials because of the high solubility of carbon in iron. This possesses significant restrictions on the type of materials which can be machined. Diamond also has poor thermal stability at temperatures above 600 °C under atmospheric pressure conditions (Westraadt et al. 2015). Above this temperature, it starts to transform into graphite which is a much softer phase. Cubic boron nitrides has relatively better thermal stability than diamond and can be used to machine ferrous materials (Goel et al. 2012). However, cubic boron nitride is not completely inert with iron during machining of ferrous alloys. Studies have shown that there is dissolution and diffusion of cBN into the flowing chip and work piece (Arsecularatne et al. 2005; Barry and Byrne 2001; Giménez et al. 2007; Narutaki and Yamane 1979; Zimmermann et al. 1997). Therefore it also does suffer from similar problems of chemical wear as diamond, although in the case of the former this is less pronounced. Improving resistance to chemical wear and thermal stability is necessary if these traditional materials are to find much wider applications as cutting tools.

The other challenge with traditional superhard materials, i.e. diamond and cubic boron nitride, is their inherently low fracture toughness. Although these materials are extremely hard and are widely employed as cutting tools in difficult to machine materials, their resistance to crack propagation (or fracture toughness) is only a few $MPa/m^{0.5}$. For polycrystalline diamond, the values of mode I fracture toughness is usually below 10 $MPa/m^{0.5}$ and can be as low as 5 $MPa/m^{0.5}$ depending on the average grain size of diamond particles, metal content and synthesis conditions (Droty et al. 1995; McNamara et al. 2015; Morrell et al. 2010; Petrovic et al. 2011). In the case of polycrystalline cubic boron nitride, values of between 8 and

14 MPa/m$^{0.5}$ have been reported (Carolan et al. 2013a). This is still far below what can be achieved with cemented carbides, i.e. up to 25 MPa/m$^{0.5}$ (Okamoto et al. 2005; Sandvik Hard 2005), and even an order of magnitude lower when compared to tool steels. The toughness of single crystal diamond or cubic boron nitride is even much lower.[2] Because of the low fracture toughness, diamond and cubic boron nitride materials are usually susceptible to unpredictable and catastrophic failure during application. Not only are such failures undesirable in terms of reduced productivity, they can cause significant damage to parts being machined and increase the scrap rate. As a result, the industry still needs superhard materials with much increased fracture toughness.

In addition to low fracture toughness, resistance to chemical wear and sometimes poor thermal stability, traditional superhard materials also present significant manufacturing challenges which involve high pressure and high temperatures usually in excess of 5 GPa and 1400 °C, respectively. Generating such conditions is an extremely expensive process. There is also a high level of complexity involved in designing press systems that can generate the required high pressure and temperature conditions. The current alternative manufacturing process to high pressure and high temperature (HPHT) is chemical vapour deposition (CVD). However, this is equally an expensive and energy-intensive process. Not only are these materials expensive to make, they are also difficult to process into final tool geometries required by end users. Therefore, there is also a requirement for making near net-shaped formats so that any secondary processing is kept to the minimum.

In order for diamond and cubic boron nitride to remain preferred superhard materials for cost-effective solutions in abrasive markets, the challenges highlighted above, i.e. low fracture toughness, resistance to chemical wear, thermal stability, manufacturing costs and difficulty of processing, need to be addressed. This chapter looks at possible solutions to overcoming some of these challenges.

2 Overcoming the Toughness Challenge

Enhancing the fracture toughness of materials which are inherently brittle is not trivial. Diamond and cubic boron nitride are intrinsically superhard because of the cubic crystal structure and short covalent bonds between their atoms. This structure offers very high resistance to plastic flow, and hence high hardness. However, the absence of plastic deformation is detrimental to the toughness of the material. As a result diamond and cubic boron nitrate are intrinsically brittle, with low fracture toughness or resistance to crack growth. The only way the toughness of these

[2] Polycrystalline materials have higher fracture toughness than single crystalline materials due to the random orientation of crystallographic planes. In single crystal materials, fracture always takes place along weaker planes (less energy barrier). By having fracture or slip planes randomly oriented as in a polycrystalline material, the resistance to crack propagation is enhanced.

materials can be enhanced is via extrinsic toughening mechanisms that inhabit crack growth or alter the way cracks propagate. In most cutting and drilling applications, diamond and cubic boron nitride materials are used in the form of sintered polycrystalline structures. Commercially available polycrystalline diamond (PCD) is prepared via a high pressure and high temperature liquid-phase sintering process. The result is an intergrown skeleton of diamond grains with metal inclusions occupying the interstices in the material. Intergrowth is made possible via the dissolution and reprecipitation of carbon atoms by using a metal solvent catalyst. On the other hand, polycrystalline cubic boron nitride consists of superhard particles (i.e. cubic boron nitride) bonded together by a binder phase and does not usually contain any intergrowth between the superhard particles. The preparation of these two materials is extensively covered in Chaps. 1 and 2.

There is always a requirement in industry for materials that are simultaneously superhard, strong and tough. However, the challenge in designing such materials is that toughness and strength are generally mutually exclusive, meaning enhancing one result in the other being sacrificed. This is also usually the case with toughness and hardness. Therefore, it is extremely difficult to improve the fracture toughness of these superhard materials without negatively affecting their hardness and strength. One way of defeating this toughness—strength (or hardness) conflict—is through biomimicry. Natural materials are known to achieve an excellent combination of strength and toughness (Chen et al. 2012; Karambelasa et al. 2013; Rabiei et al. 2010; Ritchie 2011; Sowmya et al. 2013). There are also other extrinsic toughening mechanisms which are discussed later in this chapter.

2.1 Biomimicry and Superhard Materials

Biomimicry is increasingly becoming a popular phenomenon in the design of novel material structures with an excellent combination of strength, hardness and toughness. The complex hierarchical microarchitectures of biological materials have already inspired the design of exceptionally tough ceramic composites (Chen et al. 2012; Karambelasa et al. 2013; Munch et al. 2008; Ritchie 2011; Sowmya et al. 2013; Torres-Sanchez and Corney 2011; Wang et al. 2000). These biomimicked multilayered composites exhibit levels of damage tolerance far greater than what can be achieved in monolithic structures. For example, Wang et al. (2000) produced fibrous and laminated silicon nitride—boron nitride (Si_3N_4/BN) composites imitating bamboos and nacre structures, respectively. In both cases, the materials showed over a tenfold increase in the work of fracture compared to monolithic silicon nitride (Si_3N_4) ceramics. Similar results were reported by Karambellas et al. (2013). They used a SHELL (sequential hierarchical engineered layer lamination) technique to fabricate Si_3N_4/BN ceramic composites mimicking the microarchitecture of *Strombus gigas* shell. Damage tolerance values of 8–9 times higher than that of monolithic Si_3N_4 were reported. These are only a few of several other examples where biomimetic ceramics and composites with

significantly higher fracture toughness compared to those of their constituents have been reported in literature (Chen et al. 2012; Munch et al. 2008; Ritchie 2011; Sowmya et al. 2013; Torres-Sanchez and Corney 2011). Understanding the functions of the microarchitectures of biomaterials with the view of replicating them in their synthetic counterparts forms a significant part of these studies.

Researchers have used several natural materials to inspire the design and fabrication of superior industrial materials. Examples of commonly used materials include bamboo, tooth, nacre, collagen fibres and bone. The bamboo is a functionally graded material with a hierarchical or layered structural design. The nodes, which occur periodically along the length of the bamboo, impart tensile strength, stiffness and rigidity on the macroscale (Amada 1995; Amada et al. 1997; Li et al. 2007). The microstructure changes gradually from outer to the inside of the material. Density of distribution of the vascular bundles, which act as the reinforcing component, is highest in the outer green layer, which experiences the maximum stresses during bending. Such a hierarchically designed structure is typical of biomaterials where an optimised structural design is used to realise superior mechanical performance. The bamboo also exhibits an asymmetric flexural and tension/compression behaviour when subjected to different loading states. Habibi et al. (2015) used multi-scale mechanical characterisations and microstructure analysis to investigate this behaviour in natural bamboo (*Phyllostachys edulis*) strips under different loading configurations (Habibi et al. 2015). They were able to show that the flexural asymmetry is mainly due to the gradient distribution of the vascular bundles along the thickness direction, whereas the hierarchical fibre/parenchyma cellular structure plays a critical role in alternating the dominant factors for determining the distinctly different failure mechanisms. A numerical model was also employed to study the effective flexural moduli of bamboo strips as a function of microstructural parameters. One of the peculiar aspects of the bamboo is the evolution of the microstructure of its outer and innermost layers under different bending states. This is important in distribution and transmission of stresses and also in relieving any local high stresses.

Other materials such as mammalian tooth (Sarikaya 2002), collagen fibres (Jager and Fratzl 2000) and bones (Buskirk et al. 2002) have also been studied and used. A mammalian tooth is an intricately structured and functionally graded composite, containing both the enamel (outer layer) and the dentin (on the inside) that are coupled through an interface region called dentin-enamel junction. The enamel is composed of long crystallites packed as bundles in enamel rods, which are organised unidirectionally normal to the tooth surface. This results in high hardness and wear resistance. The dentin is primarily composed of mineralised collagen fibres that form a randomly intertwined, continuous network. The result is a soft but highly tough material. Combining the two components (enamel and dentin) gives a functionally graded composite material with an excellent combination of hardness (on the contact surface), strength and good fracture toughness (provided by the tougher inner region). Figure 7.1a shows the schematic of a mammalian tooth. The ratio between the thickness of the enamel (d) and that of the dentin (R-d) is critical to realising the desired combination of hardness, strength and toughness. As shown

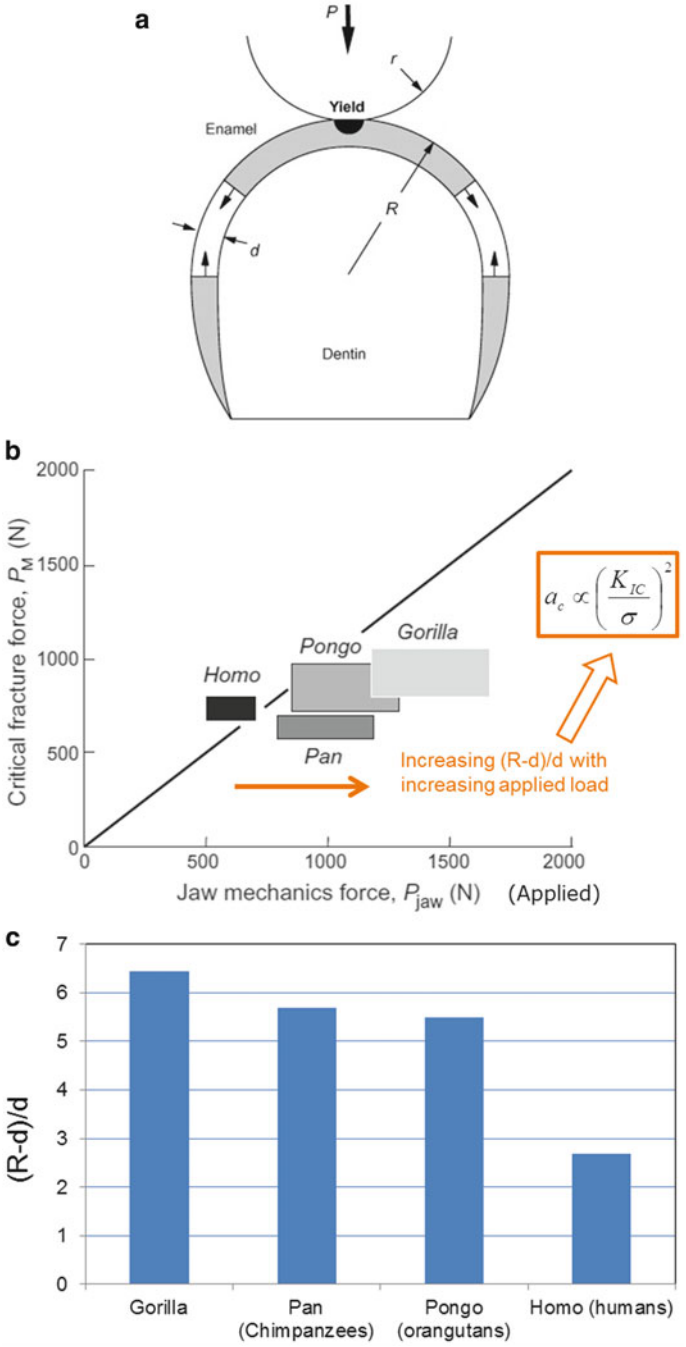

Fig. 7.1 (**a**) The schematic of a mammalian tooth structure showing the two regions, enamel and dentin, (**b**) and (**c**) the relationship between the force generated by jaw mechanics, critical fracture force and structure of the tooth in terms of the thickness ratio of the enamel to dentin (figures reproduced from data published by Lee et al. (2010))

by Lee et al. (2010), there is a correlation between this ratio and the allowable applied force. The integrated jaw mechanics design ensures that the maximum force that can be generated by the jaws does not exceed the tooth fracture load, thereby providing some safety measure.

The critical fracture force is the force required to induce cracks in the structure. Given that the microstructure composition of the enamel is similar between the different tooth types, this is fairly constant. However, different tooth structures allow for different crack lengths before catastrophic failure would occur. From Fig. 7.1b, c, it can be seen that as the applied load increases (i.e. jaw mechanics force), so does the (R-d)/d ratio. In other words, where higher loads are expected, the thickness of the enamel is desired to be a lot smaller than that of the dentin, i.e. a higher (R-d)/d ratio. This can be related to the critical flaw size concept as proposed in Griffith's failure criteria as given by Eq. 7.1:

$$a_c \propto \left(\frac{K_{IC}}{\sigma}\right)^2, \tag{7.1}$$

where a_c is the critical flaw size at which catastrophic failure occurs and K_{IC} and σ are, respectively, the mode I fracture toughness (critical stress intensity factor) and remotely applied load. This simply states that under given loading conditions, there exists a critical crack length at which catastrophic failure or fracture would occur. Assuming a constant value of K_{IC}, the critical flaw size varies inversely with the applied load. In the case of the tooth structure and the results of the study by Lee et al. (2010), it can be deduced that the ratio of the enamel thickness to that of the dentin, i.e. d/(R−d), behaves in a very similar way to the critical flaw size of Eq. 7.1.

The stiffness and toughness of this composite structure can also be easily estimated by using the analogue of springs in series. Take the example of two concentric layers in Fig. 7.2, composed of one inner region (material 1) with elastic modulus E_1 and thickness t_1 and outer region (material 2) with modulus E_2 and thickness t_1. The respective stiffness of the two regions, k_1 and k_2, can be determined as

$$k_1 = \frac{E_1 A}{t_1} \text{ and } k_2 = \frac{E_2 A}{t_2}, \tag{7.2}$$

where A is the unit cross-section area. The equivalent stiffness for springs connected in series is then given by

$$k_{eq} = \frac{1}{\frac{1}{k_1} + \frac{1}{k_2}} = \frac{1}{\frac{t_1}{E_1 A} + \frac{t_2}{E_2 A}} = \frac{E_1 E_2 A}{t_1 E_2 + t_2 E_1} \tag{7.3}$$

The equivalent elastic modulus, E_{eq}, is related to the equivalent stiffness through

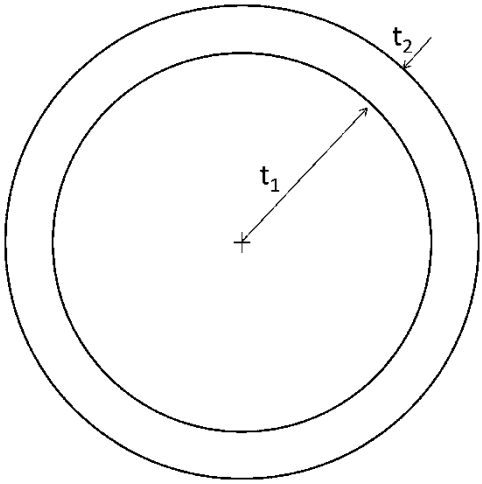

Fig. 7.2 Bi-concentric layered (functionally graded) structure

$$k_{eq} = \frac{E_{eq}A}{t_1 + t_2}, \text{ thus } E_{eq} = \frac{E_1 E_2 (t_1 + t_2)}{t_1 E_2 + t_2 E_1} \tag{7.4}$$

As the thickness of the outer layer, t_2, decreases, the stiffness of the composite approaches that of the inner region and vice versa. Similarly, the equivalent fracture energy values of a multilayered structure with layers arranged perpendicular to the direction of crack propagation can be treated as an additive quantity of respective volume ratios as shown in Eq. 7.5:

$$G_{eq} = \frac{G_1 t_1}{t_1 + t_2} + \frac{G_2 t_2}{t_1 + t_2}, \text{ and } G_{IC} = \frac{{K_{IC}}^2}{E} \text{ for a perfectly brittle material,} \tag{7.5}$$

where G_{IC} and K_{IC} are the mode I fracture energy and fracture toughness, respectively.

The structure of the bone is in many aspects different from the tooth and other natural materials as it is based on controlled porosity and density at several length scales. The observation that bones never fracture in the vicinity of the natural holes in them (where blood vessels pass through) is explained by the fact that the composition of the bone varies around the holes such that it is denser and stronger wherever the stresses are higher (in the vicinity of the hole) and less dense where it needs to be more flexible (weight-optimised solution). This again points to how intelligently biomaterials are designed (i.e. with a very high level of material efficiency and economy). These structures are also made of basic and relatively inferior materials such as calcium carbonate. However, the structures are highly optimised in order to realise properties and performance that is several orders of magnitude better than their constituents.

Collagen fibres are another natural material that can inspire the design of high-strength structural components. These fibres are composed of assemblies of parallel

collagen molecules arranged with a longitudinal stagger. It is thought that this staggered structure ensures much higher strength than can be realised from strictly parallel arrangement of collagen molecules or platelets (Jager and Fratzl 2000).

In terms of a natural material that has received a lot of attention over the years for its extraordinary mechanical performance and damage tolerance, and also mostly mimicked in material design, the nacre (abalone shell) tops the list. It is known to exhibit fracture toughness values that are 2–3 orders of magnitude higher than either of its constituent phases (Karambelasa et al. 2013; Ritchie 2011; Wang et al. 2000; Shao et al. 2013). This is usually attributed to its carefully arranged hierarchical multiphase, multilayered and functionalised brick-and-mortar architecture. The bricks or platelets, which are mineralised aragonite (calcium carbonate), form 95 vol.% of the structure separated by a protein layer (mortar) which forms the other 5 vol.% (Rabiei et al. 2010; Ritchie 2011; Shao et al. 2013). Despite this composition, it presents fracture toughness in energy terms of up to 3000 times higher than that of $CaCo_3$ (Wang et al. 2000). The platelets are closed-packed at a given layer, but they are staggered through the thickness. This hierarchic design results in a very high-performing material which easily adapts to different loading conditions. For example, when the resolved stresses are normal to the platelet plane, the organic matrix bridge between the platelets keeps them together and prevents uncontrolled crack growth. If the resolved stresses are shear, then the platelets slide successively over the organic matrix. This segmented layered structural design concept (used in nacre) can be used to design strong and yet tough materials for use in industrial applications such as superhard cutting tools.

The structure exhibits several levels of hierarchy, spanning all the way from nanoscale (e.g. mineral nanofibres and platelets imbedded within proteins) to micro- and macro-scales (Bechtle et al. 2010). Fundamentally, the nacre can be thought of as a brick-and-mortar structure as shown in Fig. 7.3.

The mineralised aragonite and organic biopolymer form the bricks and mortar, respectively. The bricks are approximately 0.5 um thick and 5–10 um wide (Ritchie 2011). The thickness of the organic layer (‘mortar’) is nanosize in dimensions with values of 10–45 nm reported in literature (Barthelat 2007, 2010; Barthelat et al. 2006; Lin and Meyers 2005; Nassif et al. 2005; Song and Bai 2003). The fracture-toughening mechanisms in the nacre can be assumed to occur at different length scales and both intrinsic and extrinsic. Intrinsic mechanisms refer to processes acting within the process zone ahead of the crack tip. These primarily relate to plasticity and are associated with making cracking or de-bonding more difficult by enlarging the plastic zone (Ritchie 2011). On the other hand, extrinsic toughening mechanisms relate to processes acting during crack propagation at the location of the crack to inhabit crack growth. These include formation of microcracks around the crack tip to reduce stress concentration, and crack bridging and friction interlocking in the wake of crack to induce some sort of crack closure (Ritchie 2011). Extrinsic toughening mechanisms arising from crack blunting, deflection and bridging at the brick-mortar interfaces have been suggested as the dominant factors in the high toughness of the nacre (Lin and Meyers 2005; Rabiei et al. 2010; Ritchie 2011). Crack deflections promote a more torturous crack path which

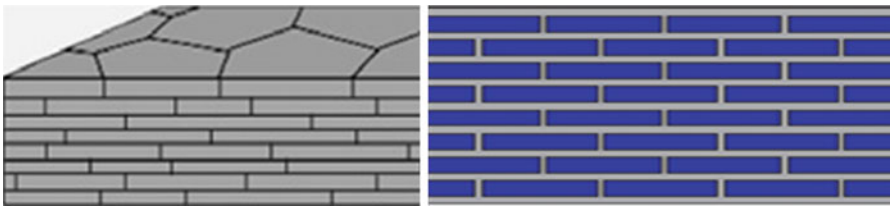

Fig. 7.3 A schematic representation of the nacre's microarchitecture (i.e. brick-mortar structure)

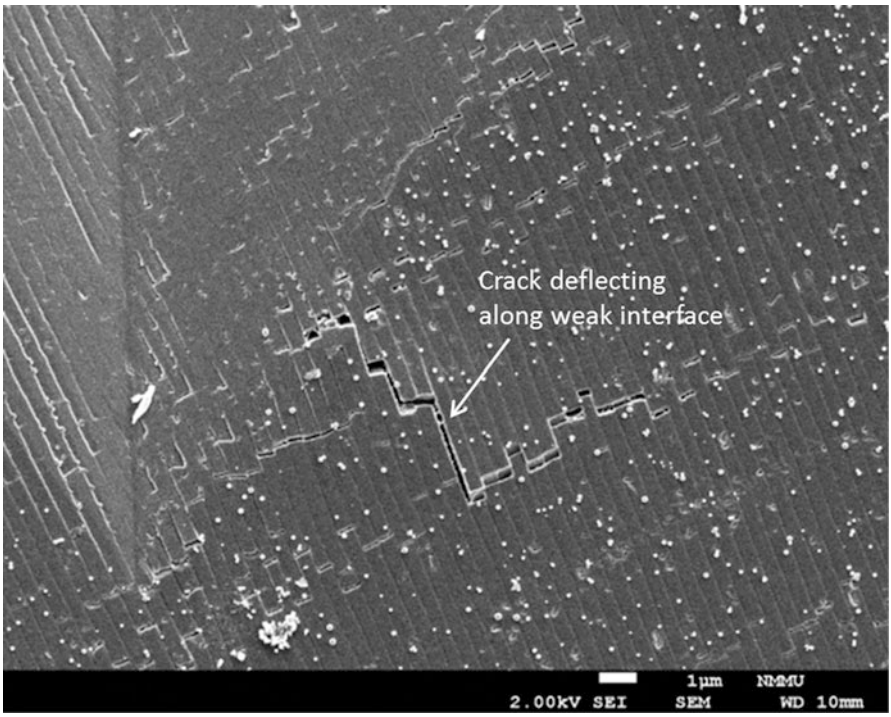

Fig. 7.4 Crack deflection in shell (nacre) structure subjected to indentation loading (in order to generate and propagate cracks in the structure). The work was performed by Dr. L. Westraadt (Nelson Mandela Metropolitan University, South Africa) on behalf of Element Six Ltd, UK

increases the resistance to crack growth. Figure 7.4 shows an example of crack deflection in a shell structure subjected to indentation loads in order to induce and grow cracks. The aim was to study the crack growth behaviour through the structure.

The pull-out effect of platelets acts as bridging elements and promotes transfer of stresses between crack surfaces (Lin and Meyers 2005; Rabiei et al. 2010). During relative sliding between neighbouring platelets, the organic ligaments are also thought to provide some bridging effect and transfer stresses (Barthelat and

Espinosa 2007; Shao et al. 2012). The adhesion between the platelets and the organic layer is very critical to the toughness of the nacre (Ritchie 2011). If the neighbouring platelets were strongly bonded together, the resulting toughness would be very low and close to that of a monolithic structure. A weak adhesion and lubricating effect provided by the organic layer allows for limited movement between the platelets. This helps relieve high local stresses and enhance the fracture toughness of the structure. However, excessive sliding between the platelets would render the material weak (Ritchie 2011). It is hypothesised that the roughened surfaces of the mineral platelets provide frictional stops which limit the amount of sliding (Chaia and Lawn 2004; Karambelasa et al. 2013; Ritchie 2011). In addition, small mineral 'bridges' linking the layers also help control the relative movement of the platelets.

Research has also shown that the fracture toughness of nacre exhibit a distinct dependence on the sizes and aspect ratios of platelets (Shao et al. 2012). This is important if the main toughening mechanism is due to crack bridging of platelets and their pull-out during the fracture process as suggested by several studies. Shao et al. (2012) showed that in order to achieve high toughness, the thickness of the platelets has to be in a certain range, with values of less than one micron proposed. On the other hand, very thin platelets are likely to break before being pulled out due to the tensile traction (Shao et al. 2012). A large aspect ratio was also suggested as beneficial for the improvement of toughness by crack bridging effect. However, it is extremely difficult to reproduce submicron features found in the nacre in most structural ceramics, and even more challenging in superhard materials, where the particle size of the powders used is already greater than a micron. In addition, having the necessary technology to replicate these structures or features at the same micro- and nanoscales is also a challenging task. Therefore, there is need to establish the most important design parameters for biomimicked ceramics between the size of the features, their aspect ratios, interface properties and stacking pattern. Effect of the interaction between these parameters is also of paramount importance.

Engineering weak interfaces in materials, either at the microstructure level or mesoscale, can greatly enhance the damage tolerance and resistance to fracture. The idea is to promote crack deflection along interface boundaries rather than cracks propagation through these boundaries. Two possible scenarios exist for a crack approaching an interface of two materials, i.e. deflect along the interface or penetrate through it. According to He and Hutchinson (1989), this is governed by the ratio between the energy required for crack deflection along the interface (G_d) versus that required for a crack to penetrate through the interface (G_p), given by Eq. 7.6:

$$\frac{G_d}{G_p} = \left(\frac{1-\beta^2}{1-\alpha}\right)\frac{|d|^2 + |e|^2 + 2\mathrm{Re}(de)}{c^2} \tag{7.6}$$

where α and β are Dundurs' parameters defined in He and Hutchinson (He and Hutchinson 1989) and c, d and e are complex valued functions of α and β. They

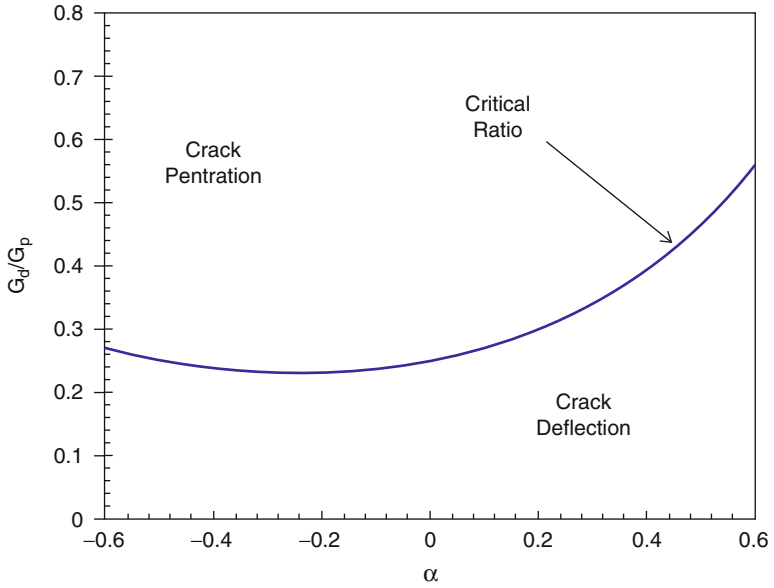

Fig. 7.5 Critical ratio of interface strength versus bulk material strength for crack deflection versus crack penetration as a function of α (data reproduced from He and Hutchinson (He and Hutchinson 1989), for α not too different to zero, the critical ratio is approximately 0.25. This corresponds to a case where the elastic properties are the same either side of an interface. The critical ratio increases to approximately 0.38 when $\alpha = 0.33$, corresponding to a modulus factor difference of two across a material interface)

reported that under given conditions, a critical ratio (G_d/G_p) exists below which crack deflection along the interface is favoured over crack penetration as illustrated in Fig. 7.5 (for $\beta = 0$). This is also confirmed in separate studies looking at crack propagation through multilayered structures (Carolan et al. 2013b). G_d and G_p can also be related to the maximum cohesive strength of the interface $\sigma_{\max}^{\text{int}}$ and the bulk $\sigma_{\max}^{\text{bulk}}$, respectively, via cohesive zone model (CZM). Therefore a critical ratio between $\sigma_{\max}^{\text{int}}$ and $\sigma_{\max}^{bulk}$ can also be determined below which crack deflection would be preferred over penetration.

Understanding this relationship between G_d and G_p is important if one wants to exploit this crack deflection mechanism in order to develop tough and damage-tolerant material. This toughening mechanism is also one of the most important in the nacre (Fig. 7.4). If the layers or 'bricks' are strongly bonded, crack penetration through the interface is more likely to occur than crack deflection. Similar results to Fig. 7.4 can also be obtained via a numerical analysis of crack growth through a brick-mortar structure mimicking the nacre. A single-edge notched sample is loaded in a three-point bend test set-up as shown in Fig. 7.6. The sample size is 36 um long and 8 um wide, with a pre-crack length $a = 2$ um and span $S = 32$ um.

The interface properties are chosen such that crack deflecting and propagation along the interface is preferred over crack penetration through the interface. This is

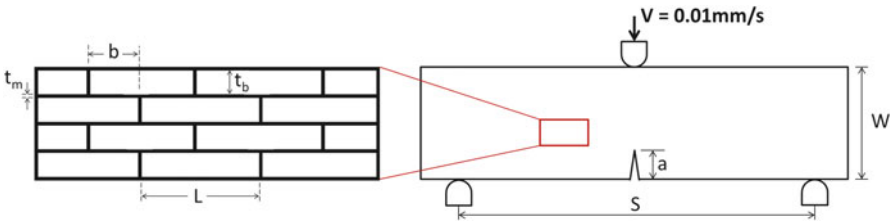

Fig. 7.6 Geometry for numerical modelling of crack propagation through a brick-mortar structure, mimicking the nacre

determined using the analysis proposed by He and Hutchinson (1989) as discussed earlier. The optimum value of σ_{max}^{int} was found to be one third of σ_{max}^{bulk}. With this value, crack propagation is predominantly through the interface (mortar). However, this also depends on other factors such as the thickness of the bricks (t_b), aspect ratio (L/t_b) and stacking pattern. The properties of the platelets used are approximated based on reported literature values for aragonite calcium carbonate, i.e. Young's modulus E = 70 GPa, cohesive strength $\sigma_{max}^{bulk} = 100$ MPa, fracture energy G = 0.1 J/m^2, density rho = 2830 kg/m^3 and Poisson's ratio = 0.1 (Bechtle et al. 2010). Details of the numerical procedure can be found in Appendix 7.1.

It is shown in these results that the work of fracture is significantly higher when cracks are forced to deflect along weak interface boundaries rather than propagating through them (Fig. 7.7).

Structures such as the nacre can be used to inform the design of superhard materials with greatly enhanced toughness. Such materials would truly revolutionise the superhard material market, especially in cutting/machining and drilling applications. They would offer high reliability, durability and predictable cutting tool breakdown characteristics. These aspects are currently lacking in traditional superhard and ultrahard materials such as polycrystalline cubic boron nitride and diamond.

2.2 *Other Ways of Creating Exceptionally Tough Superhard Materials*

Apart from mimicking natural materials, there are also other general methods of designing superhard materials with superior toughness. Examples of these include dispersing a tough phase in a superhard material matrix (Khan et al. 2010; Li et al. 2008a; Oksman and Craig 1998; Roether and Baccaccin 2005; Yun et al. 2004), engineering controlled defects (Evans et al. 1997; Hutchinson 1989; Shum and Hutchinson 1990), functionally graded structures (Buskirk et al. 2000; Baccaccini 2005; Jeong-Ho and Paulino 2002; Mishnaevsky 2005; Munch et al. 2008), nanostructuring (Li et al. 2008a, b; Tan and Wie 1998), imbedding a three-dimensionally interpenetrating network of a tough phase inside a brittle

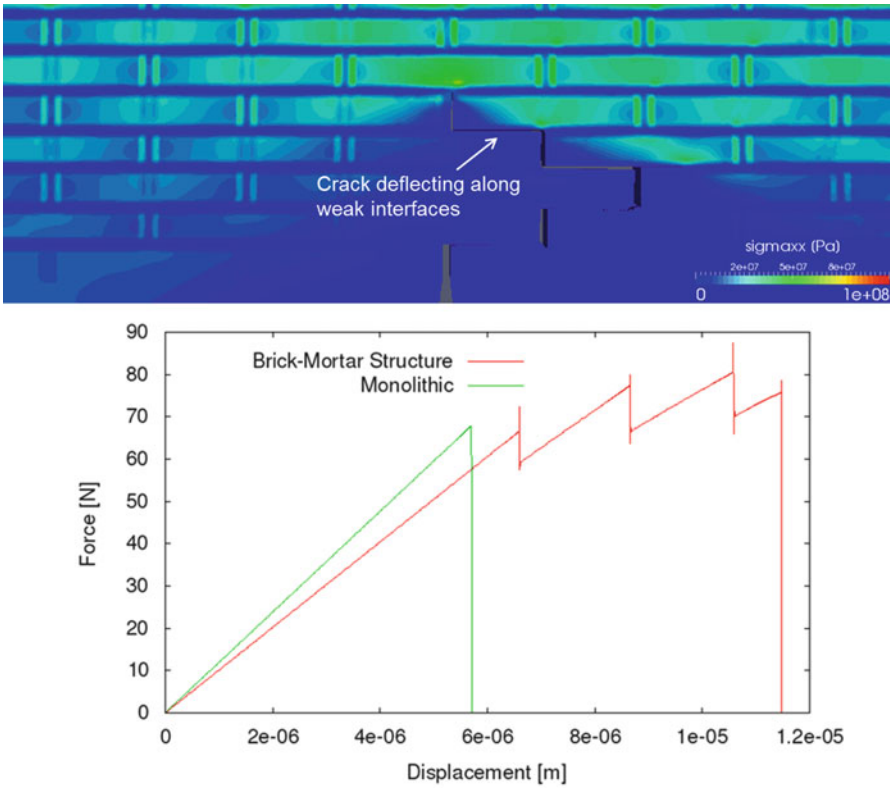

Fig. 7.7 Numerical prediction of crack growth through the brick-mortar structure, showing crack deflection along weak interfaces (*top*). The work of fracture is significantly higher in a brick-mortar structure compared to a monolithic one (*bottom*). This is mainly due to the structure providing a more torturous path for crack. Bricks with high aspect ratios may also provide an interlocking mechanism and contribute to the increasing R-curve behaviour

matrix (Lin et al. 2014; Wang et al. 2010; Wanga and Liu 2008) and several other toughening mechanisms extensively covered in literature. The above mechanisms are also key features of natural materials as seen in the previous section (i.e. Sect. 2.1). The general concept of functionally graded structures, apart from it being a key aspect of biomimicked materials, has been extensively used in order to design engineering materials with a good combination of toughness and hardness (or strength). Functionally graded materials are composites in which the volume fraction of constituent materials varies gradually, usually along the component's thickness. The result is a non-uniform microstructure with continuously graded macro-properties. The 'layers' are stacked in a predefined sequence in order to achieve desired properties, which are usually superior in comparison to monolithic materials (Mishnaevsky 2005; Munch et al. 2008). Such designs open up several opportunities for optimising both material and component structures to achieve high performance and material efficiency (Jeong-Ho and Paulino 2002) and can be

adapted to most industrial materials (including the superhard materials) design relatively easy.

The technique of using layered structures or functionally graded materials is now widely being used in designing ceramics with enhanced fracture toughness (Buskirk et al. 2002; Jeong-Ho and Paulino 2002; Mortensen and Suresh 1997). In many ways and as seen in Sect. 2.1, these designs are inspired by biomaterials whose extraordinary properties are thought to result from their peculiar microstructures, i.e. architecture and arrangement and distribution of the microstructural elements. The emphasis in these functionally graded materials is to achieve an optimum combination of two or more properties, e.g. hardness and toughness. For example, Fig. 7.8 shows the results of numerical modelling of crack propagation through a graded structure consisting of a relatively tougher material ('blue', material A) sandwiched between layers of a less tough one ('red', material B). The properties of material A (red) and material B (blue) are summarised in Table 7.1. The numerical model employs a cohesive zone model (CZM) approach with crack growth taking place through the natural process of de-bonding of the cohesive zone under loading (Carolan et al. 2013b). Details of the numerical procedure can be found in Appendix 7.1.

It is clear that a graded structure offers more resistance to crack growth as indicated by the time taken for crack to grow by a similar length under identical loading conditions compared to a monolithic structure (which is composed of only material B). In the monolithic structure, it takes the crack 10 microseconds to grow by 7.5 mm, whereas the time required in a graded structure is 160 microseconds, representing a 16-fold increase.

A superhard material can also be toughened by dispersing a second phase in its matrix. This toughening mechanism has already been successfully employed to improve fracture toughness in brittle ceramics. The process normally involves adding a tougher dispersed phase to a ceramic matrix. Examples include the works of Walter et al. (1997), Magniez et al. (2011), Evans (1997), Raj and Thompson (1994) and Tan and Wie (1998). A tougher second phase network would absorb energy through plastic deformation and hence retard crack growth or extension. On the other hand, it was also shown by Evans (1997) and Evans et al. (1997) that the second dispersed phase does not necessary has to be a ductile phase. It can be brittle second phase particles which fail in the stress field of a growing crack, resulting in controlled microfracture. The goodness with using brittle particles is that the overall hardness of the composite would not be sacrificed but may even be further enhanced. This would open up possibilities of designing superhard materials (i.e. diamond and cubic boron nitride composites) with favourable fracture performance without any deterioration in abrasion resistance. The dispersed second phase can also be used as localised stress raisers which would facilitate crack bifurcation and/or multiple crack fronts, resulting in increased fracture resistance. The concept of toughening by microcracks has been suggested by a number of researchers (Evans et al. 1997; Hutchinson 1989; Shum and Hutchinson 1990). The rationale is to minimise the maximum energy release rate (G) among the various crack tips. Therefore, a material that can generate multiple

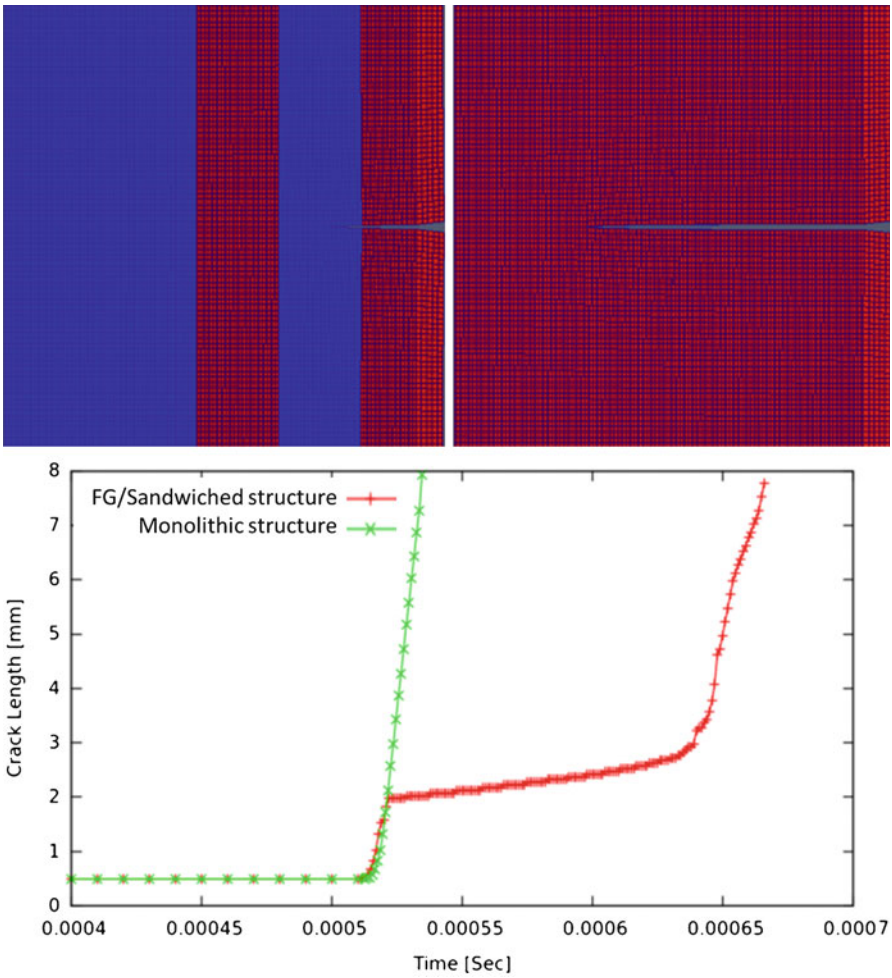

Fig. 7.8 Numerical simulation of crack propagation through a graded structure consisting of a relatively tougher material ('*blue*', material A) sandwiched between layers of a less tough one ('*red*', material B) as shown in top images. The graded structure offers better resistance to crack propagation that a monolithic one

Table 7.1 Material properties of material A and material B, with the former being the tougher of the two materials

Material property	Material A	Material B
E	900 MPa	1000 MPa
G	81 J/m^2	40 J/m^2
σ_{max}	1200 MPa	1600 MPa

cracks under loading would behave tougher than a material with only one major crack since multiple crack fronts entail that the net energy supplied to a system has to be divided up between several cracks, resulting in a much slower rate of crack growth. The other mechanism that can be facilitated by inducing evenly or randomly distributed/dispersed micro-defects in a material is that it would facilitate crack bifurcation. The size, shape and distribution of these micro-defects are critical and would, thus, require to be optimised. Based on this optimisation, it is possible to improve fracture resistance without significantly compromising the overall strength and hardness of the material, which is desirable for superhard materials.

In order to fully realise the benefit of using a 'second dispersed phase' as a toughening mechanism, one has to consider several key factors that require optimisation. These include the volume fraction of the dispersed phase; the microstructural parameters of the inclusions such as shape, aspect ratio and size; and the differences in elastic properties, strength and fracture toughness of the matrix and inclusions. In addition, the thermal expansion mismatch between the matrix and inclusions need to be optimised in order to get a favourable residual stress state of the resulting composite/structure. The properties of the matrix/inclusion interfaces are also important, i.e. whether one requires that the inclusions are strongly or weakly bonded to the matrix. The latter may be beneficial in deflecting cracks at the interfaces between the inclusions and the matrix as discussed earlier in the case of the nacre (Sect. 2.1).

Apart from the toughening mechanisms discussed above, there are still several others that can potentially be applied to superhard materials. The most important aspect is controlling what is happening in the vicinity of a growing crack (controlled microfracture) such as through transformation toughening and crack shielding (Ritchie 1999). However, to be able to appreciate these mechanisms and effectively employ them to improve a material's fracture resistance, one has to first understand the mechanisms of crack propagation in superhard materials, which by their nature are intrinsically brittle. The mechanisms of crack growth in brittle materials are quite distinct from those commonly encountered in ductile materials such as metals. In the later, crack growth is predominantly due to intrinsic microstructural damage mechanisms, which promote crack extension ahead of the crack tip, whereas in brittle materials it is usually controlled by extrinsic crack-tip shielding mechanisms which act primarily behind the crack tip to retard crack growth (Ritchie 1988, 1999). Figure 7.9 illustrates the two competing toughening mechanisms, i.e. extrinsic toughening which is predominant in brittle materials and intrinsic toughening which dominate fracture in ductile materials.

In ductile materials, intrinsic damage mechanisms typically involve processes which create microcracks or voids, e.g. by dislocation pile-ups or interface decohesion, in the highly stressed region ahead of the crack tip, leading to classical failure by cleavage, intergranular cracking or microvoid coalescence, and may also involve the repetitive blunting and resharpening of the crack tip in the case of cyclic loading (Neumann 1969). The creation of several microcracks in a highly stressed region, which precedes microcrack coalescence, is one of the main reasons for the high toughness of ductile materials. Extrinsic shielding mechanisms are caused by the creation of inelastic zones in the crack wake or from physical contact between

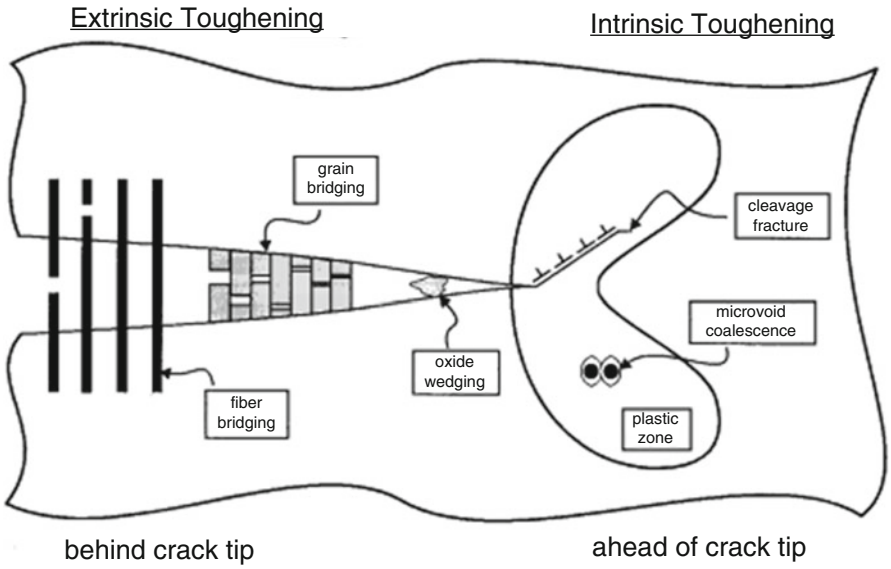

Fig. 7.9 Competition between extrinsic and intrinsic toughening mechanisms, with the former controlling the fracture process in brittle materials (Ritchie 1999)

the crack surfaces via wedging, bridging, sliding or combinations of these factors (Ritchie 1988). The typical example is 'zone shielding' such as transformation and microcrack toughening in ceramics and rocks, where the in situ dilatant phase transformations or the microcracking of precipitates/particles ahead of the crack tip can lead to inelastic zones in the crack wake which impart closing tractions on the crack surfaces (Ritchie 1988). The other example is that of 'contact shielding' caused by bridging tractions imposed across a crack by unbroken fibres, laminated layers or a particulate phase in composite materials, or the wedging of corrosion debris or fracture surface asperities during crack closure. Its should be noted here that intrinsic mechanisms are an inherent property of the material and thus are active irrespective of the length of the crack or the geometry of the test specimen and control the driving forces (e.g. the stress intensity or mode I, II and III fracture toughness) responsible for initiating a crack. On the other hand, extrinsic mechanisms act in the crack wake and, hence, are critically dependent on crack size and responsible for the development of resistance-curve (R-curve) behaviour resulting in improved fracture resistance (e.g. Evans 1997; Becher 1991). For example, Evans (1997) demonstrated that more than a fivefold increase in fracture toughness of zirconia can be achieved by inducing an in situ phase transformation at the crack tip (transformation toughening) or by causing the in situ microcracking of particles (microcrack toughening), both processes causing a dilation around the crack tip which is constrained by surrounding elastic material. There are several literatures that the reader can consult on toughening mechanisms and how they can be applied to inherently brittle materials such as the superhard materials discussed in this chapter.

3 Cost-Effective Manufacturing and Processing of Superhard Materials

The manufacturing and processing of traditional superhard materials, e.g. diamond and cubic boron nitride, is extremely challenging and expensive. In order to synthesis these materials, one requires access to extremely high temperatures and pressures usually in excess of 1400 °C and 5 GPa, respectively. In addition, processing superhard materials into final formats required by end users using traditional material removal machining methods is not a trivial task. All these have an impact on the overall cost of manufacturing superhard materials for cutting tools. The other challenge is that industry continues to require superhard parts and cutting tools with complex geometries. Unfortunately, traditional superhard material manufacturing technologies lack the ability to compete in a market where customers require customised complex components. This challenge can be overcome by additive manufacturing, in particular 3D printing, given the nearly unlimited design freedom that it provides (Faes et al. 2015). In addition, using additive manufacturing technologies would not only reduce material waste but also a significant step towards reducing the current costs associated with superhard materials manufacturing and processing.

3.1 Additive Manufacturing Technologies

As cutting tools and other superhard parts continue to require more intricate geometries such as chip-breakers, additive manufacturing technologies such as 3D printing or laser sintering will be key enablers to realising this at a favourable cost. Current methods of preparing such geometries are based on machining already sintered polycrystalline diamond or cubic boron nitride blanks/blocks either using laser ablation, electron discharge machining or via mechanical grinding operation. The ability to form the required final geometry via additive manufacturing is an appealing concept. However, the biggest challenge is that the sintering or synthesis of both diamond and cubic boron nitride needs high pressure due to their phase transformations at higher temperatures required to form sintered bodies (see Chap. 2 for details). Therefore, the most feasible approach at the moment is forming near net-shaped green bodies of required geometries via appropriate techniques such as 3D printing and then subjecting such geometries to the high pressure and high temperature sintering process. This does not necessarily reduce the high cost of the HPHT process but having a near net-shaped part reduces the amount of further processing required. The other thing that 3D printing techniques offer is the ability to form very intricate shapes which cannot be achieved any other way in a cost-effective manner. The current printing technologies can now produce parts to the resolution of few microns.

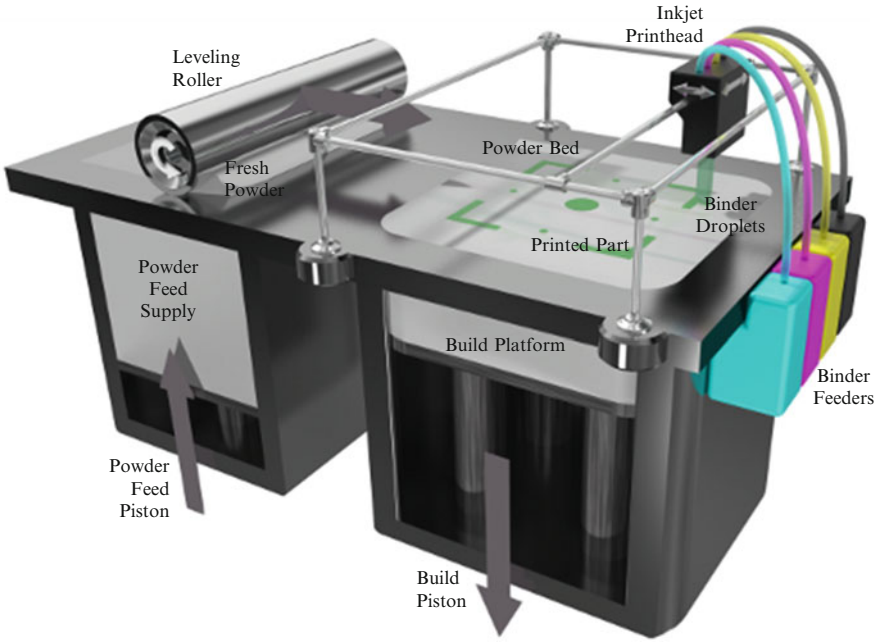

Fig. 7.10 Schematic of the Inkjet 3D printer from http://techrefectory.blogspot.co.uk (author: Sahil Bansal)

Three-dimensional printing is a layer-type additive manufacturing technique involving the deposition of powdered material in layers and selective binding of the powder by either 'inkjet' printing of a binder material or laser sintering. The unbound powders are then removed in order to recover the printed part. This process can be applied to the production of metal, ceramic and metal/ceramic composite parts. Figure 7.10 shows the schematic of a typical inkjet 3D printer used for printing ceramic parts.

3D printing provides significant opportunities for additive manufacturing of hard metals and superhard products. Applications for such may include microwear parts in electronic applications, mechanical components, complex moulds and dies and specialist cutting tools with integral coolant channels (Brookes 2015). Other applications are for printing ceramic and superhard microinjection moulding dies and moulds for handling superabrasive materials. Several researchers are already using 3D printing to manufacture hard metal parts and coatings. Zhang et al. (2015) employed 3D printing, which in their study is referred to as 'Laser Engineered Net Shaping (LENS™)', to deposit hard coatings of Ti-Si-N with three different Ti-Si ratios on commercially pure titanium substrate (Zhang et al. 2015). The coatings were later analysed and found to show graded microstructures and in situ formed phases. The hardness of the coatings were found to be favourable but with still a lot of scope for optimisation. Nevertheless, the possibility to use 3D printing for this purpose was demonstrated. Other examples include the work of Fu et al. (2013)

who fabricated silicon/silicon carbide ceramic composites using 3D printing of Si/SiC/dextrin powder blends. In this case, the parts (green bodies) had to undergo further heat treatments before final parts were realised. Companies such as NanoSteel have been using 3D laser printing/sintering to manufacture high-hardness ferrous metal matrix composite (MMC) parts using nano-particulate powders (NanoSteel 2015). The parts are prepared in a single 3D printing step and do not need to undergo any further processing and are reported to be 99.9 % dense, crack-free and with the wear resistance matching M2 tool steels made via conventional subtractive manufacturing technology (i.e. casting and machining). The hardness of these printed parts is about 61.91 HRC (Hardness Rockwell C). The lack of post-processing is thought to be a significant benefit as it reduces production costs. Kennametal and Valenite corporations are also looking into the fabrication of cemented carbide (i.e. tungsten carbide/cobalt) cutting tools using 3D printing (http://www.mit.edu/~tdp/6.html). In this case, the key opportunity that additive manufacturing is thought to offer over the current practice of dry pressing is the several degrees of flexibility (including geometry, in composition and in response to market demand).

Three-dimensional printing can also be integrated with other manufacturing and processing technologies. For example, Ahn et al. (2015) developed a novel nano-scale 3D printing process that integrated nanoparticle printing, micromachining and focused ion beam technology. An aerodynamically focused nanoparticle (AFN) printing, which is a room-temperature direct printing technique using shock-induced aerosol generation, was adopted for material formation, and focused ion beam was used for profiling the positioned material. In order to assist and bridge these two processes at different scales, micromachining using tools with diameters of 30 μm was employed. This integrated process enabled various 2.5D and 3D structures to be printed using metal/ceramic nanoparticles with no requirement for any post-treatment (Ahn et al. 2015).

It is clear that the current market trend is pushing towards the use of these additive technologies in order to reduce material waste/cost, increase responsiveness to market needs (especially for customised and complicated 3D shapes) and eliminate the need for post-processing (i.e. towards a single-step manufacturing process). Superhard materials and products would greatly benefit from such technologies given the challenges they present during post-processing steps in order to make the final geometries required by end users. There is also an increasing market need for micro-tools with 3D complex geometries which probably would not be made any other way other than through 3D printing or similar technologies.

Appendix 7.1: Numerical Modelling of Crack Propagation

The numerical model employs a cohesive zone model (CZM) to simulate crack propagation, using OpenFOAM software (a 3D finite volume C++ library). Fatigue crack growth is also incorporated into the model through the introduction

of a damage variable, D, into the CZM. Damage accumulates until sufficiently high to initial a crack or extend an already existing one. Cracks are grown through the natural process of de-bonding of the cohesive zone under cyclic loading. Decaying cohesive properties means that energy dissipation under fatigue fracture is less than the material toughness under monotonic loading. The model had been validated separately using experimental data before being employed in this analysis.

Numerical Analysis

The Cauchy momentum balance equation for a continuous media, neglecting body forces and assuming infinitesimal displacements U, can be given by

$$\rho \frac{\partial^2 \mathbf{U}}{\partial t^2} = \nabla . \boldsymbol{\sigma}, \tag{7.7}$$

where ρ is the density and $\boldsymbol{\sigma}$ is the Cauchy stress tensor defined by the constitutive law. In the case of an isothermal multi-material linear elastic model, $\boldsymbol{\sigma}$ is given by

$$\boldsymbol{\sigma} = \mu \left[\nabla \mathbf{U} + (\nabla \mathbf{U})^{\mathrm{T}} \right] + \lambda \, \mathrm{tr}(\nabla \mathbf{U}) \mathbf{I}, \tag{7.8}$$

where μ and λ are the shear modulus and second lame coefficient, respectively, and ∇ is the gradient operator. The normal and tangential components of the traction vector $\mathbf{t} = \mathbf{n}.\boldsymbol{\sigma}$ can be expressed as shown by [ZT,Alojz] given in Eqs. 7.8 and 7.9:

$$t_n = (2\mu + \lambda) \, \mathbf{n}.\nabla \mathbf{U} - (\mu + \lambda) \, \mathbf{n}.\nabla \mathbf{U}_t + \lambda \, \mathbf{n} \, \mathrm{tr}(\nabla_t \mathbf{U}_t) \tag{7.9}$$

$$\mathbf{t}_t = \mu \, \mathbf{n}.\nabla \mathbf{U}_t - \mu \nabla_t U_n \tag{7.10}$$

where $\nabla_t = (\mathbf{I} - \mathbf{nn}).\nabla$ is the tangential gradient operator and $\mathbf{n}$ is the unit normal vector. The subscripts n and t represent the normal and tangential components of the vector, respectively. A cohesive zone model (CZM) is employed to predict the fracture process. This assumes the fracture formation as a gradual phenomenon in which the separation of the new crack surfaces takes place across an extended crack tip, or cohesive zone, and is resisted by cohesive tractions as shown in Fig. 7.11 (Carolan et al. 2013b). Crack growth is through the natural process of de-bonding of the cohesive zone under loading. The numerical procedure allows prediction of crack propagation along internal control volume faces. When the failure criterion is satisfied (i.e. $t_n \geq \sigma_{\max}$ mode I and $\mathbf{t}_t \geq \tau_{\max}$ for mode II), these internal faces are transformed into cohesive zone boundary faces. $\sigma_{\max}$ and $\tau_{\max}$ represent the maximum cohesive strength of the material in tension and shear, respectively. The traction forces specified at the new boundary faces follow a prescribed traction-separation law or cohesive zone model.

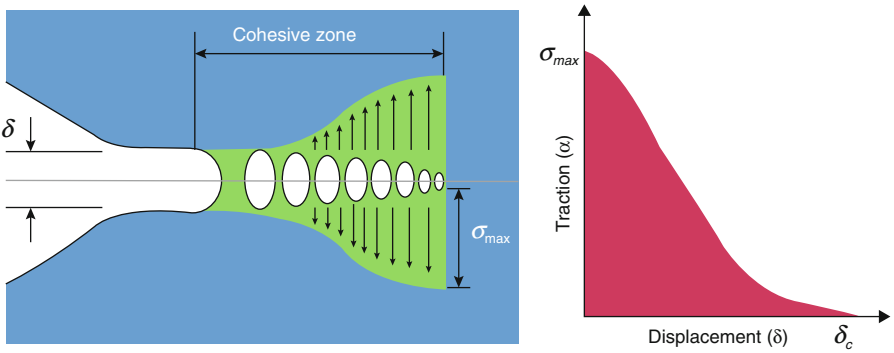

Fig. 7.11 Traction-separation relationship in the cohesive zone (Reproduced from (Carolan et al. 2013b))

The current study employs a linear cohesive zone model. This only requires two parameters to fully describe the model, i.e. the fracture energy G_c and the maximum cohesive strength as shown in Fig. 7.5 for mode I and mode II crack, respectively. Cracks can initiate and propagate under any of the two models, or a mixture thereof, depending on which condition is satisfied. According to the model, the traction between cohesive faces decreases with the separation distance between the faces. Fracture is assumed to have taken place when the critical separation distance is reached. At this point the cohesive faces become traction-free. Under all scenarios (i.e. mode I, mode II and mixed mode I & II), both the opening normal t_{cn} and shear t_{ct} cohesive tractions are assumed to decrease at the same rate.

For Mode I

$$t_{cn} = \sigma_{\max}\left(1 - \frac{\delta}{\delta_C}\right) \text{and} \, t_{cn} = \sigma_{\max}\left(1 - \frac{\delta}{\delta_C}\right) \tag{7.11}$$

For Mode II

$$t_{ct} = \tau_{\max}\left(1 - \frac{\gamma}{\gamma_C}\right) \text{and} \, t_{cn} = \sigma_{\max}\left(1 - \frac{\gamma}{\gamma_C}\right) \tag{7.12}$$

where δ and γ, are respectively, the normal and tangential components of the separation distance and the subscript C denotes the critical values at which cohesive

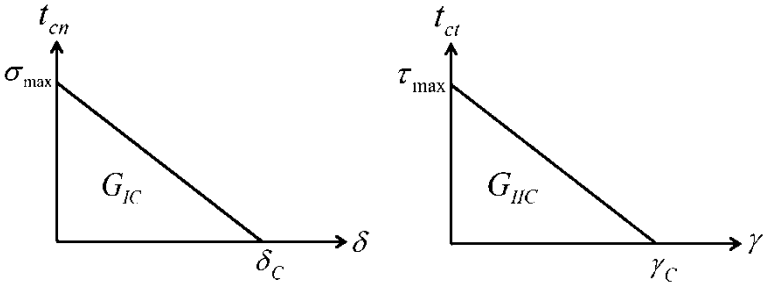

Fig. 7.12 Mode I (*left*) and Mode II (*right*) traction-separation laws, linear model

faces become traction-free. In the case of mixed mode I and II crack, the effective traction t_{eff}, effective separation distance δ_{eff} and effective maximum cohesive strength $\sigma_{\max}^{eff}$ are used instead:

$$t_{eff} = \sqrt{t_n^2 + |\mathbf{t}_t|^2} \geq \sigma_{\max}^{eff} \text{ and } \sigma_{\max}^{eff} = \sqrt{\sigma_{\max}^2 + \tau_{\max}^2} \tag{7.13}$$

$$\delta_{eff} = \sqrt{\delta^2 + \gamma^2} \text{ and } \sigma_{\max}^{eff} = \sqrt{\delta_C^2 + \delta_C^2} \tag{7.14}$$

The traction between the cohesive faces is then defined by

$$t_{cn} = t_{0n}\left(1 - \frac{\delta_{eff}}{(\delta_{eff})_C}\right) \tag{7.15}$$

$$t_{ct} = t_{0t}\left(1 - \frac{\delta_{eff}}{(\delta_{eff})_C}\right) \tag{7.16}$$

where t_{0n} and t_{0t} are the initiation tractions in the normal and tangential directions determined when the condition $t_{eff} = \sqrt{t_n^2 + |\mathbf{t}_t|^2} \geq \sigma_{\max}^{eff}$ is satisfied (Fig. 7.12).

Fatigue Crack Growth

For modelling fatigue crack growth, a damage variable, D, is introduced into the cohesive zone model (Abdul-Baqi et al. 2005; Arias et al. 2004; Roe and Siegmund 2003; Ural et al. 2009). A crack is initiated or extended when the combination of accumulated damage and traction satisfies the failure criteria, i.e. $t_n \geq \sigma_{\max}(1 - D)$

for mode I. The same applies to mode II and mixed mode. The damage accumulated during each time step (or loading cycle) ΔD is given by

$$\Delta D = (1 - D)^m \frac{\left|\Delta\widetilde{\delta}\right|}{\delta_C} \left[\frac{t - \sigma_{th}}{\sigma_{\max}}\right] \text{and} \, \Delta D \geq 0 \tag{7.17}$$

where m is a constant which control the decay of the reaction force at the final stage of damage (Abdul-Baqi et al. 2005), t is the traction at a face (normal traction in case of mode I fracture), $\Delta\widetilde{\delta}$ is the incremental deformation or loading separation distance and σ_{th} is the material's fatigue threshold (or fatigue endurance limit). The condition $\Delta D \geq 0$ ensures that the accumulated damage is always positive and either increases or stays the same with successive loading cycles. A zero value of m indicates that total accumulated damage, D, is not taken into account when calculating ΔD, and the opposite being true for a non-zero value. The total accumulated damage (during current time step or current loading cycle), D_{t_n} is, thus, given by

$$D_{t_n} = D_{t_{n-1}} + \Delta D \tag{7.18}$$

where $D_{t_{n-1}}$ is total damage during the previous time step. The following observations can be made from the above Eqs. 7.7 to 7.9.

- The crack only initiates or extends if damage, accumulated or current, is greater than some critical value. $D_{\max}$, for a given traction, t.
- The increment in damage is related to the increment in deformation, $\Delta\widetilde{\delta}$, weighted by the current traction or load level.
- There exists a fatigue limit, σ_{th}, below which cyclic loading can proceed infinitely without failure. Damage can only accumulate if the current traction is above this limit.

The modified cohesive parameters, taking into account the accumulated damage, can thus be defined as for mode I: $\widetilde{\sigma}_{\max} = \sigma_{\max}(1 - D_{\max})$ and $\delta_C = \delta_C(1 - D_{\max})$.

References

Abdul-Baqi A, Schreurs P, Geers M (2005) Fatigue damage modelling in solder interconnects using a cohesive zone approach. Int J Solids Struct 42:927–942

Ahn S-H, Yoon H-S, Jang K-H, Kim E-S, Lee H-T et al (2015) Nanoscale 3D printing process using aerodynamically focused nanoparticle (AFN) printing, micro-machining, and focused ion beam (FIB). CIRP Ann Manuf Technol 64(1):523–526, ISSN 0007–8506

Amada S (1995) Hierarchical functionally gradient structures of bamboo. Funct Gradient Mater 20 (1):35–37

Amada S, Ichikawa Y, Munekata T, Nagase Y, Shimizu H (1997) Fibre texture and mechanical graded structure of bamboo. Compos Part B: Eng 28(1–2):13–20
Arias I, Serebrinsky S, Ortiz M (2004) A cohesive model of fatigue of ferroelectric materials under electro-mechanical cyclic loading. Active Mater Behav Mech Proc SPIE, 371–377
Arsecularatne JA, Zhang LC, Montross C (2005) Wear and tool life of tungstene carbide, PCBN and PCD tools. Int J Mach Tools Manuf 46(5):482–491
Baccaccini A (2005) Glass-containing composite materials: alternative reinforcement concepts. In: Handbook of ceramic composites. Springer, Bostan
Barry J, Byrne G (2001) Cutting tool wear in the machining of hardened steels: Part II: cubic boron nitride cutting tool wear. Wear 247(2):152–160, ISSN 0043–1648
Barthelat F (2007) Biomimetics for next generation materials. Philos Trans R Soc A 365:2907–2919
Barthelat F (2010) Nacre from mollusc shells: a model for high-performance structural materials. Bioinsp Biomim 5:035001
Barthelat F, Espinosa HD (2007) An experimental investigation of deformation and fracture of nacre – mother of pearl. Exp Mech 47:311–324
Barthelat F, Li CM, Comi C, Espinosa HD (2006) Mechanical properties of nacre constituents and their impact on mechanical performance. J Mater Res 21:1977–1986
Barthelat F, Tang H, Zavattieri PD, Li CM, Espinosa HD (2007) On the mechanics of mother-of-pearl: a key feature in the material hierarchical structure. J Mech Phys Solids 55:306–337
Becher P (1991) Microstructural design of toughened ceramics. J Am Ceram Soc 74:255–269
Bechtle S, Fung Ang S, Schneider GA (2010) On the mechanical properties of hierarchically structured biological materials. Biomaterials 31:6378–6385
Brookes KJA (2015) 3D-printing style additive manufacturing for commercial hardmetals. Metal Powder Rep 70(3):137–140, ISSN 0026–0657
Buskirk SR, Venkataraman S, Ifiu PG, Rapoff AJ (2002) Functionally graded biomimetic plate with hole Collection of Technical Papers – AIAA/ASME/ASCE/AHS/ASC Structures. Struct Dyn and Mat Conf 2:1015–1021
Carolan D, Ivanković A, Murphy N (2013a) A combined experimental–numerical investigation of fracture of polycrystalline cubic boron nitride. Eng Fract Mech 99:101–117. doi:10.1016/j.engfracmech.2012.09.008, ISSN 0013–7944
Carolan D, Tuković Z, Murphy N, Ivanković A (2013b) Arbitrary crack propagation in multi-phase materials using the finite volume method. Comput Mater Sci 69:153–159, ISSN 0927–0256
Chaia H, Lawn BR (2004) Fracture mode transitions in brittle coatings on compliant substrates as a function of thickness. J Mater Res 19(6):1752–1761
Chen P-Y, McKittrick J, Meyers MA (2012) Biological materials: functional adaptations and bio-inspired designs. Prog Mater Sci 57:1492–1704
Droty MD, Dauskardt RH, Kant A, Ritchie RO (1995) Fracture of synthetic diamond. J Appl Phys 78(5):3083–3088
Evans A (1997) Design and life prediction issues for high-temperature engineering ceramics and their composites. Acta Mater 45(1):23–40
Evans A, Heuer A, Porter D (1997) The fracture toughness of ceramics. In 4th conference on fracture, Canada
Faes M, Valkenaers H, Vogeler F, Vleugels J, Ferraris E (2015) Extrusion-based 3D printing of ceramic components. Proc CIRP 28:76–81, ISSN 2212–8271
Fu Z, Schlier L, Travitzky N, Greil P (2013) Three-dimensional printing of SiSiC lattice truss structures. Mater Sci Eng A 560:851–856, ISSN 0921–5093
Giménez S, Van der Biest O, Vleugels J (2007) The role of chemical wear in machining iron based materials by PCD and PCBN super-hard tool materials. Diamond Relat Mater 16:435–445
Goel P, Khan ZA, Siddiquee AN, Gupta RK (2012) Influence of slab milling process parameters on surface integrity of HSLA: a multi-performance characteristics optimization. Int J Adv Manuf Technol 61(9–12):859–871

Habibi MK, Samaei AT, Gheshlaghi B, Lu J, Lu Y (2015) Asymmetric flexural behavior from bamboo's functionally graded hierarchical structure: underlying mechanisms. Acta Biomater 16(2015):178–186

He M, Hutchinson J (1989) Int J Solids Struct 25:1053–1067

Hutchinson J (1989) Mechanisms of toughening in ceramics. In Theoretical and applied mechanics, IUTAM. Elsevier Science Publishers B.V. North-Holland

Jager I, Fratzl P (2000) Mineralised collagen fibrils: a mechanical model with a staggered arrangement of mineral particles. Biophysics 79:1737–1746

Jeong-Ho K, Paulino G (2002) Mixed-mode fracture of orthotropic functionally graded materials using finite element and the modified crack closure method. Eng Fract Mech 69:1557–1586

Karambelasa G, Santhanama S, Wing ZN (2013) Strombus gigas inspired biomimetic ceramic composites via SHELL – sequential hierarchical engineered layer lamination. Ceram Int 39:1315–1325

Kennam et al (2015) High-temperature machining guide. Machining guides. www.kennametal.com. Accessed 05 Nov 2015

Khan U, May P, O'Neill A, Coleman J (2010) Development of stiff, strong, yet tough composites by the addition of solvent exfoliated graphene to polyurethane. Carbon 48(14):4035–4041

Lee JJW, Morris D, Constantino PJ, Lucas PW, Smith TM, Lawn BR (2010) Properties of tooth enamel in great apes. Acta Biomater 6(12):1742–7061. doi:10.1016/j.actbio.2010.07.023, ISSN 4560–4565

Li J, Shi X, Wang L, Liu F (2007) Synthesis of biomorphological mesoporous TiO2 templated by mimicking bamboo membrane in supercritical CO2. J Colloid Interface Sci 315(1):230–236

Li G, Li P, Yu Y, Jia X, Zhang S, Yang X, Ryu S (2008a) Novel carbon fiber/epoxy composite toughened by electrospun polysulfone nanofibers. Mater Lett 62:511–514

Li G, Li P, Zhang C, Yu Y, Liu H, Zhang S, Jia X, Yang X, Xue S (2008b) Inhomogeneous toughening of carbon fiber/epoxy composite using electrospun polysulfone nanofibrous membranes by in situ phase separation. Compos Sci Technol 68:987–994

Lin A, Meyers MA (2005) Growth and structure in abalone shell. Mater Sci Eng A 390:27–41

Lin S, Xiong D, Liu M, Bai S, Zhao X (2014) Thermophysical properties of SiC/Al composites with three dimensional interpenetrating network structure. Ceram Int 40:7539–7544

Magniez K, Chaffraix T, Fox B (2011) Toughening of a carbon-fibre composite using electrospun poly(hydroxyether of Bisphenol A) nanofibrous membranes through inverse phase separation and inter-domain etherification. Materials 4:1967–1984

McNamara D, Alveen P, Carolan D, Murphy N, Ivanković A (2015) Fracture toughness evaluation of polycrystalline diamond as a function of microstructure. Eng Fract Mech 143:1–16, ISSN 0013–7944

Mishnaevsky LJ (2005) Numerical experiments in the mesomechanics of materials. Darmstadt University of Technology, Germany

Morrell R, Danzer R, Supanic P, Harrer W, Puchegger S, Peterlik H (2010) Meso-scale mechanical testing methods for diamond composite materials. Int J Refract Met Hard Mater 28(4):508–515

Mortensen A, Suresh S (1997) Functionally graded metals and metal-ceramic composites. Int Mater Rev 42(3):85–116

Munch E, Launey ME, Alsem DH, Saiz E, Tomsia AP, Ritchie RO (2008) Tough, bio-inspired hybrid materials. Science 322:1516–1520

NanoSteel (2015) NanoSteel at Powder Met 2015. Powder Met (MPIF), San Diego, 17–20 May

Narutaki N, Yamane Y (1979) Tool wear and cutting temperature of cBN tools in machining of hardened steels. Ann ICRP 28(1):23–28

Nassif N, Pinna N, Gerhke N, Antonietti M et al (2005) Amorphous layer around aragonite platelets in nacre. Proc Natl Acad Sci USA 102:12653–12655

Neumann P (1969) Coarse slip model in fatigue. Acta Metall 17:1219–1225

Okamoto S, Nakazono Y, Otsuka K, Shimoitani Y, Takada J (2005) Mechanical properties of WC/Co cemented carbide with larger WC grain size. Mater Charact 55(4–5):281–287, ISSN 1044–5803

Oksman K, Craig C (1998) Mechanical properties and morphology of impact modified polypropylene-wood flour composites. J Appl Polym Sci 67:1503–1513

Petrovic M, Carolan D, Ivankovic A, Murphy N (2011) Role of rate and temperature on fracture and mechanical properties of PCD. Key Eng Mater 452(452–453):153–156

Rabiei R, Bekah S, Barthelat F (2010) Failure mode transition in nacre and bone-like materials. Acta Biomater 6:4081–4089

Raj R, Thompson L (1994) Design of the microstructural scale for optimum toughness in metallic composites. Acta Metall Mater 42(12):4135–4142

Ritchie R (1988) Mechanisms of fatigue crack propagation in metals, ceramics and composites: role of crack-tip shielding. Mater Sci Eng A103:15–28

Ritchie R (1999) Mechanisms of fatigue-crack propagation in ductile and brittle solids. Int J Fract 100:55–83

Ritchie RO (2011) The conflicts between strength and toughness. Nat Mater 10:817–822

Roe K, Siegmund T (2003) An irreversible cohesive zone model for interface fatigue crack growth simulation. Eng Fract Mech 70:209–232

Roether J, Baccaccin A (2005) Dispersion-reinforced glass and glass-ceramic matrix composites. In Handbook of ceramic composites, United Kingdom, Springer, p 554

Sandvik Hard Materials (2005) Cemented carbide, Sandvik new developments and applications. http://www2.sandvik.com/sandvik

Sarikaya M (2002) Biomimetics: nanomechanical design of materials through biology. In: ASCE engineering mechanics. Columbia University, New York

Scott D (2006) The history and impact of synthetic diamond cutters and diamond enhanced inserts on the oil and gas industry. Ind Diam Rev 66(1):48–55

Shao J-J, Vail TP, Wang Q-J, Jiang Y, Zhang X-L (2013) Anatomical references for tibial sagittal alignment in total knee arthroplasty: a comparison of three anatomical axes based on 3D reconstructed CT images. Chin Med J (Engl) 126(20):3840–3844

Shao Y, Zhao H-P, Feng X-Q, Gao H (2012) Discontinuous crack-bridging model for fracture toughness analysis of nacre. J Mech Phys Solids 60:1400–1419

Shum D, Hutchinson W (1990) On toughening by microcracks. Mech Mater 9:83–90

Song F, Bai YL (2003) Effects of nanostructures on the fracture strength of the interfaces in nacre. J Mater Res 18:1741–1744

Sowmya S, Bumgardener JD, Chennazhia KP, Naira SV, Jayakumar R (2013) Role of nanostructured biopolymers and bioceramics in enamel, dentin and periodontal tissue regeneration. Prog Polym Sci 38:1748–1772

Tan H, Wie Y (1998) Toughening mechanisms of nano-composite ceramics. Mech Mater 30:111–123

Torres-Sanchez C, Corney JR (2011) A novel manufacturing strategy for bio-inspired cellular structures. Int J Design Eng 4(1):5–22

Ural A, Krishnan VR, Papoulia KD (2009) A cohesive zone model for fatigue crack growth allowing for crack retardation. Int J Solids Struct 46:2453–2462

Walter M, Ravichandran G, Ortiz M (1997) Computational modelling of damage evolution in unidirectional fiber reinforced ceramic matrix composites. Comput Mech 20:192–198

Wang C, Huang Y, Zan Q, Guo H, Cai S (2000) Biomimetic structure design: a possible approach to change the brittleness of ceramics in nature. Mater Sci Eng C 11:9–12

Wang T, Dangsheng X, Tianle Z (2010) Preparation and wear behavior of carbon/epoxy resin composites with an interpenetrating network structure derived from natural sponge. Carbon 40:2435–2441

Wanga Y, Liu Z (2008) Tribological properties of high temperature self-lubrication metal ceramics with an interpenetrating network. Wear 265:1720–1726

Westraadt JE, Sigalas I, Neethling JH (2015) Characterisation of thermally degraded polycrystalline diamond. Int J Refract Met Hard Mater 48:286–292

Yun N, Won Y, Kim S (2004) Toughening of epoxy composite by dispersing polysulfone particle to form morphology spectrum. Polym Bull 52:365–372

Zhang Y, Sahasrabudhe H, Bandyopadhyay A (2015) Additive manufacturing of Ti-Si-N ceramic coatings on titanium. Appl Surf Sci 346(15):428–437, ISSN 0169–4332

Zimmermann M, Lahres M, Viens DV, Laube BL (1997) Investigations of the wear of cubic boron nitride cutting tools using Auger electron spectroscopy and X-ray analysis by EPMA. Wear 209(1–2):241–246, ISSN 0043–1648